

CONTENTS

Ramanuj Kumar, Surjeet S. Gour, Anish Pandey, Shrestha Kumar, Abhijeet Mohan, Pratik Shashwat, Ashok K. Sahoo <i>Design and Analysis of a Novel Concept-Based Unmanned Aerial Vehicle with Ground Traversing Capability</i>	169
Andreea S. Turiac, Małgorzata Zdrodowska <i>Data Mining Approach in Diagnosis and Treatment of Chronic Kidney Disease</i>	180
Zbigniew Kamiński <i>Calculation of the Optimal Braking Force Distribution in Three-Axle Trailers with Tandem Suspension</i>	189
Muhammad B. Hafeez, Marek Krawczuk, Hasan Shahzad <i>An Overview of Heat Transfer Enhancement Based Upon Nanoparticles Influenced by Induced Magnetic Field with Slip Condition via Finite Element Strategy</i>	200
Michał Chlost, Michał Gdula <i>A New Method of the Positioning and Analysis of the Roughness Deviation in 5-Axis Milling of External Cylindrical Gear</i>	207
Stanisław Noga, Edward Rejman, Paweł Bałon, Bartłomiej Kielbasa, Robert Smusz, Janusz Szostak <i>Analytical and Numerical Analysis of Injection Pump (Stepped) Shaft Vibrations using Timoshenko Theory</i>	215
Krzysztof Nowik, Zbigniew Oksiuta <i>Experimental and Numerical Small Punch Tests of the 14Cr ODS Ferritic Steel</i>	225
Dariusz Szpica, Marcin Kisiel, Jarosław Czaban <i>Simulation Evaluation of the Influence of Selected Geometric Parameters on the Operation of the Pneumatic Braking System of a Trailer with a Differential Valve</i>	233
Heorhiy Sulym, Andrii Vasylyshyn, Iaroslav Pasternak <i>Influence of Imperfect Interface of Anisotropic Thermomagnetoelastical Bimaterial Solids on Interaction of Thin Deformable Inclusions</i>	242
Mehmet Aladag, Monika Bernacka, Magdalena Joka-Yildiz, Wojciech Grodzki, Przemysław Zamojski, Izabela Zgłobicka <i>Reverse Engineering of Parts with Asymmetrical Properties using Replacement Materials</i>	250
Marcin Zastempowski, Andrzej Bochat, Lubomir Hujo, Juraj Jablonicky, Maciej Janiec <i>Impact of Cutting Units' Design on Biomass Cutting Resistance</i>	259
Oleh Knysh, Ivan Rehei, Nazar Kandiak, Serhij Ternytskyi, Bohdan Ivaskiv <i>Experimental Evaluation of Eccentric Mechanism Power Loading of Movable Pressure Plate in Die-Cutting Press</i>	266
Samrawit A. Tewelde, Marek Krawczuk <i>Nonlinearity Effects Caused by Closed Crack in Beam and Plate: A Review</i>	274
Mateusz Kukla, Maksymilian Rachel <i>Numerical Model and an Analysis of Inertial Accumulator Operation under Selected Working Conditions</i>	286
Radosław Patyk, Łukasz Bohdal, Szymon Gontarz <i>Experimental and Numerical Investigations and Optimisation of Grain-Oriented Silicon Steel Mechanical Cutting Process</i>	292
<i>Abstracts</i>	XXI

ABSTRACTS

Ramanuj Kumar, Surjeet S. Gour, Anish Pandey, Shrestha Kumar, Abhijeet Mohan, Pratik Shashwat, Ashok K. Sahoo

Design and Analysis of a Novel Concept-Based Unmanned Aerial Vehicle with Ground Traversing Capability

Unmanned aerial vehicle (UAV) is a typical aircraft that is operated remotely by a human operator or autonomously by an on-board microcontroller. The UAV typically carries offensive ordnance, target designators, sensors or electronic transmitters designed for one or more applications. Such application can be in the field of defence surveillance, border patrol, search, bomb disposals, logistics and so forth. These UAVs are also being used in some other areas, such as medical purposes including for medicine delivery, rescue operations, agricultural applications and so on. However, these UAVs can only fly in the sky, and they cannot travel on the ground for other applications. Therefore, in this paper, we design and present the novel concept-based UAV, which can also travel on the ground and rough terrain as an unmanned ground vehicle (UGV). This means that according to our requirement, we can use this as a quadcopter and caterpillar wheel-based UGV using a single remote control unit. Further, the current study also briefly discusses the two-dimensional (2D) and three-dimensional (3D) SolidWorks models of the novel concept-based combined vehicle (UAV + UGV), together with a physical model of a combined vehicle (UAV + UGV) and its various components. Moreover, the kinematic analysis of a combined vehicle (UAV + UGV) has been studied, and the motion controlling kinematic equations have been derived. Then, the real-time aerial and ground motions and orientations and control-based experimental results of a combined vehicle (UAV + UGV) are presented to demonstrate the robustness and effectiveness of the proposed vehicle.

Andreea S. Turiac, Małgorzata Zdrodowska

Data Mining Approach in Diagnosis and Treatment of Chronic Kidney Disease

Chronic Kidney Disease (CKD) is a general definition of kidney dysfunction that lasts more than 3 months. When CKD is advanced, the kidneys are no longer able to cleanse the blood of toxins and harmful waste products and can no longer support the proper functioning of other organs. The disease can begin suddenly or develop latently over a long period of time without the presence of characteristic symptoms. The most common causes are other chronic diseases – predominantly diabetes and hypertension. Therefore, it is very important to diagnose the disease in its early stages and opt for a suitable treatment – encompassing medication, diet and exercises – to attenuate its side effects. The purpose of this paper is to analyse and select those patient characteristics that may influence the prevalence of chronic kidney disease, as well as to extract classification rules and action rules that can be useful for medical professionals in efficiently and accurately diagnosing patients with CKD. The first step of the study was feature selection and evaluation of its effect on classification results. The study was repeated for four models – containing all available patient data, features identified by doctors as major factors in CKD and models with features selected using Correlation-based Feature Selection and Chi-Square Test. Sequential Minimal Optimisation (SMO) and Multilayer Perceptron had the best performance for all four cases, with an average accuracy of 98.31% for SMO and 98.06% for Multilayer Perceptron, results that were confirmed by taking into consideration the F1-Score, which, for both algorithms, was above 0.98. For all these models, the classification rules were extracted. The final step was action rule extraction. The paper shows that appropriate data analysis allows for building models that can support doctors in diagnosing a disease and, additionally, support their decisions on treatment. Action rules can be important guidelines for doctors. They can reassure the doctor in his diagnosis or indicate new, previously unseen ways to cure the patient.

Zbigniew Kamiński

Calculation of the Optimal Braking Force Distribution in Three-Axle Trailers with Tandem Suspension

Heavy agricultural trailers can be equipped with a three-axle chassis with a tandem axle set at the rear and one mounted on a turntable at the front. In such trailers, selection of the distribution of braking forces that meet the requirements of the EU Directive 2015/68, with regard to braking, largely depends on the type of tandem suspension used. The requirements for brake force distribution in agricultural trailers of categories R3 and R4 are described. On this basis, a methodology for calculating the optimal linear distribution of braking forces, characteristic of agricultural trailers with air braking systems, was developed. An analysis of the forces acting on a 24-tonne three-axle trailer during braking was performed for five different suspensions of the rear tandem axle. An optimization algorithm using the quasi Monte Carlo method was described, on the basis of which a computer program for selection of the linear distribution of braking forces was developed. The calculations were made for an empty and loaded trailer with and without the weight of the tandem suspension. The most uniform distribution of braking forces was obtained for two leaf spring with dynamic equalization and air suspension, in which the ratio of the braking force of the tandem axle and the total braking force varied between 22.9% and 25.5% for the different calculation variants. A large variation in the braking force distribution was achieved for the two leaf spring suspension, in which the ratio of tandem axle braking force and the total braking force ranged from 2.7% to 6.4% for the leading axle and from 27.8% to 36.2% for the trailing axle. The presented calculation methodology can be used in the initial phase of the design of air braking systems for three-axle agricultural trailers.

Muhammad B. Hafeez, Marek Krawczuk, Hasan Shahzad

An Overview of Heat Transfer Enhancement Based Upon Nanoparticles Influenced by Induced Magnetic Field with Slip Condition via Finite Element Strategy

The mathematical model of heat generation and dissipation during thermal energy transmission employing nanoparticles in a Newtonian medium is investigated. Dimensionless boundary layer equations with correlations for titanium dioxide, copper oxide, and aluminium oxide are solved by the finite element method. Parameters are varied to analyze their impact on the flow fields. Various numerical experiments are performed consecutively to explore the phenomenon of thermal performance of the combination fluid. A remarkable enhancement in thermal performance is noticed when solid structures are dispersed in the working fluid. The Biot number determines the convective nature of the boundary. When the Biot number is increased, the fluid temperature decreases significantly. Among copper oxide, aluminium oxide, and titanium oxide nanoparticles, copper oxide nanoparticles are found to be the most effective thermal enhancers.

Michał Chlost, Michał Gdula

A New Method of the Positioning and Analysis of the Roughness Deviation in 5-Axis Milling of External Cylindrical Gear

Five-axis milling is a modern, flexible and constantly developing manufacturing process, which can be used for the machining of external cylindrical gears by means of cylindrical end mills and special disc mills on universal multi-axis machining centres. The article presents a new method of positioning the tip and the axis of the end mill and the disc cutter in order to ensure a constant value of deviation of the theoretical roughness R_{th} along the entire length of the tooth profile. The first part presents a mathematical model of the five-axis milling process of the cylindrical gear and an algorithm for calculating the R_{th} deviation values. The next section describes the positioning of the end mill and the disc cutter. Then, a new method for the empirical determination of the distribution of the involute root angle Δu_i and the data description by means of the interpolation function are presented and described. In the conducted numerical tests, the influence of the geometrical parameters of the cylindrical gear on the deviation R_{th} is determined, assuming a constant R_{th} value in the five-axis milling process.

Stanisław Noga, Edward Rejman, Paweł Bałon, Bartłomiej Kielbasa, Robert Smusz, Janusz Szostak

Analytical and Numerical Analysis of Injection Pump (Stepped) Shaft Vibrations using Timoshenko Theory

The free transverse vibrations of shafts with complex geometry are studied using analytical methods and numerical simulations. A methodology is proposed for evaluating the results of a natural transverse vibration analysis as generated by finite element (FE) models of a shaft with compound geometry. The effectiveness of the suggested approach is tested using an arbitrarily chosen model of the injection pump shaft. The required analytical models of the transverse vibrations of stepped shafts are derived based on the Timoshenko thick beam theory. The separation of variables method is used to find the needed solutions to the free vibrations. The eigenvalue problem is formulated and solved by using the FE representation for the shaft and for each shaft-simplified model. The results for these models are discussed and compared. Additionally, the usefulness of the Myklestad–Prohl (MP) method in the field of preliminary analysis of transverse vibration of complex shaft systems is indicated. It is important to note that the solutions proposed in this paper could be useful for engineers dealing with the dynamics of various types of machine shafts with low values of operating speeds.

Krzysztof Nowik, Zbigniew Oksiuta

Experimental and Numerical Small Punch Tests of the 14Cr ODS Ferritic Steel

Nowadays, various small specimen test techniques have gained wide popularity and appreciation among researchers as they offer undoubted benefits in terms of structural material characterisation. This paper focuses on small punch tests (SPTs) performed on small-sized disc specimens to assess the mechanical properties of 14Cr oxide dispersion strengthened (ODS) steel. A numerical model was established to support experimental data and gain deeper insight into complex strain states developing in a deformed specimen. Modern evaluation procedures were discussed for obtaining mechanical properties from the small punch force-deflection response and were compared with the literature. Applicability and universality of those relations at different test conditions were also studied. It appeared that different ball diameters used had negligible influence on yield point but strongly affected ultimate strength estimation. It was found that friction belongs to decisive factors determining strain distribution in samples, as dry conditions increase the peak strain and move its location farther from the punch pole.

Dariusz Szpica, Marcin Kisiel, Jarosław Czaban

Simulation Evaluation of the Influence of Selected Geometric Parameters on the Operation of the Pneumatic Braking System of a Trailer with a Differential Valve

This article presents simulation models of trailer air brake systems in configurations without a valve and with a differential valve, thus demonstrating the rationale for using a valve to improve system performance. Simplified mathematical models using the lumped method for systems without and with a differential valve are presented. The proposed valve can have two states of operation depending on the configuration of relevant parameters. These parameters can include the length of the control pipe, the throughput between chambers in the control part of the valve and the forcing rise time. Based on the calculations, it was found that the differential valve with large control pipe lengths can reduce the response time of the actuator by 42.77% relative to the system without the valve. In the case of transition of the valve to the tracking action, this time increases only by 9.93%. A force rise time of 0.5 s causes the transition of the valve from the accelerating action to the tracking action, with 9.23% delay relative to the system without a valve. The calculations can be used in the preliminary assessment of the speed of operation of pneumatic braking systems and in the formulation of guidelines for the construction of a prototypical differential valve. In conclusion, it is suggested to use a mechatronic system enabling smooth adjustment of the flow rate between chambers of the control system of the differential valve.

Heorhiy Sulym, Andrii Vasylyshyn, Iaroslav Pasternak

Influence of Imperfect Interface of Anisotropic Thermomagnetoelastic Bimaterial Solids on Interaction of Thin Deformable Inclusions

This work studies the problem of thermomagnetoelastic anisotropic bimaterial with imperfect high-temperature conducting coherent interface, whose components contain thin inclusions. Using the extended Stroh formalism and complex variable calculus, the Somigliana-type integral formulae and the corresponding boundary integral equations for the anisotropic thermomagnetoelastic bimaterial with high-temperature conducting coherent interface are obtained. These integral equations are introduced into the modified boundary element approach. The numerical analysis of new problems is held and results are presented for single and multiple inclusions.

Mehmet Aladag, Monika Bernacka, Magdalena Joka-Yildiz, Wojciech Grodzki, Przemysław Zamojski, Izabela Zgłobicka

Reverse Engineering of Parts with Asymmetrical Properties using Replacement Materials

Reverse engineering (RE) aims at the reproduction of products following a detailed examination of their construction or composition. Nowadays, industrial applications of RE were boosted by combining it with additive manufacturing. Printing of reverse-engineered elements has become an option particularly when spare parts are needed. In this paper, a case study was presented that explains how such an approach can be implemented in the case of products with asymmetric mechanical properties and using replacement materials. In this case study, a reverse engineering application was conducted on a textile machine spare part. To this end, the nearest material was selected to the actual material selection and some mechanical tests were made to validate it. Next, a replacement part was designed by following the asymmetric push-in pull-out characteristic. Finally, the finite element analysis with Additive Manufacturing was combined and validated experimentally.

Marcin Zastempowski, Andrzej Bochat, Lubomir Hujo, Juraj Jablonicky, Maciej Janiec

Impact of Cutting Units' Design on Biomass Cutting Resistance

The paper presents mathematical models describing the moments of resistance to cutting on the cutting drum shafts in the biomass cutting process. The mathematical procedures described in the paper have been verified on a test stand developed and constructed by the authors, which reflects real conditions of the process of cutting plant material into pieces of specified lengths. Experimental verification proved that the developed mathematical models are adequate for drums of both cylindrical and conical constructions. The value of the average error did not exceed 13%. Following the mathematical elaboration and verification studies, the authors carried out calculations for machines currently available on the market that are equipped with drum cutting units. The calculations were carried out for the most commonly cut material, i.e. for maize, straw and green plant materials. The obtained results confirm the complexity of the problem arising from a wide range of numerical values of cutting resistance, which is contained in the range of 400–1,800 nm. The compiled database can be practically applied in the selection of machines for specific field works, and the mathematical models developed and verified in the study can be applied at the stage of designing new designs of cutting drums used in forage harvesters.

Oleh Knysh, Ivan Rehei, Nazar Kandiak, Serhij Ternytskyi, Bohdan Ivaskiv
Experimental Evaluation of Eccentric Mechanism Power Loading of Movable Pressure Plate in Die-Cutting Press

The paper reports experimental research on torques during cardboard cutting in the die-cutting press with eccentrics in the drive of the movable pressure plate. To conduct the research, an experimental bench with eccentrics in the drive of the die-cutting press is designed and manufactured. The manufactured experimental device for the research on cardboard blanks provides the possibility of getting dependencies of loadings at different parameters of the die-cutting process. The experimental approach envisages the use of the strain gauge measurement method and the wireless module for data collecting, as well as the software for its processing, for getting trustworthy results with minimum faults. The method gives an opportunity to study the torque values during the cardboard-cutting efforts on the drive shaft. The paper shows changes in the torque value on the drive shaft during the kinematic cycle with and without the use of cardboard blank. The angle of the drive shaft rotation during the cutting process was evaluated at selected values of the cardboard thickness. The relationship between the linear cutting efforts and the cardboard thickness, its fibre direction, cutting rule type and rotational speed of the drive shaft is elaborated. This kind of data is approximated by a logarithmic function (logarithmic curve), at R^2 from 0.90 to 0.98. The thickness of the cardboard significantly influences the value of the linear cutting effort at all the studied parameters.

Samrawit A. Tewelde, Marek Krawczuk
Nonlinearity Effects Caused by Closed Crack in Beam and Plate: A Review

The effect of nonlinearity is high sensitivity in damage detection, especially for closed cracks and delamination. This review illustrates the results of several researchers dealing with nonlinear effects caused by the closure of cracks in the structure, i.e., beam and plate structures. Early detection of damage is an important aspect for the structure and, therefore, continuous progress is being made in developing new and effective methods that use nonlinear effects for early detection of damage and barely visible cracks, i.e., closed cracks and delamination, as well as for the determination of crack size and location. After analysing various methods, the merits, drawbacks and prospects of a number of nonlinear vibration methods for structural damage detection are discussed, and recommendations are made for future researchers.

Mateusz Kukla, Maksymilian Rachel
Numerical Model and an Analysis of Inertial Accumulator Operation under Selected Working Conditions

The aim of this paper was to create a computational model that will enable the evaluation of the operation of a conventional inertia accumulator. This is an issue that is relevant as storage of energy is becoming increasingly important, in particular when it comes to generating electricity from renewable sources. In the course of the conducted works, an analytical model was developed based on the available literature, and then, it was introduced into the environment for numerical calculations. Four variants resulting from different geometrical parameters of the flywheel were adopted successively. On this basis, a series of simulations were performed, which allowed for obtaining the characteristics of the analysed solutions. As a consequence, a number of characteristics related to the mechanical power and energy of the simulated kinetic energy accumulators were obtained. The test results therefore provide a basis for comparing kinetic energy accumulators with different geometries and drive solutions.

Radosław Patyk, Łukasz Bohdal, Szymon Gontarz
Experimental and Numerical Investigations and Optimisation of Grain-Oriented Silicon Steel Mechanical Cutting Process

The process of mechanical cutting of magnetic materials has many advantages in the form of high efficiency with reduced process costs in relation to other cutting technologies; no thermal stresses in the material, which significantly deteriorate the magnetic properties; or the possibility of shaping materials taking into account long cutting lines. In industrial practice, it is very difficult to ensure appropriate conditions for the cutting process and its proper control. Currently, there are no data on the selection of technological parameters of the mechanical shear slitting process of grain-oriented silicon steel in terms of the obtained cutting surface quality and the obtained magnetic properties of the workpiece. The article presents the possibilities of forecasting the characteristic features of the cut edge and selected magnetic properties of grain-oriented silicon steel. For this purpose, proprietary numerical models using FEA (Finite Element Analysis) were used. Then, experimental studies were carried out, and the optimisation task was developed. The developed results enable the correct selection of technological parameters of the process, ensuring the appropriate quality of the cut edge of steel and minimal interference with the magnetic properties.

DESIGN AND ANALYSIS OF A NOVEL CONCEPT-BASED UNMANNED AERIAL VEHICLE WITH GROUND TRAVERSING CAPABILITY

Ramanuj KUMAR^{*}, Surjeet S. GOUR^{*}, Anish PANDEY^{*}, Shrestha KUMAR^{*},
Abhijeet MOHAN^{*}, Pratik SHASHWAT^{*}, Ashok K. SAHOO^{*}

^{*}School of Mechanical Engineering, Kalinga Institute of Industrial Technology Deemed to be University,
An Institute of Eminence, Patia, Campus-8, Bhubaneswar, 751024, Odisha, India

ramanujme@kiit.ac.in, surjeetgour59@gmail.com, anish06353@gmail.com, 1602403@kiit.ac.in,
1602389@kiit.ac.in, 1602351@kiit.ac.in, asahoofme@kiit.ac.in

received 26 November 2021, revised 16 February 2022, accepted 1 March 2022

Abstract: Unmanned aerial vehicle (UAV) is a typical aircraft that is operated remotely by a human operator or autonomously by an on-board microcontroller. The UAV typically carries offensive ordnance, target designators, sensors or electronic transmitters designed for one or more applications. Such application can be in the field of defence surveillance, border patrol, search, bomb disposals, logistics and so forth. These UAVs are also being used in some other areas, such as medical purposes including for medicine delivery, rescue operations, agricultural applications and so on. However, these UAVs can only fly in the sky, and they cannot travel on the ground for other applications. Therefore, in this paper, we design and present the novel concept-based UAV, which can also travel on the ground and rough terrain as an unmanned ground vehicle (UGV). This means that according to our requirement, we can use this as a quadcopter and caterpillar wheel-based UGV using a single remote control unit. Further, the current study also briefly discusses the two-dimensional (2D) and three-dimensional (3D) SolidWorks models of the novel concept-based combined vehicle (UAV + UGV), together with a physical model of a combined vehicle (UAV + UGV) and its various components. Moreover, the kinematic analysis of a combined vehicle (UAV + UGV) has been studied, and the motion controlling kinematic equations have been derived. Then, the real-time aerial and ground motions and orientations and control-based experimental results of a combined vehicle (UAV + UGV) are presented to demonstrate the robustness and effectiveness of the proposed vehicle.

Key words: unmanned aerial vehicle, unmanned ground vehicle, rough terrain, quadcopter, caterpillar wheel, kinematic analysis

1. INTRODUCTION

1.1. Background and literature review

Unmanned aerial vehicles (UAVs) come under low-cost, light-weight and low airspeed aircraft, which are generally used to obtain aerial photographs [1] and in other remote sensing data collections. However, it is not easy to take aerial images in dense forest conditions with existing UAVs [2]. Therefore, in this condition, we can go for an unmanned ground vehicle (UGV) to capture the photographs. Further, we need a common vehicle, which can work as a UAV and UGV simultaneously according to our requirements and environmental conditions. UAV problems [3] can be divided into various categories such as navigation, motion planning, trajectory tracking, surveillance and so on. Moreover, these problems can be mathematically represented through the Newton–Euler method or Lagrangian formula, and both methods are applied for an underactuated complex UAV system. The purpose of trajectory tracking is to control the motion of a quadcopter in a predefined path by calculating the rotor velocities of a quadcopter. UAVs are also known as drones, and they have a simple mechanical chassis and are mainly lifted and propelled by four independent blades or rotors. In addition, these UAVs come in different sizes, shapes and number of rotors. Glida et al. [4] presented the dynamic analysis of a quadcopter. They optimised

the various controlling parameters such as roll, pitch and yaw angles by implementing a cuckoo search optimisation algorithm. Labadi and Cherkaoui [5] used the Euler–Newton formula to design the dynamic model for a quadcopter. They tried to solve the external disturbance problem using the proportional integral derivative (PID) sliding mode control. However, in that investigation, only computer simulation results were displayed, and real-time experimental results were not obtained. Hassani et al. [6] used Newtonian formalism and designed a robust adaptive non-linear controller to solve the path-tracking problem of a quadcopter under disturbed environment conditions.

Most researchers [4, 5, 6, 7] have tried to solve the trajectory tracking problems under disturbed conditions. However, they have only shown the computer simulation results in their work, and have not reported the real-time experiment results of a quadcopter. A particle swarm optimisation (PSO)-tuned adaptive neuro-fuzzy inference system (ANFIS) controller is implemented by Selma et al. [7] to achieve a robust trajectory tracking scheme for a three-degree freedom quadcopter in a disturbed environment condition. An extensive review article on motion planning of quadcopters or drones and their various control techniques was reported by Elijah et al. [8], and although these authors discussed the physical results associated with the experimental deployment of a quadcopter, they were not elaborately reported in that work. Moreover, Heidari and Saska [9] briefly discussed the different types of quadcopters such as fixed-wing and multi-rotor and their

advantages and disadvantages in various applications with a comparative analysis. The research by Abdalla and Al-Baradie [10] integrated the PSO algorithm with the PID controller to design a steer control scheme for a quadcopter. The cognitive architecture-based decision-making control method for UAVs was designed by Pinto et al. [11].

Route planning with optimum path selection is also an important problem in UAV motion. Many researchers have also addressed this problem, and some related works [12, 13, 14, 15, 16] are cited here. Route planning for a quadcopter or UAV is to search the optimal flight path from the source point to a destination to reduce the time and energy [12]. Therefore, Xu et al. [12] implemented a gravitational search algorithm to address this issue. The MATLAB graphical user interface module was used to show the different 2D and 3D flight motion results. Another similar type of work was found in an article by Zhang and Duan [13], in which the authors applied a differential evolution algorithm for the global route planning of a UAV in a 3D environment. Further, previous studies applied some more optimisation algorithms such as the genetic algorithm (GA) [14], ant colony optimisation (ACO) [15], water drops optimisation algorithm [16] and hybrid GA [17] to search feasible optimal routes for UAVs. However, they have not focused on designing a UAV and its real-time experimental results. Silva et al. [17] used the flight-gear simulator to show the fly motion results of a UVA under different wind speeds and directions. Comparative performance analysis of different multi-objective evolutionary algorithms as a path planner of UAV has been studied by Besada-Portas et al. [18]). Cui and Wang [19] implemented the reinforcement learning algorithm to design local and global path planners for a UAV among static and moving obstacles. Yao and Zhao [20] suggested the model predictive control algorithm to search optimal or sub-optimal collision-free trajectories for a UAV in the midst of dynamic obstacle conditions. However, Besada-Portas et al. [18]; Cui and Wang [19]; and Yao and Zhao [20] have shown the software-based computer simulation results of UAVs in their studies. Heidari and Saska [9] developed a heuristic approach-based open-loop control system to select optimal values of the dynamic control parameters such as thrust force and torque of a quadcopter for trajectory optimisation.

After summarising the above-cited scientific literature, we find that most of the work has been based on either trajectory tracking control or path planning of a UAV or quadcopter. Moreover, many authors have only presented the software-based simulation results in their studies, and they have not focused on any new concept-based quadcopter designing. Therefore, we have tried to design and fabricate the novel concept-based UAV in this work, which can also travel on the ground and rough terrain, as a UGV.

1.2. Important contribution

This paper’s contributions are summarised as follows: First, a new concept-based combined vehicle (UAV + UGV) is designed and fabricated, which can fly as a quadcopter or UAV, and it can also travel on the ground, rough terrain and rough narrow paths as a UGV or a wheeled robot. Next, the various kinematic equations are explained briefly and embedded in the microcontroller. Then, the flying and ground motion and orientation of the UAV and caterpillar wheel-based UGV are controlled during navigation through a single control unit or remote controller. Further, the SolidWorks model of a combined vehicle (UAV + UGV) and its

various connected parts is briefly discussed with different 2D and 3D pictorial representations. Finally, the other equipped electronic hardware components of a combined vehicle (UAV + UGV) and its real-time flying and ground motions and orientation results are presented to demonstrate the robustness and effectiveness of the designed vehicle.

1.3. Paper organisation

The rest of the paper is organised as follows: Section 2 reveals the kinematic equations for the UAV and its attached caterpillar wheel-based UGV arrangement, which are applied to control the flying and ground motion and orientation of the whole vehicle. The various 2D and 3D SolidWorks models of a combined vehicle (UAV + UGV) are presented in Section 3. Section 4 briefly discusses the various electronic components of a combined vehicle (UAV + UGV) and shows the real-time experimental results. Finally, Section 5 provides the salient points of the current investigation, together with the conclusions reached.

2. KINEMATIC STUDY OF THE UAV AND ITS ATTACHED CATERPILLAR WHEEL-BASED UGV

This section reveals the kinematic equations for the UAV and its attached caterpillar wheel-based UGV, which are used to control the flying and ground motion and orientation of a combined vehicle (UAV + UGV). Fig. 1 shows the pictorial representation of various kinematic and dynamic indices of only UAV in the 3D workspace.

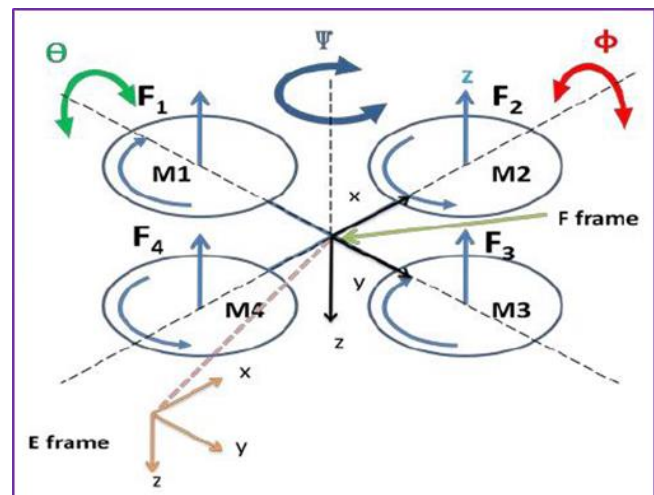


Fig. 1. Pictorial representation of various kinematic and dynamic indices of only UAV in the 3D workspace. UAV, unmanned aerial vehicle

Lightweight glass fibre is used to construct the frame of the UAV because the structural rigidity of this glass fibre is high. The centre part of the frame carries various electronic components such as flight controller, motor driver, receiver, battery, Arduino microcontroller and so on. The frame also has four spider arms protruding from it, which accommodate brushless DC motors, and the motors provide sufficient rotational motions to the rotors. These rotors are fixed to the tip of motors and produce adequate thrust to lift off a combined vehicle. The arms also consist of the

electronic speed controller (ESC) for controlling the rotational speed of the motors, and the ESC controls the directions of the UAV. This UAV performs six motions in total (three translations and three rotations) by using its attached four rotors, and it consists of multiple input and output control systems. In Fig. 1, $A_E = [X_E, Y_E, Z_E]^T$ defines the absolute linear position vector of the UAV and $\dot{A}_E = [\dot{X}_E, \dot{Y}_E, \dot{Z}_E]^T$ represents the linear velocity vector with respect to the E reference frame in the 3D workspace. The $\alpha = [\theta, \phi, \Psi]^T$ is the angular displacement or attitude vector with respect to the E reference frame, where ϕ , θ and Ψ reveal the Euler angles of roll, pitch and yaw, respectively. A

$$R_R = \begin{bmatrix} c(\theta)c(\Psi) & s(\phi)s(\theta)c(\Psi) - c(\phi)s(\Psi) & c(\phi)s(\theta)c(\Psi) + s(\phi)s(\Psi) \\ c(\theta)s(\Psi) & s(\phi)s(\theta)s(\Psi) + c(\phi)c(\Psi) & c(\phi)s(\theta)c(\Psi) - s(\phi)c(\Psi) \\ -s(\theta) & s(\phi)c(\theta) & c(\phi)c(\theta) \end{bmatrix} \quad (1)$$

$$\begin{bmatrix} \dot{X}_E \\ \dot{Y}_E \\ \dot{Z}_E \end{bmatrix} = R_R \cdot \dot{A}_F = \begin{bmatrix} c(\theta)c(\Psi) & s(\phi)s(\theta)c(\Psi) - c(\phi)s(\Psi) & c(\phi)s(\theta)c(\Psi) + s(\phi)s(\Psi) \\ c(\theta)s(\Psi) & s(\phi)s(\theta)s(\Psi) + c(\phi)c(\Psi) & c(\phi)s(\theta)c(\Psi) - s(\phi)c(\Psi) \\ -s(\theta) & s(\phi)c(\theta) & c(\phi)c(\theta) \end{bmatrix} \cdot \begin{bmatrix} \dot{x}_F \\ \dot{y}_F \\ \dot{z}_F \end{bmatrix} \quad (2)$$

$$\dot{X}_E = \dot{x}_F \cdot (c(\theta)c(\Psi)) + \dot{y}_F \cdot (s(\phi)s(\theta)c(\Psi) - c(\phi)s(\Psi)) + \dot{z}_F \cdot (c(\phi)s(\theta)c(\Psi) + s(\phi)s(\Psi)) \quad (3)$$

$$\dot{Y}_E = \dot{x}_F \cdot (c(\theta)s(\Psi)) + \dot{y}_F \cdot (s(\phi)s(\theta)s(\Psi) + c(\phi)c(\Psi)) + \dot{z}_F \cdot (c(\phi)s(\theta)c(\Psi) - s(\phi)c(\Psi)) \quad (4)$$

$$\dot{Z}_E = \dot{x}_F \cdot (-s(\theta)) + \dot{y}_F \cdot (s(\phi)c(\theta)) + \dot{z}_F \cdot (c(\phi)c(\theta)) \quad (5)$$

where R_R describes the rotational matrix for the UAV from the F body frame to the E reference frame and c and s denote the cosine and sine trigonometry terms, respectively. The angular transformation matrix R_T from the F body frame to the E reference frame can be formulated as:

$$R_T = \begin{bmatrix} 1 & s(\phi)t(\theta) & c(\phi)t(\theta) \\ 0 & c(\phi) & -s(\phi) \\ 0 & \frac{s(\phi)}{c(\theta)} & \frac{c(\phi)}{c(\theta)} \end{bmatrix} \quad (6)$$

where t symbolises the tangent trigonometry term. After calculating the linear velocities of the UAV, we calculate the values of angular velocities from the F body frame to the E reference frame as:

$$\begin{bmatrix} \dot{\theta} \\ \dot{\phi} \\ \dot{\Psi} \end{bmatrix} = R_T \cdot \beta = \begin{bmatrix} 1 & s(\phi)t(\theta) & c(\phi)t(\theta) \\ 0 & c(\phi) & -s(\phi) \\ 0 & \frac{s(\phi)}{c(\theta)} & \frac{c(\phi)}{c(\theta)} \end{bmatrix} \cdot \begin{bmatrix} \dot{m} \\ \dot{n} \\ \dot{o} \end{bmatrix} \quad (7)$$

$$\dot{\theta} = \dot{m} + \dot{n} \cdot (s(\phi)t(\theta)) + \dot{o} \cdot (c(\phi)t(\theta)) \quad (8)$$

$$\dot{\phi} = \dot{n} \cdot (c(\phi)) - \dot{o} \cdot (s(\phi)) \quad (9)$$

$$\dot{\Psi} = \dot{n} \cdot \left(\frac{s(\phi)}{c(\theta)}\right) + \dot{o} \cdot \left(\frac{c(\phi)}{c(\theta)}\right) \quad (10)$$

For the dynamic equations of motion for the UAV, we consider the Newton–Euler formula [5, 6].

The caterpillar wheel-based UGV is made up of lightweight glass fibre panels and joined with the base of the UAV's frame using nut and bolt. The two holes on each side of the fibre panels are punched to connect the four DC motors, and these motors are attached with the caterpillar driving wheels, which carry the mechanical frame. The two caterpillar driving wheels set, connected on the left side of a combined vehicle (UAV + UGV), are controlled as a left-wheel driving system. Similarly, another two caterpillar driving wheels set, attached on the right side of a combined vehicle, are completely run on the ground as a right-wheel driving system. U_L denotes the left-wheel driving system, and U_R repre-

combined vector $q = [A_E, \alpha]^T$ represents the linear and angular position vectors of the UAV. Similarly, $A_F = [x_F, y_F, z_F]^T$ defines the absolute linear position vector of the UAV and $\dot{A}_F = [\dot{x}_F, \dot{y}_F, \dot{z}_F]^T$ represents the linear translation velocity vector with respect to the F body frame in the 3D workspace. And $\beta = [\dot{m}, \dot{n}, \dot{o}]^T$ defines the angular velocity vector with respect to the F body frame. The kinematic study of the UAV reveals the relationship between the reference frame and the body frame [5]. The rotation and translation kinematic equations can be described as follows:

sents the right-wheel driving system in the kinematic equations. Fig. 2 illustrates the graphical representation of various kinematic and dynamic indices of the caterpillar wheel-based UGV system in the 2D workspace.

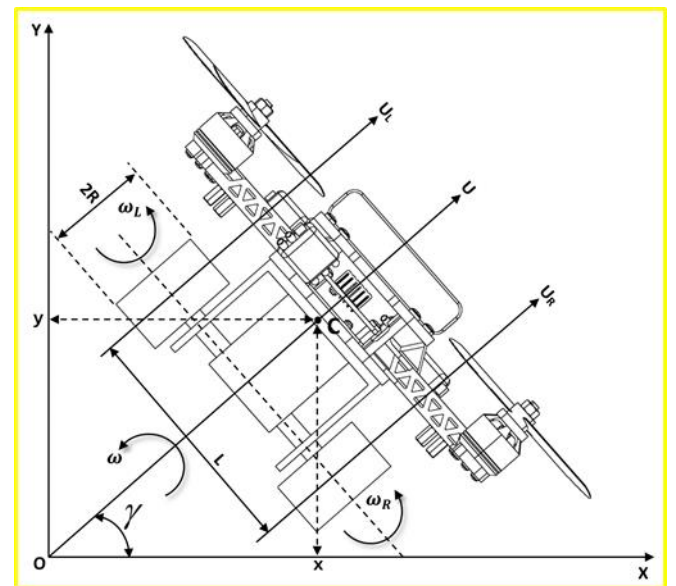


Fig. 2. Graphical representation of various kinematic and dynamic indices of caterpillar wheel-based UGV system in the 2D workspace (UGV, unmanned ground vehicle)

The axes (x, y) are the current location of the UGV system from the origin O point in the global frame $\{O, X, Y\}$. In Fig. 2, γ indicates the steering control angle of the UGV with respect to an axis (O, X) , L is the track width between the left and right driving systems, R is the radius of the wheel and C is the centre of mass of the UGV. The following kinematic equations control the velocities and steering angle of the UGV:

$$U = \frac{R}{2} \cdot (\omega_R + \omega_L) = \frac{U_R + U_L}{2} \quad (11)$$

$$\omega = \dot{\gamma} = \frac{R}{L} \cdot (\omega_R - \omega_L) = \frac{U_R - U_L}{L} \quad (12)$$

where U and ω symbolise the centre (mean) linear velocity and centre angular velocity of the UGV, respectively. These U and ω control the motion and orientation of the UGV in the C/C++ micro-controller programming, respectively. Next, ω_R and ω_L represent the angular velocities of the right-wheel driving system and left-wheel driving system, respectively.

Further, the following equations express the velocity (linear and angular) with respect to time:

$$\frac{dx}{dt} = \dot{x}(t) = U \cdot \cos \gamma = \frac{R}{2} (\omega_R + \omega_L) \cdot \cos \gamma \quad (13)$$

$$\frac{dy}{dt} = \dot{y}(t) = U \cdot \sin \gamma = \frac{R}{2} (\omega_R + \omega_L) \cdot \sin \gamma \quad (14)$$

$$\frac{d\theta}{dt} = \dot{\theta}(t) = \omega = \frac{R}{L} (\omega_R - \omega_L) \quad (15)$$

Next, the following conditions are used for the linear and angular motion controls of the UGV:

1. If ($U_R = U_L$), then the UGV travels straight.
2. If ($U_R > U_L$), then the UGV turns left.
3. If ($U_R < U_L$), then the UGV turns right.

3. BRIEF DESCRIPTION OF THE VARIOUS COMPONENTS OF THE UAV AND ITS ATTACHED CATERPILLAR WHEEL-BASED UGV

This section provides a brief description of various components of a combined vehicle (UAV + UGV). We have used Solid-Works software to design the prototype model, and we have presented the different 2D and 3D views of a combined vehicle (UAV + UGV). Figs. 3–8 illustrate the various 2D and 3D views of a combined vehicle (UAV + UGV). Tab. 1 (ESC, electronic speed controller; UAV, unmanned aerial vehicle; UGV, unmanned ground vehicle.) summarises the defined part numbers and names of the various components of a combined vehicle (UAV + UGV). A brief description of some figures and the connections of various components has been provided below.

Tab. 1. Part numbers and names of the various components of a combined vehicle (UAV + UGV)

Part Number	Part Name
1	Rotors or blades
2	Brushless motors for rotors
3	Electronic system box
4	Right wheel driving system
5	Left wheel driving system
6	UGV's frame
7	Spider arms
8	DC motors for UGV's wheels
9	Shafts of right side DC motors
10	Shafts of Left Side DC Motors
11	UAV's frame
12	Bolt to connect arms
13	Nut
14	ESC

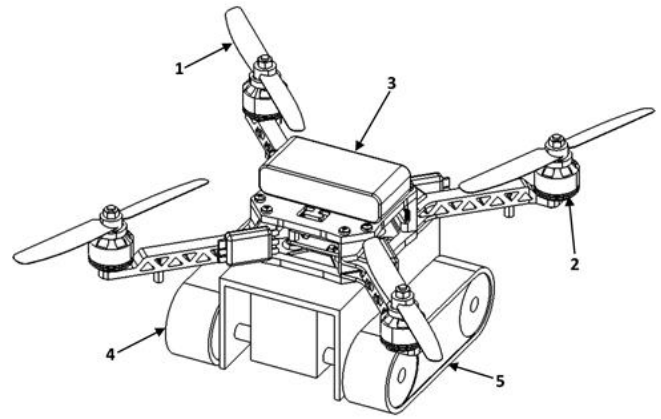


Fig. 3. Isometric view of a combined vehicle (UAV + UGV), (UAV, unmanned aerial vehicle; UGV, unmanned ground vehicle)

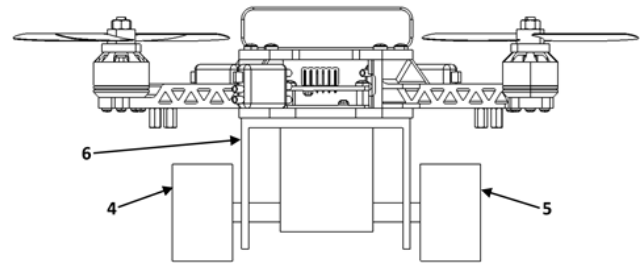


Fig. 4. Front view of a combined vehicle (UAV + UGV), (UAV, unmanned aerial vehicle; UGV, unmanned ground vehicle)

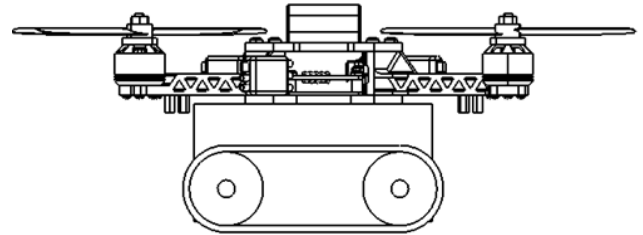


Fig. 5. Side view of a combined vehicle (UAV + UGV), (UAV, unmanned aerial vehicle; UGV, unmanned ground vehicle)

As illustrated in Fig. 3, the proposed vehicle (UAV + UGV) includes rotors or blades (1), brushless motors for rotors (2), an electronic system box (3), right wheel driving system (4), left wheel driving system (5), a UGV's frame (6) and a UAV's frame (11). The ground traversing device or UGV facilitates the whole vehicle (UAV + UGV) to traverse the ground or any terrain. In a vehicle (UAV + UGV), the electronic system box (3) is used to control the flying and ground motions and orientation of the aerial driving mechanism and ground traversing mechanism. The electronic system box (3) includes one transceiver configured to communicate between the remote control and vehicle and transfers the data, e.g. video or image data and commands, enabling the electronic system box (3) to control the aerial driving and the ground traversing mechanism. This electronic system box (3) is configured to control the aerial driving mechanism and the ground traversing mechanism independently. In a combined vehicle (UAV + UGV), the electronic system box (3) may include one or more sensors configured to measure one or more attributes pertaining to, by way of example but not limited to, location, environment and properties of the ground surface. For example, a combined vehicle (UAV + UGV) may include ground penetrating radar

(GPR) sensors that may sense one or more properties of the ground surface, such as but not limited to the type of rock, soil and ice; availability of freshwater; pavements; and structures. With the help of the GPR sensors, the UAV can detect improvised explosive devices (IED) and landmines, which is advantageous in the field of defence. Moreover, it can be useful in research areas where the surface changes in materialistic property need to be detected.

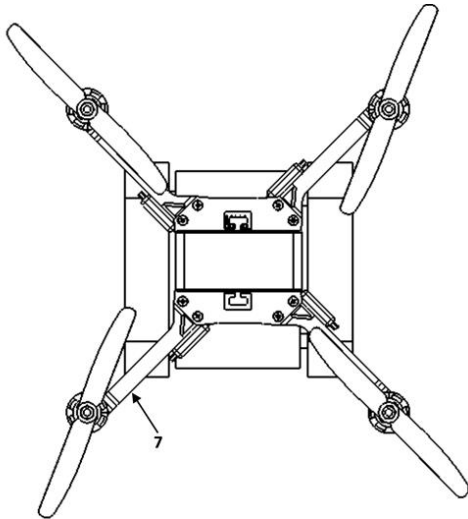


Fig. 6. Top view of a combined vehicle (UAV + UGV), (UAV, unmanned aerial vehicle; UGV, unmanned ground vehicle)

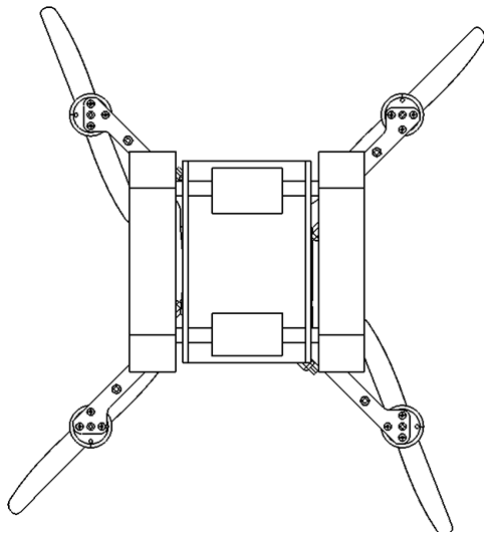


Fig. 7. Bottom view of a combined vehicle (UAV + UGV), (UAV, unmanned aerial vehicle; UGV, unmanned ground vehicle)

The electronic system box (3) includes a calibration unit and a compass unit. The calibration unit may allow, for example, the calibration of a vehicle (UAV + UGV) regarding a predefined plane in a coordinate system, e.g. to determine the roll and pitch angle of a vehicle (UAV + UGV) with respect to the gravity vector (e.g. from planet Earth). Thus, an orientation of a vehicle (UAV + UGV) in a coordinate system may be determined. The orientation of a vehicle (UAV + UGV) may be calibrated using the calibration unit before a vehicle (UAV + UGV) is operated in-flight modus. However, any other suitable function for navigation of a vehicle (UAV + UGV), e.g. for determining a position, a flight velocity, a flight direction and so on, may be implemented in the electronic

system box (3). In a vehicle (UAV + UGV), the UAV's frame (11) includes a camera to capture an image of the surroundings and to provide the captured image to the microcontroller of an electronic system box (3). This electronic system box (3) is configured to process the captured images and determine one or more attributes pertaining to the object. For example, the electronic system box (3) identifies the position of objects in the image. The electronic system box (3) consists of a transmitter that may be configured to transmit information such as, but not limited to, information about the captured image to a server or the remote location.

Fig. 8 depicts an exploded view of a combined vehicle (UAV + UGV), which indicates all the important components of a vehicle. The UAV's driving assembly includes rotors or blades (1), spider arms (7) and brushless motors (2) for aerial movement. In an aspect, the UAV's driving assembly consists of four brushless motors (2), and motors (2) are attached with the spider arm (7). In a vehicle (UAV + UGV), the UAV's frame also includes a driving circuit ESC (14) that is attached to the brushless motors (2). The driving circuit may also be operatively connected to the electronic system box (3). The electronic system box (3) provides an input signal to the driving circuits to drive the brushless motors (2). In a UAV's driving assembly, the rotors or blades (1) are configured to rotate in at least two anticlockwise and clockwise directions. The rotation of rotors or blades (1) provides an upward lift to the UAV and facilitates a vehicle (UAV + UGV) to move in the air. In a vehicle (UAV + UGV), the ground traversing device or UGV includes the UGV's frame (6), caterpillar wheel-based right-wheel driving system (4), left-wheel driving system (5) and DC motors (8). The ground traversing device is attached to the lower portion of the UAV's frame (11). The configuration of the ground traversing device with the vehicle enables the vehicle to traverse on the surface, i.e. provides the ground traversing capability. In a vehicle (UAV + UGV), the ground traversing device includes a control unit to control the rotation of the DC motors (8). The control unit is implemented as a hardware component in an electronic system box (3). In a different embodiment, the control unit is implemented as a computer program product, which includes a computer-readable storage medium employing a set of instructions. The ground traversing device also consists of the DC motors (8) configured to rotate selectively in clockwise and anticlockwise directions. The motor driver of the ground traversing device controls the direction of the rotation of the DC motors (8) and the amount of the rotation of the DC motors (8).

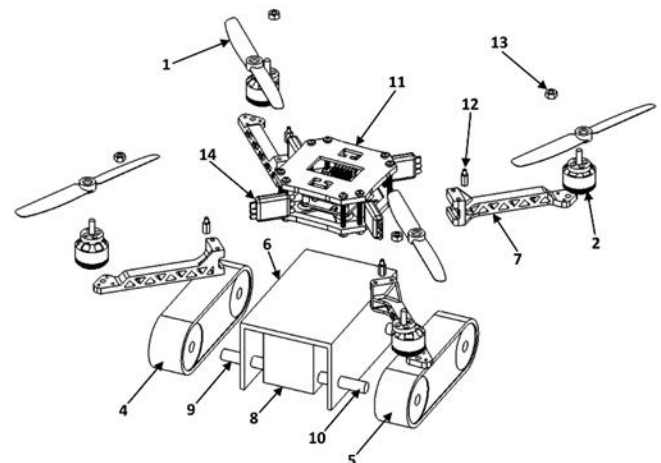


Fig. 8. Exploded view of all the components of a combined vehicle (UAV + UGV), (UAV, unmanned aerial vehicle; UGV, unmanned ground vehicle)

The ground traversing device also includes a caterpillar wheel-based right-wheel driving system (4) and a left-wheel driving system (5) operatively coupled to the shafts of the right-side DC motors (9) and the left-side DC motors (10), respectively, and configured to rotate in the clockwise and anticlockwise directions. The coupling of DC motors (8) enables the caterpillar wheel-based right wheel driving system (4) and left wheel driving system (5) to rotate in the direction of the rotation. Particularly, the rotation of the DC motors (8) in a clockwise direction facilitates the rotation of the caterpillar wheels in a clockwise direction, and the rotation of the DC motors (8) in an anticlockwise direction provides the rotation of the caterpillar wheels in an anticlockwise direction. In an embodiment, the ground traversing device or UGV system is attached to the existing vehicle to provide the ground traversing capability. The electronic box system (3) provides the input to the driving circuits to drive the DC motors (8). As illustrated in Fig. 8, the UGV's frame (6) of the ground traversing device is attached to the lower portion of a UAV's frame (11). This UGV's frame (6) is attached to UAV's frame (11) by bolt (12) and nut (13). The UGV's frame (6) of the ground traversing device is attached to the aerial driving assembly, at its one side that is opposite to another side of the UGV's frame (6), at which the wheel and DC motors (8) are attached for the ground traversing mechanism.

4. EXPERIMENTAL STUDY

This section briefly discusses the various electronic components of a combined vehicle (UAV + UGV). It also presents the experimental results to demonstrate the effectiveness of the developed vehicle in real-time applications. In addition, we describe the working principle of various electronic components that are used in a vehicle. Fig. 9 A–E illustrates snapshots of the different views (isometric, top, bottom, front and side) of the physical model of a combined vehicle (UAV + UGV). Moreover, this figure shows the various electronic components of a vehicle. The chassis and spider arms of a combined vehicle (UAV + UGV) are made up of lightweight glass fibre. A combined vehicle's length, width and height are 60 cm, 60 cm and 16 cm, respectively. The length of each spider arm is 49 cm. Similarly, the track width and wheel-base distance of the UGV's caterpillar driving wheels are 26 cm and 21 cm, respectively. The attached electronic components of a vehicle and their specifications are given in Tab. 2 (ESC, electronic speed controller; UAV, unmanned aerial vehicle; UGV, unmanned ground vehicle). The vehicle's ground and aerial motions are controlled with the help of these electronic components.

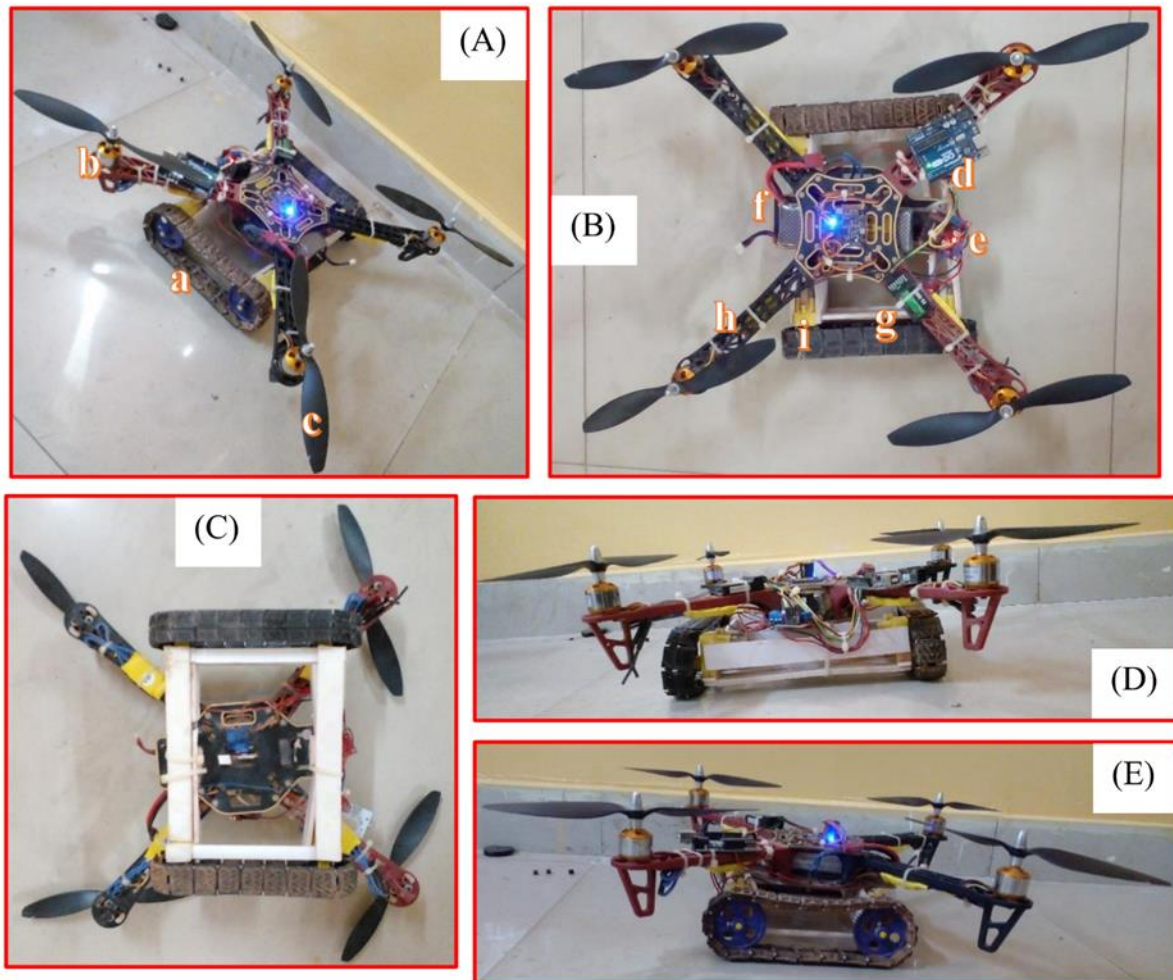


Fig. 9. Snapshots of different views of the physical model of a combined vehicle (UAV + UGV) with the information of various electronic components: (a) Isometric view, (b) Top view, (c) Bottom view, (d) Front view, (e) Side view, (note: a – Caterpillar wheel driving system, b – Brushless motors for rotors, c – Rotors or Blades, d – Arduino microcontroller, e – Motors driver, f – LiPo battery, g – ESC, h – Spider arms, i – DC motors for UGV's wheels. ESC, electronic speed controller; UAV, unmanned aerial vehicle; UGV, unmanned ground vehicle)

Tab. 2. Specifications of various electronic components of a combined vehicle (UAV + UGV)

Name	Specification
Microcontroller	Arduino UNO (ATmega328P)
Switch	On-off switch
Motors for UGV's caterpillar wheel	12 V, 100 RPM, DC Motor
Motors for rotor or blade	Brushless motor, A2212/13T, 1,000 KV
Motors driver for UGV's caterpillar wheel	L298N, dual DC motor driver
Flight controller board	Naze32, Rev6, 32-bit, 6DOF
Transmitter and receiver for a combined vehicle (UAV + UGV)	CT6B Remote six channel transmitter and receiver
ESC	30 Amp
Caterpillar wheels	Wheel radius: 30 mm; Thickness of wheel: 30 mm; Shaft bore diameter: 6 mm
Jumper wire	Male and female jumper wires
Power	Rechargeable lithium-polymer (LiPo) battery, 11.1 V, 3,300 mAh

The UAV's motion is controlled by the remote controller, it provides signals to the UAV's receiver and then the receiver sends the signal to the central flight controller. After that, the flight controller controls the speed of rotors with the help of an ESC. The motion and orientation of the UGV's caterpillar wheel are controlled by four independent DC motors, which provide the required torque during motion on the ground and rough terrain. The differential drive control method is used to control the motion of a vehicle during navigation on the ground. All the DC motors are attached to a combined vehicle's dual DC motor driver. The driver's direction and velocity control pins are connected to the Arduino UNO microcontroller to control the speed and provide left and right turns and backward and forward motions to the vehicle. One lithium-polymer (LiPo) battery of 11.1 V and 3,300 mAh gives power to the vehicle during the ground and aerial motions. The voltage regulator IC-7085 is used to drop from 11.1 V to 5 V and supplies power to the Arduino microcontroller.



Fig. 10. Snapshots of aerial motion control-based experimental results of a combined vehicle (UAV + UGV), (UAV, unmanned aerial vehicle; UGV, unmanned ground vehicle)



Fig. 11. Navigation result snapshots of a combined vehicle (UAV + UGV) moving on an uneven and rough terrain (UAV, unmanned aerial vehicle; UGV, unmanned ground vehicle)

The various kinematic equations of a combined vehicle (UAV + UGV) mentioned in Section 3 are embedded in the micro-controller to control the flying and ground motions. The kinematic equations of the UAV provide the three translations (linear velocities) and three rotation (angular velocities) commands to the rotors during aerial motion. Similarly, the kinematic equations of the UGV control the velocities and steering of a vehicle during navigation on the ground and rough terrain. We have tested this combined vehicle as an aerial vehicle in the sky and as a ground vehicle on uneven terrain, rough terrain and narrow paths. Fig. 10A–F shows snapshots of aerial motion control-based experimental results of a combined vehicle (UAV + UGV). As shown in the figure, first, the vehicle starts, ready to fly in the sky, and then flies in the sky successfully during our experiment. After conducting the first test of a combined vehicle (UAV + UGV) as an aerial vehicle, we navigate this vehicle on uneven terrain, rough terrain

and narrow paths. Fig. 11A–F illustrates the navigation result snapshots of a combined vehicle (UAV + UGV) moving on uneven and rough terrain. In addition, we have run this vehicle in a narrow path to show its robustness, and snapshots of the experimental result are presented in Fig. 12A–E. Moreover, we have also recorded a combined vehicle’s real-time linear and angular velocities (UAV + UGV) during both aerial and ground motion tests.

Fig. 13 reveals the real-time recorded linear velocity (meters per second) values of a combined vehicle (UAV + UGV) during the aerial motion control-based experimental results indicated in Fig. 10. Similarly, Figs 14 and 15 show the real-time recorded angular velocity (degrees per second) and linear velocity (meters per second) values of a right- and left-wheel driving system of a combined vehicle (UAV + UGV), respectively, when a vehicle travels on a rough narrow path, as indicated in Fig. 12.

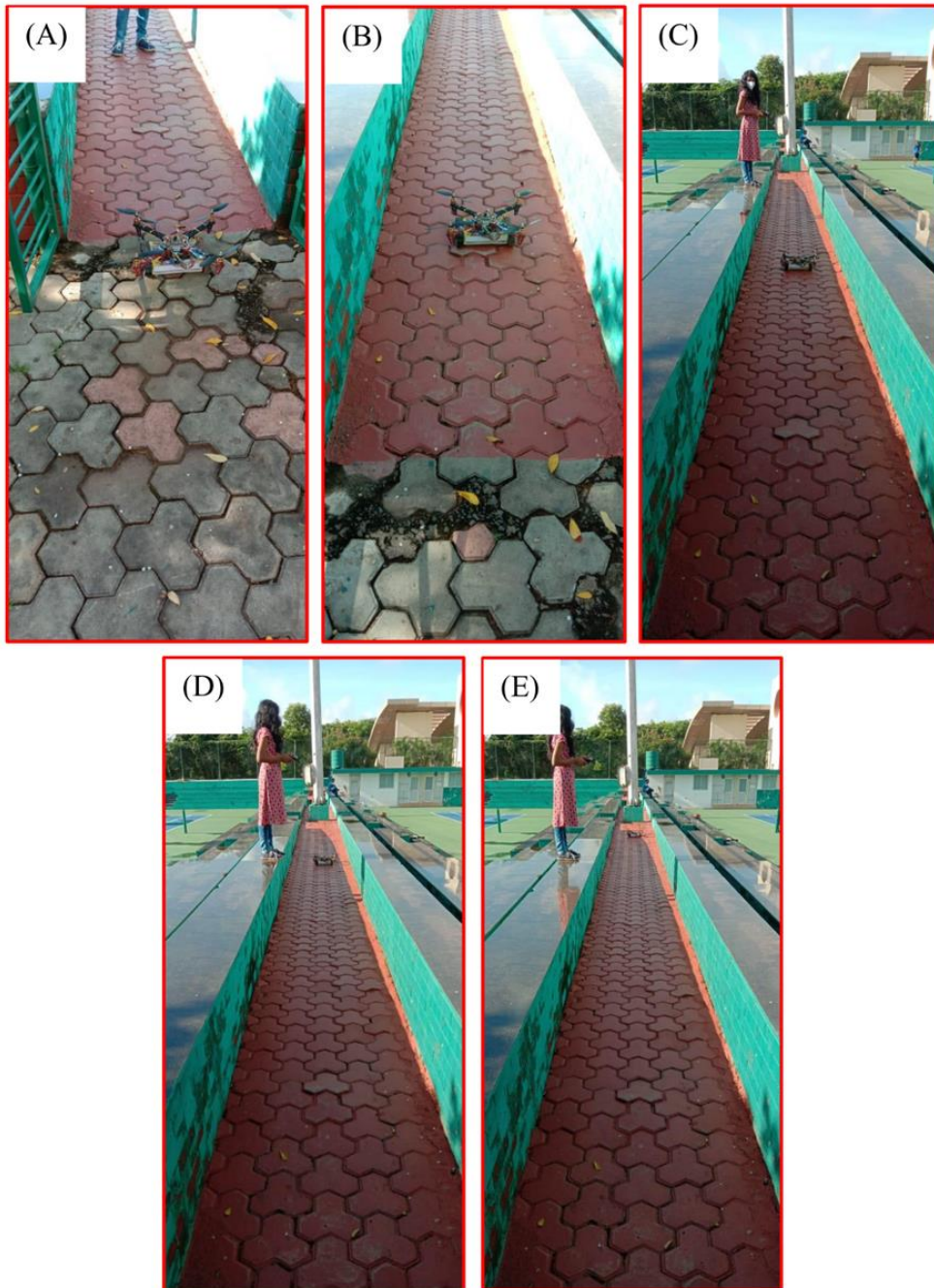


Fig. 12. Snapshots of experimental result of a combined vehicle (UAV + UGV) moving on a rough narrow path, (UAV, unmanned aerial vehicle; UGV, unmanned ground vehicle)

5. CONCLUSION AND FUTURE WORK

In order to provide more flexibility to the existing UAVs or quadcopters, a novel concept-based combined vehicle (UAV + UGV) was designed and studied. The main contribution of this work is the development of a novel concept-based UAV, which can also travel on ground, rough terrain and narrow paths as a UGV according to our requirements. Another objective of this present work was to provide an improved combined vehicle (UAV + UGV) capable of taking off and landing vertically, thereby eliminating the need for any runway. The important contributions of this paper can be summarised as follows: First, the kinematic equations for both a UAV and its attached caterpillar wheel-based

UGV are established and implemented in the microcontroller to control the flying and ground motion and orientation of a vehicle (UAV + UGV). Then, using SolidWorks software, the different 2D and 3D pictorial representations of a combined vehicle (UAV + UGV) are displayed. Its various components and their connections with each other are also explained briefly in this investigation. Finally, the presented experimental outcomes confirm that our developed vehicle (UAV + UGV) has given significant results in both air and ground, including rough terrain. Finally, and importantly, our future research work can include dynamic analysis by incorporating Newton–Euler equations to show the reference trajectory tracking control scheme for a combined vehicle (UAV + UGV).

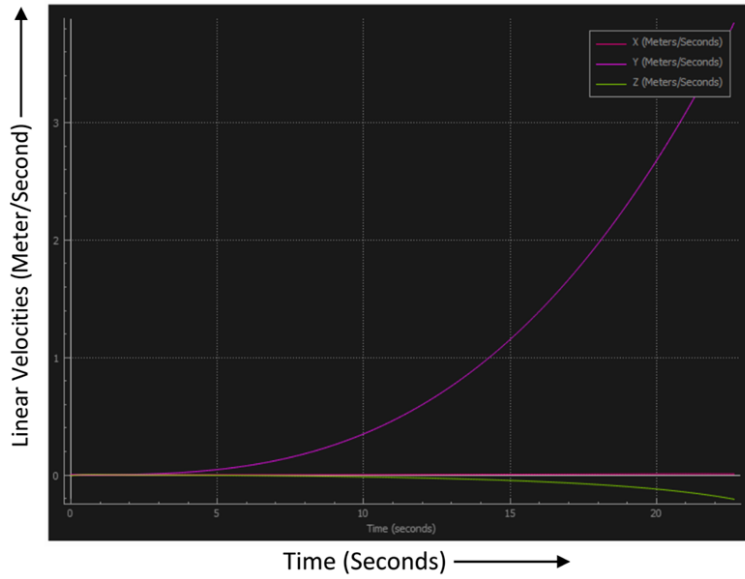


Fig. 13. Real-time recorded linear velocity (meters per second) values of a combined vehicle (UAV + UGV) during the aerial motion control-based experimental results indicated in Fig. 10, (UAV, unmanned aerial vehicle; UGV, unmanned ground vehicle)

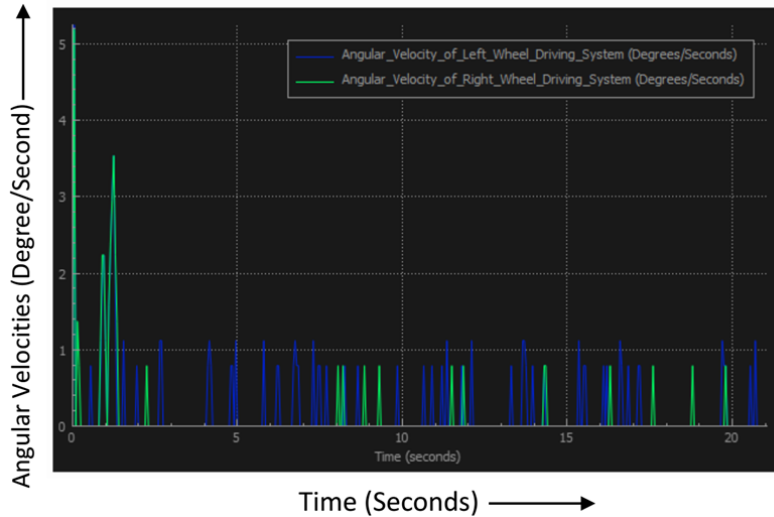


Fig. 14. Real-time recorded angular velocity (degrees per second) values of a right- and left-wheel driving system of a combined vehicle (UAV + UGV), when vehicle travels on a rough narrow path as indicated in Fig. 12, (UAV, unmanned aerial vehicle; UGV, unmanned ground vehicle)

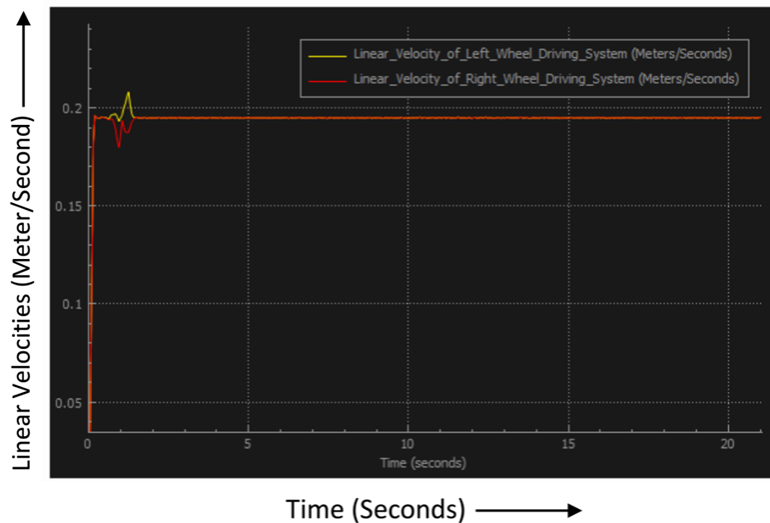


Fig. 15. Real-time recorded linear velocity (meters per second) values of a right- and left-wheel driving system of a combined vehicle (UAV + UGV), when vehicle travels on a rough narrow path as indicated in Fig. 12, (UAV, unmanned aerial vehicle; UGV, unmanned ground vehicle)

REFERENCES

1. Xiang H, Tian L. Development of a low-cost agricultural remote sensing system based on an autonomous unmanned aerial vehicle (UAV). *Biosystems Engg.* 2011;108(2):174–190.
2. Tahar KN, Ahmad A. A simulation study on the capabilities of rotor wing unmanned aerial vehicle in aerial terrain mapping. *Int J of Phy Sci.* 2012;7(8):1300–1306.
3. Wang Z, McDonald ST. Convex relaxation for optimal rendezvous of unmanned aerial and ground vehicles, *Aero Sci and Tech.* 2020;99:1–19.
4. Glida HE, Abdou L, Chelih A, Sentouh C. Optimal model-free backstepping control for a quadrotor helicopter. *Nonlin Dyna.* 2020;100(4):3449–3468.
5. Labbadi M, Cherkaoui M. Novel robust super twisting integral sliding mode controller for a quadrotor under external disturbances. *Int J of Dyna and Cont.* 2020;8:805–815.
6. Hassani H, Mansouri A, Ahaitouf A. Robust autonomous flight for quadrotor UAV based on adaptive nonsingular fast terminal sliding mode control. *Int J of Dyna and Cont.* 2021;9(2):619–635.
7. Selma B, Chouraqui S, Abouaïssa H. Optimal trajectory tracking control of unmanned aerial vehicle using ANFIS-IPSO system. *Int J of Info Techn.* 2020;12(2):383–395.
8. Elijah T, Jamisola RS, Tjiparuro Z, Namoshe M (2020). A review on control and maneuvering of cooperative fixed-wing drones. *Int J of Dyna and Cont.* 202;9(3):1332–1349.
9. Heidari H, Saska M. Trajectory Planning of Quadrotor Systems for Various Objective Functions. *Robo.* 2021;39(1):137–152.
10. Abdalla M, Al-Baradie S. Real time optimal tuning of quadcopter attitude controller using particle swarm optimization, *J of Eng and Techno Sci.* 2020;52(5):745–764.
11. Pinto MF, Honório LM, Marcato AL, Dantas MA, Melo AG, Capretz M, Urdiales C. ARCoG: An Aerial Robotics Cognitive Architecture. *Robo.* 2021;39(3):483–502.
12. Xu H, Jiang S, Zhang A. Path Planning for Unmanned Aerial Vehicle Using a Mix-Strategy-Based Gravitational Search Algorithm. *IEEE Access,* 2021;9:57033–57045.
13. Zhang X, Duan H. An improved constrained differential evolution algorithm for unmanned aerial vehicle global route planning. *Appl Soft Comp.* 2015;26:270–284.
14. Roberge V, Tarbouchi M, Labonté G. Comparison of parallel genetic algorithm and particle swarm optimization for real-time UAV path planning. *IEEE Trans on Indu Informat.* 2012;9(1):132–141.
15. Mou C, Qing-Xian W, Chang-Sheng J. A modified ant optimization algorithm for path planning of UCAV. *Appl Soft Comp.* 2008;8(4):1712–1718.
16. Duan H, Liu S, Wu J. Novel intelligent water drops optimization approach to single UCAV smooth trajectory planning. *Aero Sci and Tech,* 2009;13(8):442–449.
17. Silva Arantes JD, Silva Arantes MD, Motta Toledo CF, Júnior OT, Williams BC. Heuristic and genetic algorithm approaches for UAV path planning under critical situation. *Int J on Art Intel Tools.* 2017;26(01):1760008–1760037.
18. Besada-Portas E, De La Torre L, Moreno A, Risco-Martin JL. On the performance comparison of multi-objective evolutionary UAV path planners. *Info Sci,* 2013;238:111–125.
19. Cui Z, Wang Y. UAV Path Planning Based on Multi-Layer Reinforcement Learning Technique. *IEEE Access.* 2021;9:59486–59497.
20. Yao M, Zhao M. Unmanned aerial vehicle dynamic path planning in an uncertain environment. *Robo.* 2015;33(3):611–621.

Ramanuj Kumar:  <https://orcid.org/0000-0002-4426-2040>

Anish Pandey:  <https://orcid.org/0000-0001-9089-3727>

Ashok Kumar Sahoo:  <https://orcid.org/0000-0003-3785-909X>

DATA MINING APPROACH IN DIAGNOSIS AND TREATMENT OF CHRONIC KIDNEY DISEASE

Andreea S. TURIAC^{*ID}, Małgorzata ZDRODOWSKA^{**ID}

^{*}Faculty of Medical Engineering, University Politehnica of Bucharest, 1-7, Gh Polizu, 011061, Bucharest, Romania

^{**}Faculty of Mechanical Engineering, Institute of Biomedical Engineering,
Białystok Technical University, ul. Wiejska 45C, 15-351 Białystok, Poland

andreea.s.turiac@gmail.com, m.zdrodowska@pb.edu.pl

received 2 November 2021, revised 14 March 2022, accepted 15 March 2022

Abstract: Chronic kidney disease is a general definition of kidney dysfunction that lasts more than 3 months. When chronic kidney disease is advanced, the kidneys are no longer able to cleanse the blood of toxins and harmful waste products and can no longer support the proper function of other organs. The disease can begin suddenly or develop latently over a long period of time without the presence of characteristic symptoms. The most common causes are other chronic diseases – diabetes and hypertension. Therefore, it is very important to diagnose the disease in early stages and opt for a suitable treatment - medication, diet and exercises to reduce its side effects. The purpose of this paper is to analyse and select those patient characteristics that may influence the prevalence of chronic kidney disease, as well as to extract classification rules and action rules that can be useful to medical professionals to efficiently and accurately diagnose patients with kidney chronic disease. The first step of the study was feature selection and evaluation of its effect on classification results. The study was repeated for four models – containing all available patient data, containing features identified by doctors as major factors in chronic kidney disease, and models containing features selected using Correlation Based Feature Selection and Chi-Square Test. Sequential Minimal Optimization and Multilayer Perceptron had the best performance for all four cases, with an average accuracy of 98.31% for SMO and 98.06% for Multilayer Perceptron, results that were confirmed by taking into consideration the F1-Score, for both algorithms was above 0.98. For all these models the classification rules are extracted. The final step was action rule extraction. The paper shows that appropriate data analysis allows for building models that can support doctors in diagnosing a disease and support their decisions on treatment. Action rules can be important guidelines for the doctors. They can reassure the doctor in his diagnosis or indicate new, previously unseen ways to cure the patient.

Key words: feature selection, classification, classification rules, action rules, data mining, chronic kidney disease

1. INTRODUCTION

Chronic kidney disease (CKD) is a common disease that affects between 8% and 16% of the population worldwide [1]. It is often misdiagnosed or underdiagnosed in the earlier stages because there are no particular evident symptoms in these stages of development, but can it can be detected through laboratory testing. Due to the lower rate of proper identification in the incipient phases of the disease, Kidney Disease Outcomes Initiative of the National Kidney Foundation has recently proposed guidelines to describe CKD. In these guidelines it is stated that CKD is characterised by structural or functional abnormalities that last and/or progress for more than 3 months, with or without decreased glomerular filtration rate (GFR), manifest by either pathological abnormalities or markers of kidney damage, including abnormalities in the specific blood or urine tests or in medical imaging tests or by a GFR less than 60 mL/min/1.73 m² for more than 3 months, with or without kidney damage [2,3].

Early detection is extremely important to minimise the chances of progression to kidney failure. There are initiating factors that can contribute to increasing the risk of developing CKD, and some of them are related to ethnicity and family health record, whether or not end-stage kidney disease is present along with high-risk factors. Other aspects that can be taken into consideration are

age, stating that the number of nephrons that loss function is increased with ageing, gender, some studies implying that the progression of CKD is more rapid at men [4]. Diabetes and hypertension are the two main causes of CKD which are responsible for up to two-third of the cases: diabetes, due to the presence of too much glucose in the blood that damage the filtering function of the kidneys and high blood pressure that can affect the blood vessels that irrigate the kidneys. Apart from them, glomerulonephritis and unknown causes are more common in countries of Asia and sub-Saharan Africa [5].

With the possibility of early detection, it will be a transition from a life-threatening condition that requires lifelong care and the imminent occurring of dialysis to a more common condition that focuses on prevention and slowing the loss of kidneys functionality [6]. Data mining is an effective instrument to extract useful hidden information from voluminous datasets. Health industry provides a large amount of complex data about patients and diseases that requires preparation, processing, modelling and evaluation for knowledge extraction that can be used by the healthcare professionals when making diagnosis decisions and treatment plans [7]. Medical data is loaded with structured and unstructured information and it is characterised by an inconvenient aspect: high dimensionality. Feature selection is a common processing procedure for dimensionality reduction, so the algo-

rithm is modelled for better understanding of the underlying trends within the dataset [8]. The analysis of medical data allows to reduce its dimensionality and also to extract certain rules that may be relevant to the diagnosis and treatment processes. It also gives the possibility to modify these rules by replacing some flexible attributes. It allows to reclassify the patient from one group to another. These rules can help doctors in their work by giving some guidance, for example on treatment options [9].

Various automatic diagnosis methods have been proposed and tested to detect the early stage of CKD. Avci et al. provides a performance comparison using different classifiers: Naive Bayes, Support Vector Machine, K-Star and the famous J48 [10]. A. Rady et al. analyse the alternative of using artificial neural network algorithms and support vector machine to determine which algorithm display the best classification results [11]. Attribute selection and clustering methods were used by S.B. Akben to create subsets of the dataset to be further evaluated with K-Nearest Neighbour. The attributes were divided into three main categories, those related to blood tests, urine tests and other parameters, and different combinations of subsets were tested [12]. By considering that some elements of information are hidden from clinical data, these techniques can facilitate, as well as lower the cost of, a less invasive approach of diagnosis.

The aim of this article is to analyse and select features and to investigate the impact of feature selection on the selected classifiers accuracy. The paper will also show the extracted classification and action rules.

2. MATERIALS AND METHODS

“Chronic Kidney Disease” is the dataset used in this paper, extracted from UCI Machine Learning Repository. It is a collection of 400 instances with 24 attributes plus the class attribute, registered during a period of approximately 2 months at the Apollo Hospitals. The characteristics of all attributes are shown in Tab. 1. The original dataset contains missing values which can lead to inaccurate results and reduce the model accuracy. Instead of eliminating the instance from the dataset, we opt for replacing the missing values using statistical methods. Supervised attribute filter ReplaceMissingValues [40] from Weka software, was used to fill the unknown values by calculating the mean of all values for a specific attributes – the mean of the column. The attributes are numeric and nominal and they indicate the results of a range of blood and urine tests and the presence or absence of common diseases that increase the risk of developing CKD. There are two classes: 250 instances distributed for ckd which means a high probability of have chronic kidney disease in early stages and 150 instances for notckd, the patients that are generally not prone to chronic kidney disease.

Tab. 1. Attribute information

No.	Attribute name	Description	Average value
1	age	age of the patient (num) in years	51
2	bp	blood pressure (num) in mm/hg	76
3	sg	specific gravity (nom)	-
4	al	albumin (nom)	-
5	su	sugar (nom)	-

6	rbc	red blood cells (nom)	normal/abnormal
7	pc	pus cell (nom)	normal/abnormal
8	pcc	pus cell clumps (nom)	present/not present
9	ba	bacteria (nom)	present/not present
10	bgr	blood glucose random (num) in mgs/dl	148
11	bu	blood urea (num) in mgs/dl	57
12	sc	serum creatinine (num) in mgs/dl	3
13	sod	sodium (num) in meq/l	138
14	pot	potassium (num) in meq/l	4.62
15	hemo	hemoglobin (num) in gms	12.5
16	pcv	packed cell volume	39
17	wbcc	white blood cell count (num) in cells/cum	8406
18	rbcc	red blood cell count(num) in millions/cmm	4.7
19	htn	hypertension (nom)	yes/no -values
20	dm	diabetes mellitus (nom)	yes/no -values
21	cad	coronary artery disease (nom)	yes/no -values
22	appet	appetite (nom)	good/poor
23	pe	pedal edema (nom)	yes/no -values
24	ane	anemia (nom)	yes/no -values
25	class	class (nom)	ckd/notckd

In order to ease the learning procedure, the raw values were transformed into descriptive data which can better express the medical information. All the numerical data were saved as nominal data and then, the individual test values were divided into specific ranges accordingly with the ones reported in literature:

- blood pressure (bp) [13]:
 - less than 60 mm/Hg – low (0);
 - 60-80 mm/Hg – normal (1);
 - 80-90 mm/Hg – prehypertension (2);
 - higher than 90 – hypertension (3);
- blood glucose random (bgr) [14]:
 - less than 70 mgs/dl – hypoglycemia (0);
 - 70-125 mgs/dl – normal (1);
 - 125-200 mgs/dl – high (2);
 - 200-350 mgs/dl – extremely high (3);
 - higher than 380 – metabolic consequences (4);
- blood urea (bu) [15]:
 - 8-21 mgs/dl – normal (1);
 - higher than 21 mgs/dl – high (2);
- serum creatinine (sc) [16]:
 - less than 1.2mg/dl – normal (1);
 - 1.2–2mg/dl – mild renal (2);
 - 2–3mg/dl – moderate renal (3);
 - higher than 3 mg/dl – severe renal (4);
- sodium (sod) [17]:
 - lower than 135 mEq/L – hyponatremia (0);
 - 135-145 mEq/L – normal (1);
 - higher than 145 mEq/L – high (2);
- potassium (pot) [18]:
 - lower than 3.5 mEq/L – close to hypokalemia (0);
 - 3.5-5 mEq/L – normal (1);
 - higher than 5 mEq/L – high (2);
- hemoglobin (hemo) [19]:

- lower than 12.5 gms – low (0);
- 12.5-17.5 gms – normal (1);
- higher than 17.5 gms – high (2);
- packed cell volumes (pcv) [20]:
 - lower than 36% – low (0);
 - 36-53% – normal (1);
 - higher than 53% – high (2);
- white blood cell count (wbcc) [21]:
 - lower than 4000 cells/cum – low (0);
 - 4000-11000 cells/cum – normal (1);
 - higher than 11000 cells/cum – high (2);
- red blood cell count (rbcc) [22]:
 - lower than 3.92 millions/cmm – low (0);
 - 3.92-5.65 millions/cmm – normal (1);
 - higher than 5.65 millions/cmm – high (2);

The first step of the research was feature selection and study their effect on the accuracy of classifying patients into healthy and chronic kidney disease groups. In this case, some of the attributes need to be removed due to their little relevance. Following methods were used for attribute reduction:

- Correlation Based Feature Selection is a fully automatic algorithm used to determine a good feature subset that contains the attributes highly predictive of the class correlated and, simultaneously, uncorrelated with each other. All the features and the class are treated in a uniform manner and the merit of each attribute is calculated using Ranker Search Method. Irrelevant features should be neglected because they have low correlation to the class and redundant features should be removed as they are highly correlated with at least one of the remaining features [23].
- Chi-Square Test for Feature Selection was used to test the relationship between the features. It starts from the assumption that two characteristics are independent of each other, and then evaluate whether this hypothesis is correct by calculating the statistics, the magnitude of the deviation between the actual and theoretical values [24].

The second part of this study was building models including all attributes and attributes extracted by feature selection. To carry out the second part of this study, models were built using either all the attributes or attributes extracted by features selection methods. Then we applied the classification to check if the selection of features gave the expected results. For classification, we used the following algorithms:

- AdaBoostM1 algorithm generates a strong classifier using a linear combination of member classifiers and selects a member classifier to minimize the error and to maximize the diversity among the member of the classifiers in each cycle [25]. It is particularly common to use decision stumps, small decision trees with two leaves, to build more complex base learners that provides good classifiers when boosted [26].
- Sequential Minimal Optimization (SMO) split the quadric programming problems into a series of smallest possible QP subproblems which are solved analytically. The main advantages of this problems are related to small memory space because it solves the problem without any extra matrix storage, and it requires less computing time due to a non-iterative routine for each small problem [27].
- Multilayer Perceptron is an artificial feed-forward neural network based on a three layers architecture: the input layer, the hidden layer with a non-linear activation function and an output layer where the classification task is performed. Each lay-

er has a various number of neurons that are trained using back propagation learning algorithm [28]. Each neuron has a mathematical function that gain the input from a previous layer and produce the output for the following layer [29].

- Naïve Bayes Classification is based on the Bayes' Theorem and provides a way of combining prior probability and conditional probabilities into a single formula and then choose the classification with the highest values. The premise of this algorithm is that all the attributes contribute equally and independently to the model. In practice, this assumption is not correct but Naïve Bayes algorithm has become an important probabilistic model with remarkable success in practice [30].
- J48 decision tree in which every detail of the information is split into minor subsets by choosing an attribute. The principle of J48 decision tree is to split every detail present in the information into minor subsets by choosing an attribute of reference. At each node, the algorithm chooses the highest worthy information-gain attribute to split the data. This process is stopped when a subset has a place with a similar class in all the instances [31].
- JRip main premise is to produce error reduction at each incremental pruning and it consists on two phases: the grow phase when it continues to add terms to the rule until it is accurate and the incrementally pruning phase of each rule [32].
- CART is a tree-building technique structured as a binary recursive partitioning as each node from the decision tree can be split in only two groups. It is a practical algorithm used in clinical setting because it creates uncomplicated rules that have a common point with the perspective of the clinicians [33].
- The idea behind the PART algorithm is to build a partial tree with a separate-and-conquer strategy: when it creates a rule, the instances covered in it are removed and the process continues with the remaining instances until there are none left [34].
- Random Trees uses a collection of tree classifiers and produces a random set of data to build a decision tree. The input data is classified at each tree and the overall decision is made by so called "votes". At a node, a random subset of training data is analysed and the best split is made for that particular subset [35].

We used a 10-fold cross-validation for testing, training and validation. The basic principle is to divide the data: a high percent of the data is used to build the model and then use the left-out samples to be predicted as unseen data [36]. In a 10-fold cross-validation the dataset is randomly split into 10 mutually exclusive subsets of approximately equal size. The model is trained and tested each time, it is trained on the entire dataset leaving out the specific fold and then it is tested on the leave-out subset. The accuracy estimated is the overall number of correct classifications divided by the number of the instances in the dataset [37].

To evaluate the above classifiers, we used Total Accuracy (ACC) and F1-Score.

ACC is the total efficiency of the classifier, which determines the probability of correct classification, i.e. the ratio of correct classification s to all classifications. It is expressed by the equation [38]:

$$ACC = \frac{TP + TN}{TP + TN + FP + FN} \quad (1)$$

A considerable disadvantage about the ACC as it does not take into consideration the differences between the types of error,

it does not punish the fact that the model classifies i.e a patient as a false negative, meaning that he is diagnosed as not having the disease when he actually has the disease (false negative values). Another aspect is related to the case when there is an unbalanced dataset, as ACC does not provide a realistic measurement – it is more effective to consult the confusion matrix (Tab. 2) [38].

Recall is the ability of a model to find all the relevant cases within the dataset, being defined as the number of true positives divided by the sum of true positives and false negatives. Precision is the ability of a classification to identify the positive features and it is defined as the number of true positives divided by the number of all instances that were classified as positives. F1-Score is an optimal blend, the harmonic mean of Recall and Precision [10]:

$$Precision = \frac{true\ positives}{true\ positives + false\ positives} \quad (2)$$

$$Recall = \frac{true\ positives}{true\ positives + false\ negatives} \quad (3)$$

$$F_1 = 2 \cdot \frac{precision \cdot recall}{precision + recall} \quad (4)$$

Tab. 2. Confusion Matrix

Hypothesized class	Actual class	
	Positives	Negatives
Yes	True Positives	False Pozitives
No	False Negatives	True Negatives

The final steps of this study were construction of classification rules and extraction the action rules from classification rules.

Action rules are constructed from classification rules which suggest an alternative to reclassify the instances. These rules indicate the changes in an attribute that need to be made to integrate an instance, in this case, a patient into a different category, all accordingly to the information from the clinicians. It is crucial to find useful rules from analysing the data and identify the relevant patterns that best describes the instances [9].

An action rule can be presented in the following form [41,42]:

$$[(\omega) \wedge (\alpha \rightarrow \beta)] \Rightarrow (\Psi \rightarrow \Omega) \quad (5)$$

where ω indicates a fixed condition features conjunction, that is a part of both groups, $(\alpha \rightarrow \beta)$ is recommended changes in flexible features value and $(\Psi \rightarrow \Omega)$ means an effect of the action, which the user wants to achieve.

3. RESULTS

To enhance the performance of the model, first, the dimension of the data set needs to be reduced, the irrelevant features or features that are little correlated with the class label should be neglected. [39] As mentioned earlier, two feature selection methods were used:

- Correlation Based Feature Selection with Ranker Search Method, taking into consideration the first 6 attributes with a merit of approximate 0.5 or higher
- Chi-Square Test choosing the first 8 most independent features, listed in the table below:

In addition, we also took into one of the models only those attributes indicated by doctors as most important in chronic kidney disease. These features include blood pressure, specific gravity, diabetes mellitus, hypertension, albumin, blood urea, serum creatinine, sodium, potassium, haemoglobin, red blood cell count and packed cell volume [1,2,4]. The results of attribute selection are shown in Tab. 3. It is important to note that 6 of all features were able to be extracted for each of the methods mentioned above. These features are highlighted with the same color in Tab. 2.

The results of classification for each of analyzed models are shown in Figs. 1-3.

Tab. 3. Feature selection results

Attributes indicated by doctors	Correlation Based Feature Selection	Chi-Square Test
blood pressure	hemoglobin	serum creatinine
specific gravity	hypertension	specific gravity
diabetes mellitus	diabetes mellitus	hemoglobin
hypertension	serum creatinine	albumin
albumin	albumin	hypertension
blood urea	packed cell volume	diabetes mellitus
serum creatinine		red blood cell count
sodium		packed cell volume
potassium		
hemoglobin		
red blood cell count		
packed cell volume		

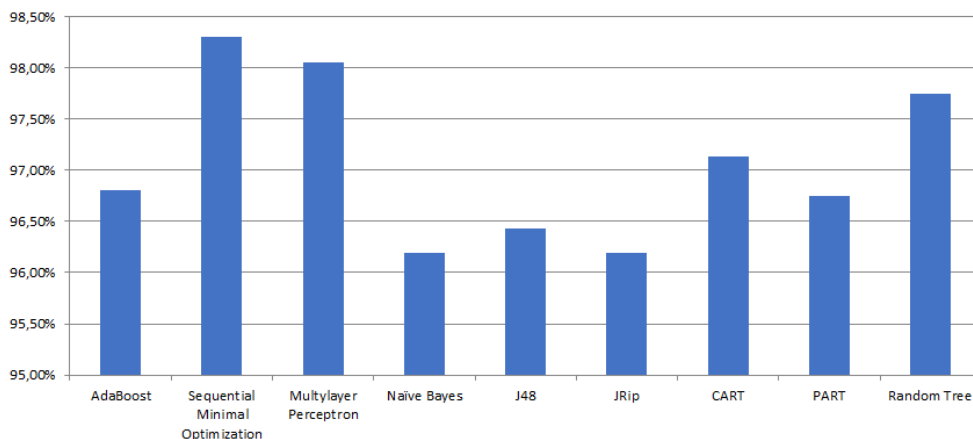


Fig. 1. Average accuracy

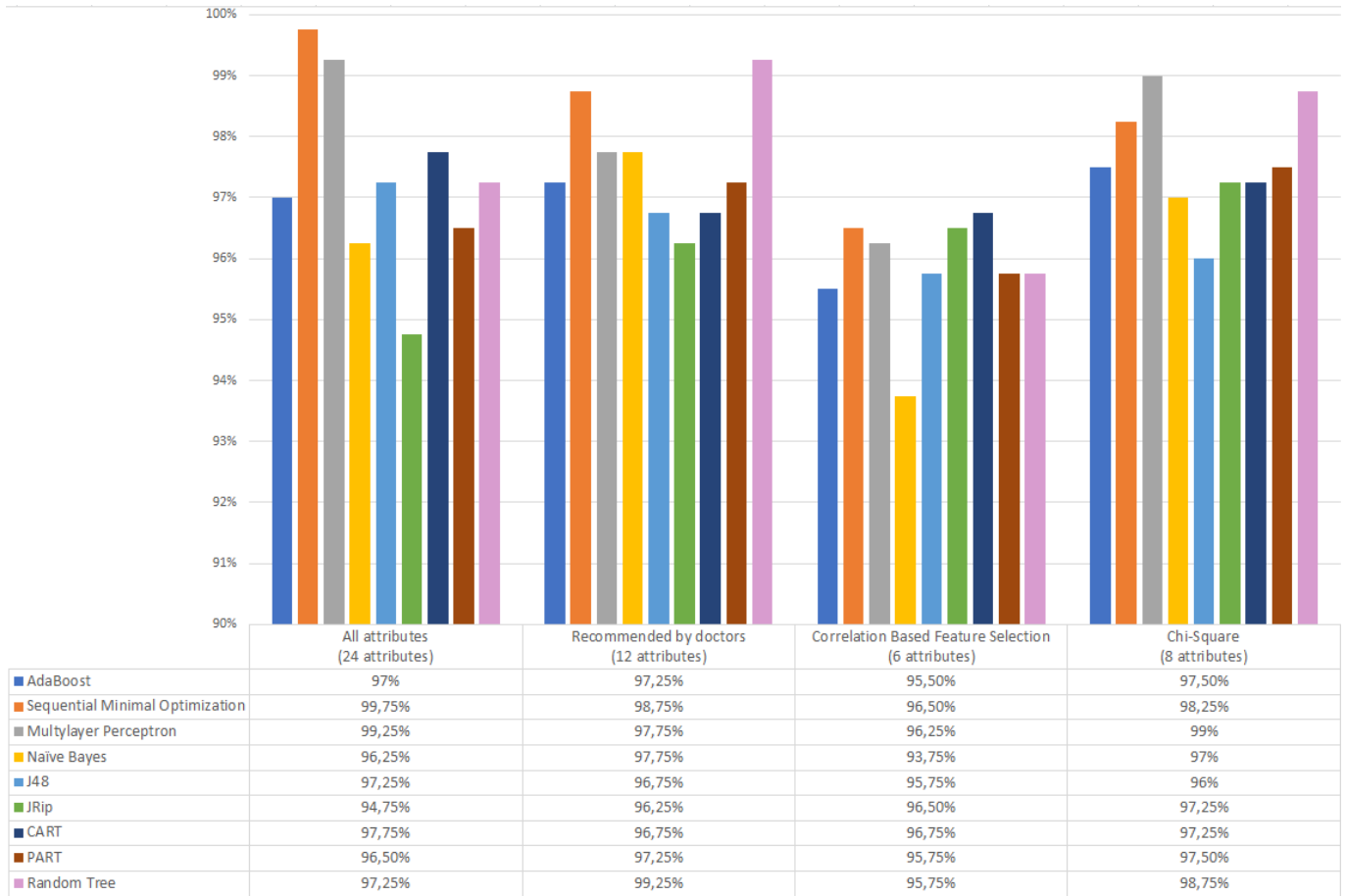


Fig. 2. Total Accuracy (ACC) Results

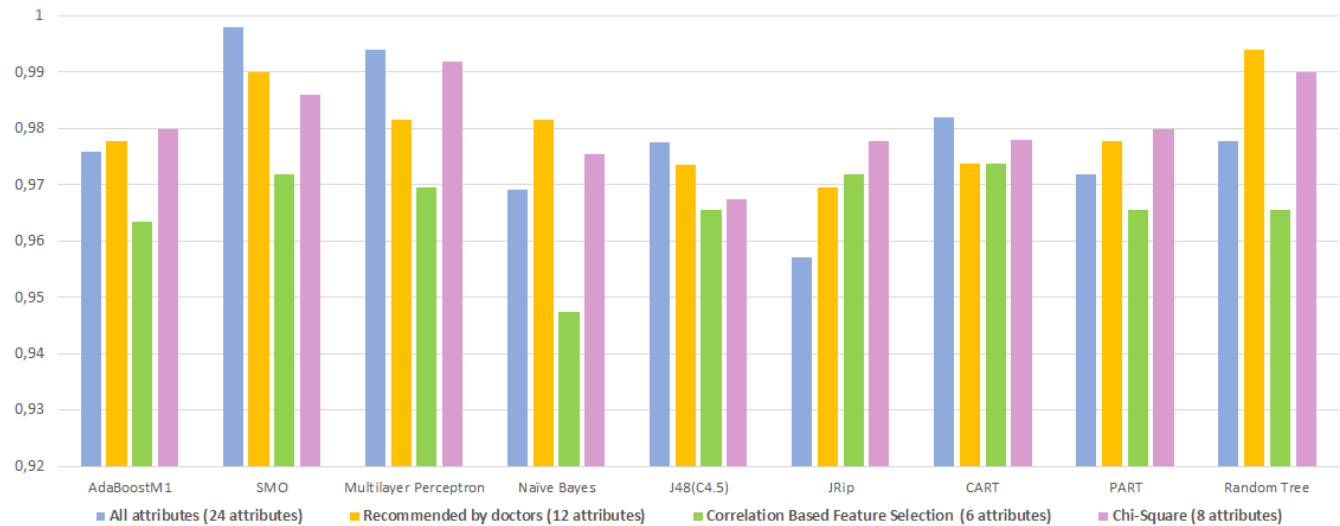


Fig. 3. F1-Score Results

The next step of the research was to identify the classification rules. These rules were obtained using the classifier algorithms mentioned earlier. A few dozen rules were obtained for each model. We compared the rules extracted for the model containing all features and for the models after feature reduction. In the following, we present dozens of rules that classify patients into a group at high risk for chronic kidney disease (underlined are those rules that were obtained in both models: the model containing all features and the models after feature selection):

- IF albumin = 0 AND hemoglobin = 1 AND serum creatinine = 1 AND hypertension = yes THEN ckd
- IF albumin = 0 AND hemoglobin = 1 AND serum creatinine = 1 AND hypertension = no AND packed cell volume = 0 THEN ckd
- IF albumin = 0 AND hemoglobin = 1 AND serum creatinine = 1 AND hypertension = no AND packed cell volume = 1 AND diabetes mellitus = yes THEN ckd

- IF albumin = 0 AND hemoglobin = 1 AND serum creatinine = 2 THEN ckd
- IF albumin = 0 AND hemoglobin = 1 AND serum creatinine = 3 THEN ckd
- IF albumin = 0 AND hemoglobin = 2 THEN ckd
- IF hemoglobin = 0 THEN ckd
- IF hemoglobin = 1 AND diabetes mellitus = no AND albumin = 0 AND serum creatinine = 2 or 3 or 4 THEN ckd
- IF hemoglobin = 1 AND diabetes mellitus = no AND albumin = 2 or 3 or 4 THEN ckd
- IF hemoglobin = 1 AND diabetes mellitus = no AND serum creatinine = 1 AND specific gravity = 2 or 3 THEN ckd
- IF hemoglobin = 1 AND diabetes mellitus = no AND serum creatinine = 2 or 3 THEN ckd
- IF hemoglobin = 1 AND diabetes mellitus = yes THEN ckd
- IF hemoglobin = 1 AND specific gravity = 1 or 2 or 3 THEN ckd
- IF hemoglobin = 1 AND specific gravity = 4 AND serum creatinine = 1 AND albumin = 0 AND packed cell volume = 0 THEN ckd
- IF hemoglobin = 1 AND specific gravity = 5 AND serum creatinine = 2 or 3 THEN ckd
- IF hemoglobin = 1 AND specific gravity = 5 AND serum creatinine = 1 AND albumin = 1 or 2 or 3 or 4 or 5 THEN ckd
- IF hemoglobin = 2 THEN ckd
- IF hypertension = no AND albumin = 0 AND diabetes mellitus = no AND specific gravity = 2 or 3 THEN ckd
- IF hypertension = no AND albumin = 0 AND diabetes mellitus = yes THEN ckd
- IF hypertension = no AND albumin = 1 or 2 or 3 or 4 THEN ckd
- IF hypertension = yes THEN ckd
- IF serum creatinine = 1 AND albumin = 0 or 5 AND hemoglobin = 0 THEN ckd
- IF serum creatinine = 1 AND albumin = 0 or 5 AND hemoglobin = 1 or 2 AND diabetes mellitus = yes THEN ckd
- IF serum creatinine = 1 AND albumin = 1 or 2 or 3 or 4 THEN ckd
- IF serum creatinine = 1 AND specific gravity = 1 or 2 or 3 THEN ckd
- IF serum creatinine = 1 AND specific gravity = 4 AND hypertension = yes THEN ckd
- IF serum creatinine = 1 AND specific gravity = 4 AND hypertension = no AND albumin = 0 AND potassium (pot) = 1 AND blood urea (bu) = 1 AND sodium = 0 THEN ckd
- IF serum creatinine = 1 AND specific gravity = 4 AND hypertension = no AND albumin = 0 AND potassium (pot) = 1 AND blood urea (bu) = 2 AND sodium = 0 THEN ckd
- IF serum creatinine = 1 AND specific gravity = 4 AND hypertension = no AND albumin = 0 AND potassium (pot) = 2 THEN ckd
- IF serum creatinine = 1 AND specific gravity = 4 AND hypertension = no AND albumin = 1 or 2 or 3 or 4 or 5 THEN ckd
- IF serum creatinine = 1 AND specific gravity = 4 or 5 AND albumin = 1 or 2 or 4 THEN ckd
- IF serum creatinine = 1 AND specific gravity = 5 AND albumin = 1 or 2 or 3 or 4 or 5 THEN ckd
- IF serum creatinine = 1 AND specific gravity = 5 or 4 AND albumin = 1 or 3 or 4 THEN ckd
- IF serum creatinine = 2 or 3 or 4 THEN ckd

- IF serum creatinine = 4 AND specific gravity = 1 or 2 or 3 THEN ckd
- IF serum creatinine = 4 AND specific gravity = 4 AND hypertension = yes THEN ckd
- IF serum creatinine = 4 AND specific gravity = 4 AND hypertension = no AND sodium = 0 THEN ckd
- IF serum creatinine = 4 AND specific gravity = 4 AND hypertension = no AND sodium = 1 AND albumin = 0 AND diabetes mellitus = yes or no THEN ckd
- IF serum creatinine = 4 AND specific gravity = 4 AND hypertension = no AND sodium = 1 AND albumin = 1 or 2 or 3 or 4 or 5 THEN ckd
- IF serum creatinine = 4 AND specific gravity = 4 AND hypertension = no AND sodium = 2 THEN ckd
- IF serum creatinine = 4 AND specific gravity = 5 AND blood pressure = 0 THEN ckd
- IF serum creatinine = 4 AND specific gravity = 5 AND blood pressure = 1 AND albumin = 1 or 2 or 3 or 4 or 5 THEN ckd
- IF serum creatinine = 4 AND specific gravity = 5 AND blood pressure = 2 or 3 THEN ckd

The classification rules read as follows: e.g. the last rule means that if serum creatinine is at level 4, specific gravity is at level 5 and blood pressure is at level 2 or 3, the patient is classified in the high probability of having chronic kidney disease in early stages group.

The final step of the study was to extract action rules that would allow the reclassification of patients from the group at high risk for chronic kidney disease to the group that are generally not prone to chronic kidney disease. Here, we also received over a hundred rules. Below there are some selected action rules extracted from the classification rules (again, underlined are those rules that were obtained in both models: the model containing all features and the models after feature selection):

- [albumin=0] \wedge [hemoglobin=1] \wedge [serum creatinine=1] \wedge [hypertension=no] \wedge [packed cell volume=1] \wedge [diabetes mellitus, yes \rightarrow no] \Rightarrow [class, ckd \rightarrow notckd]
- [hemoglobin=1] \wedge [diabetes mellitus=no] \wedge [albumin, 4 \rightarrow 5] \Rightarrow [class, ckd \rightarrow notckd]
- [hemoglobin=1] \wedge [diabetes mellitus=no] \wedge [albumin=0] \wedge [serum creatinine, 2 \rightarrow 1] \Rightarrow [class, ckd \rightarrow notckd]
- [hemoglobin=1] \wedge [diabetes mellitus=no] \wedge [serum creatinine=1] \wedge [specific gravity, 2 \rightarrow 1] \Rightarrow [class, ckd \rightarrow notckd]
- [hemoglobin=1] \wedge [diabetes mellitus=no] \wedge [serum creatinine=1] \wedge [specific gravity, 3 \rightarrow 4] \Rightarrow [class, ckd \rightarrow notckd]
- [hemoglobin=1] \wedge [diabetes mellitus=no] \wedge [serum creatinine=4] \wedge [rbcc, 0 \rightarrow 2] \Rightarrow [class, ckd \rightarrow notckd]
- [hemoglobin=1] \wedge [specific gravity=4] \wedge [serum creatinine=1] \wedge [albumin=0] \wedge [packed cell volume, 0 \rightarrow 2] \Rightarrow [class, ckd \rightarrow notckd]
- [hemoglobin=1] \wedge [specific gravity=4] \wedge [serum creatinine=1] \wedge [albumin=0] \wedge [packed cell volume=1] \wedge [rbcc, 0 \rightarrow 1] \Rightarrow [class, ckd \rightarrow notckd]
- [hemoglobin=1] \wedge [specific gravity=5] \wedge [albumin, 2 \rightarrow 4] \Rightarrow [class, ckd \rightarrow notckd]
- [hemoglobin=1] \wedge [specific gravity=5] \wedge [serum creatinine=1] \wedge [albumin, 1 \rightarrow 0] \Rightarrow [class, ckd \rightarrow notckd]
- [hypertension=no] \wedge [albumin, 3 \rightarrow 5] \Rightarrow [class, ckd \rightarrow notckd]

- [hypertension=no] \wedge [albumin, 4 \rightarrow 5] \Rightarrow [class, ckd \rightarrow notckd]
- [hypertension=no] \wedge [albumin=0] \wedge [diabetes mellitus=no] \wedge [specific gravity, 2 \rightarrow 1] \Rightarrow [class, ckd \rightarrow notckd]
- [hypertension=no] \wedge [albumin=0] \wedge [diabetes mellitus=no] \wedge [specific gravity, 3 \rightarrow 4] \Rightarrow [class, ckd \rightarrow notckd]
- [serum creatinine=1] \wedge [albumin=0] \wedge [hemoglobin=1] \wedge [diabetes mellitus, yes \rightarrow no] \Rightarrow [class, ckd \rightarrow notckd]
- [serum creatinine=1] \wedge [albumin=0] \wedge [hemoglobin=2] \wedge [diabetes mellitus, yes \rightarrow no] \Rightarrow [class, ckd \rightarrow notckd]
- [serum creatinine=1] \wedge [specific gravity=4] \wedge [albumin, 1 \rightarrow 0] \Rightarrow [class, ckd \rightarrow notckd]
- [serum creatinine=1] \wedge [specific gravity=4] \wedge [albumin, 3 \rightarrow 2] \Rightarrow [class, ckd \rightarrow notckd]
- [serum creatinine=1] \wedge [specific gravity=4] \wedge [albumin, 4 \rightarrow 5] \Rightarrow [class, ckd \rightarrow notckd]
- [serum creatinine=1] \wedge [specific gravity=4] \wedge [hypertension=no] \wedge [albumin=0] \wedge [pot=1] \wedge [bu =1] \wedge [sod, 0 \rightarrow 1] \Rightarrow [class, ckd \rightarrow notckd]
- [serum creatinine=1] \wedge [specific gravity=5] \wedge [albumin, 1 \rightarrow 0] \Rightarrow [class, ckd \rightarrow notckd]
- [serum creatinine=1] \wedge [specific gravity=5] \wedge [albumin, 1 \rightarrow 2] \Rightarrow [class, ckd \rightarrow notckd]
- [serum creatinine=1] \wedge [specific gravity=5] \wedge [albumin, 1 \rightarrow 5] \Rightarrow [class, ckd \rightarrow notckd]
- [serum creatinine=1] \wedge [specific gravity=5] \wedge [albumin, 3 \rightarrow 0] \Rightarrow [class, ckd \rightarrow notckd]
- [serum creatinine=1] \wedge [specific gravity=5] \wedge [albumin, 3 \rightarrow 2] \Rightarrow [class, ckd \rightarrow notckd]
- [serum creatinine=1] \wedge [specific gravity=5] \wedge [albumin, 3 \rightarrow 5] \Rightarrow [class, ckd \rightarrow notckd]
- [serum creatinine=1] \wedge [specific gravity=5] \wedge [albumin, 4 \rightarrow 0] \Rightarrow [class, ckd \rightarrow notckd]
- [serum creatinine=1] \wedge [specific gravity=5] \wedge [albumin, 4 \rightarrow 2] \Rightarrow [class, ckd \rightarrow notckd]
- [serum creatinine=1] \wedge [specific gravity=5] \wedge [albumin, 4 \rightarrow 5] \Rightarrow [class, ckd \rightarrow notckd]

The action rules read as follows: e.g. the last action rule means that if serum creatinine is at level 1, specific gravity is at level 5, and albumin level is changed from 4 to 5, then we can reclassify the patient from the high probability of having chronic kidney disease in early stages group to the patients that are generally not prone to chronic kidney disease.

4. DISCUSSION

Chronic Kidney Disease means a chronic disease associated with kidney failure. Currently, kidney function is traditionally assessed by blood and urine tests. However, it is important to develop a CKD system to recognize the early stages of CKD and its symptoms. In this way, preventive measures can be taken to manage the disease at an early stage and avoid its complications.

Classification, one of the methods of data mining that involves finding a way to map data into a set of predefined classes, can be helpful here. Based on test results, we can assign a given patient to the appropriate disease class. In our work, we made a classification this for four models: containing all available patient data, containing features identified by doctors as major factors in chronic kidney disease, and models containing features selected using

Correlation Based Feature Selection and Chi-Square Test.

Here we see that for each model, the highest accuracy was obtained for the Sequential Minimal Optimization and Multilayer Perceptron algorithms. These results are also confirmed by the F1-Score.

For the model with all the attributes Sequential Minimal Optimization and Multilayer Perceptron performs particularly well, with an accuracy of 99.75%, respectively 99.25% and an F1-Score of 0.998, respectively 0.994.

For the model of attributes with references in the literature, those recommended by clinicians Random Tree has the highest accuracy of 99.25% and F1-Score of 0.994, followed by Sequential Minimal Optimization – 98.75% and F1-Score of 0.989 and Multilayer Perceptron – 97.75% and F1-Score of 0.981.

For the model with attributes reduced with Correlation Based Feature Selection CART and JRIP have the highest accuracy with a 96.75% and 0.973 F1-Score, respectively 96.5% and 0.971 F1-Score, closely followed by Sequential Minimal Optimization – 96.5% and Multilayer Perceptron 96.25%.

For the model with attributes reduced with Chi-Square Test Multilayer Perceptron has the best results with an accuracy of 99% and a F1-Score of 0.991, followed by Random Tree 98.75% accuracy and 0.989 F1-Score and Sequential Minimal Optimization with 98.25% accuracy and 0.979 F1-Score.

It is worth mentioning that other authors [43, 44] also worked on the same database. They often used other feature selection methods and other classification methods and also achieved high accuracy rates.

Based on our models, we also extracted dozens of decision rules and then action rules that would allow the reclassification of patients from the group at high risk for chronic kidney disease to the group that are generally not prone to chronic kidney disease.

The overall objective of this analysis is to find methods to correctly predict the presents of chronic kidney disease in early stages and to find optimal guidance and particular treatment for each patient based on the results. Our study was conducted using the results of a survey of 400 individuals. This may be an insufficient research sample. In order to use intelligent algorithms for optimal diagnosis, larger verified datasets are required. The feature selection made with Chi-Square Test performed very well with Multilayer Perceptron, Random Tree and SMO algorithms and this hybrid method can be improved by creating larger datasets with the attributes identified with feature selection.

5. CONCLUSION

Chronic kidney disease is a lifestyle disease that affects more and more people. This disease is special because it can be a consequence or complication of all other diseases of civilization, from obesity, diabetes, hypertension and cardiovascular diseases. Too rarely diagnosed, it occurs much more frequently than previously thought. Its course is very often hidden, therefore this chronic kidney disease is a real challenge for the XXI century medicine.

Therefore, a very important aspect is the proper and early diagnosis and the support of doctors in the process of diagnosis and treatment. Data mining, which is increasingly used in medicine and its related fields, can be helpful here. Data mining allows for a different way of looking at the disease and the factors causing it. It is based on the research of doctors, but also looks for

completely different correlations. It can connect the features that are not obvious. Appropriate data analysis allows for building models that can support doctors in diagnosing a disease, support their decisions on treatment or rehabilitation of a patient. An important aspect of data mining are classification rules and action rules. Especially the latter can be an important guideline for doctors. They can reassure the doctor in his diagnosis or indicate new, previously unseen ways to cure the patient.

REFERENCES

- Chen TK, Knicely DH, Grams ME. Chronic Kidney Disease Diagnosis and Management: A Review. *JAMA - Journal of the American Medical Association*. 2019;322(13):1294–1304. doi: 10.1001/jama.2019.14745
- Coresh J, Astor BC, Greene T, Eknoyan G, Levey AS. Prevalence of chronic kidney disease and decreased kidney function in the adult US population: Third National Health and Nutrition Examination Survey. *American Journal of Kidney Diseases*. 2003;41(1):1–12. doi: 10.1053/ajkd.2003.50007.
- Tuominen TK, Jämsä T, Oksanen J, Tuukkanen J, Gao TJ, Lindholm TS, Jalovaara PK. Composite implant composed of hydroxyapatite and bone morphogenetic protein in the healing of a canine ulnar defect. *Annales Chirurgiae et Gynaecologiae*. 2001;90(1):32–36 .
- Evans PD, Taal MW. Epidemiology and causes of chronic kidney disease. *Chronic Renal Failure*. 2011;39(7):402–406.
- Jha V, Garcia-Garcia G, Iseki K, Li Z, Naicker S, Plattner B, et al. Chronic kidney disease: Global dimension and perspectives. *The Lancet: series Global Kindey Disease*. 2013;382(9888):260–272.
- Levey AS, Astor BC, Stevens LA, Coresh J. Chronic kidney disease, diabetes, and hypertension: What's in a name. *Kidney International*. 2010;78(1):19–22. doi: 10.1038/ki.2010.115.
- Kunwar V, Chandel K, Sabitha AS, Bansal A. Chronic Kidney Disease analysis using data mining classification techniques. 6th International Conference - CloudSystem and Big Data Engineering (Confluence). 2016;300–305. doi: 10.1109/CONFLUENCE.2016.7508132.
- Manonmani M, Balakrishnan S. Feature Selection Using Improved Teaching Learning Based Algorithm on Chronic Kidney Disease Dataset. *Procedia Computer Science*. 2020;171(2019):1660–1669. doi: 10.1016/j.procs.2020.04.178
- Dardzińska A. *Action Rules Mining*. Springer-Verlag, Berlin. 2013.
- Avci E, Karakus S, Ozmen O, Avci D. Performance comparison of some classifiers on Chronic Kidney Disease data. 6th International Symposium on Digital Forensic and Security (ISDFS). 2018;1-4. doi: 10.1109/ISDFS.2018.8355392.
- Rady EHA, Anwar AS. Prediction of kidney disease stages using data mining algorithms. *Informatics in Medicine Unlocked*. 2019;15:100178. doi: 10.1016/j.imu.2019.100178.
- Akben SB. Early Stage Chronic Kidney Disease Diagnosis by Applying Data Mining Methods to Urinalysis, Blood Analysis and Disease History. *IRBM*. 2018;39(5):353–358. doi: 10.1016/j.irbm.2018.09.004.
- Simunovic VL. *Basic & General Clinical Skills*. CreateSpace Independent Publishing Platform. 2013.
- Freeth A. *Diabetes Causes, Myths, Treatment, and Home Care*. eMediHealth. 2019.
- Juho K, Minami Y, Haruki S, Matsue Y, Shimazaki K, Kadowaki H, Ishida I, Kambayashi K, Arashi H, Sekiguchi H, Hagiwara N. Persistent high blood urea nitrogen level is associated with increased risk of cardiovascular events in patients with acute heart failure. *ESC Heart Failure*. 2017;4(4):545–553.
- Piñol-Ripoll G, De La Puerta I, Purroy F. Serum creatinine is an inadequate screening test for renal failure in ischemic stroke patients. *Acta Neurologica Scandinavica*. 2009;120(1):47–52. doi: 10.1111/j.1600-0404.2008.01120.x.
- Strazzullo P, Leclercq C. Nutriente information: Sodium. *Advances in Nutrition*. 2014;5(2):188–90 doi: 10.3945/an.113.005215.
- Kardalas E, Paschou SA, Anagnostis P, Muscogiuri G, Siasos G, Vryonidou A. Hypokalemia: A clinical update. *Endocrine Connections*. 2018;7(4):135–146. doi: 10.1530/EC-18-0109.
- Walker HK, Hall WD HJ. *Clinical Methods: The History, Physical, and Laboratory Examinations*. 3rd edition. 1990.
- Fairbanks VF, Tefferi A. Normal ranges for packed cell volume and hemoglobin concentration in adults: Relevance to "apparent polycythemia." *European Journal of Haematology*. 2000;65(5): 285–296. doi: 10.1034/j.1600-0609.2000.065005285.x.
- White Blood Cell Count. *Nursing Critical Care*. 2019;14:1-40. doi: 10.1097/01.CCN.0000549633.67301.6d
- Red Blood Cell Count. *Nursing Critical Care*. 2020;15(1):1-38. doi: 10.1097/01.CCN.0000612852.86589.d2
- Hall MA. *Correlation-based Feature Selection for Machine Learning*. Doctoral thesis. University of Waikato. 1999.
- Sun J, Zhang X, Liao D, Chang V. Efficient method for feature selection in text classification. 2017 International Conference on Engineering and Technology (ICET). 2017;1–6. doi: 10.1109/ICEngTechnol.2017.8308201.
- An TK, Kim MH. A new Diverse AdaBoost classifier. *Artificial Intelligence and Computational Intelligence*. 2010;1:359–363. doi: 10.1109/AICI.2010.82.
- Kegl B. *Introduction to AdaBoost*. 2014. Available from: <http://citeseerx.ist.psu.edu/viewdoc/download?doi=10.1.1.679.8866&rep=rep1&type=pdf>, 10 October 2021.
- Zeng ZQ, Yu H Bin, Xu HR, Xie YQ, Gao J. Fast training Support Vector Machines using parallel Sequential Minimal Optimization. *rd International Conference on Intelligent System and Knowledge Engineering*. 2008;997–1001. doi: 10.1109/ISKE.2008.4731075.
- Abirami S, Chitra P. Energy-efficient edge based real-time healthcare support system. *Advances in Computers*. 2020;117(1):339–368. doi: 10.1016/bs.adcom.2019.09.007
- Kumar Y, Sahoo G. Analysis of Parametric & Non Parametric Classifiers for Classification Technique using WEKA. *International Journal of Information Technology and Computer Science* 2012; 4(7):43–9. doi: 10.5815/ijitcs.2012.07.06.
- Humphris CW. *Computer Science Principles V10*. CreateSpace Independent Publishing Platform. 2013.
- Saravana N, Gayathri V. Performance and Classification Evaluation of J48 Algorithm and Kendall's Based J48 Algorithm (KNJ48). *International Journal of Computer Trends and Technology*. 2018;59(2):73–80. doi: 10.14445/22312803/ijctt-v59p112.
- Waseem S, Salman A, Muhammad AK. Feature subset selection using association rule mining and JRip classifier. *International Journal of Physical Sciences*. 2013;8(18):885–96. doi: 10.5897/ijps2013.3842.
- Lewis RJ, Ph D, Street WC. *An Introduction to Classification and Regression Tree (CART) Analysis*. 2000. Available from: <https://citeseerx.ist.psu.edu/viewdoc/download?doi=10.1.1.95.4103&rep=rep1&type=pdf>, 10 October 2021.
- Frank E, Witten IH. *Generating accurate rule sets without global optimization*. Hamilton, New Zealand: University of Waikato, Department of Computer Science. 1998.
- Kalmegh S. Analysis of WEKA Data Mining Algorithm REPTree , Simple Cart and RandomTree for Classification of Indian News. *International Journal of Innovative Science, Engineering & Technology*. 2015;2(2):438–446.
- Bro R, Kjeldahl K, Smilde AK, Kiers HAL. Cross-validation of component models: A critical look at current methods. *Analytical and Bioanalytical Chemistry*. 2008;390(5):1241–1251. doi: 10.1007/s00216-007-1790-1.
- Kohavi R. *A Study of Cross-Validation and Bootstrap for Accuracy Estimation and Model Selection*. Morgan Kaufmann. 1995.
- Novakovic J, Veljovi A, Ilic S, Papic Z, Tomovic M. Evaluation of Classification Models in Machine Learning. *Theory and Applications of Mathematics & Computer Science*. 2017;7(1):39–46.

39. Aggarwal CC. [ed.] *Data Classification - Algorithms and Applications*, Chapman and Hall/CRC. 2014.
40. Maimon O, Rokach L. [ed.] *Data Mining and Knowledge Discovery Handbook: A Complete Guide for Practitioners and Researchers*. Berlin, Springer. 2005.
41. Ras ZW, Dardzinska A. Action Rules Discovery Based on Tree Classifiers and Meta-actions. *Lecture Notes in Artificial Intelligence*. 2009;5722:66–75.
42. Ras ZW, Dardzinska A. Action Rules Discovery without Pre-existing Classification Rules. *Lecture Notes in Computer Science*, 2008; 5306:181-190
43. Jongbo OA, Adetunmb AO, Ogunrinde RB, Badeji-Ajisafe B. Development of an ensemble approach to chronic kidney disease diagnosis. *Scientific African*, 2020;8:e00456. doi: 10.1016/j.sciaf.2020.e00456
44. Senan EM, Al-Adhaileh MH, Alsaade FW, et al. Diagnosis of Chronic Kidney Disease Using Effective Classification Algorithms and Recursive Feature Elimination Techniques. *Journal of Healthcare Engineering*. 2021;2021:1004767. doi: 10.1155/2021/1004767.

Acknowledgements: This work is supported by the Ministry of Science and Higher Education of Poland under research project No. WZ/WM-IIB/3/2021.

Andreea S. Turiac:  <https://orcid.org/0000-0002-1548-5640>

Małgorzata Zdrodowska:  <https://orcid.org/0000-0003-4383-5713>

CALCULATION OF THE OPTIMAL BRAKING FORCE DISTRIBUTION IN THREE-AXLE TRAILERS WITH TANDEM SUSPENSION

Zbigniew KAMIŃSKI^{*} 

^{*}Faculty of Mechanical Engineering, Białystok University of Technology, ul. Wiejska 45C, 15-351 Białystok, Poland

z.kaminski@pb.edu.pl

received 8 February 2022, revised 15 March 2022, accepted 16 March 2022

Abstract: Heavy agricultural trailers can be equipped with a three-axle chassis with a tandem axle set at the rear and one mounted on a turntable at the front. In such trailers, selection of the distribution of braking forces that meet the requirements of the EU Directive 2015/68, with regard to braking, largely depends on the type of tandem suspension used. The requirements for brake force distribution in agricultural trailers of categories R3 and R4 are described. On this basis, a methodology for calculating the optimal linear distribution of braking forces, characteristic of agricultural trailers with air braking systems, was developed. An analysis of the forces acting on a 24-tonne three-axle trailer during braking was performed for five different suspensions of the rear tandem axle. An optimization algorithm using the quasi Monte Carlo method was described, on the basis of which a computer program for selection of the linear distribution of braking forces was developed. The calculations were made for an empty and loaded trailer with and without the weight of the tandem suspension. The most uniform distribution of braking forces was obtained for two leaf spring with dynamic equalization and air suspension, in which the ratio of the braking force of the tandem axle and the total braking force varied between 22.9% and 25.5% for the different calculation variants. A large variation in the braking force distribution was achieved for the two leaf spring suspension, in which the ratio of tandem axle braking force and the total braking force ranged from 2.7% to 6.4% for the leading axle and from 27.8% to 36.2% for the trailing axle. The presented calculation methodology can be used in the initial phase of the design of air braking systems for three-axle agricultural trailers.

Key words: agriculture trailer, tandem axle, air braking system, braking force distribution, optimization

1. INTRODUCTION

Heavy agricultural trailers with laden weights of about 25 tonnes can be designed as full three-axle trailers [26]. A full trailer is typically towed via a single-point drawbar that is also used to steer the front axle by rotating the front running gear [7]. At the rear of the trailer is mounted a tandem axle set comprising two axles spaced close to each other, usually from 1.2 m to 1.85 m [8, 13]. Tandem axles are used to increase the load-carrying capacity of a vehicle and to distribute the load between both axles, independent of the road surface roughness [18].

Tandem axle suspension may be grouped according to the basic design [14, 18, 24]. In agricultural trailers, different types of tandem axles are used, that is, walking beam, bogie (with single inverted parabolic spring), two leaf spring, two leaf spring and rods, two leaf spring with dynamic equalization and air suspension [1, 3, 29, 30].

In many types of tandem suspension for agricultural trailers, the axle load is transferred through the load leveller or equalizer beam used to balance the axle loads during normal operation with the brakes not applied [25]. Unfortunately, some mechanisms that are used to create good static load equalization have just the opposite effect on the dynamic load transfer [13]. When braking in vehicles with two leaf spring tandem suspension (two leaf spring and rods), the sum of the front spring seat force is less than the sum of the rear seat force, and the corresponding leading and trailing axle loads are no longer equal [25]. This resulting action is

called the inter-axle load transfer [13, 25]. Transferring the load between the axles causes the front axle to lock before the rear axle is locked and has a negative effect on braking performance. For example, in a truck equipped with two-elliptic leaf suspension the dynamic load of the leading axle approaches zero for a deceleration of approximately 0.55 g [18]. The friction utilization diagram indicates that the tandem rear axle is slightly braked while the front axle is greatly underbraked. If lockup occurs on the leading axle, then the directional stability is reduced. An additional improvement can be achieved by changing the tandem axle design to include push rods. Then, the wheels unlocked deceleration increases to 0.38 g from an original value of 0.25 g for an adhesion coefficient of 0.6 [18]. The directional stability can be completely lost if lockup occurs on the trailing axle [13]. Another unwanted result of poor inter-axle load transfer is that the suspension can produce an under-damped mode. Occasionally, this can result in a 'tandem hoop', which can cause a partial degradation of the vehicle's braking and handling performance [13]. The survey results [11] showed that the semi-trailer with the air suspension system can reduce the dynamic load coefficient from 14.8% to 29.3%, in comparison with the semi-trailer using the leaf spring suspension system.

Since 2016, EU agricultural vehicle legislation [6] has required agricultural trailers to achieve the same braking performance as commercial vehicle trailers (min. 50% braking efficiency for vehicles operating above 30 km/h). In addition, for agricultural trailers with a total mass of more than 3,500 kg (categories R3 and R4) and moving at a speed of more than 40 km/h, a specific distribu-

tion of braking forces between the axles of the vehicle is required. The braking efficiency has a direct influence on the vehicle braking distance and the vehicle's travelling direction stability in any road condition [28]. The adoption of the new European legislation in the field of agricultural vehicles places a high demand on the manufacturers of agricultural trailers, tractors and machinery in terms of braking systems [9].

The design process of a new brake system begins with the selection of the brake force distribution [21]. Generally, for the correct design of a vehicular brake system, it is essential that the ideal brake force distribution among the individual axles be known for empty and loaded vehicles [19]. In the case of two-axle vehicles, the relationships are simple and can be given in terms of either the vehicle deceleration or the rear axle brake force as a function of the front axle brake force [10]. Advanced optimization methods and strategies for selecting the distribution of braking forces are constantly being developed for passenger cars [10, 27, 34] and trucks [28, 35].

An analytical method of calculation of the brake force distribution in two-axle agricultural trailers was described in [16 and 20]. For a three-axle trailer, however, the analysis is more complex as the middle and rear axle loads are functions of the loading as well as the type and the geometry of the tandem axle suspension [18]. Therefore, even for three-axle vehicles with the simplest tandem suspensions, like walking beam and bogie [16] or two-elliptic leaf spring suspension [28], optimization methods are used to calculate and select the braking force distribution.

This paper is the result of a demand by agricultural machinery companies for new solutions for the calculation of the braking force distribution in three-axle trailers with different types of tandem suspension, filling a gap in the research. The quasi Monte Carlo method was used to search for an optimal linear force distribution, which is mostly used in the air brake system of trailers.

The rest of the paper is organized as follows: in section 2, the requirements of the braking force distribution of three-axle trailers are described; in section 3, the analysis of forces acting during braking on a three-axle trailer with different types of tandem suspension is presented; in section 4, the quasi Monte Carlo method and the algorithm of linear brake force distribution are described. The results of the optimization calculation for the different tandem axles are analysed and discussed in section 5. Finally, the summary and conclusions are drawn in section 6.

The results of the paper are expected to provide a reference for designing and evaluating the braking system of three-axle agricultural trailers and improving their braking performance.

2. REQUIREMENTS FOR BRAKING PERFORMANCE AND BRAKE FORCE DISTRIBUTION FOR THREE-AXLE TRAILER

When choosing the distribution of braking force between vehicle axles, an ideal distribution should be sought. The ideal braking condition is achieved when each axle and each axle assembly has the same rate of utilized adhesion, which is equal to the braking rate z of the vehicle. For a three-axle trailer with tandem axle at the rear, this condition can be written as follows:

$$f_1 = f_2 = f_{2i} = z \quad z = \frac{T_1 + \sum T_{2i}}{R_1 + \sum R_{2i}} \quad (1)$$

where T_1 and R_1 are the braking force and normal reactions of the road surface on the wheels of the front axle, T_{2i} and R_{2i} are the braking forces and normal reactions of the road surface on the wheels of the rear tandem axle, and i is the axle number in the rear axle assembly.

The adhesion utilization rates used by the front axle and rear axle assembly are calculated based on the following relationship:

$$f_1 = \frac{T_1}{R_1} \quad f_2 = \frac{\sum f_{2i} R_{2i}}{\sum R_{2i}} \quad (2)$$

With the braking distribution at the ideal level, the straight line stopping distance is minimized as a result of each axle reaching its maximum braking force capability [23], and the braking efficiency requirements are met with reserve (Tab. 1).

Tab. 1. The required service braking efficiency for towed agricultural vehicles [6]

Vehicle category	Braking rate z [%] at $p = 6.5$ bar	
	$v \leq 30$ km/h	$v > 30$ km/h
Trailers R2, R3, R4 and towed machines S2	$\geq 35\%$	$\geq 50\%$

Due to trailer load variations, it is practically impossible to achieve an ideal brake distribution, even when using braking force regulators. Therefore, for agricultural vehicles with speed above 40 km/h, the allowable limits for derogation of the adhesion utilization rates for individual axles against the ideal distribution have been determined. In the considerations regarding the distribution of brake forces, each part of a tractor-trailer unit is treated as a single vehicle, without taking into account the force in the coupling. From 2016, two solutions have been allowed, as shown in Fig. 1 [6].

The first solution: the adhesion utilization rate for each axle assembly must meet the condition of ensuring the minimum required braking performance as:

$$f_{1,2} \leq \frac{z+0.07}{0.85} \quad \text{when } 0.1 \leq z \leq 0.61 \quad (3)$$

and the condition of previous locking of the front axle wheels to ensure directional stability as:

$$f_1 > z > f_2 \quad \text{when } 0.15 \leq z \leq 0.30 \quad (4)$$

The second solution: the adhesion utilization rates by the axles should be within a given band, and then the limits of wheel locking are determined by the following relationships:

$$\begin{aligned} f_1 &\geq z - 0.08 \\ f_{1,2} &\leq z + 0.08 \end{aligned} \quad \text{when } 0.15 \leq z \leq 0.30 \quad (5)$$

In addition, the adhesion utilization curve for the rear axle assembly should fulfill the condition:

$$f_2 \leq \frac{z-0.02}{0.74} \quad \text{when } 0.30 \leq z \leq 0.61 \quad (6)$$

For precise calculations, the divisor in the inequality (6) should be set as 0.7381.

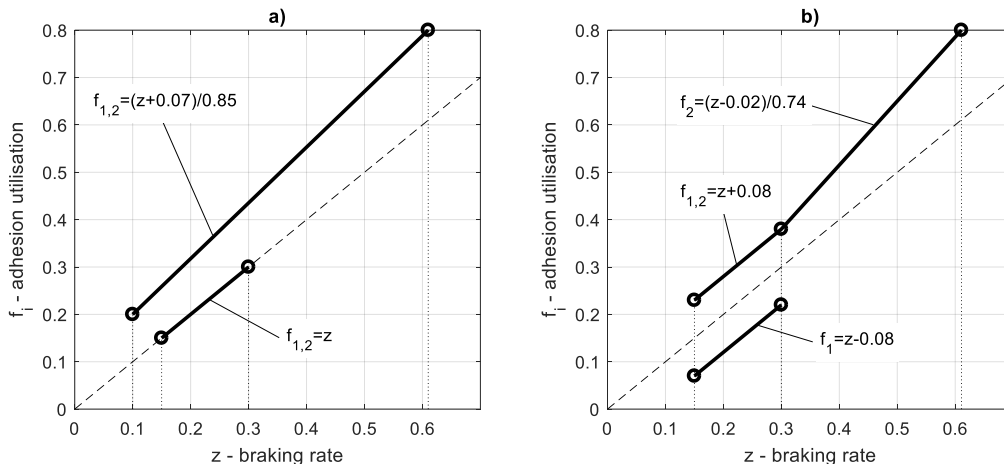


Fig. 1. Limit values of adhesion utilization in accordance with the Commission Delegated Regulation (EU) 2015/68 [6]:
(a) – first solution, (b) – second solution

The wheel-lock sequence requirements are regarded as met if the adhesion utilized by the front axle is greater than that utilized by at least one of the rear axles at braking rates between 0.15 and 0.30 [6]:

$$f_1 > f_{2i} \text{ for any } i \quad (7)$$

3. BRAKING OF THREE-AXLE TRAILER

For analysis of the brake force distribution, a rigid two-dimensional trailer model is proposed. In this model a suspension system with a different type and geometry of tandem axle is used. The forces acting on a decelerating three-axle agricultural trailer with tandem suspension are illustrated in Fig. 2. For simplicity, it is assumed that aerodynamic and rolling resistances are omitted.

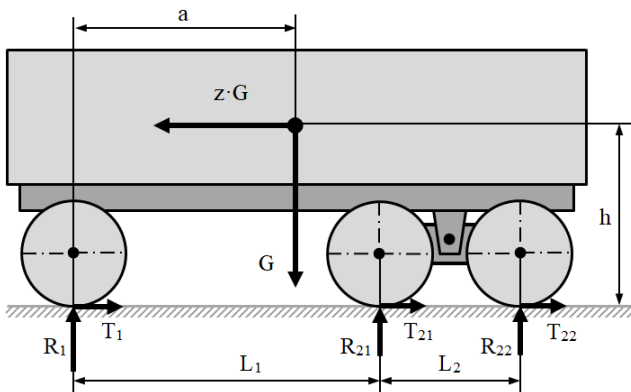


Fig. 2. Forces acting on a three-axle trailer with tandem suspension (ISO coordinate system [15])

The forces T_1 , T_{21} and T_{22} which induce braking deceleration are obtained from the axle brake force and are considered to be known functions of the brake line pressure [4, 6]. Using the notation from Fig. 2, the equations of force and moment equilibrium are given as:

$$\sum X = z \cdot G - T_1 - T_{21} - T_{22} = 0 \quad (8)$$

$$\sum Z = R_1 + R_{21} + R_{22} - G = 0 \quad (9)$$

$$\sum M_1 = R_{21}L_1 + R_{22}(L_1 + L_2) - G \cdot a + z \cdot G \cdot h = 0 \quad (10)$$

where T_1 , T_{21} and T_{22} are the brake forces, R_1 , R_{21} and R_{22} are the axle loads, L_1 is the inter-axle spacing, L_2 is the tandem axle spread, a is the distance from the centre of gravity to the front axle, h is the centre of gravity height, G is the trailer weight and z is the braking rate.

To determine the vertical reactions, the system of Eqs. (8)–(10) should be supplemented with an additional relationship between reactions R_{21} and R_{22} , which depends on the type and parameters of the tandem axle suspension.

3.1. Walking beam and bogie suspension

The simplest form of tandem axle suspension is a walking beam [1] located on either side of the vehicle (Fig. 3a). The walking beams are pivotally mounted onto the hanger of the trailer frame at a location intermediate between the forward and rear axles. The tandem axles may be rigidly attached to the ends of the walking beam using, for example, a U-bolt. In the bogie suspension, instead of walking beams, parabolic tapered springs are mounted upside down to the frame (Fig. 3b). The springs are anchored to the trailer frame by a cradle and U-bolts to allow for motion between the two axles [3].

The forces acting on the walking beam and bogie suspension are shown in Fig. 3.

Both tandem suspensions can be described by the same set of force and moment equilibrium equations as:

$$\sum X = z \cdot G_2 - T_{21} - T_{22} + T_2 = 0 \quad (11)$$

$$\sum Z = R_{21} + R_{22} - R_2 - G_2 = 0 \quad (12)$$

$$\sum M_2 = R_{22}d_2 - R_{21}d_1 + G_2b_2 - z \cdot G_2(h_s - h_2) + (T_{21} + T_{22})h_s = 0 \quad (13)$$

where T_2 and R_2 are the horizontal and vertical reaction forces in the single-point support between the suspension and trailer frame, d_1 and d_2 are the beam (parabolic spring) lengths, h_s is the height of the support position, b_2 is the distance of the centre of unsprung weight from a support, h_2 is the height of the centre of unsprung weight and G_2 is the unsprung weight.

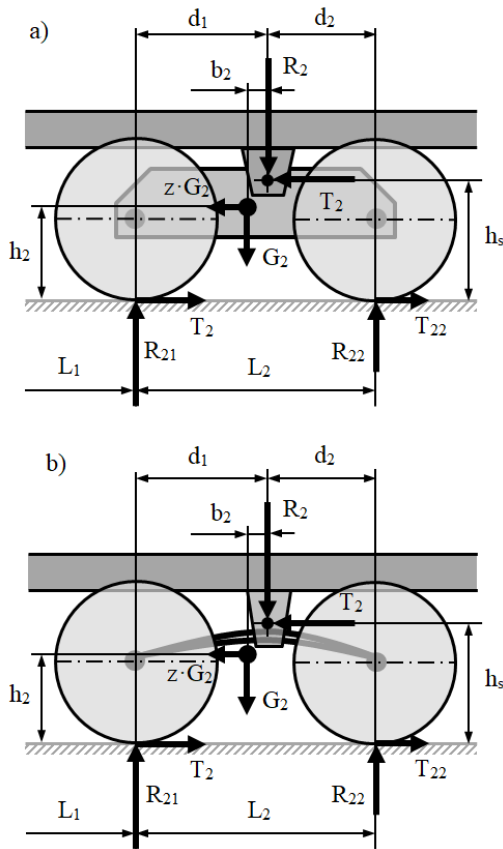


Fig. 3. Forces acting on a (a) walking beam and (b) bogie suspension

By solving the system of Eqs. (9), (10) and (13) together, taking into account from Eq. (8) that $T_{21} + T_{22} = z \cdot G - T_1$, the dynamic axle loads during braking on a three-axle trailer are obtained as:

$$R_1 = G \left(1 - \frac{a}{L} + z \frac{h}{L} \right) - G_2 \left(\frac{b_2}{L} - z \frac{h_s - h_2}{L} \right) - (z \cdot G - T_1) \frac{h_s}{L} \quad (14)$$

$$R_{21} = G \left(\frac{a}{L} - z \frac{h}{L} \right) \frac{d_2}{L_2} + \frac{L_1 + L_2}{L_2} \left[G_2 \left(\frac{b_2}{L} - z \frac{h_s - h_2}{L} \right) + (z \cdot G - T_1) \frac{h_s}{L} \right] \quad (15)$$

$$R_{22} = G \left(\frac{a}{L} - z \frac{h}{L} \right) \frac{d_1}{L_2} - \frac{L_1}{L_2} \left[G_2 \left(\frac{b_2}{L} - z \frac{h_s - h_2}{L} \right) + (z \cdot G - T_1) \frac{h_s}{L} \right] \quad (16)$$

where $L_2 = d_1 + d_2$ is the tandem wheelbase and $L = L_1 + d_1$ is the trailer wheelbase.

By omitting the unsprung weight G_2 , Eqs. (14)–(16) can be simplified and presented in a slightly different form [16].

3.2. Two leaf spring suspension

In two leaf spring tandem suspension, the two types of springs most commonly available are the double eye leaf spring and the slipper spring. In agricultural trailers the second type is more popular [1, 3, 29]. Slipper springs have an eye formed at one end only, with the other end formed into a reverse curve. The front eye of the leading and trailing spring is pivotally attached directly to the front hanger and equalizer beam, respectively, with pin joints

(Fig. 4). The rear end of the springs is captured in the equalizer beam or rear hanger.

The forces acting on the two leaf spring suspension with two unsprung weights are shown in Fig. 4.

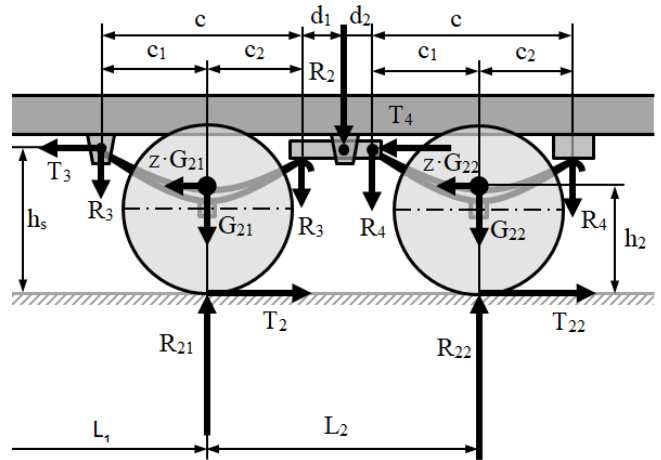


Fig. 4. Forces acting on a two leaf spring suspension

For the unsprung weight G_{21} , the following force and moment equilibrium equations are applicable:

$$\sum X = z \cdot G_{21} - T_{21} + T_3 = 0 \quad (17)$$

$$\sum Z = R_{21} - R_3 - R_{32} - G_{21} = 0 \quad (18)$$

$$\sum M_3 = -R_{32}c + R_{21}c_1 - G_{21}c_1 - z \cdot G_{21}(h_s - h_2) + T_{21}h_s = 0 \quad (19)$$

The equations of force and moment equilibrium for the unsprung weight of the G_{22} suspension are written as:

$$\sum X = z \cdot G_{22} - T_{22} + T_4 = 0 \quad (20)$$

$$\sum Z = R_{22} - R_4 - R_{42} - G_{22} = 0 \quad (21)$$

$$\sum M_4 = R_{42}c - R_{22}c_2 + G_{22}c_2 - z \cdot G_{22}(h_s - h_2) + T_{22}h_s = 0 \quad (22)$$

From Eqs. (19) and (22), the reactions acting on the ends of the equalizer beam are determined as:

$$R_{32} = (R_{21} - G_{21}) \frac{c_1}{c} - z \cdot G_{21} \frac{h_s - h_2}{c} + T_{21} \frac{h_s}{c} \quad (23)$$

$$R_{32} = [(R_{21} - G_{21})c_1 - z \cdot G_{21}(h_s - h_2) + T_{21}h_s] / c$$

$$R_{42} = (R_{22} - G_{22}) \frac{c_2}{c} + z \cdot G_{22} \frac{h_s - h_2}{c} - T_{22} \frac{h_s}{c} \quad (24)$$

$$R_{42} = [(R_{22} - G_{22})c_2 + z \cdot G_{22}(h_s - h_2) - T_{22}h_s] / c$$

After substituting the expressions (23) and (24) into the equilibrium equation of force moments acting on the equalizer beam:

$$R_{32}d_1 = R_{42}d_2 \quad (25)$$

A new relationship is obtained which, together with Eqs. (9) and (10), creates a system of three equations enabling the determination of the dynamic axle loads during braking of the trailer:

$$R_1 = G - \frac{L_2}{MN} \left\{ G(a - z \cdot h) \frac{c_1(d_1 - d_2) + c \cdot d_2}{L_2} + G_{21}d_1[c_1 + z(h_s - h_2)] - G_{22}d_2[c_2 - z(h_s - h_2)] - (T_{21}d_1 + T_{22}d_2)h_s \right\} \quad (26)$$

$$R_{21} = \frac{L_1+L_2}{MN} \left\{ G(a - z \cdot h) \frac{d_2 c_2}{L_1+L_2} + G_{21} d_1 [c_1 + z(h_s - h_2)] - G_{22} d_2 [c_2 - z(h_s - h_2)] - (T_{21} d_1 + T_{22} d_2) h_s \right\} \quad (27)$$

$$R_{22} = \frac{L_1}{MN} \left\{ G(a - z \cdot h) \frac{c_1 d_1}{L_1} - G_{21} d_1 [c_1 + z(h_s - h_2)] + G_{22} d_2 [c_2 - z(h_s - h_2)] + (T_{21} d_1 + T_{22} d_2) h_s \right\} \quad (28)$$

where $MN = c_2 d_2 L_1 + c_1 d_1 (L_1 + L_2)$

3.3. Two leaf-two rod suspension

A different version of the tandem axle configuration uses two springs with slipper-type ends only. Vertical forces are transmitted into the trailer frame by the front and rear hanger brackets and pivoted equalizer beam [1, 3, 29]. Longitudinal forces are transmitted by connecting the radius rods between the axles and front and centre hanger bracket, respectively (Fig. 5).

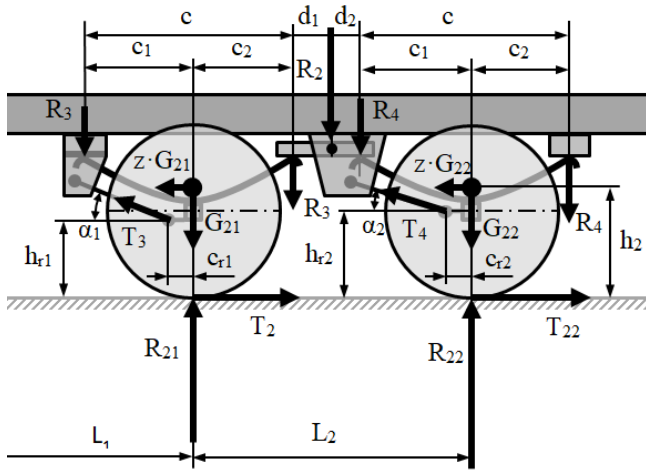


Fig. 5. Forces acting on a two leaf-two rod suspension

The parameters α_1 and α_2 as well as h_{r1} and h_{r2} have a significant impact on the suspension's operation. This design uses a decreased radius rod angle α_2 and a reduction in pivot height h_{r2} at the rear axle to reduce inter-axle load transfer during braking [25].

The following force and moment equilibrium equations for unsprung weights G_{21} and G_{22} are applicable:

$$\sum X = z \cdot G_{21} - T_{21} + T_3 \cos \alpha_1 = 0 \quad (29)$$

$$\sum Z = R_{21} + T_3 \sin \alpha_1 - R_3 - R_{32} - G_{21} = 0 \quad (30)$$

$$\sum M_3 = -R_{32}c + R_{21}c_1 - G_{21}c_1 - z \cdot G_{21}(h_s - h_2) + T_{21}h_s - T_3 \cos \alpha_1 (h_s - h_{r1}) + T_3 \sin \alpha_1 (c_1 - c_{r1}) \quad (31)$$

$$\sum X = z \cdot G_{22} - T_{22} + T_4 \cos \alpha_2 = 0 \quad (32)$$

$$\sum Y = R_{22} + T_4 \sin \alpha_2 - R_4 - R_{42} - G_{22} = 0 \quad (33)$$

$$\sum M_4 = R_{42}c - R_{22}c_2 + G_{22}c_2 - z \cdot G_{22}(h_s - h_2) + T_{22}h_s - T_4 \cos \alpha_2 (h_s - h_{r2}) - T_4 \sin \alpha_2 (c_2 + c_{r2}) \quad (34)$$

From Eqs. (31) and (34), the reaction forces acting on the ends of the equalising beam are determined as:

$$R_{32} = (R_{21} - G_{21}) \frac{c_1}{c} - z \cdot G_{21} \frac{h_{r1}-h_2}{c} + T_{21} \frac{h_{r1}}{c} + (T_{21} - z \cdot G_{21}) \tan \alpha_1 \frac{c_1 - c_{r1}}{c} \quad (35)$$

$$R_{42} = (R_{22} - G_{22}) \frac{c_2}{c} + z \cdot G_{22} \frac{h_{r2}-h_2}{c} - T_{22} \frac{h_{r2}}{c} + (T_{22} - z \cdot G_{22}) \tan \alpha_2 \frac{c_2 + c_{r2}}{c} \quad (36)$$

which are interrelated by the equation of moments of forces:

$$R_{32}d_1 = R_{42}d_2 \quad (37)$$

Solving Eqs. (9), (10) and (35)–(37) together, the trailer axle loads are obtained as:

$$R_1 = G - \frac{L_2}{MN} \left\{ G(a - z \cdot h) \frac{c_1(d_1-d_2)+c \cdot d_2}{L_2} + G_{21} d_1 [c_1 + z(h_{r1} - h_2)] - G_{22} d_2 [c_2 - z(h_{r2} - h_2)] - (T_{21} d_1 h_{r1} + T_{22} d_2 h_{r2}) + ED \right\} \quad (38)$$

$$R_{21} = \frac{L_1+L_2}{MN} \left\{ G(a - z \cdot h) \frac{d_2(c-c_1)}{L_1+L_2} + G_{21} d_1 [c_1 + z(h_{r1} - h_2)] - G_{22} d_2 [c_2 - z(h_{r2} - h_2)] - (T_{21} d_1 h_{r1} + T_{22} d_2 h_{r2}) + ED \right\} \quad (39)$$

$$R_{22} = \frac{L_1}{MN} \left\{ G(a - z \cdot h) \frac{c_1 d_1}{L_1} - G_{21} d_1 [c_1 + z(h_{r1} - h_2)] + G_{22} d_2 [c_2 - z(h_{r2} - h_2)] + (T_{21} d_1 h_{r1} + T_{22} d_2 h_{r2}) - ED \right\} \quad (40)$$

where: $MN = d_2 L_1 c_2 + c_1 d_1 (L_1 + L_2)$

$$ED = (T_{22} - z \cdot G_{22}) \tan \alpha_2 d_2 (c_2 + c_{r2}) - (T_{21} - z \cdot G_{21}) \tan \alpha_1 d_1 (c_1 - c_{r1})$$

Eqs. (38)–(40) simplify significantly if $\alpha_1 = \alpha_2 = 0$, because then $ED = 0$.

3.4. Two leaf spring with equalization

A tandem two leaf spring suspension with equalization [18] has two slipper springs and mechanical braking load compensation (Fig. 6). The rear end of the front spring is connected to the rear end of the rear spring by a rocker arm pivotally connected to a centre hanger bracket. This rocker arm ensures that static (and impact) loads are equally distributed between the two axles. Another design solution for a non-reactive tandem suspension with a bell crank lever and rod linkage is described in [14]. The forces acting on the two leaf spring suspension with equalization are shown in Fig. 6.

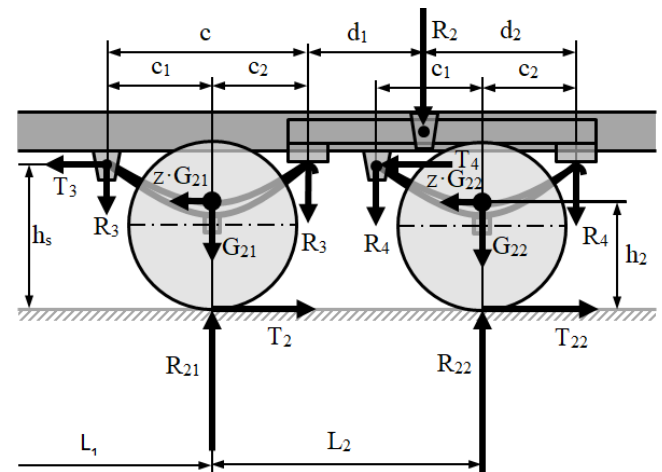


Fig. 6. Forces acting on two leaf spring suspension with equalization

The equations of force and moment equilibrium for the unsprung weights G_{21} and G_{22} of suspension are written as:

$$\sum X = z \cdot G_{21} - T_{21} + T_3 = 0 \quad (41)$$

$$\sum Z = R_{21} - R_3 - R_{43} - G_{21} = 0 \quad (42)$$

$$\sum M_3 = -R_{43}c + R_{21}c_1 - G_{21}c_1 - z \cdot G_{21}(h_s - h_2) + T_{21}h_s = 0 \quad (43)$$

$$\sum X = z \cdot G_{22} - T_{22} + T_4 = 0 \quad (44)$$

$$\sum Z = R_{22} - R_4 - R_{42} - G_{22} = 0 \quad (45)$$

$$\sum M_4 = -R_{42}c + R_{22}c_1 - G_{22}c_1 - z \cdot G_{22}(h_s - h_2) + T_{22}h_s = 0 \quad (46)$$

From Eqs. (43) and (47), the reaction forces acting on the ends of the equalizing beam are calculated as:

$$R_{43} = (R_{21} - G_{21}) \frac{c_1}{c} - z \cdot G_{21} \frac{h_s - h_2}{c} + T_{21} \frac{h_s}{c} \quad (47)$$

$$R_{42} = (R_{22} - G_{22}) \frac{c_1}{c} - z \cdot G_{22} \frac{h_s - h_2}{c} + T_{22} \frac{h_s}{c} \quad (48)$$

which are related by the equilibrium of moments equation:

$$R_{43}d_1 = R_{42}d_2 \quad (49)$$

By solving the system of Eqs. (9), (10), (47)–(49), the dynamic axle loads are obtained during braking the trailer as:

$$R_1 = \frac{1}{L} \left[G(L - a + z \cdot h) - (G_{21}d_1 - G_{22}d_2) \left(1 + z \frac{h_s - h_2}{c_1} \right) + (T_{21}d_1 - T_{22}d_2) \frac{h_s}{c_1} \right] \quad (50)$$

$$R_{21} = \frac{1}{L} \left[G(a - z \cdot h) \frac{d_2}{L_2} + (G_{21}d_1 - G_{22}d_2) \frac{L_1 + L_2}{L_2} \left(1 + z \frac{h_s - h_2}{c_1} \right) - \frac{L_1 + L_2}{L_2} (T_{21}d_1 - T_{22}d_2) \frac{h_s}{c_1} \right] \quad (51)$$

$$R_{22} = \frac{1}{L} \left[G(a - z \cdot h) \frac{d_1}{L_2} - (G_{21}d_1 - G_{22}d_2) \frac{L_1}{L_2} \left(1 + z \frac{h_s - h_2}{c_1} \right) + \frac{L_1}{L_2} (T_{21}d_1 - T_{22}d_2) \frac{h_s}{c_1} \right] \quad (52)$$

where $L_2 = d_1 + d_2$ and $L = L_1 + d_1$

3.5. Air suspension

In the air suspension the air springs are mounted onto the trailing arms via a cross-member and attached to the frame on the top (Fig. 7). The trailing arms mount pivotally to the hanger brackets and axle housings. All the air bags are connected with one another through air pipes to balance the axle loads. The vertical forces are distributed across the hanger brackets and air bags. Longitudinal forces due to braking are applied to the trailer frame through the hanger brackets.

The equilibrium equations of the forces and moments acting on the suspension with unsprung weights G_{21} and G_{22} are expressed as follows:

$$\sum X = z \cdot G_{21} - T_{21} + T_2 = 0 \quad (53)$$

$$\sum Z = R_{21} - R_2 - R_3 - G_{21} = 0 \quad (54)$$

$$\sum M_3 = -R_3c + R_{21}c_1 - G_{21}c_1 - z \cdot G_{21}(h_s - h_2) + T_{21}h_s = 0 \quad (55)$$

$$\sum X = z \cdot G_{22} - T_{22} + T_4 = 0 \quad (56)$$

$$\sum Z = R_{22} - R_4 - R_5 - G_{22} = 0 \quad (57)$$

$$\sum M_4 = -R_5c + R_{22}c_1 - G_{22}c_1 - z \cdot G_{22}(h_s - h_2) + T_{22}h_s = 0 \quad (58)$$

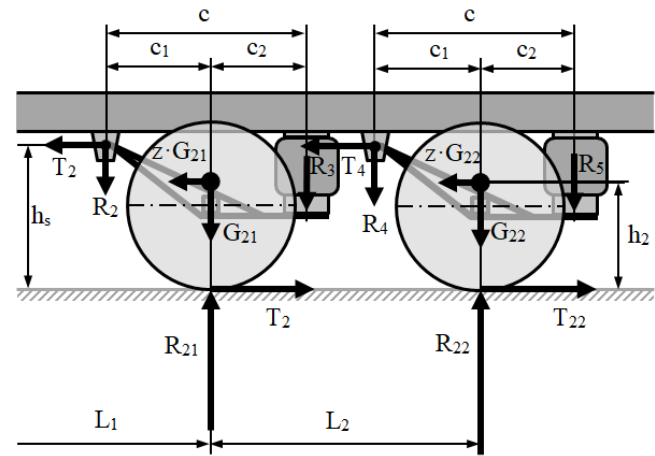


Fig. 7. Forces acting on air tandem suspension

Assuming that the pressure in the airbags is the same, the vertical reactions transmitted by the air springs are equal ($R_3 = R_5$). Then from Eqs. (55) and (58), at ($G_{21} = G_{22}$), the relationship between the tandem axle loads is obtained as:

$$R_{21}c_1 + T_{21}h_s = R_{22}c_1 + T_{22}h_s \quad (59)$$

Solving the system of Eqs. (9), (10) and (59), the trailer axle loads are obtained as:

$$R_1 = G \left(1 - \frac{a}{L} + z \frac{h}{L} \right) + \frac{L_2}{2L} (T_{21} - T_{22}) \frac{h_s}{c_1} \quad (60)$$

$$R_{21} = \frac{1}{2} G \left(\frac{a}{L} - z \frac{h}{L} \right) - \frac{L_1 + L_2}{2L} (T_{21} - T_{22}) \frac{h_s}{c_1} \quad (61)$$

$$R_{22} = \frac{1}{2} G \left(\frac{a}{L} - z \frac{h}{L} \right) + \frac{L_1}{2L} (T_{21} - T_{22}) \frac{h_s}{c_1} \quad (62)$$

where $L = L_1 + L_2/2$.

4. METHOD OF SELECTION OF LINEAR BRAKE FORCE DISTRIBUTION

In compressed air brake systems of agricultural vehicles, different types of load-dependent brake force regulators are used to achieve an approximation of an ideal brake force distribution. The automatic load sensing valves (LSV) currently mounted on heavy trailers have the task of adjusting the braking pressure on an axle (or possibly several axles) relative to the respective load status [32]. With properly designed braking forces, this prevents locking of the wheels when the vehicle is unladen or partially laden. In mechanically suspended trailers, the regulation is relative to the spring deflection. In air-suspended axles, the braking pressure of the pneumatic brake cylinders is dependent on the control pressure of the air springs.

As the pressure distribution characteristic of the load sensing valve is all substantially a straight line, the distribution of braking forces between the front and rear axles can also be considered as linear (radial).

A direction coefficient of the brake force distribution line passing through the origin of coordinate system $T_{2T}=f(T_1)$ is calculated as the braking force ratio:

$$i_P = \frac{T_{21}+T_{22}}{T_1} = \frac{T_{2T}}{T_1} \quad (63)$$

where T_{2T} is the total braking force of the tandem axles.

Similarly, a linear distribution of braking forces, variable or fixed (in the absence of a regulator of braking forces), can be applied to the tandem axle unit as:

$$i_S = \frac{T_{22}}{T_{21}} \quad (64)$$

Using the relations (8), (63) and (64), the braking forces can be described by a parametric equation with the braking rate z as a variable:

$$\begin{aligned} T_1 &= z \cdot G \cdot \frac{1}{1+i_P} & T_{2T} &= z \cdot G \cdot \frac{i_P}{1+i_P} & T_{21} &= T_{2T} \cdot \frac{1}{1+i_S} \\ T_{22} &= T_{2T} \cdot \frac{i_S}{1+i_S} \end{aligned} \quad (65)$$

The values of the i_P and i_S ratios can theoretically change in a very wide range from zero to infinity; extreme values are achieved if the braking force of one of the axles is equal to zero. Therefore, the braking force distribution coefficients were used to represent the participation of each axle's braking force (braking force distribution proportion), and defined as the ratio of the braking force of the individual axle to the total braking force of the trailer. Namely:

$$\beta_1 = \frac{T_1}{z \cdot G} \quad \beta_2 = \frac{T_{2T}}{z \cdot G} \quad \beta_{21} = \frac{T_{21}}{z \cdot G} \quad \beta_{22} = \frac{T_{22}}{z \cdot G} \quad (66)$$

The values of these coefficients can theoretically change from 0 to 1, and in addition, the following relations are fulfilled:

$$\beta_1 + \beta_2 = 1 \quad \beta_{21} + \beta_{22} = \beta_2 \quad (67)$$

Using relations (66) and (67), the braking force of a single axle and tandem axle unit can be calculated as:

$$\begin{aligned} T_1 &= \beta_1 z \cdot G & T_{2T} &= (1 - \beta_1) z \cdot G & T_{21} &= \beta_{21} z \cdot G \\ T_{22} &= (1 - \beta_1 - \beta_{21}) z \cdot G \end{aligned} \quad (68)$$

In order to find the optimal solutions for the linear braking force distribution, the Monte Carlo method [5, 17, 22] was used to search for an acceptable range of variability of the β_1 and β_{21} coefficients. An example block diagram of the algorithm for optimal selection of the braking force distribution coefficients is shown in Fig. 8.

The optimum values of the braking force distribution coefficients are determined in the process of minimizing the objective function consisting of the residual sum of squares:

$$OF = \frac{w_1(f_1 - f_2)^2 + w_2(f_{21} - f_{22})^2}{w_1 + w_2} \quad (69)$$

where w_i are the weighting factors.

The objective function formulated in this way prefers solutions with the smallest differences between the values of adhesion f_i utilized by individual axles. Since to meet the requirements (3)–(6), it is more important to reduce the difference between adhesion values f_1 of the front axle and f_2 of the rear axle assembly than to reduce the difference between values of adhesion f_{21} and f_{22} utilized by the rear axles, therefore $w_1 > w_2$ should be taken in the OF criterion.

Before calculating the objective function, the inequality constraints (3), (4) for the first solution or (5), (6) for the second solution are checked:

$$f_1^{up} \geq f_1 = \frac{T_1}{R_1} \geq f_1^{down} \quad f_2 = \frac{T_{21}+T_{22}}{R_{21}+R_{22}} \leq f_2^{up} \quad (70)$$

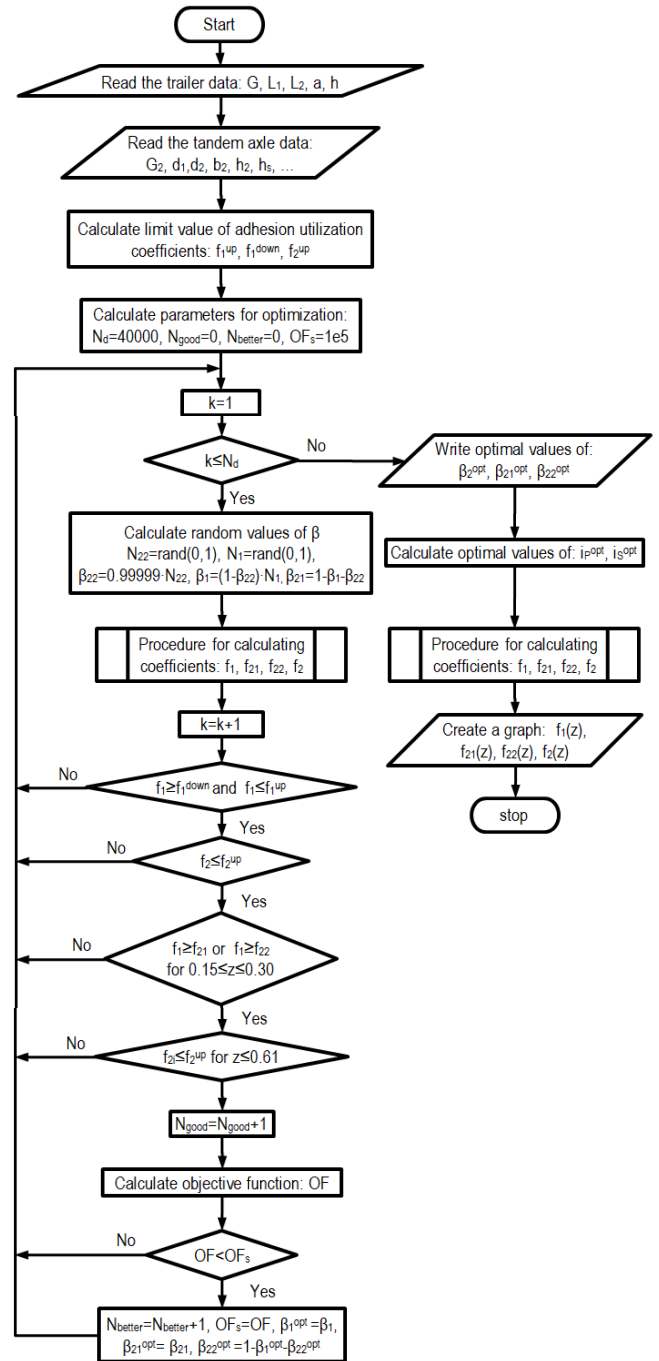


Fig. 8. Block diagram of an algorithm for the optimization of brake forces of a three-axle trailer using the Monte Carlo method (OF_s – initial value of the objective function, N_d – number of draws, N_{good} – number of good solutions, meeting inequality constraints, N_{better} – number of better solutions, reducing the value of the objective function)

In order to simplify the notation of borderline equations, they have been presented as the product of the algebraic and logical expressions. For the first solution:

$$f_1^{down} = z \cdot (0.15 \leq z \leq 0.30) \quad (71)$$

$$f_1^{up} = f_2^{up} = (z + 0.07)/0.85 \cdot (0.10 \leq z \leq 0.61) \quad (72)$$

For the second solution:

$$f_1^{down} = (z - 0.08) \cdot (0.15 \leq z \leq 0.30) \quad (73)$$

$$f_1^{up} = (z + 0.08) \cdot (0.15 \leq z \leq 0.30) \quad (74)$$

$$f_2^{up} = (z + 0.08) \cdot (0.15 \leq z \leq 0.30) + \left(\frac{z-0.3}{0.7381} + 0.36\right) \cdot (0.3 < z \leq 0.61) \quad (75)$$

Then condition (7) for multi-axle vehicles is checked:

$$f_1 > f_{21} \quad \text{or} \quad f_1 > f_{22} \quad \text{for} \quad z = 0.15 \div 0.30 \quad (76)$$

In addition, an extra condition is adopted for the adhesion utilized rates of the rear axle:

$$f_{2i} \leq f_2^{up} \quad \text{for} \quad z \leq 0.61 \quad (77)$$

which in fact limits excessive increase of the coefficient f_{22} for $z \leq 0.61$.

5. RESULTS OF OPTIMIZATION CALCULATIONS

Based on the algorithm described above, a computer program was developed in the MATLAB environment [31] to calculate the optimal distribution of braking forces for three-axle trailers with tandem rear axle suspension. The MATLAB algorithm of the Hammersley sequence [12] from Burkardt [2] was used to generate quasi-random numbers N_{22} and N_1 (Fig. 8). The Hammersley

Point Set in two dimensions is one of the simplest low discrepancy sequences and has been used in numerical and graphics applications, with a significant improvement in terms of error [33].

The technical data of the laden and unladen trailer as well as the data of tandem suspensions adopted for optimization calculations are presented in Tab. 2. To ensure comparability of the calculation results, the same mass $m_2 = 1,700$ kg was used for all types of suspension and some geometrical parameters of suspensions obtained based on the literature data [1, 3] were unified. Changes in some suspension dimensions for laden and unladen weight were also omitted.

The results of calculation of the braking force distribution for the laden and unladen trailer are presented in Tabs. 3 and 4. The number of draws was set as $N_d = 40,000$. The objective functions (69) were calculated in the range of $0.1 \leq z \leq 0.66$ with a step size of 0.01 for the following values of weighting factors $w_1 = 0.6$ and $w_2 = 0.4$.

For most types of tandem suspension, the same values of the optimal braking force distribution ratios were obtained (Tab. 3), applying both solutions described in section 2. The values after the dash are obtained taking into account the weight of the tandem suspension.

Tab. 2. Trailer and tandem suspension technical data [1, 3]

Trailer		Tandem suspension				
Unladen	Laden	Bogie (3.1)	Two leaf spring (3.2)	Two leaf two rod (3.3)	Two leaf equal. (3.4)	Air susp. (3.5)
$m = 7,700$ kg	$m = 24,000$ kg	$d_1 = 0.705$ m	$c_1 = 0.454$ m	$c_1 = 0.497$ m	$c_1 = 0.454$ m	$c_1 = 0.5$ m
$L_1 = 4.35$ m	$L_1 = 4.35$ m	$d_2 = 0.645$ m	$c = 0.93$ m	$c = 0.97$ m	$c = 0.93$ m	$c = 0.88$ m
$L_2 = 1.35$ m	$L_2 = 1.35$ m	$h_s = 0.567$ m	$h_s = 0.717$ m	$h_{r1} = h_{r1} = 0.467$ m	$h_s = 0.717$ m	$h_s = 0.717$ m
$a = 3.11$ m	$a = 3.04$ m	$h_2 = 0.547$ m	$h_2 = 0.567$ m	$h_2 = 0.567$ m	$h_2 = 0.567$ m	$h_2 = 0.567$ m
$h = 1.19$ m	$h = 1.57$ m	$b_2 = 0.03$ m	$d_1 = d_2 = 0.21$ m	$d_1 = d_2 = 0.19$ m	$d_1 = d_2 = 0.675$ m	
				$\alpha_1 = \alpha_2 = 15^\circ$		

Tab. 3. The results of the optimization of brake force distribution in a three-axle trailer for suspension described in sections 3.1 and 3.3–3.5 (L – laden, U – unladen, L_w , U_w – laden and unladen with weight of suspension)

Suspension		OF	β_1	β_{21}	β_{22}	i_p	i_s
Bogie (3.1)	U- U_w	0.2051–0.2049	0.4755–0.4758	0.3563–0.3608	0.1682–0.1634	1.1031–1.1018	0.4722–0.4530
	L- L_w	0.2638–0.2631	0.5359–0.5298	0.3167–0.3264	0.1473–0.1438	0.8659–0.8876	0.4651–0.4406
2 leaf 2 rod (3.3)	U- U_w	0.2831–0.3681	0.5311–0.5364	0.1316–0.1162	0.3373–0.3475	0.8827–0.8645	2.5632–2.9910
	L- L_w	0.3708–0.3989	0.5888–0.5849	0.1141–0.1085	0.2971–0.3067	0.6982–0.7098	2.6041–2.8276
2 leaf equal. (3.4)	U- U_w	0.0585–0.0707	0.4881–0.4983	0.2553–0.2548	0.2565–0.2469	1.0486–1.0068	1.0046–0.9692
	L- L_w	0.1016–0.1082	0.5413–0.5413	0.2296–0.2296	0.2291–0.2291	0.8473–0.8473	0.9981–0.9981
air susp. (3.5)	U- U_w	0.0585–0.0585	0.4881–0.4881	0.2553–0.2553	0.2565–0.2565	1.0486–1.0486	1.0046–1.0046
	L- L_w	0.1016–0.1016	0.5413–0.5413	0.2296–0.2296	0.2291–0.2291	0.8473–0.8473	0.9981–0.9981

Tab. 4. The results of the optimization of brake force distribution in a three-axle trailer for two leaf spring suspension described in section 3.2 (L-laden, U-unladen, L_w , U_w – laden and unladen with weight of suspension)

Solution		OF	β_1	β_{21}	β_{22}	i_p	i_s
I	U- U_w	1.3757–1.0286	0.6269–0.5973	0.0573–0.0641	0.3158–0.3386	0.5952–0.6743	5.5072–5.2780
	L- L_w	1.4814–1.3513	0.6734–0.6542	0.0484–0.0452	0.2782–0.3006	0.4850–0.5285	5.7452–6.6487
II	U- U_w	1.5155–1.0286	0.6009–0.5973	0.0371–0.0641	0.3620–0.3386	0.6641–0.6743	9.7537–5.2780
	L- L_w	1.7692–1.4772	0.6426–0.6417	0.0267–0.0363	0.3308–0.3220	0.5563–0.5583	12.401–8.8715

Slightly different values of the optimal coefficients of the braking force distribution for the first and second solutions were obtained for the two leaf spring suspension (section 3.2) and therefore they are presented separately in Tab. 4.

Based on the calculation results of the β_1 , β_{21} , β_{22} , i_P and i_S ratios presented in Tabs. 3 and 4, it can be seen that the distribution of the braking forces in a three-axle trailer significantly depends on the trailer loading and tandem suspension used in it.

The air suspension (section 3.5) and two leaf spring suspension with equalization (section 3.4) can be considered as the best in terms of the optimization criterion used (lowest OF value).

The trailer with these suspensions has a uniform distribution of braking forces, close to the ideal one, at which the value of coefficient β_1 is about 50%, the values of coefficients β_{21} and β_{22} are about 25%, and values of the i_P and i_S coefficients are about 1. Greater values of the objective function OF were obtained for the bogie suspension (section 3.1) and even greater for the two leaf–two rod suspension (section 3.3). Nevertheless, for all these suspensions, the same values of calculated parameters of the braking force distribution were obtained, regardless of the applied

solution. However, this does not apply to the suspension (3.2), which, due to the calculated values of the objective function, differs significantly from the others.

The results of calculating the brake force distribution coefficients for two leaf spring suspension indicate a large variation in the distribution of the braking forces of tandem axles, where the β_{21} coefficient of the leading axle is only about 2.7–6.4%. This may cause wheel lock on this axle according to the literature [13, 18]. An example of the course of the adhesion utilization rates $f_i(z)$ through the axles for an optimal distribution of brake forces for an unladen and a laden trailer with two leaf spring tandem suspension is shown in Fig. 9a and c. The adhesion utilization curve f_{21} of the leading tandem axle tends to infinity for $z > 0.7$ in the case of the unladen trailer (Fig. 9a) and for $z > 0.65$ in the case of the laden trailer (Fig. 9c) due to wheel separation from the road surface ($R_{21} = 0$). Meanwhile, for a trailer with air suspension of tandem axles, the adhesion utilization curves f_{21} , f_{22} and f_2 almost match for both the unladen (Fig. 9b) and laden trailers (Fig. 9d), which means that the coefficients of the adhesion utilization of both tandem axles are the same.

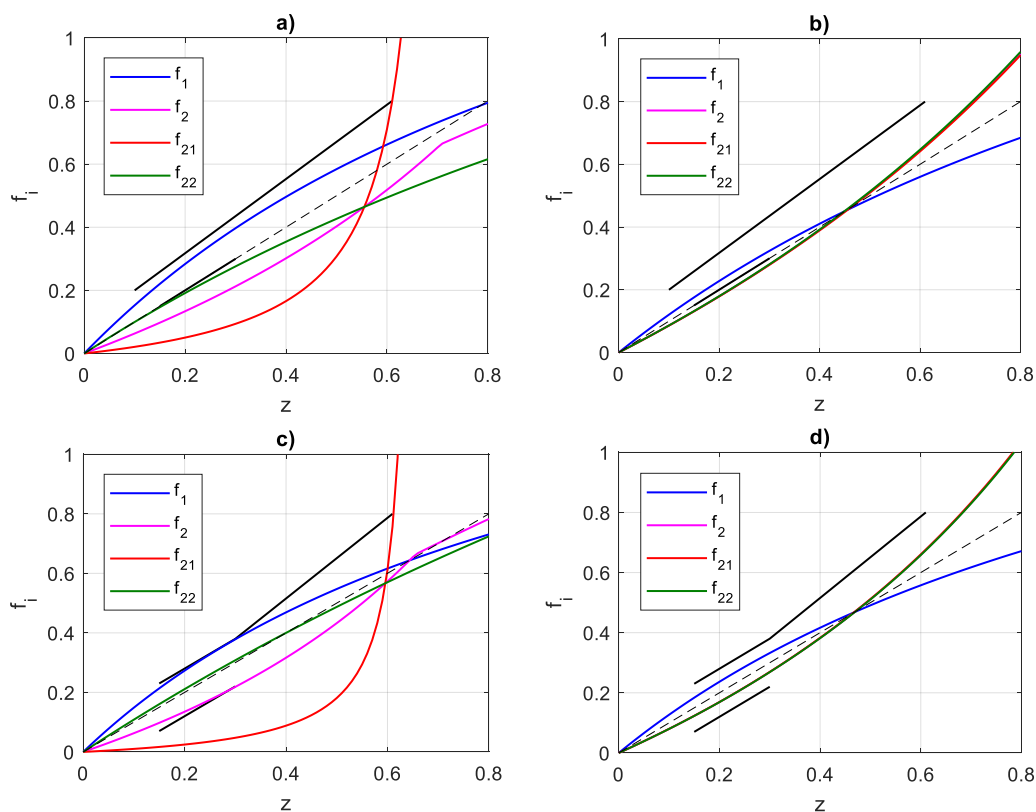


Fig. 9. The runs $f_i(z)$ for an optimal distribution of brake forces in a three-axle trailer (disregarding the weight of the tandem suspension): (a) – an unladen trailer with two leaf spring tandem suspension (I solution), $\beta_{21} = 5.7\%$, $\beta_{22} = 31.6\%$; (c) – a laden trailer with two leaf spring tandem suspension (II solution), $\beta_{21} = 2.7\%$, $\beta_{22} = 33.1\%$; (b) – an unladen trailer with air tandem suspension, $\beta_{21} = 22.5\%$, $\beta_{22} = 25.6\%$; (d) – a laden trailer with air tandem suspension (II solution), $\beta_{21} = 23\%$, $\beta_{22} = 22.9\%$

Comparing the calculation results obtained without and with the weight of the tandem suspension, it can be concluded that, in the case of suspensions 3.1, 3.4 and 3.5, the influence of this weight on the distribution of braking forces is negligible. The differences in the values of the braking force distribution coefficients do not exceed 1%. However, in the case of suspension 3.3, the differences in the calculated values of the i_S coefficient amount to approximately 16.7%, and in the case of suspension 3.2, even up to 46%.

6. SUMMARY AND CONCLUSIONS

The described method of optimizing the selection of the linear distribution of the braking forces of heavy three-axle agricultural trailers with various types of rear tandem axles can be used in the design of air braking systems, in which braking force correctors with radial characteristics were applied. The calculations of the braking force distribution took into account the requirements of the

EU Directive 2015/68 [6] in terms of braking performance and stability.

Optimization calculations made with the Monte Carlo method for a three-axle trailer with a load capacity of about 16 tonnes showed that the distribution of the braking forces significantly depends on the type of tandem suspension of the rear axles. The lowest values of the minimized objective function were achieved with the use of tandem axles with air suspension and two leaf spring suspension with equalization. For these two tandem suspensions, the adhesion utilization rates for individual axles are closest to the straight line illustrating the ideal distribution of braking forces, in which the adhesion utilized by each axle is the same and equal to the braking rate. The values for the β_{2i} ratios of the individual tandem axle and the total braking force of trailer are equalised and range from approximately 22.9% to 25.5% for the various calculation variants (I and II solution, laden and unladen trailer, without and with unsprung weight). The highest values of the objective function were obtained for the two leaf spring tandem suspension. For this suspension, the β_{21} ratio of the leading axle ranges from 2.7% to 6.4% and the β_{22} ratio of the trailing axle from 27.8% to 36.2%. Moreover, the calculations showed that the load transfer between the axles of this tandem suspension can lead to premature blocking of the leading axle wheels at braking ratios above 0.65. The results of the calculations are qualitatively consistent with the findings presented in [13, 18].

From the optimization calculation results obtained without and with the weight of the tandem suspension, it can be concluded that in the case of suspensions 3.1, 3.4 and 3.5, the influence of this weight on the distribution of braking forces is negligible.

REFERENCES

1. Agriculture Equipment Brochure. 2015. Available from: http://www.bpwtranspec.com.au/wp-content/uploads/2013/03/BPW_Agriculture_Equipment_brochure.pdf
2. Burkardt J. The Hammersley Quasi Monte Carlo (QMC) Sequence. Available from: https://people.sc.fsu.edu/~jburkardt/m_src/hammersley/hammersley.html
3. Colaert Essieux. General Catalogue. 2019. Available from: <http://www.colaertessieux.fr/PDF/COLAERT-ESSIEUX-GENERAL-CATALOGUE.pdf>
4. Day A.J. Braking of Road Vehicles. Oxford: Butterworth-Heinemann, 2014.
5. Dimov IT. Monte Carlo Methods for Applied Scientists. World Scientific; 2007. Available from: <https://www.worldscientific.com/worldscibooks/10.1142/2813>
6. European Commission. Commission Delegated Regulation (EU) 2015/68 of 15 October 2014 supplementing Regulation (EU) No 167/2013 of the European Parliament and of the Council with regard to vehicle braking requirements for the approval of agricultural and forestry vehicles. 2015.
7. Fancher P, Winkler C. Directional performance issues in evaluation and design of articulated heavy vehicles. *Vehicle System Dynamics*. 2007;45(7–8):607–47.
8. Gillmann R. Axle spacing and load equivalency factors. *Transportation Research Record: Journal of the Transportation Research Board*. 1999;1655(1):227–32.
9. Glišović J, Lukić J, Šušteršič V, Čatić D. Development of tractors and trailers in accordance with the requirements of legal regulations. In: 9th International Quality Conference. Faculty of Engineering, University of Kragujevac; 2015; 193–202.
10. Goodarzi A, Behmadi M, Esmailzadeh E. An optimised braking force distribution strategy for articulated vehicles. *Vehicle System Dynamics*. 2008;46(sup1):849–56.
11. Ha, DV, Tan, VV., Niem, VT., Sename, O. Evaluation of Dynamic Load Reduction for a Tractor Semi-Trailer Using the Air Suspension System at all Axles of the Semi-Trailer. *Actuators* 2022;11:12. <https://doi.org/10.3390/act11010012>
12. Hammersley JM. Monte Carlo methods for solving multivariable problems. *Numerical Properties of Functions of More Than One Independent Variable*. 1960;86(3):844–74.
13. Harwood DW. Review of Truck Characteristics as Factors in Roadway Design. Washington, D.C.: Transportation Research Board; 2003. Available from: <https://www.nap.edu/catalog/23379>
14. Heisler H. 10 - Suspension. In: Heisler H, editor. *Advanced Vehicle Technology*. 2nd ed. Oxford: Butterworth-Heinemann; 2002; 368–449.
15. ISO 8855:2011. Road vehicles — Vehicle dynamics and road-holding.
16. Kamiński Z, Radzajewski P. Calculations of the optimal distribution of brake force in agricultural vehicles categories R3 and R4. *Eksplot i Niezawodn*. 2019;21(4):645–53.
17. Kroese DP, Taimre T, Botev ZI. *Handbook of Monte Carlo Methods*. Wiley; 2011.
18. Limpert R. *Engineering Design Handbook: Analysis and Design of Automotive Brake Systems*. HQ, US Army Materiel Development and Readiness Command; 1976.
19. Limpert R. An investigation of the brake force distribution on tractor-semitrailer combinations. *Society of Automotive Engineers*; 1971. Available from: <https://www.sae.org/content/710044/>
20. Miatluk M, Kaminski Z. Brake systems of road vehicles. Calculations. Białystok: Wydawnictwo Politechniki Białostockiej; 2005.
21. Mital A, Desai A, Subramanian A, Mital A. *Product development: A structured approach to consumer product development, design, and manufacture*. 2nd ed. Elsevier Science; 2014.
22. Morton DP, Popova E. Monte-Carlo Simulations for Stochastic Optimization. In: *Encyclopedia of Optimization*. Boston, MA: Springer US; 1529–37.
23. NHTSA heavy duty vehicle brake research program: Report no. 1 — stopping capability of air braked vehicles. National Highway Traffic Safety Administration; 1985. by Richard W. Radlinski and S. F. Williams. Available from: <https://books.google.pl/books?id=ptbZvgEACAAJ>
24. Nunney MJ. *Light and Heavy Vehicle Technology*. Routledge; 2007.
25. Pierce PR. Controlled load transfer during braking on a four-spring trailer suspension. *Society of Automotive Engineers*; 1985. Available from: <https://www.sae.org/content/852344/>
26. [26] Road Safety Authority. Revised Standards for Agricultural Vehicles RSA Guide. Ballina, Republic of Ireland: Road Safety Authority; 2015.
27. Sun B, Wang P, Gao S, Yu J, Wang Z. Development of braking force distribution strategy for Dual-Motor-Drive Electric Vehicle. *Journal of Engineering and Technological Sciences*. 2018;50(2):179–201.
28. Tang G, Zhao H, Wu J, Zhang Y. Optimization of braking force distribution for three-axle truck. *Society of Automotive Engineers*; 2013. Available from: <https://www.sae.org/content/2013-01-0414/>
29. Titan Agricultural Catalogue – Tires, wheels, tracks, axles. 2015. Available from: http://titanaust.com.au/wp-content/uploads/2015/10/TITA0053-C1L3P2-Agricultural-Catalogue-COMplete_LR.pdf
30. Van Straelen B. Lastverlagerung und Bremskraftverteilung bei Einachs- und Doppelachsanhängern. *Grundlagen der Landtechnik*. 1983;33(6):183–9.
31. Venkataraman P. *Applied Optimization with MATLAB Programming*. 2nd ed. Hoboken: Wiley & Sons, Inc.; 2009
32. WABCO. *Pneumatic Braking System Agriculture and Forestry. Product Catalogue*. 2017. Available from: <https://www.wabco-customercentre.com/catalog/docs/8150100823.pdf>

33. Wong T-T, Luk W-S, Heng P-A. Sampling with Hammersley and Halton Points. *Journal of Graphics Tools*. 1997;2(2):9–24.
34. Xu J, Zhang X. Optimization algorithm for vehicle braking force distribution of front and rear axles based on brake strength. 12th World Congress on Intelligent Control and Automation (WCICA). IEEE; 2016; 3353–60.
35. Zhao LH, Cao QG, Li YS, Gao NZ. An optimization technique of braking force distribution coefficient for truck. *Proceedings 2011 International Conference on Transportation, Mechanical, and Electrical Engineering (TMEE)*. IEEE. 2011;1784–7.

Acknowledgments: This research was founded through subsidy of the Ministry of Science and Higher Education of Poland for the discipline of mechanical engineering at the Faculty of Mechanical Engineering Bialystok University of Technology WZ/WM-IIM/4/2020.

Zbigniew Kamiński:  <https://orcid.org/0000-0003-2693-5077>

NOMENCLATURE

i – tandem axle index ($i=1$, leading axle; $i=2$, trailing axle)
 a – distance from the centre of gravity to front axle [m]
 b_2 – distance of centre of unsprung weight from a support [m]
 c – leaf spring length [m]
 c_1, c_2 – leaf spring arm length [m]
 c_{ri} – i -th distance from rod pivot to centre of axle [m]
 d_1, d_2 – beam (parabolic spring) length, equalizer beam length [m]
 f_1, f_2 – adhesion utilization rate of front and rear axle assembly
 G – trailer weight [N]
 G_2 – unsprung weight of beam (parabolic spring) [N]
 G_{2i} – unsprung weight of i -th tandem axle [N]
 h – centre of gravity height [m]
 h_s – height of support position [m]
 h_2 – height of centre of unsprung weight [m]
 h_{ri} – i -th rod pivot height [m]
 i_P – braking force ratio
 i_S – tandem braking force ratio
 L_1 – inter-axle spacing [m]
 L_2 – tandem axle spread [m]
 R_1 – front axle load [N]
 R_{2i} – i -th tandem axle load [N]
 T_1 – front axle braking force [N]
 T_{2i} – i -th braking force of tandem axle [N]
 z – braking rate of trailer [-]
 α_i – i -th rod angle [°]
 β_1 – ratio of front axle to total braking force
 β_2 – ratio of tandem axle to total braking force
 β_{2i} – ratio of i -th tandem axle to total braking force

AN OVERVIEW OF HEAT TRANSFER ENHANCEMENT BASED UPON NANOPARTICLES INFLUENCED BY INDUCED MAGNETIC FIELD WITH SLIP CONDITION VIA FINITE ELEMENT STRATEGY

Muhammad B. HAFEEZ^{*}, Marek KRAWCZUK^{**}, Hasan SHAHZAD^{**}

^{*}Faculty of Mechanical Engineering and Ship Technology, Institute of Mechanics and Machine Design,
Gdansk University of Technology, ul. Narutowicza 11/12, 80-233 Gdańsk, Poland

^{**}Faculty of Materials and Manufacturing, College of Mechanical Engineering and Applied Electronics Technology,
Beijing University of Technology, 100 Pingleyuan, Chaoyang District, Beijing 100124, China

muhammad.bilal.hafeez@pg.edu.pl, marek.krawczuk.pg.edu.pl, hasanshahzad99@hotmail.com

received 2 February 2022, revised 6 April 2022, accepted 10 April 2022

Abstract: The mathematical model of heat generation and dissipation during thermal energy transmission employing nanoparticles in a Newtonian medium is investigated. Dimensionless boundary layer equations with correlations for titanium dioxide, copper oxide, and aluminium oxide are solved by the finite element method. Parameters are varied to analyze their impact on the flow fields. Various numerical experiments are performed consecutively to explore the phenomenon of thermal performance of the combination fluid. A remarkable enhancement in thermal performance is noticed when solid structures are dispersed in the working fluid. The Biot number determines the convective nature of the boundary. When the Biot number is increased, the fluid temperature decreases significantly. Among copper oxide, aluminium oxide, and titanium oxide nanoparticles, copper oxide nanoparticles are found to be the most effective thermal enhancers.

Key words: magnetohydrodynamic flow, porous medium, nanofluids, heat transfer, thermal performance, convective boundary conditions, FEM

1. INTRODUCTION

Fluid flows in porous media have a variety of uses in everyday life, including oil movement in the soil, and fluid seepage through sands and rocks, among others. Numerous research on the impact of fluid flow and heat transport has been done in light of this fact. For example, [1] examined the function of porous media and nanoparticles in heat and mass transmission during homogeneous and heterogeneous chemical reactions. The effect of a magnetic field on the transport of heat energy in a Maxwellian fluid along the channel field, under the influence of the porous medium, was discussed in [2]. For example, in [3], the pore diameters of heterogeneous porous media were optimized during random convection inside a two-sided lid-driven cavity. Numerical solutions for improving heat conduction of water–iron oxide nanofluids in the presence of a porous medium were discovered in [4]. The effect of porous media on MHD natural convection in a cone containing cadmium telluride nanofluid was investigated in [5]. [6] investigated the effects of nano-sized particles on heat energy transport during convective heat transfer in magnetohydrodynamic (MHD) flow in the presence of sinusoidal resistive force generated by porous media. Refer [7] reported the numerical solution of MHD nanofluid flow in porous media, including the effects of velocity slip and non-linear thermal radiation using the finite element technique (FEM).

An electrically conducting fluid subjected to a magnetic field behaves substantially differently from an electrically conducting

nanofluid due to the Lorentz force's influence on fluid movement and heat energy transmission. MHD flow occurs when a fluid is exposed to a magnetic field, as has been extensively addressed. [8] examined the heat transport in a fluid filled chamber under the influence of an external magnetic field, for example. The transmission of energy during MHD fluid flow around a cylinder was investigated in [9]. The effects of magnetic fields on the transmission of momentum and heat energy in a radiative fluid containing nanoparticles were discussed in [10]. In [11], we performed a computational simulation to look at the increase in heat transmission in MHD flow over a moving surface. [12] investigated the effects of magnetic field and nanoparticles on current and ion slip in three-dimensional flow. [13] used numerical simulation to model two-phase MHD non-Newtonian flow between nanoparticle-filled plates. In [14], the numerical solution for an unstable MHD Maxwell nanofluid flow over a stretching sheet in the presence of thermo-diffusion and radiation was obtained using the FEM. The MHD free convection of a nanofluid flowing across a vertical cone was studied using finite element analysis in [15].

Many academics working in the field of thermal system design are constantly coming up with new ways to create more efficient thermal systems. The most frequent method involves the dispersion of metallic nanoparticles in a base liquid, and several aspects of this process have already been discussed. Diffusion of nano-sized particles in the base liquid has improved thermal performance and generated a more efficient working fluid than the base fluid, both experimentally and conceptually. Nanofluids are these forms of fluids. The invention of nanofluids has inspired research-

ers, and various papers have been published. For example, in [16], the authors discussed an increase in the transport of heat energy in an electrically conducting fluid exposed to a magnetic field. They used the lattice Boltzmann method to analyze the underlying physics. The impact of nano-sized alumina particle dispersion on heat energy and momentum transfer in MHD fluid was investigated in [17], which discussed an increase in the wall heat flux due to a rise in thermal conductivity. In [18], we looked at Walter B rheology and applied mathematical models to improve mixed convective heat and mass transmission. They used numerical simulations to look into different physical aspects. The influence of metallic nano-sized particles on the efficacy of thermal conduction of the working fluid was studied theoretically in [19]. [20] investigated the transport mechanism in the three-dimensional flow of an MHD fluid incorporating nano-sized particles and found a considerable improvement in the working fluid's thermal performance. The influence of nano-sized solid objects on the thermal effectiveness of a working fluid was explored using natural convection in a hollow [21] with an elliptical heater. The best analytic approach utilized in [22] is to determine a nano-material's thermal performance. They also discovered the effect of heat dissipation on temperature distribution in nanomaterials and an increase in working fluid efficiency due to the inclusion of metallic nanostructures. The effects of porous media and thermal radiation on the transmission of energy and momentum in a liquid containing solid nanoparticles were investigated in [23]. A mathematical model for homogeneous-heterogeneous chemical reactions during mass transport of MHD Eyring-Powell fluid on a spinning disc was developed by an author [24]. [25] looked studied the effects of porous media and non-linear thermal radiation on the thermal properties of a fluid subjected to nanostructure dispersion in mass transport, taking chemical processes into account. [26] employed mathematical models to investigate the effect of nanoparticle hybridity on the effectiveness of thermal conductivity of fluid across a moving surface when heat dissipation is significant. [27] investigated the effect of metallic nanoparticle hybridity on the thermal performance of a working fluid subjected to an external magnetic field using mathematical modeling. [28] investigated the flow across a revolving disc with an external magnetic field and thermal radiations. Readers are encouraged to look up prior works [29-32] and their references for further information on nanofluids and their applications. The effects of an induced magnetic field and changes in thermal conductivity on the flow of a second-grade fluid in the presence of a porous medium have also been studied [34-35].

This research aims to investigate the thermal properties of a nanofluid under convective boundary circumstances (BCs). This project is divided into five pieces. In Section 2, mathematical modeling is explained. Section 3 discusses the solution technique. Section 4 presents and discusses the outcomes. Finally, the paper is concluded with a short conclusion.

2. PHYSICAL SETUP AND DESCRIPTION

Let us consider the dispersion of three types of nanometallic structures, i.e., CuO, Al₂O₃ and TiO₂, in water, in order to investigate the increase in its thermal conductivity. Nano-water is subjected to an applied magnetic field. The nano-water mixture over a hot vertical surface experiences convection. This nano-water mixture is also assumed to be a heat-generating mixture. The

buoyant force is significant under the Boussinesq calculation. The fluid flows through a porous medium and hence experiences a resistive force. The simplified partial differential equations PDE are as follows [33]:

$$\frac{\partial u}{\partial x} + \frac{\partial v}{\partial y} = 0, \tag{1}$$

$$u \frac{\partial u}{\partial x} + v \frac{\partial u}{\partial y} = \frac{\mu_{nf}}{\rho_{nf}} \frac{\partial^2 u}{\partial y^2} + \beta_{nf} g (T_f - T_\infty) - \frac{\sigma_{nf} B_0^2 u}{\rho_{nf}} - \mu_{nf} \frac{u}{k_1}, \tag{2}$$

$$u \frac{\partial T_f}{\partial x} + v \frac{\partial T_f}{\partial y} = \frac{k_{nf}}{(\rho c_p)_{nf}} \frac{\partial^2 T_f}{\partial y^2} + \frac{\mu_{nf}}{(\rho c_p)_{nf}} \left(\frac{\partial u}{\partial y} \right)^2 + \frac{\sigma_{nf} B_0^2 u^2}{(\rho c_p)_{nf}} + \frac{Q_0}{(\rho c_p)_{nf}} (T_f - T_\infty) \tag{3}$$

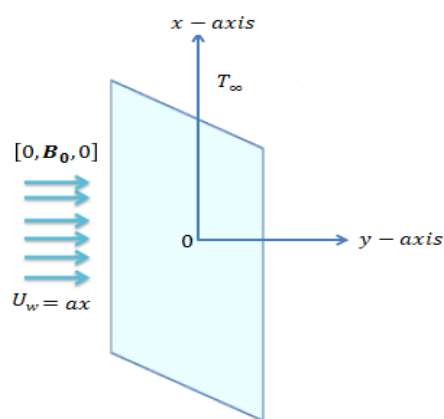


Fig. 1. Schematics - The physical arrangement and system of coordinates are shown herein

The required BCs are:

$$u(x, 0) = ax, v(x, 0) = 0, -\gamma k_f \frac{\partial T}{\partial y}(x, 0) = h_f (T_f - T(x, 0)) \tag{4}$$

$$u(x, \infty) = 0, T_f(x, \infty) = T_\infty.$$

where $[u, v, 0]$ represents the velocity, g represents the gravitational acceleration, ρ is the density, μ represents the kinematic viscosity, σ stands for the electrical conductivity, c_p represents the specific heat constant, k represents the thermal conductivity, nf represents the nanofluid, β_{nf} is the thermal expansion coefficient and γ is the thermal slip effect.

The correlations of the nanoparticles are as follows:

$$\rho_{nf} = (1 - \phi)\rho_f + \phi\rho_s, \beta_{nf} = (1 - \phi)\beta_f + \phi\beta_s,$$

$$\mu_{nf} = \frac{\mu_f}{(1 - \phi)^{2.5}},$$

$$(\rho c_p)_{nf} = (1 - \phi)(\rho c_p)_f + \phi(\rho c_p)_s,$$

$$\sigma_{nf} = \sigma_f \left[1 + \frac{3(r-1)\phi}{(r+2) - (r-1)\phi} \right],$$

$$r = \frac{\sigma_s}{\sigma_f}, \frac{k_{nf}}{k_f} = \frac{(k_s + 2k_f) - 2\phi(k_f - k_s)}{(k_s + 2k_f) + \phi(k_f - k_s)}. \tag{5}$$

The following new variables convert Eqs. (1)–(5) into dimensionless forms:

$$u = ax f'(\eta), v = -\sqrt{av_f} \psi, \psi = (av_f)^{\frac{1}{2}} x f(\eta),$$

$$\eta = \left(\frac{a}{v_f} \right)^{\frac{1}{2}} y, \theta(\eta) = \frac{T - T_\infty}{T_w - T_\infty}, \tag{6}$$

And, hence, one can get:

$$f''' + \phi_1 [ff'' - f'^2] - [M\phi_2(1 - \phi)^{2.5} + K]f' + Gr\phi_1 \left(1 - \phi + \phi \frac{\beta_s}{\beta_f}\right) \theta = 0, \tag{7}$$

$$\theta'' + \frac{k_f}{k_{nf}} Pr \phi_3 \left[f\theta' - 2f'\theta + \beta^* \theta + \frac{Ec}{\phi_4} f'^2 \right] + \phi_2 \frac{k_f MECPPr}{k_{nf}^{1.2}}. \tag{8}$$

The dimensionless BCs are:

$$\left. \begin{aligned} f(0) = 0, f'(0) = 1, \theta'(0) = \frac{Bi}{\gamma} [1 - \theta(0)], \\ \theta(\infty) = 0, f'(\infty) = 0. \end{aligned} \right\} \tag{9}$$

The derivatives involved in Eq. (9) are with respect to the variable η . M is the magnetic parameter, Hartmann number is Ha , Grashof number is Gr , β^* is the heat generation parameter, K is porous medium parameter, Prandtl number is denoted by Pr , Ec is the Eckert number and Bi is the Biot number. These are stated as follows:

$$Gr = \frac{\beta_f g(T_f - T_\infty)}{U_0 \alpha}, Pr = \frac{\nu_f}{\alpha_f}, M = \frac{\sigma_f B_0^2}{\rho_f \alpha}, K = \frac{\nu_f}{ak_1}, \beta^* = \frac{Q}{a(\rho c_p)_{naf}}, Ec = \frac{U_0^2}{c_p T_0}, Bi = \frac{hf}{k_f} \tag{10}$$

ϕ_1, ϕ_2, ϕ_3 and ϕ_4 are given by

$$\phi_1 = (1 - \phi)^{2.5} \left(1 - \phi + \phi \frac{\rho_s}{\rho_f}\right), \phi_2 = \left(1 + \frac{3(r-1)\phi}{(r+2)-(r-1)\phi}\right), \phi_3 = \left(1 - \phi + \phi \frac{(\rho c_p)_s}{(\rho c_p)_f}\right), \phi_4 = (1 - \phi)^{2.5} \left(1 - \phi + \phi \frac{(\rho c_p)_s}{(\rho c_p)_f}\right).$$

The divergent velocity is

$$C_f = \frac{\tau_{xy}|_{y=0}}{\rho_f U_0^2} = \frac{1}{Re_x^2 (1-\phi)^{2.5}} f''(0).$$

The Nusselt number is

$$Nu = \frac{xq_w}{k_f(T_f - T_\infty)} = \frac{Re_x^{\frac{1}{2}} k_{rf}}{k_f} \theta'(0).$$

The Reynolds number is $Re_x = \frac{ax^2}{\nu_f}$.

3. NUMERICAL APPROACH

3.1. Numerical procedure

The modelling for the exchange of heat and mass through dimensionless rules are done using the FEM. This is a ground-breaking strategy that has been used in several recent studies. The following is the process for putting FEM into practice.

- The domain $[0, \infty]$ is discretised into line segments such that each element has two nodes.
- The linear weight and shape functions are given by

$$S_j = (-1)^{j-1} \left(\frac{\xi_{j+1} - \xi}{\xi_{j+1} - \xi_j} \right), i=1, 2, \dots$$

- The residual error is integrated over $[\eta_e, \eta_{e+1}]$.
- The dependent unknowns are approximated over the element $[\eta_e, \eta_{e+1}]$ by the finite element approximations:

$$f = \sum_{j=1}^2 S_j f_j, \theta = \sum_{j=1}^2 S_j \theta_j, \phi = \sum_{j=1}^2 S_j \phi_j, h = \sum_{j=1}^2 S_j h_j,$$

where f_j, h_j, θ_j and ϕ_j are to be computed. S_j is the shape function. Hence, the stiffness elements are as follows:

$$K_{ij}^{11} = \int_{\eta_e}^{\eta_{e+1}} S_i S_j' d\eta, K_{ij}^{12} = \int_{\eta_e}^{\eta_{e+1}} -S_i S_j d\eta,$$

$$K_{ij}^{22} = \int_{\eta_e}^{\eta_{e+1}} \left(-\left(\frac{v_{hnf}}{\nu_f}\right) \left(1 + \frac{1}{\beta}\right) S_i' S_j' - \bar{h} S_i S_j - \bar{f}(\bar{h})' S_i S_j' - M \left(\frac{\sigma_{hnf}}{\sigma_f}\right) \left(\frac{\rho_f}{\rho_{hnf}}\right) S_i S_j - K S_i S_j \right) d\eta,$$

$$K_{ij}^{23} = \int_{\eta_e}^{\eta_{e+1}} (Gr)_t S_i S_j d\eta, K_{ij}^{24} = \int_{\eta_e}^{\eta_{e+1}} (Gr)_c S_i S_j d\eta,$$

$$K_{ij}^{33} = \int_{\eta_e}^{\eta_{e+1}} \left(-\left(\frac{K_{hnf}}{K_f}\right) \left(\frac{\rho_f}{\rho_{hnf}}\right) \left(\frac{(C_p)_f}{(C_p)_{hnf}}\right) S_i' S_j' + Pr \bar{f} S_i S_j' + Pr \beta^* S_i S_j \right) d\eta,$$

$$K_{ij}^{32} = \int_{\eta_e}^{\eta_{e+1}} \left(\left(\frac{v_{hnf}}{\nu_f}\right) \left(\frac{(C_p)_f}{(C_p)_{hnf}}\right) \left(1 + \frac{1}{\beta}\right) Pr Ec(\bar{h})' S_i S_j' \right. \\ \left. + MEc \left(\frac{\sigma_{hnf}}{\sigma_f}\right) \left(\frac{(C_p)_f}{(C_p)_{hnf}}\right) + \left(\frac{\rho_f}{\rho_{hnf}}\right) Pr S_i S_j \right) d\eta,$$

$$K_{ij}^{34} = \int_{\eta_e}^{\eta_{e+1}} -(Pr D_f) S_i' S_j' d\eta,$$

$$K_{ij}^{44} = \int_{\eta_e}^{\eta_{e+1}} -S_i' S_j' + Sc \bar{f} S_i S_j' d\eta,$$

$$K_{ij}^{43} = \int_{\eta_e}^{\eta_{e+1}} -Sr Sc S_i' S_j' d\eta,$$

where \bar{f} and \bar{h} are the computed nodal values.

- The non-linear equations are as follows:

$$[K\{\pi\}]\{\pi\} = \{F\}.$$

These are solved using Picard linearisation as follows:

$$[K\{\pi\}^{r-1}]\{\pi\}^r = \{F\},$$

where $\{\pi\}^{r-1}$ is the nodal value computed at $(r - 1)$ of the iteration and $\{\pi\}^r$ is the nodal value computed at the r th iteration.

The following equation is used to calculate the error:

$$error = \left| \frac{\pi^r - \pi^{r-1}}{\pi^{r-1}} \right|, \max \left| \frac{\pi^r - \pi^{r-1}}{\pi^{r-1}} \right| < \varepsilon,$$

while taking $\varepsilon = 10^{-5}$.

4. OUTCOMES AND DISCUSSION

The normalised governing boundary value problems with correlations for the thermo-physical properties are transformed into initial value problems. The transformed initial value problems with initial conditions are solved by FEM.

The parametric simulations are then conducted to examine the dynamics of the flow variables. Simulations are run to select the nanoparticles among CuO, Al₂O₃ and TiO₂ so that the system works in an efficient manner. Fig. 2 shows the velocity profiles of copper nanofluids, aluminium nanofluids and titanium nanofluids when $Gr = 0.2$ and 0.5 . This figure explains that the velocity of titanium nanofluid achieves the highest value, compared to CuO nanofluid and all nanofluids, for both cases when $Gr = 0.2$ and 0.5 . This figure also explains that the velocity of copper nanofluids, aluminium nanofluids and titanium nanofluids increases on

increasing the magnitude of Gr . The Grashof number is significant because it shows the ratio of the buoyant force caused by spatial variations in fluid density (induced by temperature differences) to the restraining force caused by the fluid's viscosity.

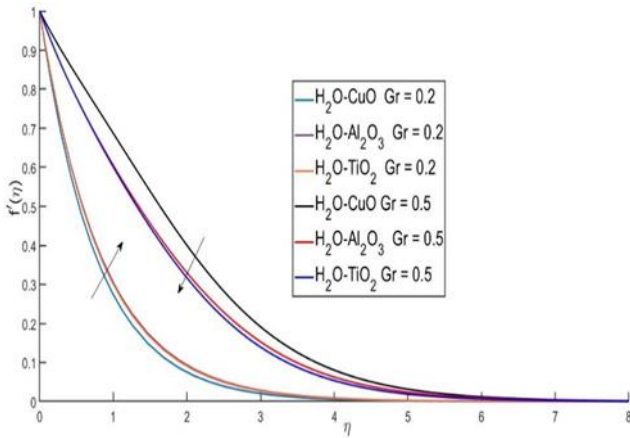


Fig. 2. Velocity profile against favourable buoyant force

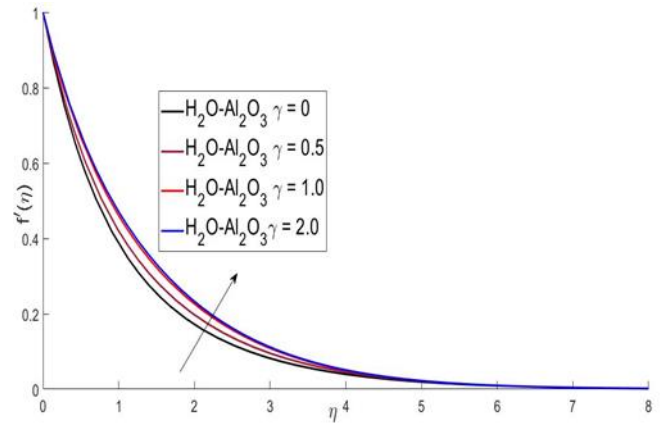


Fig. 5. Velocity profile against thermal effect

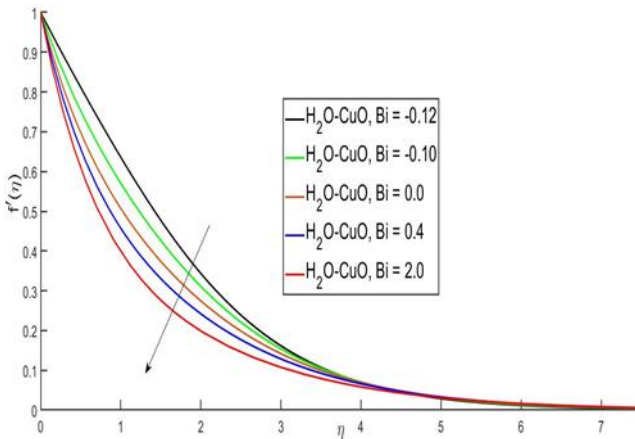


Fig. 3. Velocity profile against Biot number

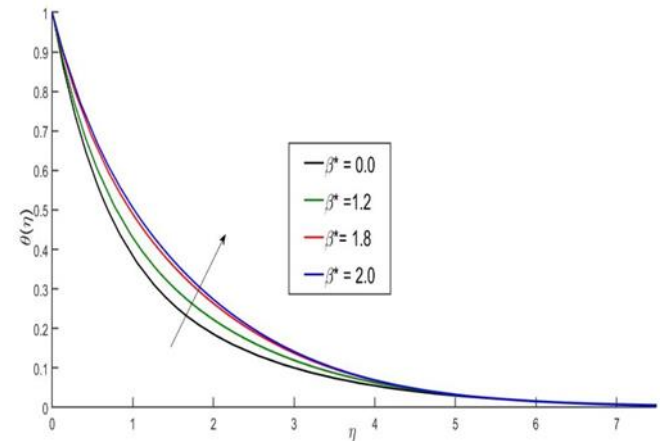


Fig. 6. Temperature profile against heat generation

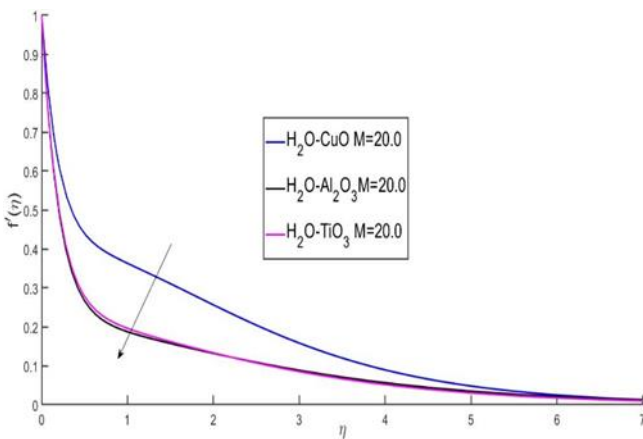


Fig. 4. Velocity profile against magnetic field

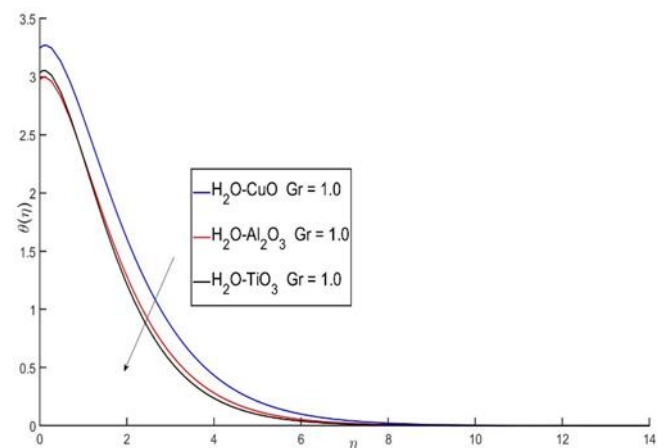


Fig. 7. Temperature profile against favourable buoyant force

Fig. 3 shows the effects of the Biot number Bi on velocity. On increasing the value of the Biot number, the velocity decreases. Because the Biot number is significant, it is used to calculate the heat transfer rate. In Fig. 4, it is noted that on increasing the magnetic field parameter M , the boundary layer's viscosity decreases

due to the application of the magnetic field on the particles of an electrical conducting fluid, causing a Lorentz force in the boundary layer. The Hall effect uses magnetic forces to reveal information about charge carriers in a substance.

Fig. 5 presents the velocity profile in relation to thermal effects; it shows that on increasing the values of thermal effects, the velocity profile increases. Fig. 6 illustrates the influence of the heat generation parameter β^* on temperature. It is observed that

on increasing the value of Ec , the boundary layer thickness also increases. In Fig. 7, we see the effects of Gr on temperature; we observed that when we increase the value of Gr , the temperature increases.

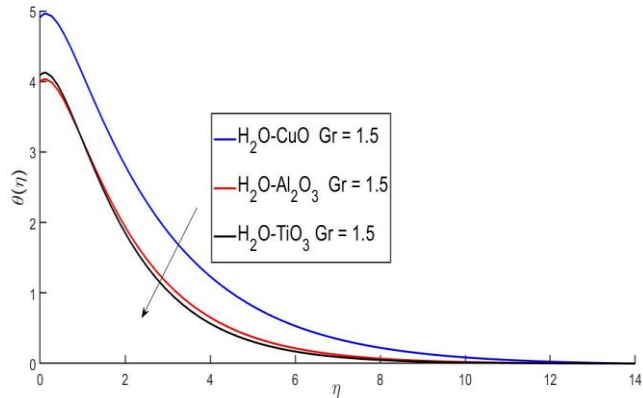


Fig. 8. Temperature profile against favourable buoyant force

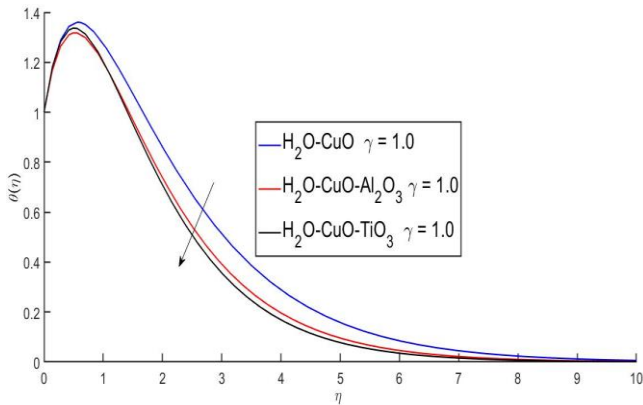


Fig. 9. Temperature profile against thermal effects

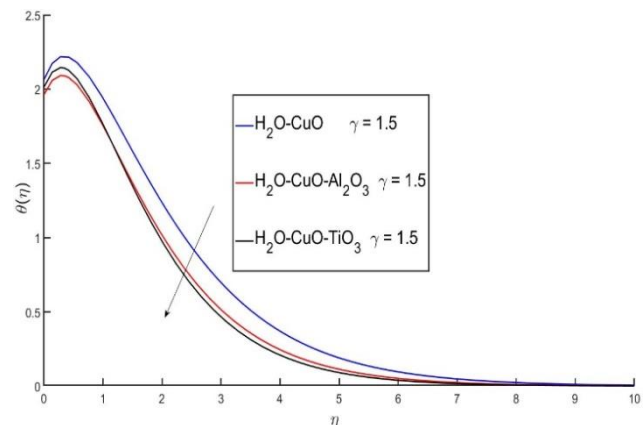


Fig. 10. Temperature profile against thermal effects

Fig. 8 shows the compression of Gr on temperature in the fluids comprising copper–water, aluminium–water and titanium–water. We notice that the viscosity of the boundary layer decreases on increasing the content of nanofluids. Figs. 9–11 show the impacts of the thermal slip parameter γ on temperature considering copper–water, aluminium–water and titanium–water nanofluids. It is observed that temperature diminishes on increasing the

value of γ . The copper nanofluid is more heat effective as compared to other nanofluids, namely aluminium and titanium nanofluids. The thermophysical properties of water and nanoparticles are presented in Tab. 1. The local skin friction coefficient and Nusselt number for copper oxide–water nanofluid with different nanoparticle factors are presented in Tab. 2.

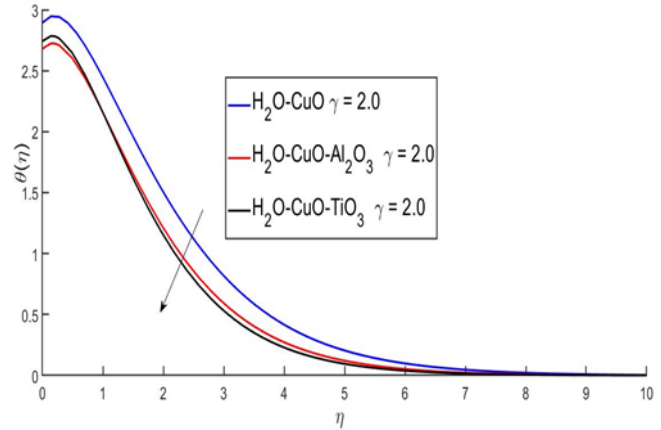


Fig. 11. Temperature profile against thermal effects

Tab. 1. Thermophysical properties of water and nanoparticles [33]

Materials	ρ (kg/m ³)	c_p (J/kgK)	k (W/mK)	$\beta \times 10^{-5}$ (K ⁻¹)	σ (S/m)
Water (H ₂ O)	997.5	4,178.0	0.6280	21.40	5.5×10^{-6}
Copper oxide (CuO) nanoparticles	6,310.0	550.5	32.90	0.85	5.96×10^7
Aluminium oxide (Al ₂ O ₃) nanoparticles	3,900.0	779.0	40.00	0.84	3.50×10^7
Titanium oxide (TiO ₂) nanoparticles	4,250.0	686.2	8.9538	0.90	2.38×10^6

Tab. 2. Local skin friction coefficient and Nusselt number for copper oxide–water nanofluid with different nanoparticle factors at $\phi = 0.2$ [33]

k_{nf}	$Re_x^{-1/2} Nu$	$Re_x^{-1/2} Nu$
0.628	0.084138154	0.993989767
0.72141	0.085608603	1.18560452
0.82458	0.086968704	1.381935016
0.9391	0.091634371	1.58355532
1.06696	0.095644211	1.79198143

5. CONCLUSION

Convection heat transfer in Newtonian fluids containing nano-solid metallic structures has been studied to investigate the enhancement in thermal conductivity, so that dispersion of nanoparticles of copper oxide, aluminium oxide, and titanium oxide may be recommended for an efficient thermal system such as automobile engines. The boundary layer's governing problems are numerically solved, and the significant studies are included.

When the Grashof number is increased, the favourable buoyancy force aids the flow, and the thickness of the MHD boundary

layer shows an increasing trend. This research is applicable for all kinds of nanoparticles.

On the flow of fluids, the fluctuation in Biot number results in a declining trend. As a result, as the Biot number increases, the flow slows down.


REFERENCES

- Khan WA, Aziz A. Double-diffusive natural convective boundary layer flow in a porous medium saturated with a nanofluid over a vertical plate: Prescribed surface heat, solute and nanoparticle fluxes. *International Journal of Thermal Sciences*. 2011;50(11):2154-60.
- Hayat T, Khan MI, Waqas M, Alsaedi A, Farooq M. Numerical simulation for melting heat transfer and radiation effects in stagnation point flow of carbon-water nanofluid. *Computer methods in applied mechanics and engineering*. 2017;315:1011-24.
- Maghsoudi P, Siavashi M. Application of nanofluid and optimization of pore size arrangement of heterogeneous porous media to enhance mixed convection inside a two-sided lid-driven cavity. *Journal of Thermal Analysis and Calorimetry*. 2019;135(2):947-61.
- Sheikholeslami M, Zeeshan A. Numerical simulation of Fe₃O₄-water nanofluid flow in a non-Darcy porous media. *International Journal of Numerical Methods for Heat & Fluid Flow*. 2018;28(3):641-60.
- Hanif H, Khan I, Shafie S. MHD natural convection in cadmium telluride nanofluid over a vertical cone embedded in a porous medium. *Physica Scripta*. 2019;94(12):125208.
- Vo DD, Hedayat M, Ambreen T, Shehzad SA, Sheikholeslami M, Shafee A, Nguyen TK. Effectiveness of various shapes of Al₂O₃ nanoparticles on the MHD convective heat transportation in porous medium. *Journal of Thermal Analysis and Calorimetry*. 2019;1-9.
- Ismail AI. Finite element simulation of magnetohydrodynamic convective nanofluid slip flow in porous media with nonlinear radiation. *Alexandria Eng. J.* 2016; 55:1305-1319.
- Saleem S, Shafee A, Nawaz M, Dara RN, Tlili I, Bonyah E. Heat transfer in a permeable cavity filled with a ferrofluid under electric force and radiation effects. *AIP Advances*. 2019;9(9):095107.
- Alharbi SO, Nawaz M, Nazir U. Thermal analysis for hybrid nanofluid past a cylinder exposed to magnetic field. *AIP Advances*. 2019;9(11):115022.
- Ghadikolaei SS, Hosseinzadeh K, Ganji DD, Hatami M. Fe₃O₄-(CH₂OH)₂ nanofluid analysis in a porous medium under MHD radiative boundary layer and dusty fluid. *Journal of Molecular Liquids*. 2018;258:172-85.
- Nawaz M, Rana S, Qureshi IH. Computational fluid dynamic simulations for dispersion of nanoparticles in a magnetohydrodynamic liquid: a Galerkin finite element method. *RSC advances*. 2018;8(67):38324-35.
- Nawaz M, Rana S, Qureshi IH, Hayat T. Three-dimensional heat transfer in the mixture of nanoparticles and micropolar MHD plasma with Hall and ion slip effects. *AIP Advances*. 2018;8(10):105109.
- Hatami M, Hosseinzadeh K, Domairry G, Behnamfar MT. Numerical study of MHD two-phase Couette flow analysis for fluid-particle suspension between moving parallel plates. *Journal of the Taiwan Institute of Chemical Engineers*. 2014;45(5):2238-45.
- Ali B, Nie Y, Khan SA, Sadiq MT, Tariq M. Finite element simulation of multiple slip effects on MHD unsteady Maxwell nanofluid flow over a permeable stretching sheet with radiation and thermo-diffusion in the presence of chemical reaction. *Processes*. 2019;7:1-18.
- Balla CS, Naikoti K. Finite element analysis of magnetohydrodynamic transient free convection flow of nanofluid over a vertical cone with thermal radiation. *Proc. Inst. Mech. Eng. Part N J. Nanoeng. Nanosyst*. 2016;230:161-173.
- Li Z, Sheikholeslami M, Mittal AS, Shafee A, Haq RU. Nanofluid heat transfer in a porous duct in the presence of Lorentz forces using the lattice Boltzmann method. *The European Physical Journal Plus*. 2019;134(1):30.
- Sheikholeslami M, Saleem S, Shafee A, Li Z, Hayat T, Alsaedi A, Khan MI. Mesoscopic investigation for alumina nanofluid heat transfer in permeable medium influenced by Lorentz forces. *Computer Methods in Applied Mechanics and Engineering*. 2019;349:839-58.
- Saleem S, Firdous H, Nadeem S, Khan AU. Convective heat and mass transfer in magneto Walter's B nanofluid flow induced by a rotating cone. *Arabian Journal for Science and Engineering*. 2019;44(2):1515-23.
- Sadiq MA, Khan AU, Saleem S, Nadeem S. Numerical simulation of oscillatory oblique stagnation point flow of a magneto micropolar nanofluid. *RSC advances*. 2019;9(9):4751-64.
- Ramzan M, Sheikholeslami M, Saeed M, Chung JD. On the convective heat and zero nanoparticle mass flux conditions in the flow of 3D MHD Couple Stress nanofluid over an exponentially stretched surface. *Scientific reports*. 2019;9(1):562.
- Dogonchi AS, Armaghani T, Chamkha AJ, Ganji DD. Natural Convection Analysis in a Cavity with an Inclined Elliptical Heater Subject to Shape Factor of Nanoparticles and Magnetic Field. *Arabian Journal for Science and Engineering*. 2019:1-3.
- Saleem S, Nadeem S, Rashidi MM, Raju CS. An optimal analysis of radiated nanomaterial flow with viscous dissipation and heat source. *Microsystem Technologies*. 2019;25(2):683-9.
- Dogonchi AS, Waqas M, Seyyedi SM, Hashemi-Tilehnoee M, Ganji DD. Numerical simulation for thermal radiation and porous medium characteristics in flow of CuO-H₂O nanofluid. *Journal of the Brazilian Society of Mechanical Sciences and Engineering*. 2019;41(6):249.
- Gholinia M, Hosseinzadeh K, Mehrzadi H, Ganji DD, Ranjbar AA. Investigation of MHD Eyring-Powell fluid flow over a rotating disk under effect of homogeneous-heterogeneous reactions. *Case Studies in Thermal Engineering*. 2019;13:100356.
- Hosseinzadeh K, Gholinia M, Jafari B, Ghanbarpour A, Olfian H, Ganji DD. Nonlinear thermal radiation and chemical reaction effects on Maxwell fluid flow with convectively heated plate in a porous medium. *Heat Transfer—Asian Research*. 2019;48(2):744-59.
- Afridi MI, Qasim M, Saleem S. Second law analysis of three dimensional dissipative flow of hybrid nanofluid. *Journal of Nanofluids*. 2018;7(6):1272-80.
- Chamkha AJ, Dogonchi AS, Ganji DD. Magneto-hydrodynamic flow and heat transfer of a hybrid nanofluid in a rotating system among two surfaces in the presence of thermal radiation and Joule heating. *AIP Advances*. 2019;9(2):025103.
- Zangoee MR, Hosseinzadeh K, Ganji DD. Hydrothermal analysis of MHD nanofluid (TiO₂-GO) flow between two radiative stretchable rotating disks using AGM. *Case Studies in Thermal Engineering*. 2019;14:100460.
- Sheikholeslami M, Jafaryar M, Barzegar GM, Alavi AH. Influence of novel turbulator on efficiency of solar collector system. *Environmental Technology and Innovation*. 2022;26:102383.
- Sheikholeslami M, Ebrahimpour Z. Thermal improvement of linear Fresnel solar system utilizing Al₂O₃-water nanofluid and multi-way twisted tape. *International Journal of Thermal Sciences*. 2022;176:107505.
- Sheikholeslami M, Farshad SA, Gerdroodbary MB, Alavi AH. Impact of new multiple twisted tapes on treatment of solar heat exchanger. *The European Physical Journal Plus*. 2022;137:86.
- Zeeshan A, Shehzad N, Atif M, Ellahi R, Sait SM. Electromagnetic Flow of SWCNT/MWCNT Suspensions in Two Immiscible Water-and Engine-Oil-Based Newtonian Fluids through Porous Media. *Symmetry*. 2022;14(2):406.
- Hafeez MB, Amin R, Nisar KS, Jamshed W, Abdel-Aty AH, Khashan MM. Heat transfer enhancement through nanofluids with applications in automobile radiator. *Case Studies in Thermal Engineering*. 2021;27:101192.

34. Bhatti MM, Arain MB, Zeeshan A, Ellahi R, Doranehgard MH. Swimming of Gyrotactic Microorganism in MHD Williamson nanofluid flow between rotating circular plates embedded in porous medium: Application of thermal energy storage. *Journal of Energy Storage*. 2022;45:103511.
35. Khan AA, Ilyas S, Abbas T, Ellahi R. Significance of induced magnetic field and variable thermal conductivity on stagnation point flow of second grade fluid. *Journal of Central South University*. 2021;28(11):3381-90.

Muhammad Bilal Hafeez:  <https://orcid.org/0000-0002-9384-8582>

Marek Krawczuk:  <https://orcid.org/0000-0002-9640-4696>

Hasan Shahzad:  <https://orcid.org/0000-0001-9154-5791>

NOMENCLATURES

C_p	Specific heat constant
Nu_x	Local Nusselt number
C_f	Skin friction coefficient
nf	Nanofluid
h_f	Heat transfer coefficient
k	Thermal conductivity of base fluid
q	Heat flux
q_w	Surface heat flux
T	Temperature of base fluid
u	Horizontal velocity field components
v	Vertical velocity field components
Bi	Biot number
Ec	Eckert number
Pr	Prandtl number
g	Gravitational acceleration
B_0	Magnetic field parameter

GREEK SYMBOLS

β_s	Thermal expansion coefficient
σ	Boltzmann constant
φ	Volume fraction of nanoparticles
γ	Slip parameter
λ	Thermal relaxation time
μ	Density of fluid
μ_{nf}	Kinematic viscosity of nanofluid
ν	Kinematic viscosity of base fluid
ρ	Density of base fluid
τ_w	Density of nanoparticle
τ_w	Surface skin friction

A NEW METHOD OF THE POSITIONING AND ANALYSIS OF THE ROUGHNESS DEVIATION IN FIVE-AXIS MILLING OF EXTERNAL CYLINDRICAL GEAR

Michał CHLOST^{*} , Michał GDULA^{*} 

^{*}Department of Manufacturing Techniques and Automation, Faculty of Mechanical Engineering and Aeronautics,
Rzeszow University of Technology, ul. W. Pola 2, Budynek C, Rzeszów, 35-959, Poland

m.chlost@prz.edu.pl, gdulam@prz.edu.pl

received 7 February 2022, revised 5 April 2022, accepted 24 April 2022

Abstract: Five-axis milling is a modern, flexible and constantly developing manufacturing process, which can be used for the machining of external cylindrical gears by means of cylindrical end mills and special disc mills on universal multi-axis machining centres. The article presents a new method of positioning the tip and the axis of the end mill and the disc cutter in order to ensure a constant value of deviation of the theoretical roughness R_{th} along the entire length of the tooth profile. The first part presents a mathematical model of the five-axis milling process of the cylindrical gear and an algorithm for calculating the R_{th} deviation values. The next section describes the positioning of the end mill and the disc cutter. Then, a new method for the empirical determination of the distribution of the involute root angle Δu_i and the data description by means of the interpolation function are presented and described. In the conducted numerical tests, the influence of the geometrical parameters of the cylindrical gear on the deviation R_{th} is determined, assuming a constant R_{th} value in the five-axis milling process.

Key words: gears, five-axis milling, theoretical roughness, tooth profile error

1. INTRODUCTION

The five-axis milling technology is currently widely used in the manufacture of components with complex geometries, including, among others, the gear wheels. The ability to control the tool in three linear and two rotary axes enables any positioning of the tool in the working space of the machine tool. The flexibility of this machining process allows replacement of the machining carried out with traditional methods, such as hobbing, shaping the surface in a five-axis milling process by means of end mill cutters [1, 2], or the increasingly used disc cutters [3].

In the process of shaping gears, the surface quality and integrity after machining are of great importance. The tooth surface profile is ultimately obtained by applying the finishing methods that were characterised by Karpuschewski et al. [4]. Krömer [5] described the deviation of the tooth shape resulting from the hobbing machining process, considering the tooth line and the tooth profile. Klocke and Staudt [6, 7] presented possible methods of path distribution on the gear tooth flank and analysed the strategy of constant radial distribution of paths, when using the ball nose cutter. Moreover, they investigated the deviation distribution for fixed and variable tool positioning. Staudt and Exner [8] conducted research on the integrity of the tooth flank surface during milling along the tooth line. The machining process was carried out under soft and hardened conditions. Guo et al. [9] conducted research to determine the influence of the geometric parameters of a gear on the distribution of shape deviation. The strategy of constant increase in the involute root angle Δu_i described by Klocke was applied. He also presented a method for determining the position of the end mill cutter, wherein the contact of the cutter operation

surface with the flank surface of the shaped tooth was locally linear.

In addition to the use of end mills and/or ball nose cutter, disc cutters are increasingly used in five-axis machining of gear teeth [3, 10 - 13]. The main advantage of using this type of tool geometry is much easier access of the cutting edge to the lower parts of the inter-tooth notch, possibility of using higher radial in feed values and the associated increase in machining efficiency, as well as the low susceptibility of the tool to elastic deformation.

The description of milling of the cylindrical gears using the disc milling cutter was provided by Talar et al. [13, 14]. They presented the possibility of modification of the profile and line of the gear tooth due to the elastic deformation of the tool.

A more common form of use of the disc milling cutter is the five-axis machining of bevel gears. Deng [10] and Shih [12] presented the method of positioning the disc cutter when machining a free surface, which is the tooth flank of a bevel gear with a circular arc tooth line. Moreover, Shih and Chen [11] presented a method of positioning a disc grinding wheel, with a similar geometry as a disc milling cutter, in the finish machining of a gear with oblique teeth. By appropriately modifying the position of the grinding wheel, they corrected the errors that occurred during the grinding process.

A completely different kinematic solution for machining was investigated by Özel [15], as he analysed the geometric errors of the tooth profile after machining with an end mill cutter. Moreover, he determined the influence of linear interpolation of the tool path on the execution accuracy of the tooth profile.

In the case of finish machining, the elastic deformation of the tool has a significant impact on the accuracy of the machined surface. Solf [16] investigated the issue of the radial correction of

tool deflection during the machining of tothing in the hardened state.

The geometric structure of the flank tooth surface after finish machining and the method of its measurement are equally important. This issue was extensively described by Suh [17], who used the coordinate measurement technique on coordinate measuring machines (CMMs), and by Chmielik et al. [18], where a profilometer was used.

The article proposes and describes a new method of tool positioning in the five-axis machining of a cylindrical gear with a straight tooth line, using the Δu_i distribution function in the mathematical modelling, which allows obtaining a constant deviation of the theoretical surface roughness R_{th} , along the entire tooth profile.

2. MATHEMATICAL MODEL OF THE TOOTH FLANK SURFACE

As Guo et al. [9] described, gear machining on five-axis machine tools consists in positioning the tool and the part in relation to the machine's coordinate system $S_m(x_m, y_m, z_m)$ with origin O_m . The machining system adopted in the five-axis milling of the cylindrical gear with a straight tooth line by means of an end mill cutter for machining is shown in Fig. 1.

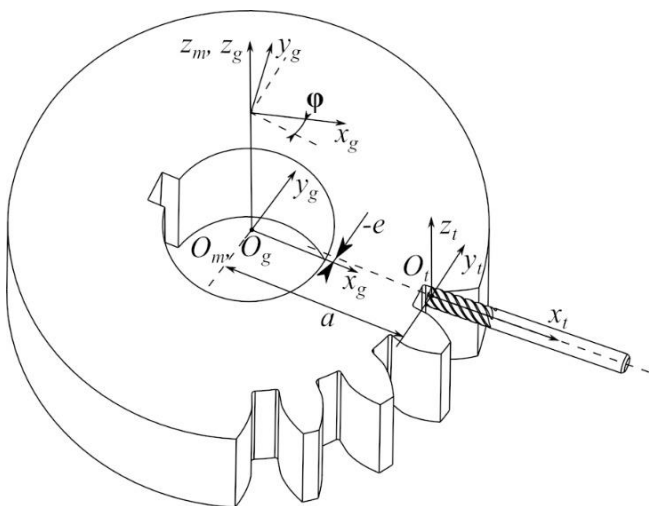


Fig. 1. The machining system adopted in the five-axis milling of the cylindrical gear with straight tooth line

Coordinate systems $S_g(x_g, y_g, z_g)$ with origin O_g and $S_t(x_t, y_t, z_t)$ with origin O_t are assigned to the part and the tool, respectively. The parameters a and e correspond to the positions of the tool tip in the S_m arrangement along the x_m, y_m axes. During machining, the tool makes the main movement along the z_m axis. For each tool, a position defined by the parameters a and e and the tool inclination angle φ are defined, which provides tangential guidance of the cutter action surface to the tooth flank surface, and positioning is achieved by changing the rotary table setting. Depending on the machined side of the tooth, this angle can be positive or negative.

The assumptions for the mathematical model are specified as average parameter values for their ranges of applicability:

- parameters $m, z > 0$, a range was assumed for m (10–20), z (20–70);

- number of tool paths $N \geq 2$, a range was assumed for N (10–20);
- pressure angle $\alpha > 0$, a range was assumed for α (20°–30°);
- the parameter of the empirical function was determined experimentally and is $x = 1/0.667$;
- diameter d of the cylindrical tool and radius r of the disc tool $d, r > 0$.

The basic geometrical parameters of a gear are shown in Fig. 2 and described by the equations Eqs. (1)–(13), which were described by Burek et al. [1].

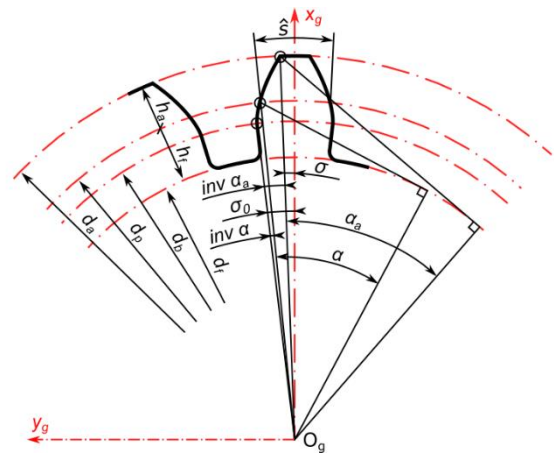


Fig. 2. Basic gear dimensions

Input parameters: m – module, z – number of teeth, α – pressure angle.

$$d_p = m \cdot z \quad (1)$$

$$h_a = m \quad (2)$$

$$h_f = 1.25 \cdot m \quad (3)$$

$$d_a = d_p + 2 \cdot h_a \quad (4)$$

$$d_f = d_p - 2 \cdot h_f \quad (5)$$

$$d_b = d \cdot \cos(\alpha) \quad (6)$$

$$r_b = \frac{d_b}{2} \quad (7)$$

$$\text{inv } \alpha = \tan(\alpha) - \alpha \quad (8)$$

$$\alpha_a = \cos^{-1} \left(\frac{d_b}{d_a} \right) \quad (9)$$

$$\text{inv } \alpha_a = \tan(\alpha_a) - \alpha_a \quad (10)$$

$$\sigma = \frac{\hat{s}}{d} \cdot \frac{180^\circ}{\pi} \quad (11)$$

$$\sigma_0 = \sigma + \text{inv } \alpha \quad (12)$$

$$u = \alpha_a + \text{inv } \alpha_a \quad (13)$$

where d_p – pitch diameter, h_a – addendum, h_f – dedendum, d_a – addendum diameter, d_f – dedendum diameter, d_b – basic diameter, r_b – basic radius, $\text{inv } \alpha$ – involute function of angle α , α_a – pressure angle on addendum, $\text{inv } \alpha_a$ – involute function of angle α_a , σ – half angle on pitch diameter, σ_0 – half angle on basic diameter and u – root angle.

The flank surface of the tooth can be described using two parameters (u, v) [19], as shown in Fig. 3. The parameter u , which is

the root angle of the involute subjected to subsequent discretisation, describes the tooth outline, and the parameter v describes the tooth line.

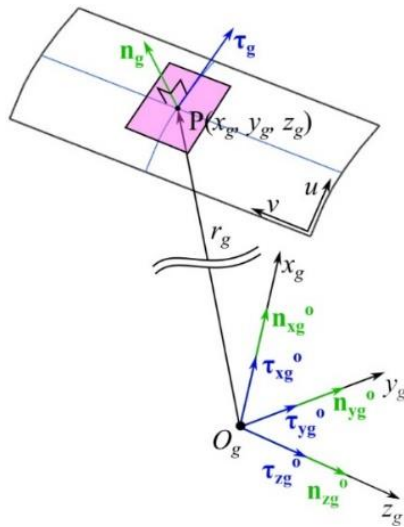


Fig. 3. Parametric description of the tooth flank surface

The position vector r_g and the normal vector n_g of the surface are described by the relationship in Eq. (14):

$$\begin{cases} r_g(u, v) = [x_g & y_g & z_g & 1] \\ n_g(u, v) = [n_{xg} & n_{yg} & n_{zg} & 1] \end{cases} \quad (14)$$

Where (x_g, y_g, z_g) are the coordinates of the end point P of position vector r_g described by Eq. (15), and (n_{xg}, n_{yg}, n_{zg}) are component vectors of the vector n_g normal to the tooth flank surface, described by Eq. (16):

$$\begin{bmatrix} x_g \\ y_g \\ z_g \end{bmatrix} = \begin{bmatrix} r_b \cos(\sigma_0 + u) + r_b u \sin(\sigma_0 + u) \\ r_b \sin(\sigma_0 + u) - r_b u \cos(\sigma_0 + u) \\ pv \end{bmatrix} \quad (15)$$

$$\begin{bmatrix} n_{xg} \\ n_{yg} \\ n_{zg} \end{bmatrix} = \begin{bmatrix} pr_b u \sin(\sigma_0 + u) \\ -pr_b u \cos(\sigma_0 + u) \\ 0 \end{bmatrix} \quad (16)$$

where r_b is the radius of the base circle, and p is a parameter describing the width of the gear rim.

An additional parameter that allows the correct positioning of the tool axis is the tangent vector τ_g to the surface at point $P(x_g, y_g, z_g)$, which is described by the dependencies Eqs. (17) and (18):

$$\tau_g(u, v) = [\tau_{xg} \quad \tau_{yg} \quad \tau_{zg} \quad 1] \quad (17)$$

where

$$\begin{bmatrix} \tau_{xg} \\ \tau_{yg} \\ \tau_{zg} \end{bmatrix} = \begin{bmatrix} r_b u \cos(\sigma_0 + u) \\ r_b u \sin(\sigma_0 + u) \\ 0 \end{bmatrix} \quad (18)$$

The transformation of the part system S_g to the machine coordinate system S_m is carried out through the rotation matrix M_{mg} , determined by the relation Eq. (19):

$$M_{mg} = \begin{bmatrix} \cos \varphi & -\sin \varphi & 0 & 0 \\ \sin \varphi & \cos \varphi & 0 & 0 \\ 0 & 0 & 1 & -p \\ 0 & 0 & 0 & 1 \end{bmatrix} \quad (19)$$

where φ is the angle of the machine part's rotation on the machine tool turntable.

The same should be done with the tool coordinate system S_t , whose transformation to the machine system S_m takes the form of the translation matrix M_{mt} , determined by the relation Eq. (20):

$$M_{mg} = \begin{bmatrix} 1 & 0 & 0 & a \\ 0 & 1 & 0 & e \\ 0 & 0 & 1 & 0 \\ 0 & 0 & 0 & 1 \end{bmatrix} \quad (20)$$

where the parameters a and e define the position of the tool in relation to the x_m and y_m axes.

3. CALCULATION OF R_{th} DEVIATION

The geometric relationships that allow the determination of the R_{th} deviation of the theoretical surface roughness and the geometric system of the five-axis machining adopted for the study are shown in Fig. 4.

In order to calculate the R_{th} deviation, it is necessary to determine the distance CD. Points A(x_{gA}, y_{gA}) and B(x_{gB}, y_{gB}) are the points that describe the flank surface of the tooth, where point A represents the first position of the tool, and point B represents the next position of the tool. Point C is at the point of intersection of the line segments AC and BC that are tangential to the tooth profile at points A and B, respectively. Segments AC and BC represent a group of lines described by the linear relationship in Eq. (21), where the parameters k_A and k_B described by the relationship Eq. (22) determine their slopes in relation to the x_g axis:

$$\begin{cases} x_{gA} = k_A y_{gA} + b_A \\ x_{gB} = k_B y_{gB} + b_B \end{cases} \quad (21)$$

where

$$\begin{cases} k_A = -\frac{n_{gyA}}{n_{gxA}} \\ k_B = -\frac{n_{gyB}}{n_{gxB}} \end{cases} \quad (22)$$

After determining the slopes of the lines, it becomes possible to derive Eq. (23) describing the term b of the linear equation of lines:

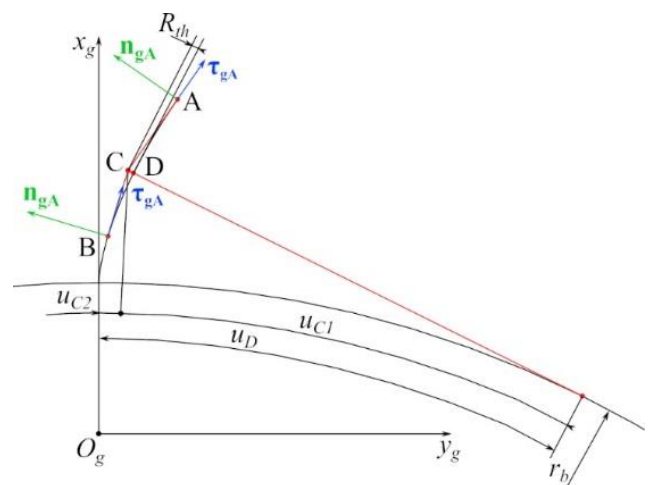


Fig. 4. The geometric structure allowing determination of the R_{th} deviation

$$\begin{cases} b_A = x_{gA} - (k_A y_A) \\ b_B = x_{gB} - (k_B y_B) \end{cases} \quad (23)$$

This allowed the creation of the system of equations Eq. (24) necessary to determine the coordinates of the intersection point C(x_{gC} , y_{gC}):

$$\begin{cases} x_{gC} = k_B \frac{b_A - b_B}{k_B - k_A} + b_B \\ y_{gC} = \frac{b_A - b_B}{k_B - k_A} \end{cases} \quad (24)$$

In order to determine the coordinates of the point D(x_{gD} , y_{gD}), the values of the involute root angle u_D should be determined. The determination of the u_D angle is described by the relationships Eqs. (25)–(28):

$$u_D = u_{C1} + u_{C2} \quad (25)$$

where

$$u_{C1} = \tan^{-1} \left(\frac{y_{gC}}{x_{gC}} \right) \quad (26)$$

$$OC = \sqrt{x_{gC}^2 + y_{gC}^2} \quad (27)$$

$$u_{C2} = \cos^{-1} \left(\frac{r_b}{OC} \right) \quad (28)$$

Finally, the coordinates of point D are determined from the system of equations Eq. (29):

$$\begin{bmatrix} x_{gD} \\ y_{gD} \\ z_{gD} \end{bmatrix} = \begin{bmatrix} r_b \cos(\sigma_0 + u_D) + r_b u \sin(\sigma_0 + u_D) \\ r_b \sin(\sigma_0 + u_D) - r_b u \cos(\sigma_0 + u_D) \\ pv \end{bmatrix} \quad (29)$$

4. POSITIONING OF THE TOOL

Three types of tool geometry are used for the five-axis machining of gears, in both soft and hardened conditions. The basic, and—so far—the most frequently used, tools are end mills with ball or cylindrical geometry [1, 6, 7, 8, 15]. Research conducted so far [6, 3] has shown that the machining conditions and machinability in the five-axis flank milling method with an end mill cutter are definitely better than with a ball end mill cutter. This can also be observed in terms of the difference in the geometry of the remains

after machining on the tooth flank surfaces and in the efficiency of machining of the toothing.

A disc cutter is the third and increasingly frequently used tool for machining gears on multi-axis milling computerised numerical control (CNC) machines. The sharp apex angle of the cutting inserts provides much better access of the tool along the entire depth of the inter-tooth notch, making it possible to machine gears with much smaller modules than in the case of an end mill cutter.

The machining system and the five-axis machining model of the tooth flank with an end mill cutter, which works tangentially to point A, are shown in Fig. 5(a). The tool axis is defined at location I as the tangent vector τ_{gA} , expressed as unit vector τ_{gA}° , and at location II as tangent vector τ_{gB} , expressed as unit vector τ_{gB}° . The position of the tool centre point (TCP), which is the zero point of the tool coordinate system S_t , is defined in Eq. (30) as a translation in the normal direction by the product with the unit vector $n_{gA(B)}^\circ$, which is determined by Eq. (31), and half the tool diameter d with reference to the point C, which describes the peak of the R_{th} deviation:

$$\begin{cases} x_{TCP} = x_{gC} + n_{xgA(B)}^\circ \frac{d}{2} \\ y_{TCP} = y_{gC} + n_{ygA(B)}^\circ \frac{d}{2} \\ z_{TCP} = z_{gC} \end{cases} \quad (30)$$

where

$$\begin{cases} n_{xgA(B)}^\circ = \frac{n_{xgA(B)}}{\|n_{xgA(B)}\|} \\ n_{ygA(B)}^\circ = \frac{n_{ygA(B)}}{\|n_{ygA(B)}\|} \\ n_{zgA(B)}^\circ = 0 \end{cases} \quad (31)$$

In this case, the unequivocal position of the tool in the space of a five-axis CNC machine tool can be determined from Eq. (32):

$$[x_{TCP}, y_{TCP}, z_{TCP}, \tau_{xgA(B)}^\circ, \tau_{ygA(B)}^\circ, 0] \quad (32)$$

The machining system and the five-axis machining model presented in Fig. 5(b) refer to the use of the disc milling cutter. Proper positioning of the tool consists in leading the action surface tangential to the tooth profile. As in the case described earlier, transformation of the TCP position described by Eq. (33) should be made, which in the reference position coincides with point C.

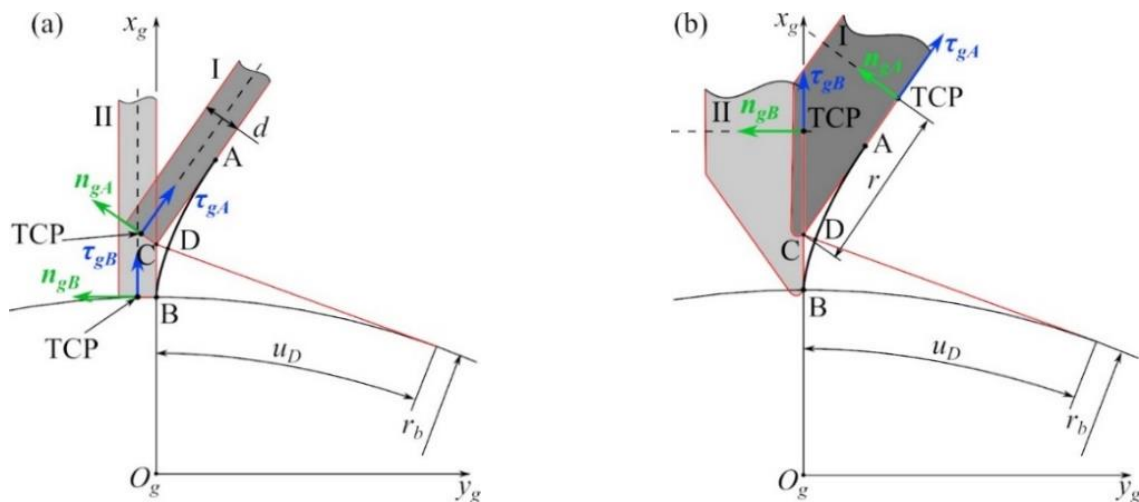


Fig. 5. Machining system and positioning method: (a) for end milling cutter; (b) for disc milling cutter in five-axis machining of toothing
Abbreviation: TCP, tool centre point

In the configuration of the machining system considering position I of the tool as the axis of rotation, the vector \mathbf{n}_{gA} normal to the curve at point A was adopted, expressed as the unit vector \mathbf{n}_{gA}° , while in position II, the normal vector \mathbf{n}_{gB} to the curve at point B, expressed as the unit vector \mathbf{n}_{gB}° , was adopted.

The translation of the TCP relative to the point C is determined by the product of the unit vector $\boldsymbol{\tau}_{gA(B)}^\circ$, expressed by Eq. (34), and the tool radius r .

$$\begin{cases} x_{TCP} = x_{gC} + \boldsymbol{\tau}_{xgA(B)}^\circ r \\ y_{TCP} = y_{gC} + \boldsymbol{\tau}_{ygA(B)}^\circ r \\ z_{TCP} = z_{gC} \end{cases} \quad (33)$$

where

$$\begin{cases} \boldsymbol{\tau}_{xgA(B)}^\circ = \frac{\boldsymbol{\tau}_{xgA(B)}}{\|\boldsymbol{\tau}_{xgA(B)}\|} \\ \boldsymbol{\tau}_{ygA(B)}^\circ = \frac{\boldsymbol{\tau}_{ygA(B)}}{\|\boldsymbol{\tau}_{ygA(B)}\|} \\ \boldsymbol{\tau}_{zgA(B)}^\circ = 0 \end{cases} \quad (34)$$

In turn, in this case, the unequivocal position of the tool in the space of a five-axis CNC machine tool can be determined from Eq. (35).

$$[x_{TCP}, y_{TCP}, z_{TCP}, \boldsymbol{n}_{xgA(B)}^\circ, \boldsymbol{n}_{ygA(B)}^\circ, 0] \quad (35)$$

The above method of positioning the disc milling cutter can find an analogous application in the case of a disc grinding wheel in the grinding of gear teeth on multi-axis CNC milling machines. The advantage of this solution is the possibility of milling and grinding the gears without the need to attach the part in another machine tool. This results in an increase in the dimensional and shape accuracy of the gear wheel. This is of particular importance in the aspect of manufacturing of aircraft gears, as well as special purpose gears for the defence industry.

5. FIVE-AXIS MILLING STRATEGIES FOR TOOTHING

The value of the theoretical surface roughness deviation R_{th} and the machining time T_c depend on the adopted positioning strategy of the milling cutter. In the literature, three basic cases of tool positioning have been distinguished [5, 6, 7, 9] for which a collate was made, assigning a given strategy to the R_{th} deviation of a gear tooth profile. These collates are presented in Fig. 6. Fig. 6(a) shows the distribution of the R_{th} deviation resulting from the arrangement of the tool paths along the tooth profile, according to the strategy of maintaining a constant increase in the involute root angle Δu_i . It was noticed that the maximum deviation R_{th} occurs in the upper part of the tooth and is 0.007 mm, and the smallest at the tooth foot, where its value is 0.0002 mm. In the case of the collate in Fig. 6(b), the distribution of paths is implemented as a strategy of constant division of the tooth height in the radial direction. In this case, the greatest deviation occurs in the lower part of the tooth and is 0.016 mm, while the smallest deviation occurs at the upper part of the tooth and is 0.0018 mm.

The last collate shown in Fig. 6(c) illustrates the strategy according to which the tool paths are distributed in such a way that the R_{th} deviation is constant along the entire length of the tooth profile. The deviation in this case is 0.0032 mm.

Depending on the adopted positioning strategy of the tool, a variable distribution of the value of the R_{th} deviation can be observed, which depends on the adopted function describing the

change of the involute root angle u . All the above figures show the distribution of the R_{th} deviation according to the machining strategy (tool positioning) for a tooth with the same geometric parameters and the same adopted number of paths. On this basis, it should be concluded that for the same number N of paths, the third strategy provides the smallest mean R_{th} deviation in the distribution along the entire tooth profile.

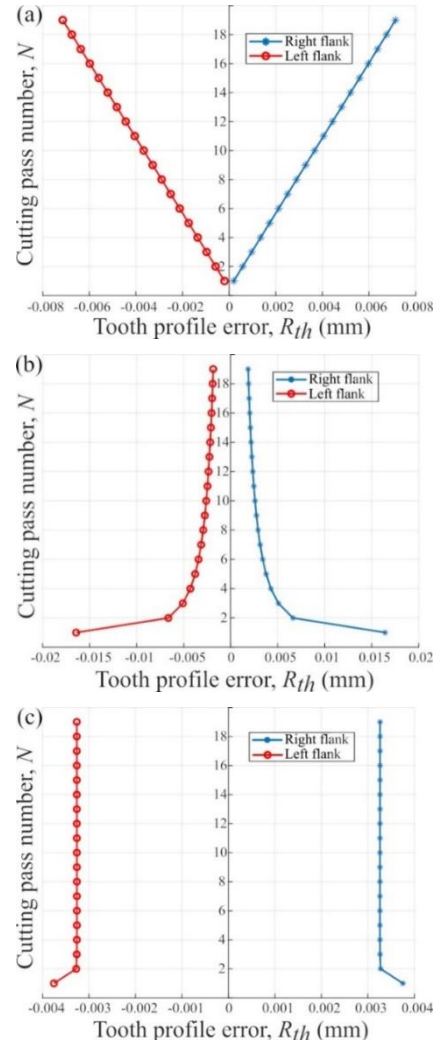


Fig. 6. Machining strategies in relation to the R_{th} deviation of the tooth profile: (a) strategy of constant increment of the involute root angle u ; (b) strategy of constant radial distribution of toolpaths; (c) strategy of constant deviation R_{th}

6. EMPIRICAL DETERMINATION OF THE DISTRIBUTION OF THE INVOLUTE ROOT ANGLE u

In order to define the function describing the R_{th} deviation distribution, it was necessary to use an empirical model. Using the computer-aided design (CAD) software, we developed a parametric sketch showing the tooth profile [1, 20] and the individual tangent lines that define the vertices of the R_{th} deviation, as shown in Fig. 7.

With the help of geometric constraints, a constant distance of the vertices from the tooth profile was imposed, and lines denoting the unwind angle of the involute were drawn. Then, based on the geometry analysis tool in the CAD environment, the values of the

unwind angle Δu_i for the individual tool paths were read. The tolerance value of the researched CAD model was set at 0.0001 mm. Based on the measured values, a graph of the value of the unwind angle Δu_i was developed, which is assumed for a given tool path i . This function is described by the relationship in Eq. (36).

$$\Delta u_i = \sqrt[x]{\frac{u^{xi}}{N-1}} \quad (36)$$

where u – involute root angle, N – number of considered tool-paths, $i=(0, 1, 2, \dots(N-1))$ – consecutive toolpaths.

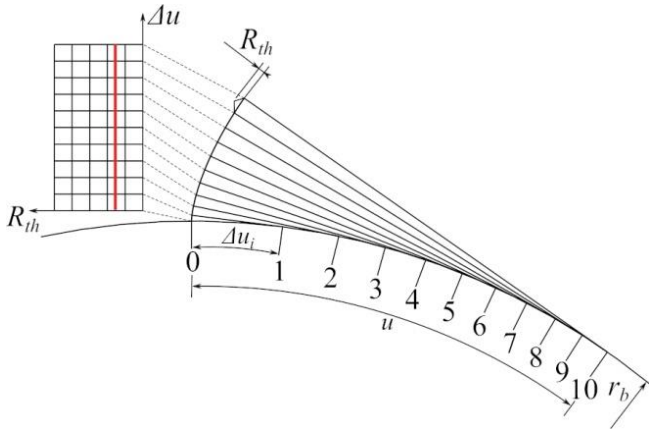


Fig. 7. Distribution of Δu_i for the constant R_{th} deviation strategy

In order to determine the degree of the root from Eq. (36), a series of x values ranging from 1/0.6 to 1/0.7 with a step size of 0.001 were analysed by the iterative method.

As a result of the simulation, the root base equal to 1/0.667 was selected since, for this value, the smallest deviation from the base function was observed for Eq. (36). The superimposed graphs of the empirically determined points and the function described by Eq. (36) with the base $x=1/0.667$ are shown in Fig. 8.

7. ANALYSIS OF R_{th} DEVIATION

For the adopted strategy of constant R_{th} deviation, numerical tests were carried out for both the end milling and the disc milling cutters. The results of these tests are shown in Fig. 9.

In individual cases, the change in the R_{th} deviation was considered depending on the number of passes of the tool N , the number of gear teeth z , the change in the normal tooth modulus m_n and the variable value of the pressure angle α , respectively shown in Fig. 9.

It was found that the results of the simulation of machining along the tooth line for both tool geometries were comparable. By analysing the results of the simulation tests, it can be concluded that the greatest increase in the value of the R_{th} deviation occurs when the number of tool passes changes as shown in Fig. 9(a), where the smallest R_{th} deviation value was 0.0029 mm for the number of paths $N = 20$; for the number of paths $N = 10$, the R_{th} deviation was 0.0118 mm.

The smallest differences in the values of the R_{th} deviation were observed for the variable value of the number of teeth of the gear as shown in Fig. 9(b), where for the number of teeth $z = 20$,

the R_{th} deviation is 0.0029 mm, while for the number of teeth $z = 70$, the highest R_{th} deviation value of 0.0040 mm was noted.

In the case of different values of the modulus m_n and the pressure angle α being defined as shown in Fig. 9(c) and (d), respectively, an increase of the R_{th} deviation is comparable. When changing the value of the module for $m_n = 10$ mm, the value of the R_{th} deviation was the smallest and amounted to 0.0029 mm, and for the value of $m_n = 20$, the value of the R_{th} deviation was 0.0058 mm. Similarly, in the case of the pressure angle α , the smallest R_{th} deviation value was noted for $\alpha = 20^\circ$ and was the same as in the case of the set module value $m_n = 10$ mm, while the largest R_{th} deviation value equal to 0.0057 mm was noted for the angle $\alpha = 30^\circ$.

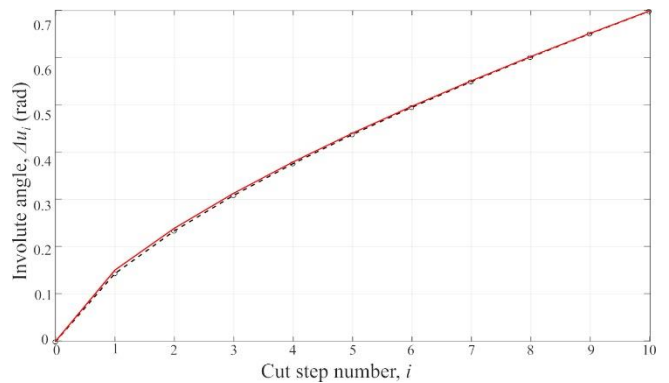


Fig. 8. Approximation of values determined empirically by the function describing the distribution of the involute root angle Δu

Moreover, it was observed, that with an increase in the value of individual parameters of both the gear wheel and the machining process, the value of the R_{th} deviation also increases, wherein depending on the parameter, this change has a different characteristic and tendency.

Another phenomenon observed is the increased value of the R_{th} deviation for the first tool path. This deviation is caused by a poorer fit of the approximation function for small involute root angles Δu_i , which occur in the tooth flank's bottom area, but these regions do not participate directly in the transmission of torque due to the apical clearance.

8. SUMMARY

The article presents and describes a new method of tool positioning assuming a constant R_{th} deviation in the five-axis machining of gears on universal CNC machines. A new mathematical model has been presented that allows determining the value of the R_{th} deviation and the position of the tool during the five-axis machining depending on the tool geometry.

As a result of the numerical tests and numerous simulations, the relationship between the gear wheel parameters and the R_{th} deviation is determined. The number of tool paths N has the greatest impact on the amount of the R_{th} deviation, while the number of teeth in the gear wheel has the smallest impact. The parameters such as the modulus m_n and the pressure angle α have a comparable coefficient of influence on the increase of the R_{th} deviation.

The adopted methodology and the developed assumptions of the five-axis machining strategy are a new proposal to solve the problem of the uneven distribution of the R_{th} deviation in the hobbing process. Depending on the expected results of further research carried out by the authors of this work, it is possible to use another function describing the distribution of the involute root

angle u , which will significantly increase the possibilities of shaping the flank profiles of the teeth. Another advantage is an increase of the machining effectiveness of gear wheels, by obtaining a much smaller R_{th} deviation than in the case of the strategy of constant increase of the involute root angle u .

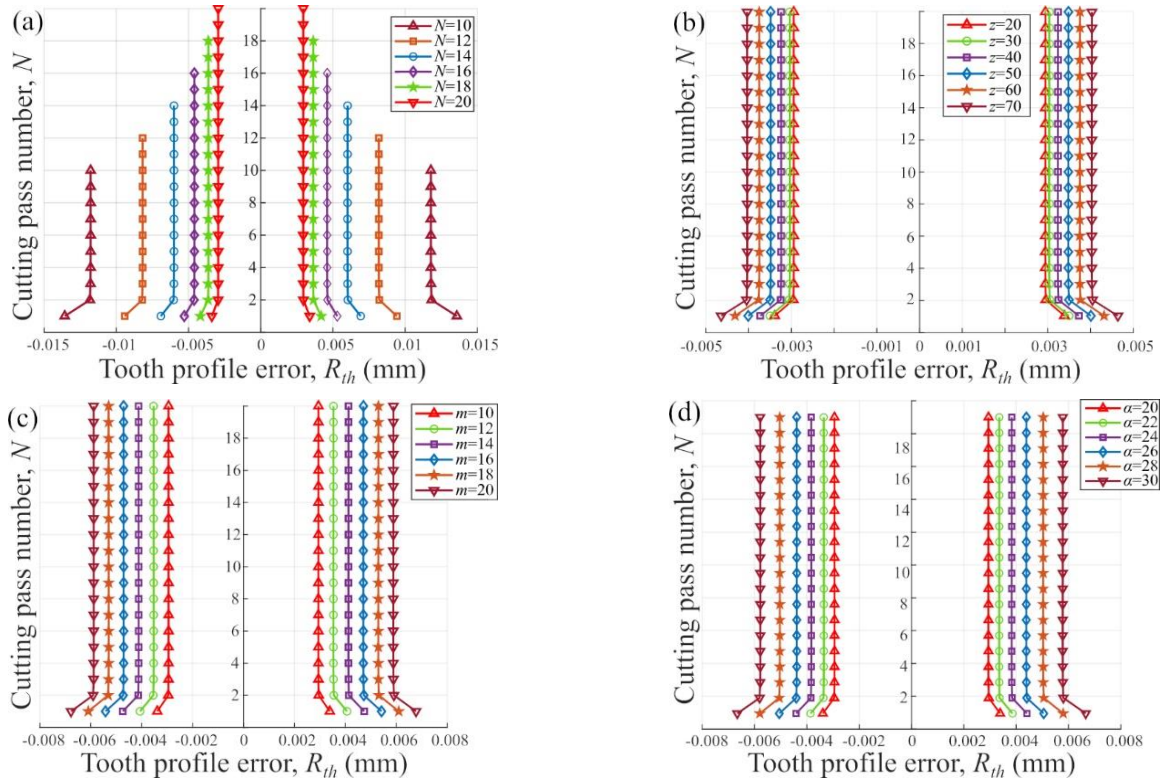



Fig. 9. Influence of the gear wheel parameters and the machining on the R_{th} deviation : (a) number of paths N ; (b) number of teeth z ; (c) normal modulus m_n ; (d) angle of pressure α

REFERENCES

- Burek J, Gdula M, Plodzień M, Buk J. Gear's tooth profile shaping in dialog and parametric programming. *Mechanik*. 2015 Feb;2:142/7.
- Safarov DT, Kondrashov AG, Khafizov II. Improving the process efficiency of helical gears' toothed rims at the stage of pre-production. *IOP Conference Series: Materials Science and Engineering*. 2019;570(012024).
- Gaiser U. 5-Axis Gear Manufacturing Gets Practical. *Gear Technology*. 2017;(March/April):32-4.
- Karpuschewski B, Knoche HJ, Hipke M. Gear finishing by abrasive processes. *CIRP Annals - Manufacturing Technology*. 2008;57(2): 621-40.
- Krömer M, Sari D, Löpenhaus C, Brecher C. Surface Characteristics of Hobbed Gears. *Gear Technology [Internet]*. 2017 [cited 2020 Feb 4];(July):68-75. www.geartechnology.com
- Klocke F, Brumm M, Staudt J. Quality and surface of gears manufactured by free form milling with standard tools. *Gear Technology*. 2015;(January/February):64-9.
- Staudt J, Löpenhaus C, Klocke F. Performance of Gears Manufactured by 5-Axis Milling. *Gear Technology [Internet]*. 2017:58-65. www.geartechnology.com
- Staudt J, Exner P. Einfluss der Oberflächenstruktur beim 5-Achs-Fräsen von Verzahnungen auf das Einsatzverhalten [Internet]. 2017 [cited 2020 Jan 24]. www.fva-net.de
- Guo E, Ren N, Liu Z, Zheng X, Zhou C. Study on tooth profile error of cylindrical gears manufactured by flexible free-form milling. *International Journal of Advanced Manufacturing Technology*. 2019;103(9-12):4443-51.
- Deng XZ, Li GG, Wei BY, Deng J. Face-milling spiral bevel gear tooth surfaces by application of 5-axis CNC machine tool. *International Journal of Advanced Manufacturing Technology*. 2014;71(5-8):1049-57.
- Shih YP, Chen SD. A flank correction methodology for a five-axis CNC gear profile grinding machine. *Mechanism and Machine Theory [Internet]*. 2012;47(1):31-45. <http://dx.doi.org/10.1016/j.mechmachtheory.2011.08.009>
- Shih YP, Sun ZH, Wu FC. A disk tool cutting method for bevel gear manufacture on a five-axis machine. *International Journal of Advanced Manufacturing Technology*. 2018;94(1-4):855-65.
- Talar R, Jablonski P, Ptaszynski W. New method of machining teeth on unspecialised machine tools. *Tehnicki Vjesnik*. 2018 Feb 1;25(1):80-7.
- Talar R, Jablonski P. Modelling of spur gear cutting kinematics for multipurpose milling center. In: 2016 21st International Conference on Methods and Models in Automation and Robotics. Institute of Electrical and Electronics Engineers Inc.; 2016. p. 1133-6.
- Özel C. A study on cutting errors in the tooth profiles of the spur gears manufactured in CNC milling machine. *International Journal of Advanced Manufacturing Technology*. 2012;59(1-4):243-51.

16. Solf M, Bieker R, Löpenhaus C, Klocke F, Bergs T. Influence of the machining strategy on the resulting properties of five-axis hard-milled bevel gears. Proceedings of the Institution of Mechanical Engineers, Part C: Journal of Mechanical Engineering Science. 2019;233(21–22):7358–67.
17. Suh SH, Lee ES, Kim HC, Cho JH. Geometric error measurement of spiral bevel gears using a virtual gear model for STEP-NC. International Journal of Machine Tools and Manufacture. 2002 Feb;42(3):335–42.
18. Chmielik IP, Czarniecki H. Evaluation of gear tooth 3D surface topography. Mechanik. 2015 Jul;7:101–10.
19. Litvin FL, Fuentes A. Gear Geometry and Applied Theory. Gear Geometry and Applied Theory. Cambridge University Press; 2004.
20. Twardoch K. Digital Geometric Modelling of Teeth Profile By Using Cad Methodology. Scientific Journal of Silesian University of Technology Series Transport. 2014;82:271–9.

Michał Chlost:  <https://orcid.org/0000-0001-9420-4239>

Michał Gdula:  <https://orcid.org/0000-0001-7760-4986>

ANALYTICAL AND NUMERICAL ANALYSIS OF INJECTION PUMP (STEPPED) SHAFT VIBRATIONS USING TIMOSHENKO THEORY

Stanisław NOGA^{*}, Edward REJMAN^{**}, Paweł BAŁON^{***},
Bartłomiej KIEŁBASA^{***}, Robert SMUSZ^{**}, Janusz SZOSTAK^{***}

^{*}Rzeszów University of Technology, Al. Powstańców Warszawy 12, 35 – 959 Rzeszów, Poland

^{**}ZPU Mirosław Pogoda, ul. Wojska Polskiego 3, 39 – 300 Mielec, Poland

^{***}AGH University of Science and Technology, WIMiR, Al. A. Mickiewicza 30-B2, 30-059 Kraków, Poland

noga@prz.edu.pl, erejman@prz.edu.pl, balonpawel@gmail.com,
bartek.kielbasa@gmail.com, robsmusz@gmail.com, szostak@agh.edu.pl

received 29 March 2022, revised 5 May 2022, accepted 12 May 2022

Abstract: The free transverse vibrations of shafts with complex geometry are studied using analytical methods and numerical simulations. A methodology is proposed for evaluating the results of a natural transverse vibration analysis as generated by finite element (FE) models of a shaft with compound geometry. The effectiveness of the suggested approach is tested using an arbitrarily chosen model of the injection pump shaft. The required analytical models of the transverse vibrations of stepped shafts are derived based on the Timoshenko thick beam theory. The separation of variables method is used to find the needed solutions to the free vibrations. The eigenvalue problem is formulated and solved by using the FE representation for the shaft and for each shaft-simplified model. The results for these models are discussed and compared. Additionally, the usefulness of the Myklestad–Prohl (MP) method in the field of preliminary analysis of transverse vibration of complex shaft systems is indicated. It is important to note that the solutions proposed in this paper could be useful for engineers dealing with the dynamics of various types of machine shafts with low values of operating speeds.

Key words: modal analysis, natural vibrations, analytical solutions, Timoshenko beam theory, shaft vibrations

1. INTRODUCTION

The progress of modern engineering requires the use of advanced tools in the field of computer-aided design and computer-aided engineering calculations at the design stage. This applies in particular to devices, assemblies and their individual elements, all of which are required to have adequate durability and reliability during operation. Such important components of devices include, among others, machine shafts [1]. One of the essential factors, which could disturb or limit the functioning of devices (e.g., pumps and others), is the vibration of the components or assemblies of these systems [1,2]. The rapid growth of computer techniques and analytical systems based on the finite element method (FEM) allows a free vibration analysis of the complex design and geometry systems to be conducted [1]. In paper [3], FEM was used to analyse lateral vibrations of the drilling rig. Cases of the system with and without damping were analysed. In paper [4], transversal vibration of a low-power electrical rotor is studied using FEM and other analytical and numerical methods. Based on the developed finite element (FE) models, the basic dynamic parameters of the analysed system are determined. FEM modelling is used in paper [5] to analyse transverse vibrations of a Timoshenko beam with an elastic foundation composed of two different regions of the Winkler type. The developed FE models were used to determine the frequencies for which there are no harmonic type of free vibrations. An important aspect is the ability to verify the developed FE

models of the designed systems. In the case of newly designed systems, conducting laboratory tests must have a strong economic justification. Therefore, it seems justified to conduct research allowing for the development of FE model verification methods with the lowest possible economic cost. The monograph by Friswell and Mottershead [6] discusses the theoretical foundations and practical applications of techniques for obtaining numerical FE models consistent with the model data in the accepted frequency range (the so-called model updating methods). Cases where reference data are obtained from analytical solutions of vibrating systems and from measurement experiments were considered. It is also worth mentioning monograph [1], in which theoretical and experimental issues concerning vibrations of systems, and the consideration of modern measuring tools and computer techniques are discussed. In works [4,5,7], the results of analytical solutions (natural frequency values) were used as reference data to verify the proposed FE models of discussed systems. A spectral element model for a spinning uniform shaft was developed in paper [8], and FEM analysis was used for evaluating the accuracy of the proposed model through some example problems. Shahgholi et al. [9] discussed the issues of transverse vibrations of a slender shaft using analytical methods. In the modelling of the studied system, the rotary inertia and gyroscopic effect are considered. Many studies use the results of theoretical analysis based on the Timoshenko beam vibration theory as a source of reference data. It is worth mentioning that the Timoshenko beam theory allows one to obtain a model that considers all important

physical phenomena in one-dimensional continuous systems [2,10]. The fundamental vibration theory of the thick (Timoshenko) beam is presented in several monographs [2, 10]. In the monograph of Noga [7], one can find an extension of the Timoshenko theory into ring systems with an elastic foundation. In paper [11], the influence of the two-parameter elastic soil on the dynamic behaviour of the Timoshenko beam with a variable cross-section was examined in the presence of conservative axial loads, and the needed theoretical issues were concisely presented in matrix form. In paper [12], the description and solution of the Timoshenko beam free and forced vibrations by using a single equation are proposed. Analysis was carried out for various cases of the boundary conditions. In article [13], exact frequencies and mode shapes were calculated for the Timoshenko beam on different boundary supports and partially loaded with a distributed mass span. They agree with the experimental data. In article [14], the authors effectively developed the Timoshenko theory for the vibration problem of the beam with functionally graded properties along their thickness. In papers [15, 16], the free vibration behaviours of a functionally graded disk-shaft rotor system reinforced with graphene nanoplatelets resting on elastic supports are investigated. In both mentioned works, equations of motion including the gyroscopic effect due to rotation are derived by employing the Lagrange formalism within the framework of Timoshenko beam theory for the shaft and Kirchhoff plate theory for the disk. Additionally, in article [16], the disk-shaft rotor with eccentric mass was included in the investigation. In contrast, in papers [17, 18], the free vibration of a rotating, functionally graded pre-twisted blades-shaft assembly reinforced with graphene nanoplatelets was analytically investigated based on the proposed coupled model. In these papers, the governing equations of motion are derived by using the Lagrange equation within the framework of the Rayleigh beam theory and Euler-Bernoulli beam theory. The work in paper [17] refers to the pre-twisted blade-shaft system, while paper [18] refers to the pre-twisted double blade-shaft system. In paper [19], the authors studied the influence of von Kármán nonlinearity on the values of frequency, thermoelastic damping and quality factors on Timoshenko beam resonators based on the modified couple stress theory. Another research field is the issue of vibrations of composite shafts. In work [20], the Bernoulli-Euler beam theory is used to achieve the exact solution for the vibration of a cross-ply laminated composite drive shaft with an intermediate joint. The joint is modelled as a frictionless internal hinge. In paper [21], a new multi-layer FE, dedicated for dynamic analysis of rotating laminated shafts, is formulated and based on layerwise and shaft theories. Another approach found in the literature on the subject concerns transfer matrix methods, where one of them is the Myklestad-Prohl (MP) method. The idea and usefulness of the MP method in the analysis of transverse vibrations of shafts were presented for the first time in paper [22]. The MP method was effectively used in paper [4] to analyse the transverse vibrations of the shaft of a low-power electric engine. In article [23], the extended transfer matrix method dedicated to the analysis of the torsion- and flexure-coupled vibration of a damped multi-degree-of-freedom shafting system subjected to external excitations is utilized. In work [24], the modification of the transfer matrix method was developed for the analysis of bending vibrations of the steel composite transmission shafting system. The needed relations were obtained based on the lamination theory and the layerwise beam theory. The achieved results were successfully verified by experimental data and FEM. In paper [25], the flexural vibration of Timoshenko beams using a distributed lumped modelling tech-

nique are discussed. Two types of elements are discussed: the so-called distributed elements (dedicated to parts of shafts with a distributed mass) and lumped elements (dedicated to parts of shafts with a concentrated mass). The obtained results are successfully verified using other techniques. In article [26], the approach was expanded for analysis of compound shafts, considering the gyroscopic effect. The proposed technique was effectively employed by the authors for a multistep gas turbine rotor system. This paper continues the authors' research [4,5,7] related to analytical modelling, FEM simulations and model quality evaluation techniques of compound mechanical systems.

The present paper deals with transverse vibrations of a shaft of complex geometry. Analytical methods and numerical simulations were used during studies. The novel methodology for evaluation of results of free transverse vibration analysis as generated by the FE models of shafts with complex geometry is presented. The required analytical models of the transverse vibrations of stepped shafts are developed based on the Timoshenko theory. Finally, the concluding remarks are made and the adequate natural forms of vibrations referring to the appropriate natural frequencies of the systems are shown.

2. FORMULATION OF THE PROBLEM

This article discusses the vibration problem of dedicated stepped shafts which operate in injection pumps. As can be seen in Fig. 1, the shaft has a compound stepped shaft arrangement. Additionally, the shaft is hollow within a certain portion of its length. This geometric shape is due to the specific structure of the injection pump. Because of the proprietary nature of the assembly construction, the specifications of the shaft are not given. Due to its complexity and usually lower values of the natural frequency [1,2,10], the case of bending vibrations of the shaft will be analysed.

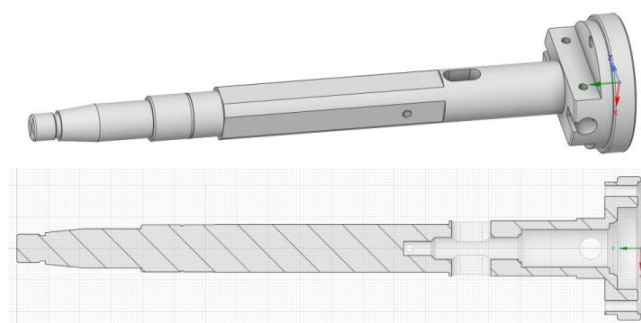


Fig. 1. Geometrical model of the system under consideration

The main goal of this work is to develop a reliable methodology for evaluating the results of natural transverse vibration analyses in the assumed frequency range as generated by the developed FE model of the pertinent shaft. It would be a more preferable situation to have the results of the experimental research of the shaft, but at the conceptual and design stage, access to this type of data is typically unrealistic. Therefore, the following methodology for evaluating the results of the natural vibration analyses generated from the elaborated FE model of the object is proposed. Based on the generated FE model of the system and for the arbitrarily chosen boundary conditions determine the values of

the natural frequencies of bending vibrations and the corresponding normal modes in the assumed frequency range. Then, a stepped shaft model (the simplified model) with simplified geometry should be developed, for which it is possible to derive analytical equations of bending free vibrations. Because the considered system does not meet the criterion of the technical theory of thin beam vibrations (the so-called Bernoulli beam theory) [2,10], therefore, while developing the equations of free vibrations, the Timoshenko beam theory (the so-called thick beam theory) will be used [2,10]. Then, for the adopted, simplified model, the FE model solution and the exact solution of the analytical model are developed, and for the previously set boundary conditions, the natural frequencies and the corresponding vibration natural forms are determined. Achieved from the simplified model, the results (which come from the analytical solutions and FEM simulation) are compared with the results received from the discussed shaft FE model and if necessary, the simplified model is modified to obtain satisfactory compliance of the results in terms of the adopted criterion.

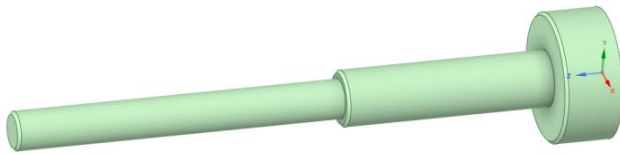


Fig. 2. Geometrical model of the three-stepped simplified shaft

In this paper, it will be shown that satisfactory results can be obtained for the discussed shaft, assuming that the simplified shaft is a three-stepped hollow shaft (see Fig. 2). In addition, the results of the FE model of the discussed system shaft will be verified with a model developed based on the MP method [22]. The considerations presented in this paper are performed under the assumption that the boundary conditions imposed on the analysed systems correspond to the conditions of a cantilever beam. Because of the specific geometry of the discussed models (see Figs. 1–5 and Tab. 1) and the relatively low value of the operating speed (<1,500 rpm), the centrifugal and gyroscopic effects of the shaft are omitted. In the authors' humble opinion, the proposed methodology will be useful for engineers dealing with the transverse vibration analysis of systems of such type, especially at the design stage.

3. THEORETICAL FORMULATION

The subject of the considerations is a stepped shaft, treated as a Timoshenko beam, with continuous segments. It is assumed that the beam has three compartments and in the individual compartments it is homogeneous with a circular-symmetric cross-section. Little vibration with no damping is considered. The vibration equation of the Timoshenko beam with the continuous segments can be written as follows [2,10]:

$$\begin{aligned}
 & -\frac{\partial}{\partial x} \left(\kappa A_i G \left(\frac{\partial w_i}{\partial x} - \phi_i \right) \right) + \rho A_i \frac{\partial^2 w_i}{\partial t^2} = 0 \\
 & -\frac{\partial}{\partial x} \left(E I_i \frac{\partial \phi_i}{\partial x} \right) - \kappa A_i G \left(\frac{\partial w_i}{\partial x} - \phi_i \right) + \rho I_i \frac{\partial^2 \phi_i}{\partial t^2} = 0
 \end{aligned} \quad (1)$$

$i = 1, 2, 3$

where $w_i = w_i(x, t)$ is the transverse beam displacement, $\phi_i = \phi_i(x, t)$ is the rotation of the beam cross section,

x and t are the coordinate and the time, κ is the shear correction factor, l_1, l_2 and l_3 are the beam dimensions, A_1, A_2 and A_3 are the cross-sectional areas of the corresponding compartments of the beam, I_1, I_2 and I_3 are the area moments of inertia of cross sections of the appropriate compartments of the beam, ρ is the mass density, E is the Young's modulus of elasticity and G is the modulus of elasticity in shear (i.e., Kirchhoff's modulus). In Eq. (1), $i = 1$ for $0 \leq x \leq l_1$, $i = 2$ for $l_1 \leq x \leq l_1 + l_2$ and $i = 3$ for $l_1 + l_2 \leq x \leq l_1 + l_2 + l_3$.

For the cantilever beam case, the appropriate boundary conditions are as follows [2,10]:

$$\begin{aligned}
 w_1(0, t) = 0, \quad \phi_1(0, t) = 0, \quad \frac{\partial \phi_3(l_1+l_2+l_3, t)}{\partial x} = 0, \\
 \frac{\partial w_3(l_1+l_2+l_3, t)}{\partial x} - \phi_3(l_1 + l_2 + l_3, t) = 0.
 \end{aligned} \quad (2)$$

In the boundary sections of homogeneous compartments of the beam, the compatibility conditions provide the following groups of equations [2,10], i.e., for $x = l_1$:

$$\begin{aligned}
 w_1(l_1, t) = w_2(l_1, t), \quad \phi_1(l_1, t) = \\
 \phi_2(l_1, t), \quad E I_1 \frac{\partial \phi_1(l_1, t)}{\partial x} = E I_2 \frac{\partial \phi_2(l_1, t)}{\partial x}, \\
 \kappa A_1 G \left(\frac{\partial w_1(l_1, t)}{\partial x} - \phi_1(l_1, t) \right) = \kappa A_2 G \left(\frac{\partial w_2(l_1, t)}{\partial x} - \phi_2(l_1, t) \right).
 \end{aligned} \quad (3)$$

and for $x = l_1 + l_2$:

$$\begin{aligned}
 w_2(l_1 + l_2, t) = w_3(l_1 + l_2, t), \quad \phi_2(l_1 + l_2, t) = \\
 \phi_3(l_1 + l_2, t), \\
 E I_2 \frac{\partial \phi_2(l_1+l_2, t)}{\partial x} = E I_3 \frac{\partial \phi_3(l_1+l_2, t)}{\partial x}, \\
 \kappa A_2 G \left(\frac{\partial w_2(l_1+l_2, t)}{\partial x} - \phi_2(l_1 + l_2, t) \right) = \kappa A_3 G \left(\frac{\partial w_3(l_1+l_2, t)}{\partial x} - \phi_3(l_1 + l_2, t) \right).
 \end{aligned} \quad (4)$$

The first two relations in Eqs (3) and (4) are the continuity conditions and the last two are the equilibrium conditions, respectively.

4. FREE VIBRATION ANALYSIS

The objective of this section is to determine an analytical solution for the free vibration of the discussed system. To solve the system Eq. (1), the Bernoulli–Fourier method (separation of variables) can be used. So, the general solution to Eq. (1) takes the following form [2,10]:

$$\begin{aligned}
 w_i(x, t) = W_i(x)T(t), \quad \phi_i(x, t) = F_i(x)T(t), \\
 T(t) = A \cos(\omega t) + B \sin(\omega t), \quad i = 1, 2, 3
 \end{aligned} \quad (5)$$

where ω is the circular frequency of the discussed system vibration. After introducing solution (5) to Eq. (1) it can produce the following equation:

$$\begin{aligned}
 W_i''(x) + a_0 W_i(x) - F_i'(x) = 0, \\
 F_i''(x) + b_i W_i'(x) - c_0 F_i'(x) = 0, \quad i = 1, 2, 3
 \end{aligned} \quad (6)$$

where

$$a_0 = \omega^2 \frac{\rho}{\kappa G}, \quad b_i = \frac{\kappa A_i G}{E I_i}, \quad c_i = \omega^2 \frac{\rho}{E} - \frac{\kappa A_i G}{E I_i}, \quad i = 1, 2, 3 \quad (7)$$

and the prime refers to the derivative of the function to x . By eliminating the function $F_i(x)$ ($i = 1, 2, 3$) from Eq. (6), one can get equations for transverse displacements $W_1(x), W_2(x)$ and $W_3(x)$ in the following form:

$$\begin{aligned} W_1^{(IV)}(x) + (a_0 + b_1 + c_1)W_1''(x) + a_0c_1W_1(x) &= 0 \\ W_2^{(IV)}(x) + (a_0 + b_2 + c_2)W_2''(x) + a_0c_2W_2(x) &= 0 \\ W_3^{(IV)}(x) + (a_0 + b_3 + c_3)W_3''(x) + a_0c_3W_3(x) &= 0 \end{aligned} \quad (8)$$

The boundary conditions (2) in terms of $W_i(x)$ take the following form:

$$\begin{aligned} W_1(0) = 0, \quad W_1'''(0) + (a_0 + b_1)W_1'(0) &= 0, \\ W_3''(l_1 + l_2 + l_3) + a_0W_3(l_1 + l_2 + l_3) &= 0, \\ W_3'''(l_1 + l_2 + l_3) + (a_0 + b_3 + c_3)W_3'(l_1 + l_2 + l_3) &= 0 \end{aligned} \quad (9)$$

And accordingly, the compatibility conditions (3) and (4) at $x = l_1$ in terms of $W_i(x)$ become:

$$\begin{aligned} W_1(l_1) = W_2(l_1), \quad \frac{1}{c_1}[W_1'''(l_1) + (a_0 + b_1)W_1'(l_1)] &= \\ \frac{1}{c_2}[W_2'''(l_1) + (a_0 + b_2)W_2'(l_1)], \quad EI_1[W_1''(l_1) + & \\ a_0W_1(l_1)] = EI_2[W_2''(l_1) + a_0W_2(l_1)], & \quad (10) \\ \kappa A_1G[W_1'''(l_1) + (a_0 + b_1 + c_1)W_1'(l_1)] = & \\ \kappa A_2G[W_2'''(l_1) + (a_0 + b_2 + c_2)W_2'(l_1)] & \end{aligned}$$

and at $x = l_1 + l_2$ they take the following form:

$$\begin{aligned} W_2(l_1 + l_2) = W_3(l_1 + l_2), \\ \frac{1}{c_2}[W_2'''(l_1 + l_2) + (a_0 + b_2)W_2'(l_1 + l_2)] &= \\ = \frac{1}{c_3}[W_3'''(l_1 + l_2) + (a_0 + b_3)W_3'(l_1 + l_2)], & \quad (11) \\ EI_2[W_2''(l_1 + l_2) + a_0W_2(l_1 + l_2)] &= \\ = EI_3[W_3''(l_1 + l_2) + a_0W_3(l_1 + l_2)], & \\ \kappa A_2G[W_2'''(l_1 + l_2) + (a_0 + b_2 + c_2)W_2'(l_1 + l_2)] = & \\ \kappa A_3G[W_3'''(l_1 + l_2) + (a_0 + b_3 + c_3)W_3'(l_1 + l_2)] & \end{aligned}$$

$$T_1 = \begin{bmatrix} \cos(\lambda_{11}l_1) & \sin(\lambda_{11}l_1) & \cosh(\lambda_{12}l_1) & \sinh(\lambda_{12}l_1) \\ c_2m21_1 \sin(\lambda_{11}l_1) & c_2m22_1 \cos(\lambda_{11}l_1) & c_2m2_1 \sinh(\lambda_{12}l_1) & c_2m2_1 \cosh(\lambda_{12}l_1) \\ m31_1 \cos(\lambda_{11}l_1) & m31_1 \sin(\lambda_{11}l_1) & m32_1 \cosh(\lambda_{12}l_1) & m32_1 \sinh(\lambda_{12}l_1) \\ m41_1 \sin(\lambda_{11}l_1) & m42_1 \cos(\lambda_{11}l_1) & m4_1 \sinh(\lambda_{12}l_1) & m4_1 \cosh(\lambda_{12}l_1) \end{bmatrix} \quad (17)$$

$$T_{21} = \begin{bmatrix} \cos(\lambda_{21}l_1) & \sin(\lambda_{21}l_1) & \cosh(\lambda_{22}l_1) & \sinh(\lambda_{22}l_1) \\ c_1m21_2 \sin(\lambda_{21}l_1) & c_1m22_2 \cos(\lambda_{21}l_1) & c_1m2_2 \sinh(\lambda_{22}l_1) & c_1m2_2 \cosh(\lambda_{22}l_1) \\ m31_2 \cos(\lambda_{21}l_1) & m31_2 \sin(\lambda_{21}l_1) & m32_2 \cosh(\lambda_{22}l_1) & m32_2 \sinh(\lambda_{22}l_1) \\ m41_2 \sin(\lambda_{21}l_1) & m42_2 \cos(\lambda_{21}l_1) & m4_2 \sinh(\lambda_{22}l_1) & m4_2 \cosh(\lambda_{22}l_1) \end{bmatrix} \quad (18)$$

$$T_{22} = \begin{bmatrix} \cos(\lambda_{21}l_{12}) & \sin(\lambda_{21}l_{12}) & \cosh(\lambda_{22}l_{12}) & \sinh(\lambda_{22}l_{12}) \\ c_3m21_2 \sin(\lambda_{21}l_{12}) & c_3m22_2 \cos(\lambda_{21}l_{12}) & c_3m2_2 \sinh(\lambda_{22}l_{12}) & c_3m2_2 \cosh(\lambda_{22}l_{12}) \\ m31_2 \cos(\lambda_{21}l_{12}) & m31_2 \sin(\lambda_{21}l_{12}) & m32_2 \cosh(\lambda_{22}l_{12}) & m32_2 \sinh(\lambda_{22}l_{12}) \\ m41_2 \sin(\lambda_{21}l_{12}) & m42_2 \cos(\lambda_{21}l_{12}) & m4_2 \sinh(\lambda_{22}l_{12}) & m4_2 \cosh(\lambda_{22}l_{12}) \end{bmatrix}, \quad l_{12} = l_1 + l_2 \quad (19)$$

$$T_3 = \begin{bmatrix} \cos(\lambda_{31}l_{12}) & \sin(\lambda_{31}l_{12}) & \cosh(\lambda_{32}l_{12}) & \sinh(\lambda_{32}l_{12}) \\ c_2m21_3 \sin(\lambda_{31}l_{12}) & c_2m22_3 \cos(\lambda_{31}l_{12}) & c_2m2_3 \sinh(\lambda_{32}l_{12}) & c_2m2_3 \cosh(\lambda_{32}l_{12}) \\ m31_3 \cos(\lambda_{31}l_{12}) & m31_3 \sin(\lambda_{31}l_{12}) & m32_3 \cosh(\lambda_{32}l_{12}) & m32_3 \sinh(\lambda_{32}l_{12}) \\ m41_3 \sin(\lambda_{31}l_{12}) & m42_3 \cos(\lambda_{31}l_{12}) & m4_3 \sinh(\lambda_{32}l_{12}) & m4_3 \cosh(\lambda_{32}l_{12}) \end{bmatrix}, \quad l_{12} = l_1 + l_2 \quad (20)$$

and

$$\begin{aligned} m21_i = \lambda_{i1}^3 - (a_0 + b_i)\lambda_{i1}, \quad m31_i = I_i(-\lambda_{i1}^2 + a_0), \\ m41_i = A_i(\lambda_{i1}^3 - (a_0 + b_i + c_i)\lambda_{i1}), \\ m22_i = -\lambda_{i1}^3 + (a_0 + b_i)\lambda_{i1}, \quad m32_i = I_i(\lambda_{i2}^2 + a_0), \\ m42_i = A_i(-\lambda_{i1}^3 + (a_0 + b_i + c_i)\lambda_{i1}), \\ m2_i = \lambda_{i2}^3 + (a_0 + b_i)\lambda_{i2}, \quad i = 1,2,3, \\ m4_i = A_i(\lambda_{i2}^3 + (a_0 + b_i + c_i)\lambda_{i2}) \end{aligned} \quad (21)$$

As in paper [13], the boundary conditions can be written as follows:

In this article, the case where the natural frequencies are below the critical value is analysed. It gives the following restrictions on the value of the frequency range:

$$\omega^2 < \frac{\kappa A_i G}{\rho I_i}, \quad i = 1,2,3 \quad (12)$$

Conditions (12) guarantee the harmonic type of free vibration. The general solution for the discussed case can be written as [2,10]:

$$W_i(x) = D_{i1} \cos(\lambda_{i1}x) + D_{i2} \sin(\lambda_{i1}x) + D_{i3} \cosh(\lambda_{i2}x) + D_{i4} \sinh(\lambda_{i2}x), \quad i = 1,2,3 \quad (13)$$

where

$$2\lambda_{i1}^2 = \alpha + \sqrt{\gamma^2 + \eta_i}, \quad 2\lambda_{i2}^2 = -\alpha + \sqrt{\gamma^2 + \eta_i}, \quad i = 1,2,3 \quad (14)$$

and

$$\alpha = \omega^2 \rho \left(\frac{1}{\kappa G} + \frac{1}{E} \right), \quad \gamma = \omega^2 \rho \left(\frac{1}{E} - \frac{1}{\kappa G} \right), \quad \eta_i = \frac{4\omega^2 \rho A_i}{EI_i}, \quad i = 1,2,3 \quad (15)$$

Substituting Eq. (13) into Eqs (10) and (11), the following matrix equations are obtained:

$$T_1 \begin{bmatrix} D_{11} \\ D_{12} \\ D_{13} \\ D_{14} \end{bmatrix} = T_{21} \begin{bmatrix} D_{21} \\ D_{22} \\ D_{23} \\ D_{24} \end{bmatrix} \text{ and } T_{22} \begin{bmatrix} D_{21} \\ D_{22} \\ D_{23} \\ D_{24} \end{bmatrix} = T_3 \begin{bmatrix} D_{31} \\ D_{32} \\ D_{33} \\ D_{34} \end{bmatrix} \quad (16)$$

where

$$T_1 = \begin{bmatrix} \cos(\lambda_{11}l_1) & \sin(\lambda_{11}l_1) & \cosh(\lambda_{12}l_1) & \sinh(\lambda_{12}l_1) \\ c_2m21_1 \sin(\lambda_{11}l_1) & c_2m22_1 \cos(\lambda_{11}l_1) & c_2m2_1 \sinh(\lambda_{12}l_1) & c_2m2_1 \cosh(\lambda_{12}l_1) \\ m31_1 \cos(\lambda_{11}l_1) & m31_1 \sin(\lambda_{11}l_1) & m32_1 \cosh(\lambda_{12}l_1) & m32_1 \sinh(\lambda_{12}l_1) \\ m41_1 \sin(\lambda_{11}l_1) & m42_1 \cos(\lambda_{11}l_1) & m4_1 \sinh(\lambda_{12}l_1) & m4_1 \cosh(\lambda_{12}l_1) \end{bmatrix} \quad (17)$$

$$T_{21} = \begin{bmatrix} \cos(\lambda_{21}l_1) & \sin(\lambda_{21}l_1) & \cosh(\lambda_{22}l_1) & \sinh(\lambda_{22}l_1) \\ c_1m21_2 \sin(\lambda_{21}l_1) & c_1m22_2 \cos(\lambda_{21}l_1) & c_1m2_2 \sinh(\lambda_{22}l_1) & c_1m2_2 \cosh(\lambda_{22}l_1) \\ m31_2 \cos(\lambda_{21}l_1) & m31_2 \sin(\lambda_{21}l_1) & m32_2 \cosh(\lambda_{22}l_1) & m32_2 \sinh(\lambda_{22}l_1) \\ m41_2 \sin(\lambda_{21}l_1) & m42_2 \cos(\lambda_{21}l_1) & m4_2 \sinh(\lambda_{22}l_1) & m4_2 \cosh(\lambda_{22}l_1) \end{bmatrix} \quad (18)$$

$$T_{22} = \begin{bmatrix} \cos(\lambda_{21}l_{12}) & \sin(\lambda_{21}l_{12}) & \cosh(\lambda_{22}l_{12}) & \sinh(\lambda_{22}l_{12}) \\ c_3m21_2 \sin(\lambda_{21}l_{12}) & c_3m22_2 \cos(\lambda_{21}l_{12}) & c_3m2_2 \sinh(\lambda_{22}l_{12}) & c_3m2_2 \cosh(\lambda_{22}l_{12}) \\ m31_2 \cos(\lambda_{21}l_{12}) & m31_2 \sin(\lambda_{21}l_{12}) & m32_2 \cosh(\lambda_{22}l_{12}) & m32_2 \sinh(\lambda_{22}l_{12}) \\ m41_2 \sin(\lambda_{21}l_{12}) & m42_2 \cos(\lambda_{21}l_{12}) & m4_2 \sinh(\lambda_{22}l_{12}) & m4_2 \cosh(\lambda_{22}l_{12}) \end{bmatrix}, \quad l_{12} = l_1 + l_2 \quad (19)$$

$$T_3 = \begin{bmatrix} \cos(\lambda_{31}l_{12}) & \sin(\lambda_{31}l_{12}) & \cosh(\lambda_{32}l_{12}) & \sinh(\lambda_{32}l_{12}) \\ c_2m21_3 \sin(\lambda_{31}l_{12}) & c_2m22_3 \cos(\lambda_{31}l_{12}) & c_2m2_3 \sinh(\lambda_{32}l_{12}) & c_2m2_3 \cosh(\lambda_{32}l_{12}) \\ m31_3 \cos(\lambda_{31}l_{12}) & m31_3 \sin(\lambda_{31}l_{12}) & m32_3 \cosh(\lambda_{32}l_{12}) & m32_3 \sinh(\lambda_{32}l_{12}) \\ m41_3 \sin(\lambda_{31}l_{12}) & m42_3 \cos(\lambda_{31}l_{12}) & m4_3 \sinh(\lambda_{32}l_{12}) & m4_3 \cosh(\lambda_{32}l_{12}) \end{bmatrix}, \quad l_{12} = l_1 + l_2 \quad (20)$$

$$K_1 \begin{bmatrix} D_{11} \\ D_{12} \\ D_{13} \\ D_{14} \end{bmatrix} + K_3 \begin{bmatrix} D_{31} \\ D_{32} \\ D_{33} \\ D_{34} \end{bmatrix} = 0 \quad (22)$$

where

$$K_1 = \begin{bmatrix} 1 & 0 & 1 & 0 \\ 0 & m22_1 & 0 & m21_1 \\ 0 & 0 & 0 & 0 \\ 0 & 0 & 0 & 0 \end{bmatrix} \quad (23)$$

$$K_3 = \begin{bmatrix} 0 & 0 & 0 & 0 \\ 0 & 0 & 0 & 0 \\ \frac{m_{313}}{I_3} \cos(\lambda_{31}l_{13}) & \frac{m_{313}}{I_3} \sin(\lambda_{31}l_{13}) & \frac{m_{323}}{I_3} \cosh(\lambda_{32}l_{13}) & \frac{m_{323}}{I_3} \sinh(\lambda_{32}l_{13}) \\ \frac{m_{413}}{A_3} \sin(\lambda_{31}l_{13}) & \frac{m_{423}}{A_3} \cos(\lambda_{31}l_{13}) & \frac{m_{43}}{A_3} \sinh(\lambda_{32}l_{13}) & \frac{m_{43}}{A_3} \cosh(\lambda_{32}l_{13}) \end{bmatrix}, \quad l_{13} = l_1 + l_2 + l_3 \quad (24)$$

Using Eq. (16), the coefficient vectors $[D_{11}D_{12}D_{13}D_{14}]^T$ and $[D_{21}D_{22}D_{23}D_{24}]^T$ can be eliminated to give:

$$\begin{bmatrix} D_{11} \\ D_{12} \\ D_{13} \\ D_{14} \end{bmatrix} = T_1^{-1} T_{21} T_{22}^{-1} T_3 \begin{bmatrix} D_{31} \\ D_{32} \\ D_{33} \\ D_{34} \end{bmatrix} \quad (25)$$

and the boundary condition (22) can be written in the matrix form:

$$[K_1 T_1^{-1} T_{21} T_{22}^{-1} T_3 + K_3] \begin{bmatrix} D_{31} \\ D_{32} \\ D_{33} \\ D_{34} \end{bmatrix} = 0 \quad (26)$$

The determinant equation in the natural frequencies is obtained from the condition of nontrivial solution. It yields the secular determinant:

$$|K_1 T_1^{-1} T_{21} T_{22}^{-1} T_3 + K_3| = 0 \quad (27)$$

where the roots of the determinant Eq. (27) $\omega = \omega_n$, ($n = 1, 2, 3, \dots$) are the exact natural frequencies. The corresponding eigenvectors of Eq. (26) together with Eq. (16) determine the eigenfunctions in terms of Eq. (13). The eigenfunctions give the normal modes of the cantilever stepped Timoshenko beam.

5. MYKLESTAD-PROHL METHOD ANALYSIS

A relatively convenient method of determining the natural frequency and the corresponding normal modes of shafts and beams is the MP numerical method [22]. In the initial assumption, it consists of the value of the natural frequency sought, and checking whether this value meets the adopted boundary conditions. If not, the calculations are repeated for the next value. The shaft (or beam) is divided into the so-called calculation points, located at the contact points of homogeneous sections of the stepped shaft (or beam). At each k – the calculation point, the following quantities are determined: shaft (beam) transverse displacement Y_k , deflection angle ψ_k , bending moment M_k and shear force T_k , according to the following equation [22]:

$$\begin{aligned} Y_{k+1} &= Y_k + z_{k+1} \psi_k + \frac{z_{k+1}^2}{2EI_{k+1}} M_k + \frac{z_{k+1}^3}{6EI_{k+1}} T_k, \\ \psi_{k+1} &= \psi_k + \frac{z_{k+1}}{EI_{k+1}} M_k + \frac{z_{k+1}^2}{2EI_{k+1}} T_k, \\ M_{k+1} &= M_k + z_{k+1} T_k, \\ T_{k+1} &= T_k + m_{k+1} \omega^2 z_{k+1}. \end{aligned} \quad (28)$$

where z_{k+1} is the distance between points k and $k + 1$, I_{k+1} is the area moment of inertia of the cross section of the shaft (beam) between points k and $k + 1$, E is the aforementioned earlier Young's modulus, m_k is the discrete mass in k -th point and ω is the assumed natural frequency. Boundary conditions for the discussed calculation case (cantilever beam) take the following form:

$$Y_0 = 0, \quad \psi_0 = 0, \quad M_{k_0} = 0, \quad T_{k_0} = 0 \quad (29)$$

where k_0 is the final calculation point. More information on the MP method can be found in reference [22].

6. FE REPRESENTATIONS

In this section the FE models of the discussed systems are formulated. The free vibration of each of the achieved discrete models (FE models of discussed objects) is described by the set of independent (decoupled) differential equations, cast in modal generalised coordinates through the use of the normal modes of the system [1]. The solution to the independent modal equations is superimposed to obtain the response of the system. To determine the eigenpairs (eigenvalue and eigenvector) related to the natural frequencies and corresponding normal modes of the discussed systems, the block Lanczos method is used [1]. The elaborated FE models are treated as approximations of the analytical models of the considered systems (especially the stepped simplified shafts).

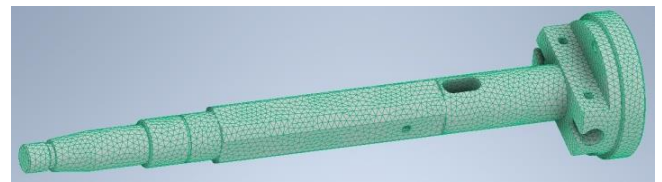


Fig. 3. FE model of the system under consideration

The modelling and analysis process are conducted using the ANSYS WORKBENCH software. To obtain models with the optimal number of elements, the surfaces resulting from the softening of feather edges are ignored in the geometrical models. This is addressed specifically for the model of the considered shaft. During the mesh generation process of the discussed systems, the 10-node tetrahedral element, with three degrees of freedom in each node, is applied. Moreover, it is assumed that the maximum length of the FE side in each model is ≤ 3.5 mm. The prepared model of the discussed shaft is shown in Fig. 3 and it includes 52,777 solid elements. The primary geometric dimensions of the accepted simplified stepped shaft (diameters: $(D_1, D_2, D_3, d_1, d_2, d_3)$ lengths: (l_1, l_2, l_3)) are shown in Fig. 4, and were partially taken from the considered system.

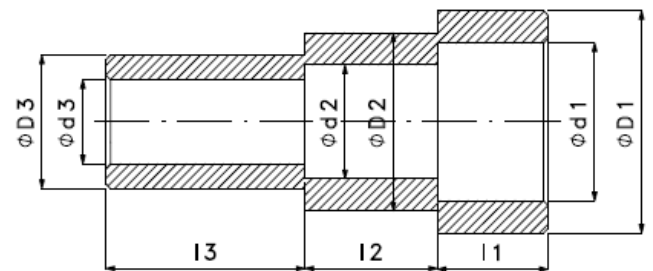


Fig. 4. Geometric dimensions of the three-stepped simplified shaft

The simplified stepped shaft FE models are prepared according to the same rules as those used with the FE model of the

discussed shaft. The two FE models of the simplified stepped shaft were developed with slight dimensional differences. The first FE model includes 32,871 FEs and the second model includes 36,158 elements. The prepared FE simplified models are shown in Fig. 5.

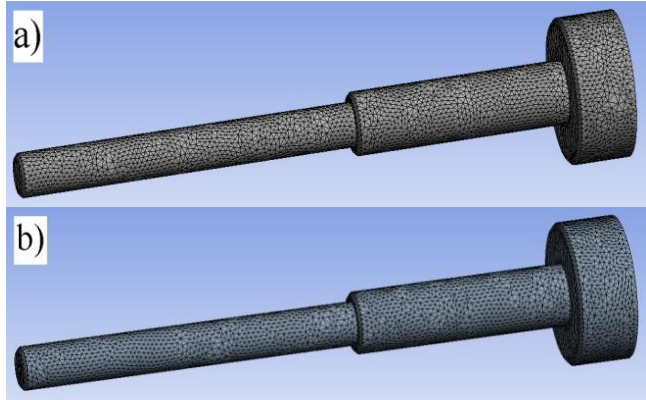


Fig. 5. FE models of the simplified stepped shaft: (a) the first model and (b) the second model

For each model case, the boundary conditions were assumed as for a cantilever beam, fixing the end of the shaft with a larger diameter. The difference between the discussed models is defined as follows [6]:

$$\varepsilon = (\omega^f - \omega^e) / \omega^e \cdot 100\% \quad (30)$$

where ω^f and ω^e are the natural frequencies of the approximate and reference models, respectively. Eq. (30) is the so-called frequency error [6]. As will be shown later, there is a significant similarity in the shape of the respective normal modes of individual models. For this reason, the similarity measure due to the normal modes (Modal Assurance Criterion (MAC indicator)) is not used.

7. NUMERICAL ANALYSIS

Numerical solutions for free vibrations analysis of the systems considered earlier are determined. This section of the study discusses and compares only the first six natural frequencies and mode shapes for transverse types of vibrations. As mentioned earlier, it is not possible to disclose the dimensions of the system under consideration, while the geometric dimensions of the three simplified stepped shafts are given in Tab. 1 and the needed technical data are given in Tab. 2. According to the theory [1,2,10], it should be expected that the normal modes of the transverse vibrations of the considered systems will occur within two perpendicular planes. In these considerations, the results of the vibration analysis of the pump shaft's FE model (see Fig. 3) are used as the reference data.

As the considered shaft does not show circular symmetry, one should expect the occurrence of slight differences in the shape of the same normal modes and in the values of the corresponding natural frequencies in the perpendicular planes mentioned. Fig. 6 shows how the vibration planes are set, where the first vibration plane is the plane shown in Fig. 6a, and the second vibration plane is the plane shown in Fig. 6b.

Tab. 1. Parameters characterising the simplified stepped shafts (see Fig. 4)

No. of the model	D_1 (mm)	D_2 (mm)	D_3 (mm)	d_1 (mm)	d_2 (mm)	d_3 (mm)	l_1 (mm)	l_2 (mm)	l_3 (mm)
1	85	37	26	29	20	0	38	139	220
2	85	37	26	27	18	4	38	139	220

Tab. 2. Technical data of the systems under study

E (Pa)	ρ (kg/m ³)	ν	κ
$2 \cdot 10^{11}$	7,850	0.3	0.9

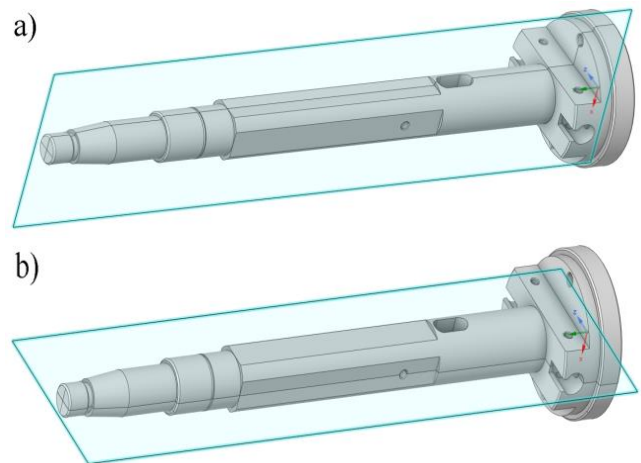


Fig. 6. Planes of transverse vibration: (a) the first plane and (b) the second plane

For example, the term transverse vibration in the first plane should be understood to mean that the potential induced transverse displacement may take place in the vertical plane, shown in Fig. 6a, while when speaking of the transverse vibration in the second plane, it is understood that it is the transverse movement in the horizontal plane shown in Fig. 6b. Tab. 3 shows the values of the natural frequencies of the shaft under consideration obtained from the FEM simulation. In the second row of Tab. 3, the frequency values refer to the vibration modes in the first plane, and the frequency values from the third row refer to the vibration modes in the second plane. When analysing the obtained results, there are slight differences in the frequency values related to individual normal modes. As mentioned earlier, the results in Tab. 3 are taken as reference data. A visualization of the relevant mode shapes is included in the Fig. 7, 12

Tab. 3. Natural frequencies of the studied shaft (FEM solution)

No. of frequencies (n)	1	2	3	4	5	6
ω_n (Hz)	199.50	1,135.49	2,747.01	4,879.47	7,504.79	10,304.44
	213.57	1,133.79	2,809.93	5,150.03	7,533.49	10,016.96

FEM, finite element method.

Tab. 4 presents the values of the natural frequencies obtained from the FEM simulation of two FE models of the three simplified stepped shafts and their respective frequency errors (30). Due to their geometry, simplified models are circularly symmetric systems. When analysing the obtained results, it can be seen that in relation to the frequency ω_1 in both cases of simplified models, the compliance of the frequency value with the value of the natural frequency of the discussed system relating to the natural form of vibrations in the second plane is better (<5%). In both the model cases, for the frequency ω_2 there is a frequency error >10%. Thus, it is generally disadvantageous. In other cases, the frequency error has absolute values of $\leq 7\%$. In general, it can be concluded that the obtained results are satisfactory and there is a significant dynamic similarity of the proposed simplified models with the reference model in terms of the adopted criterion (the frequency error (30)).

Tab. 4. Result of simulation for the auxiliary models (FEM solution)

n						
No. of auxiliary models	1	2	3	4	5	6
Natural frequencies of the first auxiliary model ω_n (Hz)						
1	219.98	984.15	2,619. 2	4,929. 0	7,370. 7	10,692
	220.00	984.26	2,619. 3	4,929. 4	7,371. 0	10,692
Natural frequencies of the second auxiliary model ω_n (Hz)						
2	226.01	995.2	2,623. 7	4,945. 2	7,397. 1	10,704
	226.01	995.3	2,624. 0	4,945. 5	7,397. 5	10,704
Frequency error of the auxiliary models ϵ_n (%)						
1	10.26	-13.33	-4.65	1.02	-1.79	3.76
	3.01	-13.19	-6.78	-4.28	-2.16	6.74
2	13.28	-12.36	-4.49	1.35	-1.44	3.88
	5.83	-12.21	-6.62	-3.97	-1.81	6.86

FEM, finite element method.

Tab. 5 presents the values of the natural frequencies obtained from the analytical solution of secular Eq. (27) relating to two models of the three stepped simplified shafts (the first four rows). The last four rows in Tab. 5 contain frequency errors (30) resulting from a comparison of the results of analytical solutions (27) with the results of the FEM simulation of the discussed system (see Tab. 3). When analysing the obtained results, it is noticed that in both cases of simplified models, for the frequency ω_2 , there is a frequency error with an absolute value >19%, so it is, of course, disadvantageous, but in other cases, the frequency error takes absolute values <7.2%. One subject of further research will be to determine why there are a relatively large absolute values of the frequency error only for the frequency ω_2 . In general, it can be concluded that the obtained results are more satisfactory as in the previous case (see Tab. 4) and there is a significant dynamic similarity between the proposed simplified analytical models (stepped Timoshenko beams) and the reference model in terms of the adopted criterion (the frequency error (30)).

Tab. 5. Result of simulation for the auxiliary models (analytical solutions)

n						
No. of auxiliary models	1	2	3	4	5	6
Natural frequencies of the first auxiliary model ω_n (Hz)						
1	198.57	896.46	2,841. 6	4,838. 5	7,362. 2	1,0286
	198.57	896.46	2,841. 6	4,838. 5	7,362. 2	1,0286
Natural frequencies of the second auxiliary model ω_n (Hz)						
2	206.16	914.51	2,830. 6	4,807. 3	7,353. 6	1,0195
	206.16	914.51	2,830. 6	4,807. 3	7,353. 6	1,0195
Frequency error of the auxiliary models ϵ_n (%)						
1	-0.47	-21.05	3.44	-0.84	-1.9	-0.18
	-7.02	-20.93	1.13	-6.05	-2.27	2.69
2	3.33	-19.46	3.04	-1.48	-2.02	-1.06
	-3.47	-19.34	0.74	-6.66	-2.39	1.78

In Tab. 6 the values of the frequency errors come from comparison of the results of analytical solutions (27), with the results of the FEM simulation of the auxiliary models (simplified stepped shaft models) shown. In this case, the results of analytical solutions (27) of the auxiliary models were taken as reference data. When analysing the obtained results, it is noticed that in relation to the first simplified model for the first natural frequency (ω_1) the frequency error is slightly >10%, for the second natural frequency (ω_2) the frequency error is $\leq 10\%$. For the remaining frequencies, the frequency error in absolute terms is <7.5%. In the case of the second simplified model, for the first two frequencies, the frequency error is slightly >9%, and for the remaining frequencies, the frequency error absolute value is <7%. With regard to the second simplified model, the FEM solution shows better compliance in terms of the adopted criterion with the analytical solution compared with the results obtained for the first simplified model. Overall, it can be said that the results presented in Tab. 6 are satisfactory.

Tab. 6. Evaluation of the quality of the auxiliary models (analytical and FEM solutions)

n						
No. of auxiliary models	1	2	3	4	5	6
Frequency error of the first auxiliary model ϵ_n (%)						
1	10.78	9.78	-7.83	1.87	0.12	3.95
	10.79	9.79	-7.82	1.88	0.12	3.95
Frequency error of the second auxiliary model ϵ_n (%)						
2	9.63	8.82	-7.31	2.87	0.59	4.99
	9.63	8.83	-7.3	2.88	0.6	4.99

FEM, finite element method

The results in Tab. 7 concern the comparison of the results obtained from the MP method with the results achieved from the FE model of the discussed system. In this case as before, the results obtained from the FE model of the discussed system (see Tab. 3) are taken as reference data. When developing the MP model of the shaft, the system was divided into 28 sections with lengths ranging from 10 mm to 20 mm, thus obtaining 29 calculation points. The required mass values at calculation points and the area moments of inertia of individual sections between the points were determined using the Autodesk Inventor environment. As in the previous cases, the boundary conditions were assumed as for a cantilever beam (Eq. 29). Relevant calculations were made in accordance with Eqs (28) and (29). As the considered shaft is not a circular-symmetric system, it should be expected that the transverse vibrations will take place in the first and second planes (Fig. 6). For this reason, it was necessary to develop two MP models, taking into account the above-mentioned planes of possible movement. In the computational process, the values of the moments of inertia were modified in a certain group of intervals and the obtained results are summarized in Tab. 7. The last two rows in Tab. 7 contain frequency errors (30) resulting from the comparison of the results of MP models solutions (28) with the results of the FEM simulation of the discussed system (see Tab. 3). The first MP model shows a satisfactory agreement with the reference model in terms of the adopted criterion (for each natural frequency, the absolute value of the frequency error is <8.21%). In the second MP model, for the frequency ω_6 there is a frequency error with the absolute value of 14.9%, which is unfavourable. The frequency errors for the remaining natural frequencies of the second MP model are at an acceptable level of value. Overall, it can be said that the results presented in Tab. 7 are satisfactory.

Tab. 7. Results of simulation by using Myklestad–Prohl models

n						
No. of models	1	2	3	4	5	6
Natural frequencies of the proposed MP models ω_n (Hz)						
1	200.7 5	1,157. 2	2,824. 8	5,027. 8	7,997. 5	1,1225
2	213.5	1,182. 4	2,928. 7	5,301. 0	8,342. 5	1,1660
Frequency error of the MP models ε_n (%)						
1	-0.62	-1.88	-2.75	-2.95	-6.16	-8.20
2	0.03	-4.11	-4.06	-2.85	-9.70	-14.9

MP, Myklestad–Prohl

Summarizing the presented results, a satisfactory compliance of the proposed simplified models and the Myklestad–Prohl models with the FE model of the analysed shaft in terms of the adopted criterion is noticed. Satisfactory compliance with the analytical models is particularly important. The obtained results confirm the correctness of the proposed verification strategy for FE models of machine shaft type systems.

Graphical visualization of the mode shapes of the system under study can be seen below (Fig 7, 8, 9, 10, 11, 12).

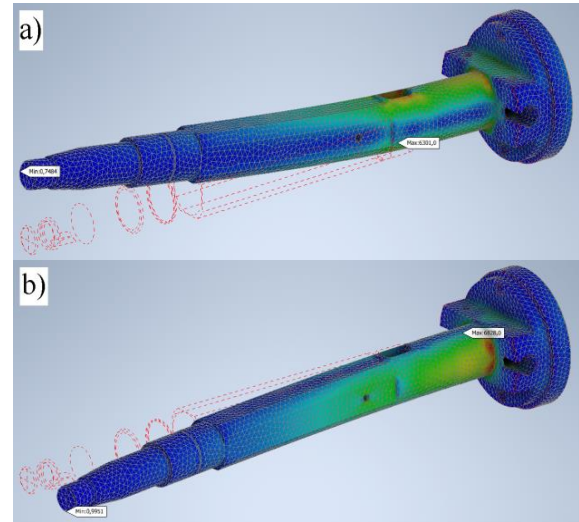


Fig. 7. Mode shapes related to the frequency ω_1 : (a) the first vibration plane and (b) the second vibration plane

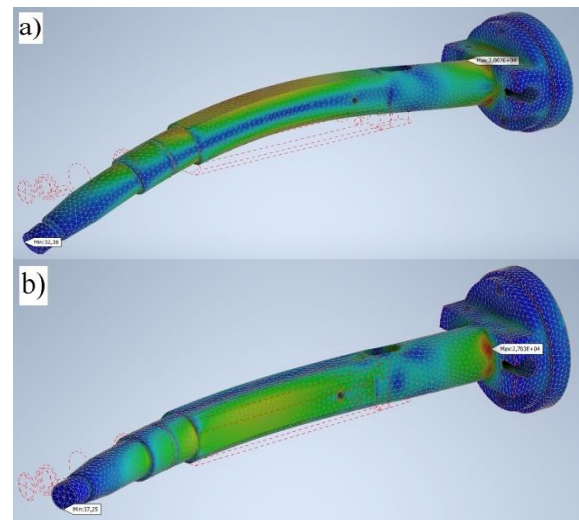


Fig. 8. Mode shapes related to the frequency ω_2 : (a) the first vibration plane and (b) the second vibration plane

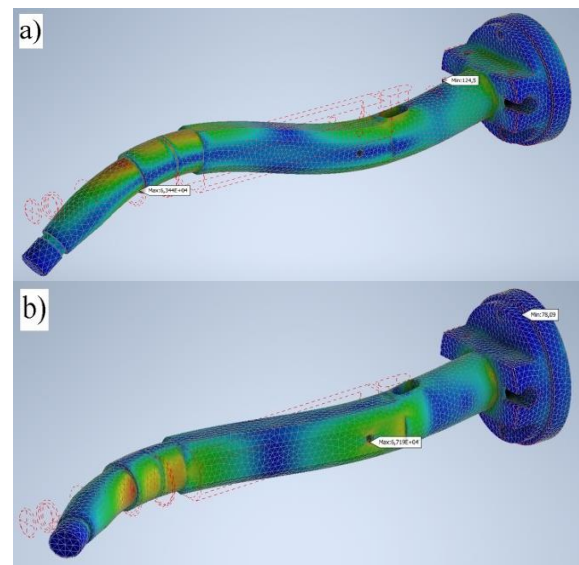


Fig. 9. Mode shapes related to the frequency ω_3 : (a) the first vibration plane and (b) the second vibration plane

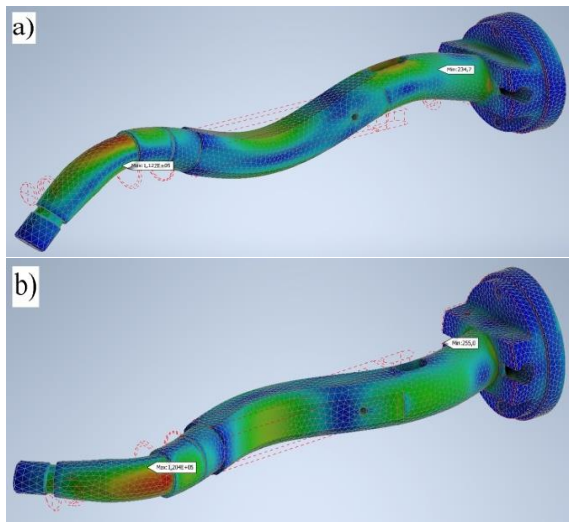


Fig. 10. Mode shapes related to the frequency ω_4 : (a) the first vibration plane and (b) the second vibration plane

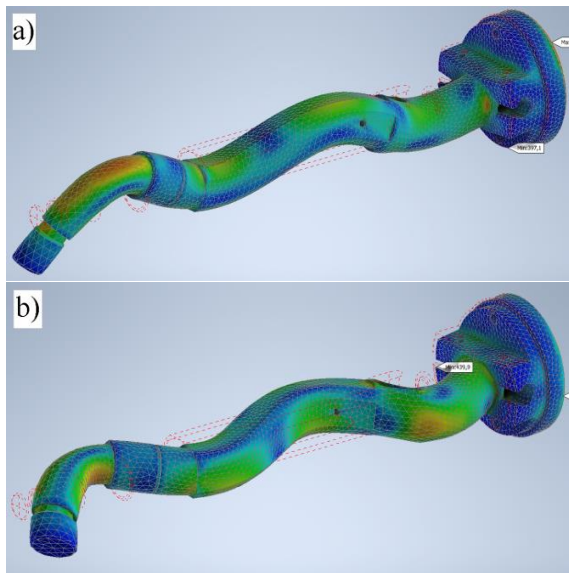


Fig. 11. Mode shapes related to the frequency ω_5 : (a) the first vibration plane and (b) the second vibration plane

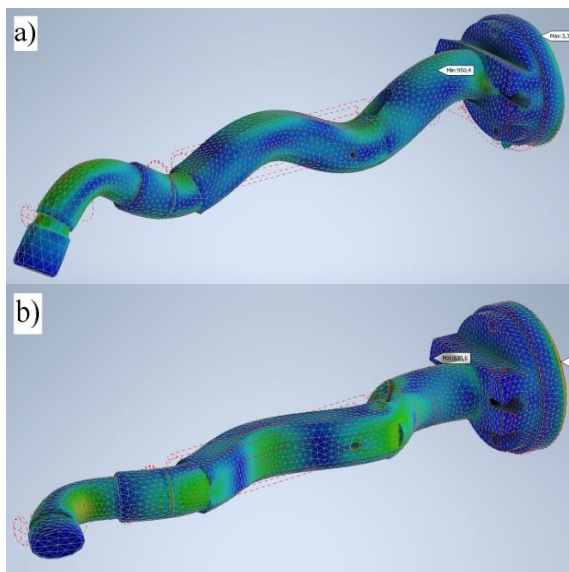


Fig. 12. Mode shapes related to the frequency ω_6 : (a) the first vibration plane and (b) the second vibration plane

8. SUMMARY

This paper presents the studies of the free transverse vibrations of shafts with compound geometry using analytical and numerical methods. The methodology for evaluating the results of the natural vibration analysis generated from the FE model of the shaft is proposed. The required analytical models of the transverse vibrations of the stepped shafts were developed based on the Timoshenko beam theory. Needed analytical solutions of the free vibrations of the discussed system are determined by using the separation of variables method. The effectiveness of the suggested approach is tested by using the selected geometrical model of the shaft dedicated to work in an injection pump. The analytical solutions are compared with the corresponding FEM solutions. The proposed analytical and numerical models give satisfactory results for a wide range of frequencies. It is remarkable how the analytical approach reduces the calculation time and computer memory requirements, and computing power when compared with the FEM solutions. The obtained results of the analysis indicate the usefulness of the MP method in the field of preliminary analysis of transverse vibrations of shaft-type systems with complex geometry. Considering the achieved results, it can be stated that when structures are analysed at their initial stage of development, simplified calculation models can be used for preliminary estimates of dynamic parameters of interest to the user. These models make it possible to pre-define the order of magnitude of the dynamic parameters of the tested objects of interest and provide some information on the quality of FEM solutions. The method proposed herein may be useful for dynamic analysis of systems such as various types of machine shafts.

REFERENCES

1. de Silva C. Vibration and Shock Handbook. Taylor & Francis. Boca Raton. 2005.
2. Rao SS, Vibration of Continuous Systems. Wiley. Hoboken. 2007.
3. Ngo VT, Xie D, Xiong Y, Zhang H, Yang Y. Dynamic analysis of a rig shafting vibration based on finite element. *Frontiers of Mechanical Engineering*. 2013;8:244-251.
4. Noga S. Dynamical analysis of the low – power electrical engine rotor. 10 European Mechanics of Materials Conference (EMMC10). Kazimierz Dolny. June 11-14. 2017:457-465.
5. Noga S, Bogacz R. Free vibration of the Timoshenko beam interacting with the Winkler foundation. *Symulacja w Badaniach i Rozwoju*. 2011;2(4):209-223.
6. Friswell M, Mottershead J. Finite Element Model Updating in Structural Dynamics. Kluwer Academic Publishers. Dordrecht. 1995.
7. Noga S. Analytical and Numerical Problems of Systems with Circular Symmetry Vibrations. Publishing House of Rzeszow University of Technology. Rzeszow. Poland (in Polish). 2015.
8. Lee U, Jang I. Spectral element model for the vibration of a spinning Timoshenko shaft. *Journal of Mechanics of Materials and Structures*. 2012;7(2):145-164.
9. Shahgholi M, Khadem SE, Bab S. Free vibration analysis of a non-linear slender rotating shaft with simply support conditions. *Mechanism and Machine Theory*. 2014;82:128-140.
10. Kaliski S. Vibration and Waves in Solids. IPPT PAN. Warsaw (in Polish). 1966.
11. Auciello NM. Vibrations of Timoshenko beams on two parameter elastic soil. *Engineering Transactions*. 2008; 56(3):187-200.
12. Majkut L. Free and forced vibrations of Timoshenko beams described by single difference equation. *Journal of Theoretical and Applied Mechanics*. 2009;47(1):193-210.

13. Chan KT, Wang XQ. Free vibration of a Timoshenko beam partially loaded with distributed mass. *Journal of Sound and Vibration*. 1997;206:353-369.
14. Awrejcewicz J, Krysko AV, Pavlov SP, Zhigalov MV, Krysko VA. Chaotic dynamics of size dependent Timoshenko beams with functionally graded properties along their thickness. *Mechanical Systems and Signal Processing*. 2017;93:415-430.
15. Zhao TY, Cui YS, Pan HG, Yuan HQ, Yang J. Free vibration analysis of a functionally graded graphene nanoplatelet reinforced disk-shaft assembly with whirl motion. *International Journal of Mechanical Sciences*. 2021;197:106335.
16. Zhao TY, Cui YS, Wang YQ, Pan HG. Vibration characteristics of graphene nanoplatelet reinforced disk-shaft rotor with eccentric mass. *Mechanics of Advanced Materials and Structures*. 2021. <https://doi.org/10.1080/15376494.2021.1904525>.
17. Zhao TY, Jiang LP, Pan HG, Yang J, Kitipornchai S. Coupled free vibration of a functionally graded pre-twisted blade-shaft system reinforced with graphene nanoplatelets. *Composite Structures*. 2021; 262:113362.
18. Zhao TY, Jiang LP, Yu YX, Wang YQ. Study on theoretical modeling and mechanical performance of a spinning porous graphene nanoplatelet reinforced beam attached with double blades. *Mechanics of Advanced Materials and Structures*. <https://doi.org/10.1080/15376494.2022.2035862>; 2022.
19. Awrejcewicz J, Krysko VA, Pavlov SP, Zhigalov MV, Kalutsky LA, Krysko VA. Thermoelastic vibrations of a Timoshenko microbeam based on the modified couple stress theory. *Nonlinear Dynamics*. 2020;99:919-943.
20. Qatu MS, Iqbal J. Transverse vibration of a two-segment cross-ply composite shafts with a lumped mass. *Composite Structures*. 2010;92:1126-1131.
21. Arab SB, Rodrigues JD, Bouaziz S, Haddar M. Dynamic analysis of laminated rotors using a layerwise theory. *Composite Structures*. 2017;182:335-345.
22. Myklestad NO. A new method of calculating natural modes of coupled bending vibration of airplane wings and other types of beams. *Journal of Aeronautical Science*. 1944;11:153-162.
23. Wu JS, Yang IH. Computer method for torsion and flexure coupled forced vibration of shafting system with damping. *Journal of Sound and Vibration*. 1995;180. (3):417-435.
24. Yang M, Zhou X, Zhang W, Ye J, Hu Y. A modified transfer matrix method for bending vibration of CFRP/Steel composite transmission shafting. *Archive of Applied Mechanics*. 2020;90:603-614.
25. Farshidianfar A, Soheil S, Abachizadeh M. Flexural vibration of Timoshenko beams. using distributed lumped modeling technique. *Aerospace Mechanics Journal*. 2008;4(1):75-84.
26. Soheil S, Abachizadeh M. Flexural vibration of multistep rotating Timoshenko shafts using hybrid modeling and optimization techniques. *Journal of Vibration and Control*. <https://doi.org/10.1177/10775463211072406>; 2022.

Acknowledgements: This paper was inspired by the work carried out under grant RPPK.01.02.00 – 18 – 0029/19 – 00 entitled: "Prace B+R dotyczące innowacyjnej pompy wtryskowej dedykowanej silnikom ciężkich pojazdów i sprzętów o przeznaczeniu specjalnym," co-financed by the European Regional Development Fund.

Stanisław Noga:  <https://orcid.org/0000-0003-3789-4899>

Edward Rejman:  <https://orcid.org/0000-0003-4716-7513>

Paweł Bałon:  <https://orcid.org/0000-0003-3136-7908>

Bartłomiej Kielbasa:  <https://orcid.org/0000-0002-3116-2251>

Robert Smusz:  <https://orcid.org/0000-0001-7369-1162>

Janusz Szostak:  <https://orcid.org/0000-0002-7789-3383>

EXPERIMENTAL AND NUMERICAL SMALL PUNCH TESTS OF THE 14Cr ODS FERRITIC STEEL

Krzysztof NOWIK^{*}, Zbigniew OKSIUTA^{*}

^{*}Institute of Mechanical Engineering, Faculty of Mechanical Engineering, Białystok University of Technology,
ul. Wiejska 45C, 15-351 Białystok, Poland

krzysztof.nowik@doktoranci.pb.edu.pl, z.oksiuta@pb.edu.pl

received 30 March 2022, revised 13 May 2022, accepted 16 May 2022

Abstract: Nowadays, various small specimen test techniques have gained wide popularity and appreciation among researchers as they offer undoubtful benefits in terms of structural material characterisation. This paper focuses on small punch tests (SPTs) performed on small-sized disc specimens to assess the mechanical properties of 14Cr oxide dispersion strengthened (ODS) steel. A numerical model was established to support experimental data and gain deeper insight into complex strain states developing in a deformed specimen. Modern evaluation procedures were discussed for obtaining mechanical properties from the small punch force-deflection response and were compared with the literature. Applicability and universality of those relations at different test conditions were also studied. It appeared that different ball diameters used had negligible influence on yield point but strongly affected ultimate strength estimation. It was found that friction belongs to decisive factors determining strain distribution in samples, as dry conditions increase the peak strain and move its location farther from the punch pole.

Key word: ODS ferritic steel, mechanical alloying, small punch testing, finite element method, yield stress, ultimate tensile strength

1. INTRODUCTION

Recently, various research methods using micro-samples have gained great importance and have become a new area of intensive research. Standard durability tests always involve large material losses, as they require relatively large samples. Therefore, in case of novel materials, it becomes very convenient to use micro-samples for testing, which are often obtained directly from the element during its working time [1,2,3,4].

One of the most remarkable techniques used to evaluate the mechanical properties of micro-sized specimens is the small punch test (SPT). Complex phenomena occurring during sample deformation along with severe plastic deformation spreading through the entire sample, often accompanied with necking and cracking, make the extraction of material parameters from the obtained force-displacement curve a difficult task, which is still an area of extensive research. SPT has gained wide attention in the field of nuclear materials, where the limitation to radiation exposure has a crucial priority [5,6,7].

Nowadays, we can observe a strong trend of gradual departure of fossil fuels in the energy sector. Researchers' efforts to develop future full-scale commercial fusion reactors are currently focused on the International Thermonuclear Experimental Reactor (ITER) megaproject, demonstrating the scientific and technological viability of fusion energy [8], advancing rapidly into the final construction stage [9]. The most critical obstacle is, however, selection of material, which would be able to withstand harsh working conditions.

Reduced activation ferritic (RAF) oxide dispersion strengthened (ODS) steels are primary candidates for the first wall of fusion reactors, due to their exceptional resistance to swelling and

high thermal conductivity accompanied with low thermal expansion. Chemical composition of modern RAF ODS alloys is exclusively based on low activation elements, usually of type Fe-Cr-W-Ti-Y₂O₃, to ensure that radioactivity from the material decays to low levels in less than 100 years [10]. These alloys typically contain 12–16 wt.% Cr (usually 14% Cr) and are reinforced with ~0.3 wt.% of Y₂O₃, which ensures superior mechanical properties. Nowadays, ODS RAF steels are characterised by good tensile and creep strength, especially at elevated temperatures, and also with great oxidation and neutron irradiation resistance [11]. In the early stage of the ODS steel development, these materials contained simply pure Y₂O₃ oxide in the form of unfavourable, large-sized precipitates with a simple crystal structure [12]. To be an effective barrier to dislocation movement, the oxides should have a size of few nanometers and must be homogeneously distributed in the Fe matrix. Although the size of oxides can be optimised by adding Ti subsequently, the more recent studies have focused on modifying the chemical composition by adding different elements, such as Al, Hf, Zr and others [13]. Despite countless alternative fabrication routes towards ODS alloys being proposed, only powder metallurgy (PM) is currently established as the technique which allows the large-scale production of these materials.

This article reports experimental data and numerical simulations of SPTs performed on Fe-14Cr-2W-0.3Ti-0.3Y₂O₃ (wt.%) ferritic ODS alloys. ODS steels belongs to the group of structural nuclear materials with a great potential for use in future fusion reactors; so, their industrial importance is unquestionable. Experimental results have been supplemented by finite FEM analysis to gain deeper insight into the SP test and evaluate the impact of friction and test rig dimensions and material properties.

2. MATERIALS AND METHODS

Herein, an ODS steel powder with nominal composition of Fe-14Cr-2W-0.3Ti-0.3Y₂O₃ (wt. %) was mechanically alloyed (MA) for 42 h in a planetary ball mill Fritsch Pulverisette 6 under H₂ atmosphere, using the commercially available, high purity elemental powders. Mechanical grinding was conducted using 100 stainless steel balls, preserving the 10:1 ball-to-powder (BPR) weight ratio and constant rotation speed of 350 rpm. After MA, the powder was encapsulated in a soft steel can and then degassed and consolidated by hot isostatic pressing (HIP) at 1,150°C under the pressure of 200 MPa for 3 h. Afterwards, material was thermo-mechanically treated by hot pressing (HP) in a closed die at 850°C and finally annealed at 1,050°C for 1 h in Ar atmosphere. A transmission electron microscopy (TEM) image of HIP-HP-HT ODS steel consists of a fine (~400 nm) and relatively uniform distribution of equiaxed grains (Fig. 1), which indicates that the material can be regarded as isotropic. Details of the manufacturing process of studied herein and similar ODS alloys can be followed in the literature [14,15].

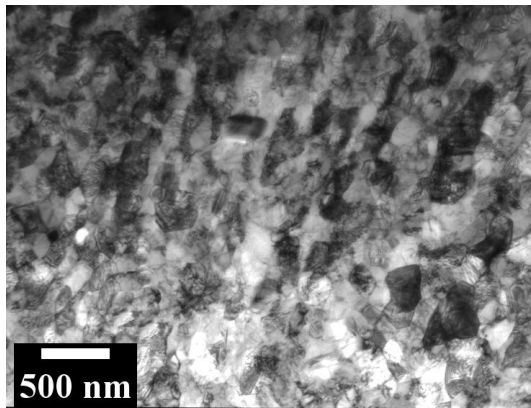


Fig. 1. TEM micrograph of 14Cr ODS steel used in this study. TEM, transmission electron microscope; ODS, oxide-dispersion strengthened

Basic elastic-plastic properties of the studied material were acquired from a uniaxial tensile test. Flat mini tensile specimens with dimensions of 2 × 5 × 27 mm with a gauge length of 6 mm were used at a strain rate of 1.0 × 10⁻⁴ s⁻¹ using a MTS 858 testing machine, equipped with a 3542 Epsilon extensometer. Three samples were used to determine mean yield σ_0 and ultimate tensile strength, which were σ_{UTS} of 844 ± 27 and 953 ± 41 MPa, respectively, which proves the isotropy of HIP-consolidated material and, as a consequence, good reproducibility of tensile results (Tab. 1). Nominal stress σ_{nom} and strain ϵ_{nom} values obtained from uniaxial tensile test were converted to true stress-true strain using the following relations (Eqs. 1 and 2):

$$\sigma = \sigma_{nom}(1 + \epsilon_{nom}) \tag{1}$$

$$\epsilon = \ln(1 + \epsilon_{nom}) \tag{2}$$

Tensile results are comparative with other ODS steels of similar chemical compositions reported by other authors [16,17]. According to De Sanctis et al. [18], shear modulus G of an ODS ferritic steel of similar chemical composition is 81 GPa. Therefore, we estimated Poisson's ratio value accordingly to $\nu = (E - 2G)/2G$, which equals to $\nu = 0.29 \approx 0.3$. Mean values

of E and ν obtained from tensile tests were used in FEM simulation to specify elastic properties, whereas the classic metal plasticity model parameters were defined based on post-yield segment of the tensile curve (after subtracting the elastic strain). Fig. 2 shows the whole tensile curve, which is used to define plasticity, with insights focusing on the work hardening region.

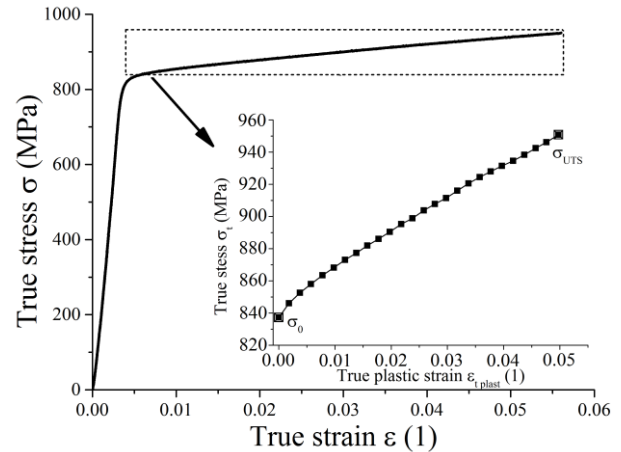


Fig. 2. True stress-strain tensile curve of studied ODS alloy used to define the plastic parameters. Insight shows the work hardening region, with squares representing data points tabularised in Abaqus. ODS, oxide-dispersion strengthened

Tab. 1. Basic elastic-plastic properties of the tested 14Cr ODS steel. These values were used in FEM simulations. ODS, oxide-dispersion strengthened; FEM, finite element method

Elastic-plastic properties	
E [GPa]	208.5 ± 4.2
ν	0.3
σ_0 [MPa]	844 ± 27
σ_{UTS} [MPa]	953 ± 41
ϵ [%]	5.48 ± 0.38

Developed in the 1980s, the SPT is one of the most commonly used methods for testing small volume samples [1,5]. Since SPT does not require large amounts of the material, it is especially useful when material availability is limited [19,20,21]. It is also practical to determine post-irradiation mechanical properties of nuclear materials since small volume samples limit radiation exposure [22,23]. Although this method has been exploited for almost 40 years, comprehensive standards for acquiring material data have only recently been established. Lack of universal methodology often makes obtained results incomparable. In Europe, the latest standardisation step for the SPT is the European standard EN 10371 "Metallic materials - Small punch test method" (2021). Also, the American National Institute of Standards and Technology (NIST) published a paper (internal report) [24] with guidelines of assessing the strength parameters using the SPT. The methodology of correlating the SPT and tensile results presented later in this work is in line with these documents and most scientific papers.

The essence of the SPT is based on pressing a spherical indenter at constant rate into a thin sample clamped between the dies [21]. The force F needed to push the ball into the material is

plotted as a function of the displacement u of the punch [5,25]. A number of specific values can be determined from the $F(u)$ curve, among which the most important are the following:

- F_{max} , the maximum force;
- u_m , the deflection at F_{max} ;
- F_e , the elastic-plastic transition force.

Due to easy accessibility, flat $\varnothing 3$ mm TEM specimens of 0.25 mm nominal thickness were chosen in this study. A constant load velocity of 0.5 mm/min was applied in Zwick Roell Z010 testing machine to press the ball into the specimen. An experimental setup exploited for the purpose of this research is shown in Fig. 3.

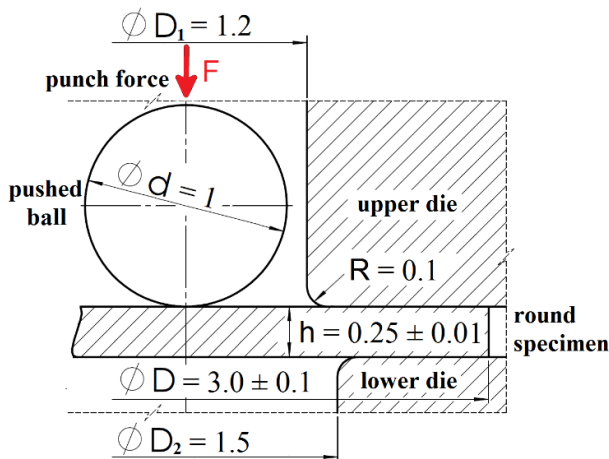


Fig. 3. Scheme of SPT setup used in the experiment. SPT, small punch test

There are mainly two different displacement measurement methods: top measurement and linear variable differential transducer (LVDT) measurement [26]. These non-identical setup combinations result in differences in the stiffness of each experimental SPT device and thus induce bias of the deflection. During SPT, when the displacement is measured as the displacement of the punch, the elastic displacement of the device and sample are added to the readings. Therefore, the elastic component of the total displacement in the raw load–displacement curves comprises both the material's and the machine's elastic response [27]. To take this error into account, the compliance correction of SPT system was performed, accordingly to procedures described in the literature [28], which is a common practice carried out for tensile and compression tests [29].

Thus, different empirical equations have been proposed to correlate SPT results with mechanical properties. Anyway, there is a complete agreement that the relationship between small punch “yield force” F_e and tensile yield strength σ_0 is linear, which can be expressed as Eq. 3 [5,30]:

$$\sigma_{0-SPT} = \alpha_1(F_e/h^2) + \alpha_2 \quad (3)$$

where the α parameters are the constants depending on test setup.

The small punch elastic-plastic transition point is not clearly defined since yielding in the specimen occurs heterogeneously [5]. As a consequence, the method of determining F_e is also a subject of debate, and different approaches have been suggested. The methodology of defining F_e in this paper is presented in Fig. 4. In this study, F_e was obtained according to a modified “two-secant” method proposed by Mao and Takahashi [31]. Normalis-

ing the equation with h^2 limits the thickness dependence of α parameters, as the force required for bending increases quadratically with its thickness [5].

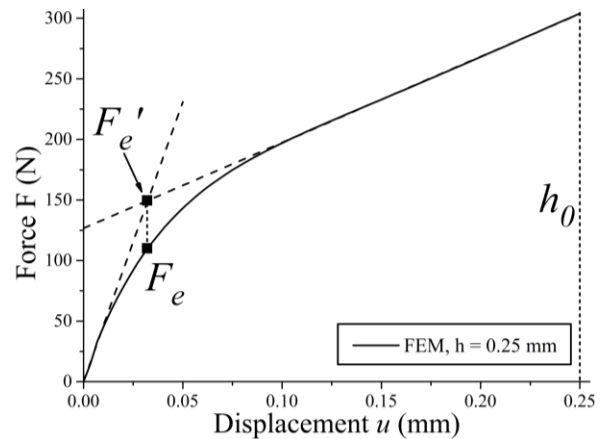


Fig. 4. Method of determining yield properties

Similar to yield strength estimation, various proposals have been evaluated to the correlate maximum SPT load (F_{max}) and the ultimate tensile strength σ_{UTS} . García et al. [30] found that Eq. 4 has low dependence on the thickness and gives the best estimate for a wide range of alloys:

$$\sigma_{UTS-SPT} = \beta_1(F_{max}/u_m h) + \beta_2 \quad (4)$$

Ultimate strength estimation is generally simple to utilize since both F_{max} and u_m are strictly defined and can be easily distinguished directly from $F(u)$ curve. β are the constant parameters, analogous to α in Eq. 3.

The FEM model, presented in Fig. 5, was developed in Abaqus. The model was designed as a two-dimensional axisymmetric assembly, which provided acceptable accuracy of calculations by rational computational time. An 8-node CAX8R elements were used to mesh the specimen part. As the indenter and both dies are multiple times stiffer than the specimen, they were modelled as infinitely stiff bodies.

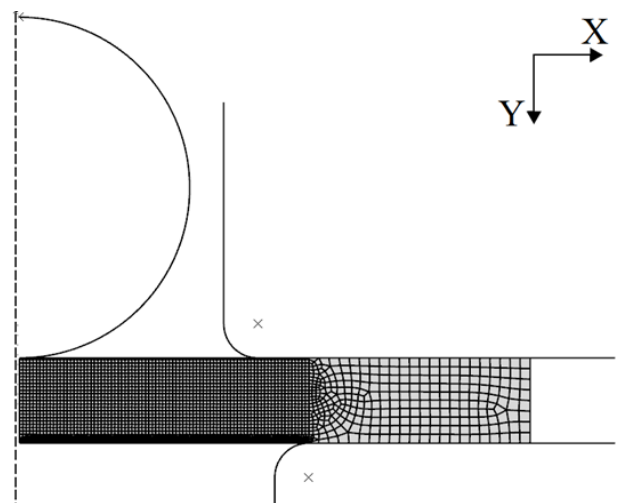


Fig. 5. FEM model of the SPT configuration in Abaqus. FEM, finite element method; SPT, small punch test.

3. RESULTS AND DISCUSSION

Numerical load-displacement curves are shown in Fig. 6. As depicted, friction coefficient has almost no effect on the initial force-displacement response until approximately up to the half of the curve. Fig. 7 shows the relationship between the μ and F_{max} . According to it, the increase in friction is accompanied by linear growth of the maximal force up to $\mu = 0.2$. Beyond that, the increase in F_{max} becomes progressively smaller, and the relationship turns into nonlinear.

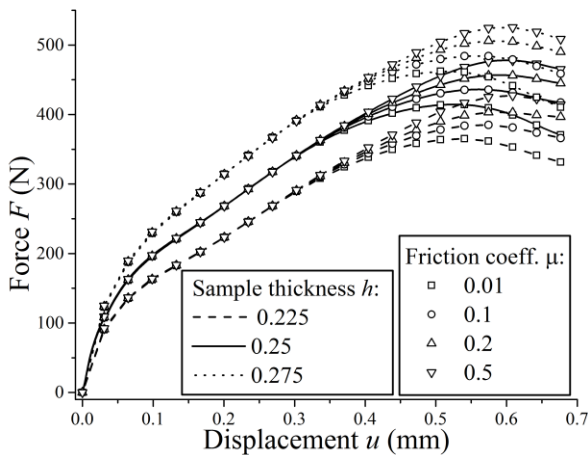


Fig. 6. Numerical force-deflection curves for various specimen thickness and friction coefficient

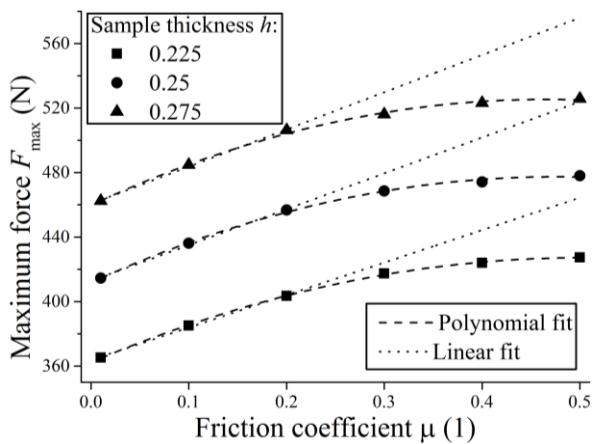


Fig. 7. The influence of friction coefficient value μ on obtained numerical maximal force F_{max} . Dotted line marks linear fit to the data

Along with specimen's deformation, biaxial stress and strain fields develop. Fig. 8 highlights the differences in plastic strain field evolution in samples deformed under contrasting friction conditions. Due to high stresses developed by pressing the ball against the elastic material, the specimen is exhibited to a serious level of deformation already at the onset of the test, as equivalent plastic strain ϵ^p reaches $\sim 10\%$ with a punch displacement of just 0.01 mm (Fig. 8a). As the loading grows, plastic strain transfers to the bottom surface and localizes there (Fig. 8b). The effect of the friction on the strain field becomes visible only at the later stage of deformation. As compared in Fig. 8cd, high μ favours the accumulation of relatively large amounts of strain in a small region of the material, which is manifested macroscopically as a neck

formed by prominent thinning at the strain localisation. Necking results in a smaller volume of high strain area and hence smaller growth of F_{max} , which explains the nonlinear trend of the $F_{max}(\mu)$ plot (Fig. 7).

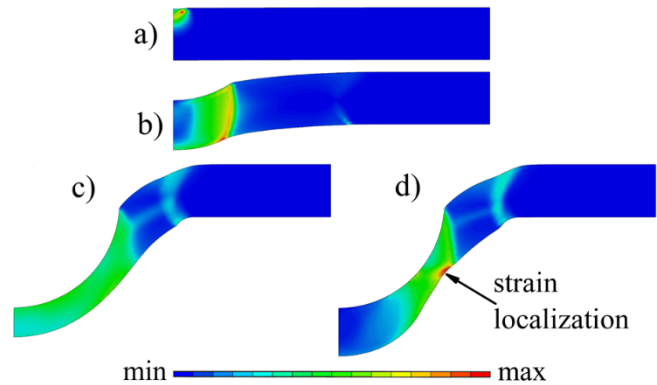


Fig. 8. Plastic strain equivalent plots at various deformation stages and friction conditions: (a) $u = 0.068$ mm, μ negligible, scale: [min 0; max 0.07]; (b) $u = 0.136$ mm, μ negligible, scale: [min 0; max 0.36]; (c) $\mu = 0.01$ and (d) $\mu = 0.5$; $u = 0.68$ mm, scale: [min 0; max 1.88]. See text for details

To gain deeper insight about plastic yielding of the material areas having direct contact with the indenter, ϵ^p curves at the specimen's reference node representing punch-specimen central point of contact were plotted in Fig. 9 as a function of punch displacement. According to it, strain immediately reaches ~ 0.02 at the moment of contact between the bodies and remains constant up to the displacement of ~ 0.2 mm, irrespectively of the assumed μ value, until the remaining surface of the specimen yet to come in contact with the punch, which deforms most easily due to absence of friction and wraps around the punch as it descends. As soon as the rest of the working surface of the punch comes with contact with the material, ϵ^p starts to rise again and the deformation at punch-specimen interface is the greater as the lower μ is. The reason for this is that the material in contact with the punch deforms easier under low friction conditions, as the resistance for the punch movement towards specimen is relatively low. In contrast, high frictional force favours sticking the punch to the material rather than deforming it, which postpones more deformation there and promotes more strain to occur at the non-contact areas.

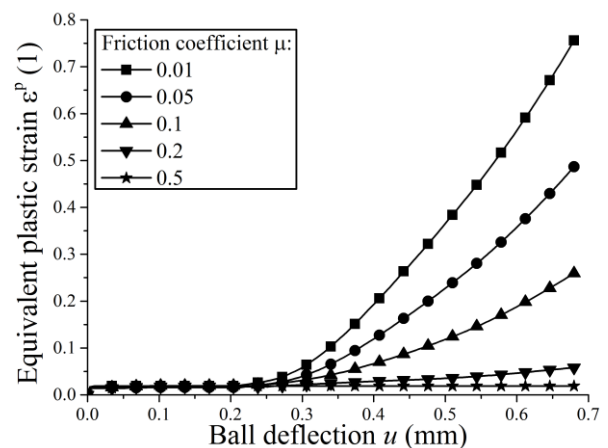


Fig. 9. Equivalent plastic strain at the punch-specimen pole

To elaborate the necking phenomenon in more detail, strain distribution along the bottom surface path (necking area) of the specimen at ultimate load was presented in Fig. 10. As the μ increases, not only the peak value of ε^p is found to be much higher but also its localisation in the material gradually moves away from the punch pole. A similar conclusion was made by other authors, who also observed that lubrication in experimental conditions reduces the ultimate load and moves the failure site closer to the pole of the punch [32].

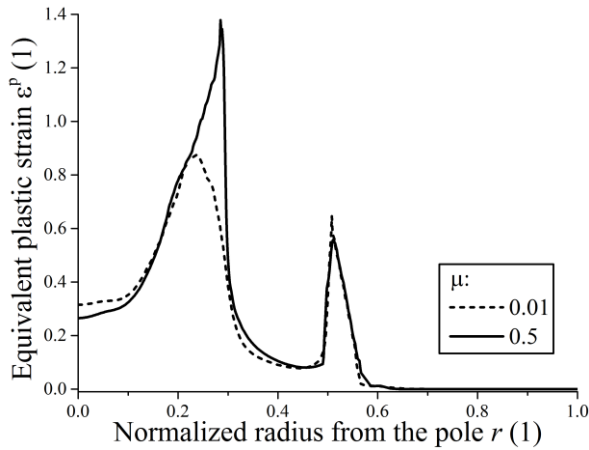


Fig. 10. Strain distribution along the bottom surface path of the specimen at ultimate load

In Fig. 11, numerical and experimental SPT curves are compared. Maximum force F_{max} and displacement at maximum force u_m values were extracted and listed in Tab. 2. Numerical curves with the friction coefficient of $\mu = 0.1$ and $\mu = 0.2$ were selected for comparison, as these values are within typical range for steel-steel friction pair and therefore should coincide well with experimental results.

Tab. 2. Maximum values of force F_{max} along with their corresponding displacements u_m at F_{max} for FEM and experimental curves (see Fig. 10). FEM, finite element method

Case	F_{max} [N]	u_m [mm]
FEM, $\mu = 0.1$	433.7	0.561
FEM, $\mu = 0.2$	452.8	0.592
Exp. 1	430.5	0.536
Exp. 2	443.7	0.538
Exp. 3	444.9	0.554
Mean experimental	439.7 ± 7.9	0.543 ± 0.010

Generally, the numerical and experimental results show good agreement. Experimental and FEM estimates of F_{max} are in very close agreement, both in case of $\mu = 0.1$ and $\mu = 0.2$. The scatter in the FEM and experimental F_{max} ranges from around 1% to 6%. In the case of the mean experimental F_{max} and u_m values (Tab. 2), $\mu = 0.1$ is preferable (0.8% and 3.4% error for F_{max} and u_m estimation, respectively) and was used in further calculations.

Another interesting detail observed in Fig. 11 is that experimental and simulated force-displacement responses, although parallel, are not exactly overlapping, especially within the range of elastic region. As it is clear that the slope of the calculated curve is much steeper than its experimental counterparts, it can be

stated that the stiffness of numerical data tend to be overestimated. The most probable explanation of this fact could be that the punch and dies were modelled as perfectly rigid, while in reality they are subjected to some deformations when transmitting the load and have defined compliance. The elastic region is also particularly influenced by various test inaccuracies, like sample thickness, settlement of experimental device parts, etc.

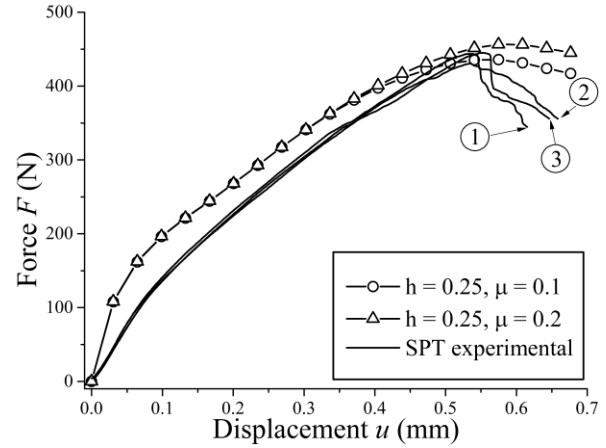


Fig. 11. Comparison of numerical and experimental small punch curves

The methods of assessing the characteristic material properties from the SPT data were also analysed. In line with [30,33], the intercept factors (α_2 , β_2) of the linear equations Eqs. 3 and 4 were neglected, and they can be written in a simplified form:

$$\sigma_{0-SPT} = \alpha(F_e/h^2) \tag{5}$$

$$\sigma_{UTS-SPT} = \beta(F_{max}/u_m h) \tag{6}$$

Tab. 3. Values of the factors used in Eqs. 5 and 6 optimised for the current study. Literature values are also given

	F_e/h^2 [MPa]	α	$F_{max}/(u_m h)$ [MPa]	β
FEM, $h = 0.225$	1,631.8	0.513	3,019.2	0.315
FEM, $h = 0.250$	1,712.2	0.489	3,092.3	0.307
FEM, $h = 0.275$	1,797.9	0.466	3,123.3	0.302
Mean FEM	$1,714.0 \pm 83.1$	0.488 ± 0.014	$3,078.3 \pm 53.5$	0.309 ± 0.003
Exp. 1	1,957.1	0.428	3,212.7	0.296
Exp. 2	2,029.3	0.413	3,298.9	0.288
Exp. 3	2,171.6	0.386	3,212.3	0.296
Mean experimental (\pm SD)	$2,052.7 \pm 109.1$	0.407 ± 0.012	$3,241.3 \pm 49.9$	0.293 ± 0.005
Bruchhausen et al. [5]	-	$\alpha_1 = 0.382$	-	$\beta_1 = 0.326$
		$\alpha_2 = 28.8$		$\beta_2 = -27.04$
García et al. [30]	-	0.476	-	0.277
Campitelli et al. [28]	316L	970 ± 40	0.400 ± 0.012	-
	F82H	$1,370 \pm 80$	0.388 ± 0.022	-

Specific SPT parameters (α , β) derived from the experimental and FEM curves were collated in Tab. 3 and compared with the results obtained by other authors. Literature data included: an extensive study conducted on a broad range of metallic materials [30], other, covering austenitic and tempered martensitic steels [28] and finally, modified 9Cr-1Mo (Grade 91) ferritic-martensitic steel used in nuclear power plants [5]. The relationships attained between σ_0 and the F_e/h^2 were plotted in Fig. 12 along with results provided by other authors.

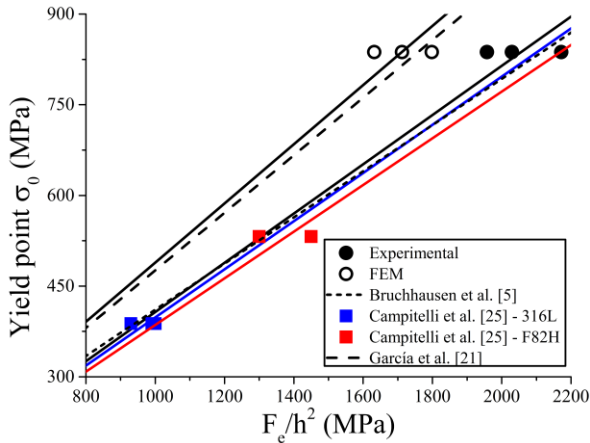


Fig. 12. Relations between F_e/h^2 and yield point σ_0 for experimental and numerical results in present study, compared with various literature data

The mean FEM-designated α value of 0.488 is closely related to the results reported by [30], where mean $\alpha = 0.475$ parameter was averaged for various alloys (including high strength, structural and stainless steels). It confirms that $\alpha = 0.475$ is indeed a good estimate for plenty of materials. As can be seen in Tab. 3, mean experimental $\alpha = 0.407$, although within the range of values contributed by other authors, shows noticeable disagreement with FEM. This scatter is a consequence of discrepancies between calculated and experimental $F(u)$ responses, particularly in the elastic region. As mentioned earlier, the elastic slope of FEM curve is generally much steeper, which affects greatly position of the intersection point of the two lines (Fig. 4) and, subsequently, the transition point F_e evaluation (error remains in the order of 15%). Hence, particular caution should be kept when assessing σ_0 from numerical curves.

The relationship between the maximum SPT load and tensile strength was studied as well. In line with Altstadt et al. [23], the scatter between the FEM and experimental estimates of σ_{UTS} is generally smaller than in case of σ_0 . Experimental β_1 is in average 5% lower than FEM value and both match well with the literature data. FEM calculations prove that normalising neither the Eq. 3 with h^2 nor Eq. 4 with $u_m h$ does not fully eradicate its thickness dependence, as they show clear linear correlation with h (Fig. 13).

Additional simulations were run to check the applicability of Eqs. 3 and 4 at varying test conditions, i.e. different indenter diameter. Other authors have already pointed out that the relationship between the SPT maximum load and ultimate strength depends strongly on test rig configuration and conditions, as these factors affect the F_{max} value markedly [3,28].

On the other hand, the incorporation of $u_m h$ into the Eq. 4 takes into account reduction of thickness (necking) occurring

during the test and appears to, at least partly, compensate different test conditions factors [30]. In Fig. 14, the FEM curve ($h = 0.25$ mm, $\mu = 0.1$) obtained for nominal ϕ 1 mm ball diameter used in experiment is compared with those obtained for ϕ 0.8 and ϕ 1.2 mm diameters.

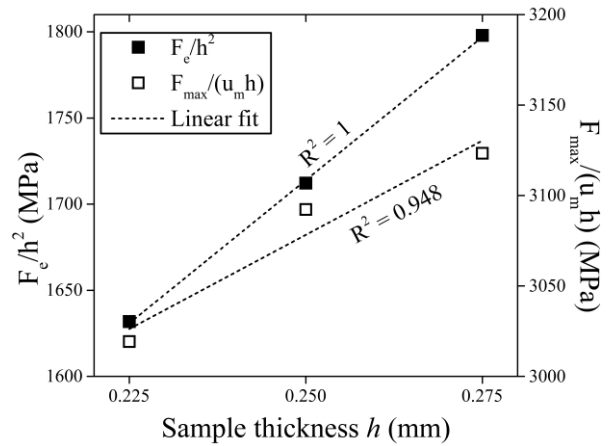


Fig. 13. Sample thickness dependence of F_e/h^2 and $F_{max}/(u_m h)$ expressions

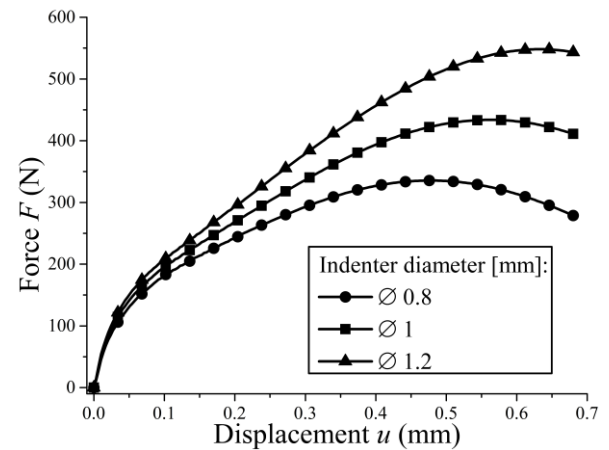


Fig. 14. Punch diameter influence on the shape of calculated load-displacement curves

As expected, the indenter diameter has remarkable influence on $F(u)$ response, particularly in the F_{max} region. The obtained data were processed analogously. As compared in Tab. 4, changing the ball diameter (in the $\pm 20\%$ range) has negligible influence on deriving yield properties. Hence, the presented method of assessing the yield point from SPT might be considered generalisable for the same material, even if the test conditions vary.

Tab. 4. Values of the factors used in Eqs. 3 and 4 obtained for various indenter diameter

Ball diameter [mm]	F_e/h^2 [MPa]	α	$F_{max}/(u_m h)$ [MPa]	β
ϕ 0.8	1,688.9	0.496	2,819.5	0.337
ϕ 1 (nominal)	1,712.2	0.489	3,092.3	0.307
ϕ 1.2	1,708.4	0.490	3,466.8	0.274

Contrarily, it turned out that the relation between SPT maximum load and σ_{UTS} has to be viewed cautiously, as normalising it with $u_m h$ is insufficient to compensate differences in F_{max} caused by different punch diameters. Interestingly, the relationship between ball diameter and $F_{max}/(u_m h)$ expression presents linear correlation (Fig. 15).

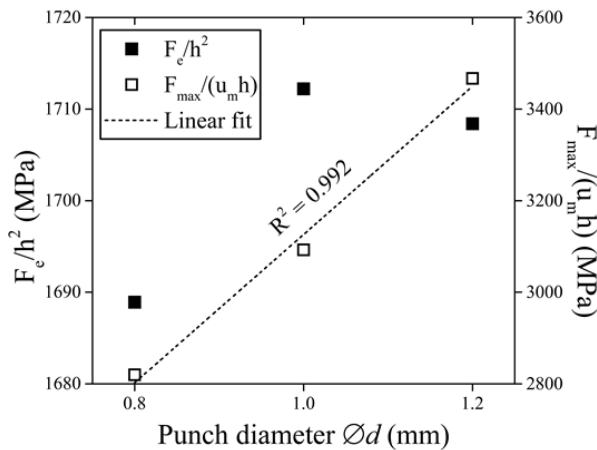


Fig. 15. Punch diameter dependence of F_e/h^2 and $F_{max}/(u_m h)$ expressions

Finally, a fractography study of tested specimens was done to determine failure micromechanisms. Fig. 16 represents the fracture surface of the broken 14Cr ODS steel after the SPT, observed in a scanning electron microscope (SEM). It may be assumed that the material exhibited mixed fracture mechanism, which is witnessed macroscopically by the coexistence of characteristic radial as well as circumferential (Fig. 16a) cracks on deformed surface. Presence of radial bursts indicates that cleavage is a predominant fracture mechanism, while ductile samples develop circumferential rupture along the sample-punch contact line [3,30]. Further evidence of hybrid fracture behaviour can be found at higher magnification observations, as dimples and cleavage planes occur simultaneously in the fracture zone (Fig. 16b).

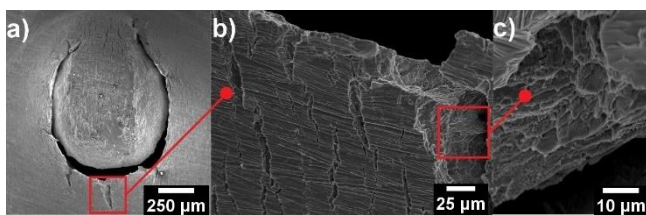


Fig. 16. SEM images of broken small punch 14Cr ODS steel specimen (details in text). SEM, scanning electron microscope; ODS, oxide-dispersion strengthened

4. CONCLUSION

Small punch and tensile tests have been performed at ambient temperature on a 14Cr ferritic ODS steel obtained via a PM route. The finite element model was developed and validated against TEM-sized ($\varnothing 3$ mm, $h = 0.25$ mm) ODS samples, which produced SPT responses comparable with experimental data. Strength parameters were extracted from the both FEM and experimental SPT results using the contemporary methodology and compared with the uniaxial tensile test results. The relations ob-

tained for F_e/h^2 as well as for $F_{max}/(u_m h)$ are within the typical range of values found in the literature. It was proven that different ball diameter used in study has no remarkable influence on deriving yield properties, but produces large scatter in ultimate strength evaluation. Despite the fact that reliable assessment of mechanical properties from the SPT curve may be still regarded as challenging, mainly because of a complex stress state which develops in tested specimens, this study confirms that a great advancement has been made in this field recently.

On the basis of FEM simulations, it can be stated that friction belongs to the key factors affecting the results of the SPT, as it directly affects the shape of force-displacement curve and strain distribution across the sample. Necking of the specimen becomes pronounced at μ values exceeding 0.2. It was found that high friction not only increases the magnitude of peak strain but also moves its location away from the punch pole. This suggests that lubrication of the test parts may be desirable as it reduces the ultimate load and allows the strain to distribute more consistently.

REFERENCES

1. Corwin WR, Rosinski ST, van Walle E. Small Specimen Test Techniques. Philadelphia (PE): Society for Testing and Materials; 1998.
2. Chen H, Hyde TH. Use of multi-step loading small punch test to investigate the ductile-to-brittle transition behaviour of a thermally sprayed CoNiCrAlY coating. Mater Sci Eng A. 2017;680:203-209.
3. Contreras M, Rodríguez C, Belzunce FJ, Betegón C. Use of the small punch test to determine the ductile-to-brittle transition temperature of structural steels. Fatigue Fract Eng Mater Struct. 2008;31(9):727-737.
4. Jaya BN, Alam Z. Small-scale mechanical testing of materials. Curr Sci. 2013;105(8):1073-1099.
5. Bruchhausen M, Holmström S, Simonovski I, Austin T, Lapetite J-M, Ripplinger S, de Haan F. Recent developments in small punch testing: Tensile properties and DBTT. Theor Appl Fract Mech. 2016;86(A):2-10.
6. Oksiuta Z, Lewandowska M, Kurzydłowski KJ. Mechanical properties and thermal stability of nanostructured ODS RAF steels. Mech Mater. 2013;67:15-24.
7. Okuda N, Kasada R, Kimura A. Statistical evaluation of anisotropic fracture behavior of ODS ferritic steels by using small punch tests, J Nucl Mater. 2009;386-388:974-978.
8. Shimomura Y, Spears W. Review of the ITER Project, IEEE Trans Appl Supercond. 2004;14(2):1369-1735.
9. Motojima O. The ITER project construction status. Nucl Fusion. 2015;55(10):104023.
10. Zinkle SJ. Challenges in Developing Materials for Fusion Technology - Past, Present and Future. Fusion Sci Technol. 2017;64(2):65-75.
11. Zhao Q, Ma Z, Yu L, Li H, Liu C, Li C, Liu Y. Tailoring the secondary phases and mechanical properties of ODS steel by heat treatment. J Mater Sci Technol. 2019;35(6):1064-1073.
12. Zhang L, Yu L, Liu Y, Liu C, Li H, Wu J. Influence of Zr addition on the microstructures and mechanical properties of 14Cr ODS steels. Mater Sci Eng A. 2017;695:66-73.
13. Li W, Hao T, Gao R, Wang X, Zhang T, Fang Q, Liu C. The effect of Zr, Ti addition on the particle size and microstructure evolution of yttria nanoparticle in ODS steel. Powder Technol. 2017;319:172-182.
14. Oksiuta Z, Mueller P, Spätig P, Baluc N. Effect of thermo-mechanical treatments on the microstructure and mechanical properties of an ODS ferritic steel. J Nucl Mater. 2011;412(2): 221-226.
15. Oksiuta Z, Oziębło A, Perkowski K, Osuchowski M, Lewandowska M. Influence of HIP pressure on tensile properties of a 14Cr ODS ferritic steel. Fusion Eng Des. 2014;89(2):137-141.
16. Li Y, Shen J, Li F, Yang H, Kano S, Matsukawa Y, Muroga T. Effects of fabrication processing on the microstructure and mechanical prop-

- erties of oxide dispersion strengthening steels. *Mater Sci Eng A*. 2016;654:203-212.
17. Zhao Q, Yu L, Liu Y, Huang Y, Ma Z, Li H, Wu J. Microstructure and tensile properties of a 14Cr ODS ferritic steel. *Mater Sci Eng A*. 2017;680:347-350.
 18. De Sanctis M, Fava A, Lovicu G, Montanari R, Richetta M, Testani C, Varone A. Mechanical Characterization of a Nano-ODS Steel Prepared by Low-Energy Mechanical Alloying. *Metals*. 2017;7(8): 283.
 19. Murty K, Charit I. *An Introduction to Nuclear Materials: Fundamentals and Applications*. Weinheim (DE): Wiley-VCH; 2013.
 20. Karthik V, Kasiviswanathan KV, Raj B. *Miniaturized Testing of Engineering Materials*. Boca Raton (FL): CRC Press; 2017.
 21. Simonovski I, Holmström S, Bruchhausen M. (2017), Small punch tensile testing of curved specimens. *Int J Mech Sci*. 2017;120: 204-213.
 22. Manahan M, Argon A, Harling O. The development of a miniaturised disk bend test for the determination of postirradiation mechanical properties. *J Nucl Mater*. 1981;104:1545-1550.
 23. Altstadt E, Ge HE, Kuksenko V, Serrano M, Houska M, Lasan M, Bruchhausen M, Lapetite J-M, Dai Y. Critical evaluation of the small punch test as a screening procedure for mechanical properties. *J Nucl Mater*. 2016;472:186-195.
 24. Lucon E, Benzing J, Hrabec N. *Development and Validation of Small Punch Testing at NIST*. Gaithersburg (MD): National Institute of Standards and Technology; 2020. doi: 10.6028/NIST.IR.8303
 25. Yang SS, Ling X, Qian Y, Ma RB. Yield Strength Analysis by Small Punch Test Using Inverse Finite Element Method. *Procedia Eng*. 2015;130:1039-1045.
 26. Moreno MF, Bertolino G, Yawny A. The significance of specimen displacement definition on the mechanical properties derived from Small Punch Test. *Mater Des*. 2016;95, 623–631.
 27. Sánchez-Ávila D, Orozco-Caballero A, Martínez E, Portolés L, Barea R, Carreño F. High-accuracy compliance correction for nonlinear mechanical testing: Improving Small Punch Test characterization. *Nucl Mater Energy*. 2021;26:100914.
 28. Campitelli EN, Spätig P, Bonadé R, Hoffelner W, Victoria M. Assessment of the constitutive properties from small ball punch test: experiment and modelling. *J Nucl Mater*. 2004;335(3):366–378.
 29. Kalidindi SR, Abusafieh A, El-Danaf E. Accurate characterization of machine compliance for simple compression testing. *Exp Mech*. 1997;37(2):210–215.
 30. García TE, Rodríguez C, Belzunce FJ, Suárez C. Estimation of the mechanical properties of metallic materials by means of the small punch test. *J Alloys Compd*. 2014;582:708–717.
 31. Mao X, Takahashi H. Development of a further-miniaturized specimen of 3 mm diameter for tem disk (\varnothing 3 mm) small punch tests. *J Nucl Mater*. 1987;150(1):42–52.
 32. Prakash RV, Arunkumar S. Influence of Friction on the Response of Small Punch Test. *Trans Indian Inst Met*. 2016;69(2):617-622.
 33. Haroush S, Priel E, Moreno D, Busiba A, Silverman I, Turgeman A, Gelbstein Y. Evaluation of the mechanical properties of SS-316L thin foils by small punch testing and finite element analysis. *Mater Des*. 2015;83:75-84.

Acknowledgements: This work is supported by the Ministry of Science and Higher Education of Poland under research project No. WI/WM-IIM/3/2022.

Krzysztof Nowik:  <https://orcid.org/0000-0003-3523-9786>

Zbigniew Oksiuta:  <https://orcid.org/0000-0002-8719-157X>

SIMULATION EVALUATION OF THE INFLUENCE OF SELECTED GEOMETRIC PARAMETERS ON THE OPERATION OF THE PNEUMATIC BRAKING SYSTEM OF A TRAILER WITH A DIFFERENTIAL VALVE

Dariusz SZPICA* , Marcin KISIEL* , Jarosław CZABAN* 

*Faculty of Mechanical Engineering, Białystok University of Technology,
ul. 45C Wiejska, 15-351 Białystok, Poland

d.szpica@pb.edu.pl, m.kisiel@windowslive.com, j.czaban@pb.edu.pl

received 10 April 2022, revised 9 June 2022, accepted 10 June 2022

Abstract: This article presents simulation models of trailer air brake systems in configurations without a valve and with a differential valve, thus demonstrating the rationale for using a valve to improve system performance. Simplified mathematical models using the lumped method for systems without and with a differential valve are presented. The proposed valve can have two states of operation depending on the configuration of relevant parameters. These parameters can include the length of the control pipe, the throughput between chambers in the control part of the valve and the forcing rise time. Based on the calculations, it was found that the differential valve with large control pipe lengths can reduce the response time of the actuator by 42.77% relative to the system without the valve. In the case of transition of the valve to the tracking action, this time increases only by 9.93%. A force rise time of 0.5 s causes the transition of the valve from the accelerating action to the tracking action, with 9.23% delay relative to the system without a valve. The calculations can be used in the preliminary assessment of the speed of operation of pneumatic braking systems and in the formulation of guidelines for the construction of a prototypical differential valve. In conclusion, it is suggested to use a mechatronic system enabling smooth adjustment of the flow rate between chambers of the control system of the differential valve.

Key words: mechanical engineering, air braking system, differential valve, simulation

1. INTRODUCTION

Modern truck tractors, farm tractors and trains are equipped with air brake systems that control the performance of brakes in trailers, semi-trailers, farm machinery and railroad cars. The brake control units allow smooth operation of the braking system in a strictly predictable and controlled manner. This makes it possible to achieve the required braking efficiency and the response time of actuators (pneumatic actuators) in response to a stimulus such as pressing the brake pedal by the driver and the operation of the main brake control valve [1]. Pneumatic braking systems of vehicles are subjected to high requirements laid down in UNECE Regulation No. 13 [2]. Considering the increasing overall dimensions of vehicle assemblies with pneumatically actuated brakes and taking into account the larger distances between pressure tanks and actuators [3], it becomes necessary to apply an intermediate component whose purpose is to increase the rate of application of the trailer's brakes and to stabilise the supply pressure to the actuators of the braking system.

The intermediate elements in the pneumatic braking systems of towed assemblies are valves of various types. These may be relay valves [4–6] that use additional air tanks located close to actuators in the form of pneumatic actuators. The use of relay valves in the construction of the system makes it possible to shorten the system's response time to an excitation and to increase the braking force. These valves can only perform a specific function without the possibility of a free transition from a proportional action to an accelerating action depending on the nature of the excitation. Therefore, the concept of using

differential valves has emerged [7–9]. The assumptions of the control theory state that a differential member in the control system influences the amplification of the output signal, which, when applied in a braking system, will positively influence the operation and response time of the system. The differential control systems operate in two ranges: in transient states, which occur in real control systems, they include an accelerating action, whereas in steady states, in which there are no changes in the output signal, the differential member maintains a tracking action [10]. There are also concepts of combination valves [11], purely pneumatic or electropneumatic [12].

The flow process is characterised by high complexity. It can be described by differential equations for the three-dimensional space using the Reynolds-averaged Navier–Stokes (RANS) method [13,14]. Dedicated software, such as KIVA, Ansys Fluent and others [15–18], is usually used to solve this problem. It is also possible, assuming certain simplifications, to reduce the space to a finite-dimensional and time-domain model of a physical system. The partial differential equations can be replaced by ordinary differential equations with a finite number of parameters. The discretisation process itself can indicate the possibility of describing the state in specific spaces, which are, for example, concentrated volumes.

Computer simulation makes it possible to graphically represent the time courses of pressure variations in the brake actuator chambers and to determine the characteristics of the pneumatic system components based on a mathematical model [19]. The realisation of the mathematical model is possible by discretizing the components, such as the lumped method [5,8,9].

Simulations using the lumped method can apply to relay valves [6], differential valves [9], or modified relay valves [1].

In a previous study [11], the differential equations formulated for various components of a dual brake valve (DBV), such as the main piston, main valve, relay piston and relay valve, were presented. The model was implemented in MATLAB/Simulink to capture the dynamic pressure characteristics of the DBV. Additionally, a mathematical model of the DBV was created in Amesim to verify the proposed approach.

The subject of a number of studies is the computational evaluation of the performance of an air braking system. Braking time delay is indicated as the main drawback of air braking systems, leading to dangerous driving situations resulting from insufficient system performance. In a previous study [12], the structure of a semitrailer tractor air brake system was optimised by adding a shuttle valve and a two-position, three-port solenoid valve between the control pipe and the charging pipe downstream of the semitrailer control valve. The simulation results showed significant improvements in braking time, stopping distance, longitudinal kinetic energy, transverse kinetic energy and phase plane. An experimental study [20] was concerned with a comprehensive evaluation of the performance of the electropneumatic braking system compared to that of the conventional pneumatic braking system. The experimental research indicated the advantage of the system with the electric part over the classic system. The efficiency of the systems, their costs and the degree of development were analysed.

In addition to road vehicles, simulations also apply to trains and railcars. In another study [21], different computer simulation scenarios were considered to study the effect of braking forces on the longitudinal dynamics of a train under different braking modes. A mathematical model of the pneumatic system and the control unit of the wagon was developed. In a study [22], fluid continuity and momentum equations were used to develop air flow equations. Using the finite element method, a braking model was obtained to account for the effect of air flow in long train pipes, as well as the effect of leakage and flow in branch pipes.

This study is an extension of another study [9], in which only the usefulness of using a differential valve in the pneumatic braking system of road trains was indicated. This study additionally includes a systematised model description along with precisely specified technical data and conditions necessary to initiate the simulation. Multivariate adjustments of the significant parameters of two braking systems, that is, without and with a differential valve, allowed to indicate the differences in the pressure courses in the selected volumes of the concentrated systems and to develop conclusions. Conclusions drawn from the analyses will allow for the evaluation of the feasibility of a differential valve in the trailer braking system. Additionally, an important issue remains whether it was necessary to use mechatronic systems which are capable of correcting, on an ongoing basis, the course of the braking process.

The structure of this article is as follows. The introduction to the mathematical modelling of the pneumatic braking systems is described in Section 2, followed by the structure of the analysed braking systems in Section 3 and their technical data and the conditions necessary to run the simulations in Section 4. The simulation results at variable transmission pipe lengths, throughputs between the chambers of the differential valve and control pressure rise times are described in Section 5. The last section presents the conclusions.

2. MATHEMATICAL MODELLING

The study uses the lumped method [8], which discretises a pneumatic system into basic members referred to as volume (V) and resistance (R). Combining the individual members V-R-V-...-R-V together allows the construction of pneumatic systems [4,23]. In developing the mathematical description of the basic components of the lumped method, the following simplifications were adopted:

- Air was treated as a thermodynamically ideal gas, being viscous and compressible.
- Isentropic flow in the adiabatic envelope took place without internal friction and without heat exchange with the surroundings.
- The state of the air was constant in each concentrated volume and depended only on time.
- The concentrated volumes were constant [8].
- The temperature during the process was constant [24].
- The connections of the individual system components were perfectly tight.
- Flow-restricting elements open and close gradually;
- The flow coefficient does not change during the transition process.

Fig. 1 shows a schematic diagram demonstrating the essence of discretisation of pneumatic system components in the lumped method.

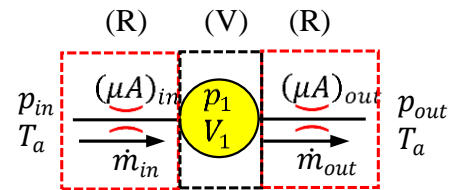


Fig. 1. Diagrams describing the equilibrium state of a concentrated volume (lumped method): p_{in} , p_1 , p_{out} – absolute inlet, in concentrated volume, outlet pressure; T_a – absolute temperature of the air; V_1 – total volume in concentrated volume; $(\mu A)_{in}$ – inlet throughputs (conductance); $(\mu A)_{out}$ – outlet throughputs (conductance); \dot{m}_{in} – inlet air mass flow; \dot{m}_{out} – outlet air mass flow; (V) – volume; (R) – resistance

Based on Fig. 1, the pressure change in the concentrated volume (V) using mass flux balance is described by relation (1).

$$\frac{dp_1}{dt} = \frac{\kappa R_g T_a}{V_1} (\dot{m}_{in} - \dot{m}_{out}), \quad (1)$$

where $\kappa = 1.4$ is adiabatic exponent and $R_g = 287.05 \text{ J/(kg K)}$ is the gas constant.

The air mass flow rate through the pneumatic drag was based on the Saint-Venant–Wantzel relation in the generalised form (Eqs (2) and (3)).

$$\dot{m}_{in} = (\mu A)_{in} \frac{p_{in}}{\sqrt{R_g T_a}} \psi_{\max} \psi(\sigma), \quad (2)$$

$$\dot{m}_{out} = (\mu A)_{out} \frac{p_1}{\sqrt{R_g T_a}} \psi_{\max} \psi(\sigma), \quad (3)$$

where ψ_{\max} is the maximum value of the Saint-Venant–Wantzel function and $\psi(\sigma)$ is the dimensionless flow function.

The maximum value of the Saint-Venant–Wantzel function for the critical pressure ratio $\sigma^* = 0.528$ [25] was calculated according to Eq. (4).

$$\psi = \sqrt{\left(\frac{2}{\kappa-1}\right)^{\frac{\kappa+1}{\kappa-1}}} = 0.578. \quad (4)$$

The dimensionless flow function was adopted according to Metiyuk–Avtushko [8] Eq. (5):

$$\psi(\sigma) = 1.13 \frac{1-\sigma}{1.13-\sigma}, \quad (5)$$

where $\sigma = \frac{p_{aft}}{p_{bef}}$ and p_{bef} and p_{aft} are the pressures before and after resistance, respectively.

Substituting Eqs (2) and (3) into Eq. (1), we obtained a differential equation describing the pressure change in the concentrated volume according to Fig. 1 (Eq. (6)).

$$\frac{dp_1}{dt} = \frac{\kappa R_g T_a}{V_1} \left((\mu A)_{in} \frac{p_{in}}{\sqrt{R_g T_a}} 0.653 \frac{p_{in}-p}{1.13 p_{in}-p} - (\mu A)_{out} \frac{p}{\sqrt{R_g T_a}} 0.653 \frac{p-p_{out}}{1.13 p-p_{out}} \right). \quad (6)$$

This equation can be used to describe pressure changes in supply reservoirs and fixed chambers of valves, connections or actuators. Flow capacities (μA) determine the flow properties of pneumatic resistors such as nozzles, valves or connections. For pneumatic pipes, the cross-sectional area should be calculated from the pipe diameter, and the value of the flow coefficient should be determined from relation (7).

$$\mu = \frac{\mu_n}{\sqrt{n}}, \quad (7)$$

where $\mu_n = 0.12 \dots 0.28$ (0.35) is the discharge coefficient of a 1-m-long pipe section and n is number of 1-m-length sections in the design pipe.

It has been suggested in a previous study [8] that the flow coefficient for pneumatic pipes can be discretised singularly to elements not exceeding 2.5 m in length. Therefore, this option was adopted in the simulation of this study.

In this way, it is possible to build pneumatic systems using a combination of members (V) and (R). Note that it is possible to connect several members (R) to one member (V).

3. ANALYSED SYSTEMS

Two air brake systems were adopted for comparative analysis: one without a differential valve (Fig. 2a) and the other with a differential valve (Fig. 2b). In the system without a differential valve, the air is accumulated in tank 1 at pressure p_{max} and supplied via pipe 2 to vehicle's brake valve 3. At the moment when valve 3 is actuated (force F appears, which in this case will be represented as a function of p_{imp}), the air will begin to flow through valve 3 to pipe 4a and further to actuator 5. In the simulations, pipe 4a will have different lengths. The concentrated volumes are constant and have been described as (p, V) . In these volumes, the pressure waveforms can be read and analysed. In the system with a differential valve (Fig. 2b), the difference consists in shortening the length of pipe 4a from Fig. 2a by 1 m, thus obtaining pipe 4b (Fig. 2b) and supplementing the missing length with pipes 7 (0.2 m) and 10 (0.8 m).

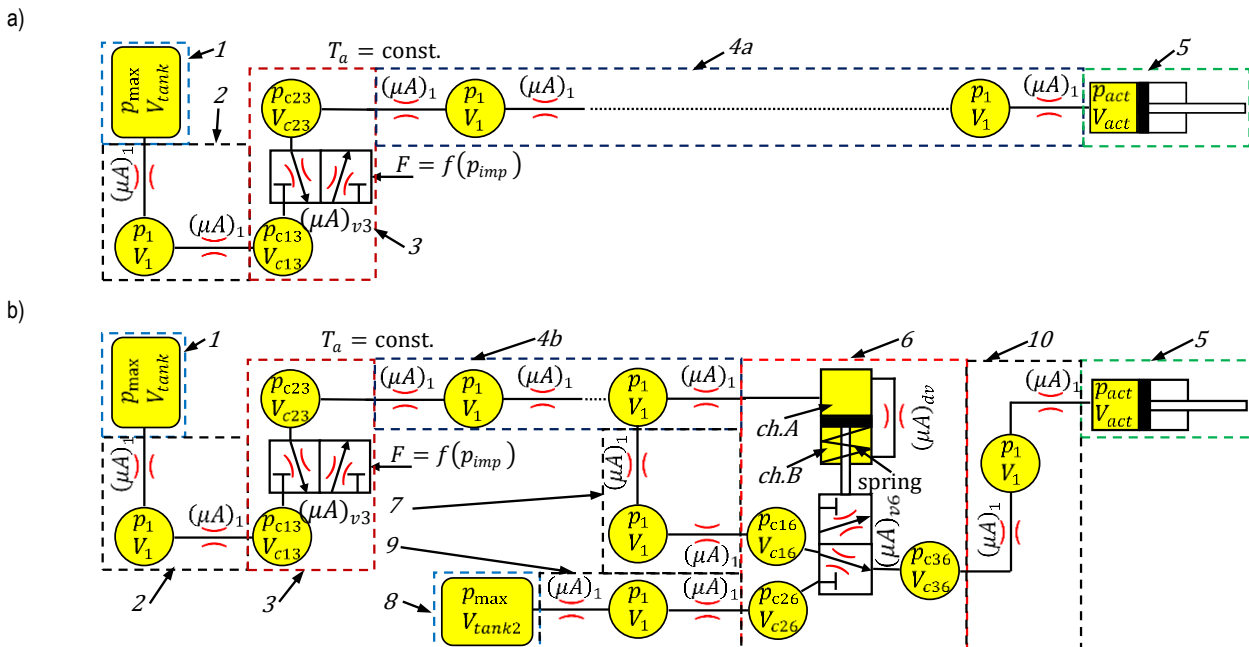


Fig. 2. Diagrams of the analysed braking systems: a – without a differential valve; b – with a differential valve; 1 and 8 – tank; 2, 4, 7, 9 and 10 – pipes; 3 – vehicle brake valve; 6 – trailer differential brake valve; description in the text and Table 1

This is dictated by the use of differential valve 6. Actuation of tractor control valve 3 causes the air to flow to pipes 4a and 7, which, in the initial stage of the differential valve operation, provides tracking action in the valve transmission part (valve bottom). Further air flows through pipe 10 to actuator 5.

The transition from the tracking action of the differential valve to the accelerating action will occur when the pressure in *ch.A* overcomes the force from the spring and the valve transfer section is switched to supply from tank 8 and pipe 9.

The accelerating action will occur until the increase in

pressure in *ch.B* combined with the force from the spring overcomes the pressure in *ch.A*. The acceleration action is mainly determined by the stiffness of the spring and the capacity between chambers *ch.A* and *ch.B*, defined as $(\mu A)_{dv}$. The values of these parameters determine the occurrence of the acceleration action and its duration. In the simulations, the spring stiffness will remain constant, while the throughput between chambers will undergo changes.

4. TECHNICAL DATA AND CONDITIONS NECESSARY TO INITIATE A SIMULATION

For the purpose of the simulation, it is necessary to assume the values of the technical parameters describing the components

of the systems under study. Tab. 1 presents the technical parameters with a breakdown into elements according to Fig. 2. In defining the parameters and initial conditions, data provided in previous studies [5,9,29] were used. The underlined values indicate their variability within specified limits. Due to the comparative nature of the simulation, the volumes of the individual valve chambers and the unit capacities of the pipes were assumed to be the same. In accordance with a previous study [8], the pipes were unit discretised to elements not exceeding 2.5 m in length. The actuator represents a fixed volume resulting from half of its operating stroke.

To initiate the simulation, initial values must be specified in the components of the systems. Tab. 2 shows the initial conditions of the simulation.

Tab. 1. Technical data of system components adopted for calculations (designations according to Figs. 2a and b)

No.	Parameter and volume	
1	$V = 40 \times 10^{-3} \text{ m}^3; T_a = 293.15 \text{ K}$	
2	$d = 13 \times 10^{-3} \text{ m}; A = 1.327 \times 10^{-4} \text{ m}^2; \mu_n = 0.2; l = 0.5 \text{ m}; n = 1; V = 66.37 \times 10^{-6} \text{ m}^3; V_1 = 66.37 \times 10^{-6} \text{ m}^3; T_a = 293.15 \text{ K}$	
3	$V_{c12} = V_{c23} = 50 \times 10^{-6} \text{ m}^3; (\mu A)_{v3} = 5 \times 10^{-4} \text{ m}^2; T_a = 293.15 \text{ K}$	
4	$d = 13 \times 10^{-3} \text{ m}; A = 1.327 \times 10^{-4} \text{ m}^2; \mu_n = 0.2; T_a = 293.15 \text{ K}$	
	<p><u>Fig. 1a – variants without a differential valve:</u></p> <p>(5m): $l = 5 \text{ m}; n = 2; V = 663.66 \times 10^{-6} \text{ m}^3; V_1 = 331.83 \times 10^{-6} \text{ m}^3$ (10m): $l = 10 \text{ m}; n = 4; V = 1.3273 \times 10^{-3} \text{ m}^3; V_1 = 331.83 \times 10^{-6} \text{ m}^3$ (15m): $l = 15 \text{ m}; n = 6; V = 1.9910 \times 10^{-3} \text{ m}^3; V_1 = 331.83 \times 10^{-6} \text{ m}^3$ (20m): $l = 20 \text{ m}; n = 8; V = 2.6546 \times 10^{-3} \text{ m}^3; V_1 = 331.83 \times 10^{-6} \text{ m}^3$</p>	<p><u>Fig. 1b – variants with a differential valve:</u></p> <p>(5m): $l = 4 \text{ m}; n = 2; V = 530.93 \times 10^{-6} \text{ m}^3; V_1 = 256.45 \times 10^{-6} \text{ m}^3$ (10m): $l = 9 \text{ m}; n = 4; V = 1.1946 \times 10^{-6} \text{ m}^3; V_1 = 298.65 \times 10^{-6} \text{ m}^3$ (15m): $l = 14 \text{ m}; n = 6; V = 1.8583 \times 10^{-6} \text{ m}^3; V_1 = 309.71 \times 10^{-6} \text{ m}^3$ (20m): $l = 19 \text{ m}; n = 8; V = 2.5249 \times 10^{-6} \text{ m}^3; V_1 = 315.24 \times 10^{-6} \text{ m}^3$</p>
5	$V = 850 \times 10^{-6} \text{ m}^3; T_a = 293.15 \text{ K}$	
6	$V_{ch.A} = V_{ch.B} = V_{c16} = V_{c26} = V_{c36} = 50 \times 10^{-6} \text{ m}^3; (\mu A)_{dv} = (3.5...12.5) \times 10^{-7} \text{ m}^2; (\mu A)_{v6} = 7.5 \times 10^{-4} \text{ m}^2; T_a = 293.15 \text{ K}; d_p = 65 \times 10^{-3} \text{ m}; d_{pt} = 10 \times 10^{-3} \text{ m}; k = 0.7 \times 10^5 \text{ N/m}$	
7	$d = 13 \times 10^{-3} \text{ m}; A = 1.327 \times 10^{-4} \text{ m}^2; \mu_n = 0.2; l = 0.2 \text{ m}; n = 1; V = 26.55 \times 10^{-6} \text{ m}^3; V_1 = 26.55 \times 10^{-6} \text{ m}^3; T_a = 293.15 \text{ K}$	
8	$V = 40 \times 10^{-3} \text{ m}^3; T_a = 293.15 \text{ K}$	
9	$d = 13 \times 10^{-3} \text{ m}; A = 1.327 \times 10^{-4} \text{ m}^2; \mu_n = 0.2; l = 1 \text{ m}; n = 1; V = 132.73 \times 10^{-6} \text{ m}^3; V_1 = 132.73 \times 10^{-6} \text{ m}^3; T_a = 293.15 \text{ K}$	
10	$d = 13 \times 10^{-3} \text{ m}; A = 1.327 \times 10^{-4} \text{ m}^2; \mu_n = 0.2; l = 0.8 \text{ m}; n = 1; V = 106.18 \times 10^{-6} \text{ m}^3; V_1 = 106.18 \times 10^{-6} \text{ m}^3; T_a = 293.15 \text{ K}$	

Glossary: d – pipe diameter; A – pipe cross-sectional area; μ_{ij} – pipe loss factor of a single section; l – pipe length; n – pipe number of components R - V ; V – tank and pipe total volume; V_1 – pipe component volume; $V_{c13}, V_{c23}, V_{c16}, V_{c26}, V_{c36}, V_{ch.A}$ and $V_{ch.B}$ – chamber volume; V_{tank} and V_{tank2} – actuator volume; T_a – air temperature; d_p – valve piston diameter; d_{pt} – valve piston rod diameter; k – spring stiffness.

Tab. 2. Initial conditions at $t = 0 \text{ s}$ (according to Fig. 2)

Parameter	Value
Pressure in tank 1 and 8, pipe 2 and 9, chamber V_{c13} and V_{c26}	$8 \times 10^5 \text{ Pa}$
Pressure in pipe 4a / 4b, 7 and 10, chamber $V_{c23}, V_{c16}, V_{c36}, V_{ch.A}, V_{ch.B}$, actuator V_{act}	$1 \times 10^5 \text{ Pa}$
Pressure of the forcing pulse p_{imp} in valve 3	$1 \times 10^5 \text{ Pa}$
Setting valves 3 and 6	As shown in Fig. 2

The pressure change in each focused volume according to Fig. 2 was created according to Eq. (6). Due to the extensiveness of the description, it will not be presented in the article.

In both analysed systems (without and with a differential valve) at the start of the simulation, valve 3 (Figs. 2a and b) opens according to the assumed rising time of the control pressure to the maximum value. The rising time is described by t_{tfp} , whose value characterises the braking mode – rapid or slow. The change in control pressure is given in the following Eq. (8):

$$\frac{dp_{imp}}{dt} = (p_{max} - p_a) \frac{t}{t_{tfp}} + p_a \text{ for } 0 \leq t < t_{tfp}. \quad (8)$$

A change in pressure p_{imp} will result in a proportional change in the throughput $(\mu A)_{v3}$ and a gradual opening of valve 3 (Fig. 2).

In a system with a differential valve (Fig. 2b), the throughput in the transferring part (at the bottom of valve 6) defined as $(\mu A)_{v6}$ will depend on the arrangement of forces in the control part (at the top of the valve). Depending on the overdrive of the transfer part, actuator 5 will be able to be supplied from pipes 4 and 7 (tracking action) or from tank 8 and pipe 9 (accelerating action).

The tracking action of valve 6 will occur when, in the control part, the force system has the following form (9):

$$p_{ch.A} F_{p_{ch.A}} \eta \leq p_{ch.B} F_{p_{ch.B}} \eta + F_s. \quad (9)$$

Then the bandwidth in the transferring part will reach the maximum value, and the power will come from wire 7 according to Eq. (10).

$$(\mu A)_{v6} = (\mu A)_{v6max} \text{ and } p = p_{c16}. \quad (10)$$

With the accelerating action of valve 6 in the control section, the force system will be of the following form (11):

$$p_{ch.A}F_{p_{ch.A}}\eta > p_{ch.B}F_{p_{ch.B}}\eta + F_s. \quad (11)$$

The throughput in the transfer section will also reach the maximum value, but the supply will come from tank 8 and pipe 9 according to Eq. (12).

$$(\mu A)_{v6} = (\mu A)_{v6max} \text{ and } p = p_{c26}. \quad (12)$$

where $F_{ch.A}$ is the cross-sectional area of piston from chamber A; $F_{ch.B}$ is the cross-sectional area of the piston from chamber $ch.B$; $\eta = 0.95$ is the coefficient of friction forces in the differential valve; F_s is the force from spring; and p is the input pressure in valve 6.

The instantaneous difference in pressure values $p_{ch.A}$ and $p_{ch.B}$ is responsible for the throughput between these chambers $(\mu A)_{dv}$. This mainly determines the occurrence or absence of the acceleration effect.

5. RESULTS OF THE SIMULATION

The differential equations describing the pressure changes in each control volume based on Eq. (6) were solved numerically by using the implicit trapezoid method combined with backward differentiation (min. step 1×10^{-6} s) in MATLAB/Simulink software [26]. This software is characterised by the ease of implementation of the adopted empirical models and the possibility of replicating the repeating subsystems using masking, as confirmed in studies [27–29].

The use of the differential valve should be assumed to reduce the operation time of the pneumatic system in the vehicle brake valve actuation – actuator relationship. In the initial part, two systems were simulated: one without a differential valve and the other with a differential valve. According to Tab. 1, the variant (20 m) was assumed and the throughput $(\mu A)_{dv} = 3.5 \times 10^{-7}$ m². Assuming an increase in the control pressure p_{imp} during 0.2 s to the maximum value, the pressure waveforms in the selected control volumes were obtained.

The system (20 m) without a differential valve is able to reach a pressure of $0.75 p_{max}$ in the control volume of the actuator in 1.218 s (Fig. 3).

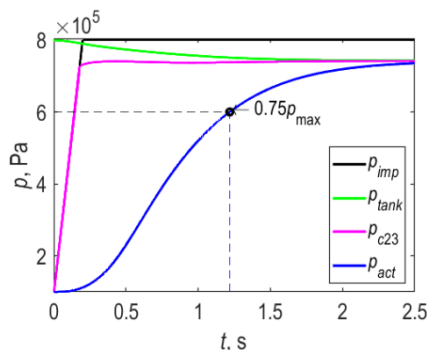


Fig. 3. Pressure curves in selected control volumes for the system without a differential valve and for the pipe length variant (20 m) at a control pressure rise time of 0.2 s; indexes: *imp* – control impulse; *tank* – tank; *c23* – chamber 23; *act* – actuator

By contrast, the system (20 m) with the differential valve achieves this pressure in 0.697 s (Fig. 4). The use of the

differential valve resulted in a 42.77% reduction response time. The pressure waveform in the actuator control volume p_{act} (Fig. 4) shows the essence of the use of the differential valve. Up to point A, the system with the differential valve exhibits a tracking action, and a slight delay in this range relative to the system without a valve (Fig. 5) is due to the flow through the transfer system of the differential valve. At point A (Fig. 4), the pressure in the chamber $ch.A$ of the control portion of the differential valve overcomes the force from the spring (Fig. 2) and, as a result, overrides the supply from tank 8.

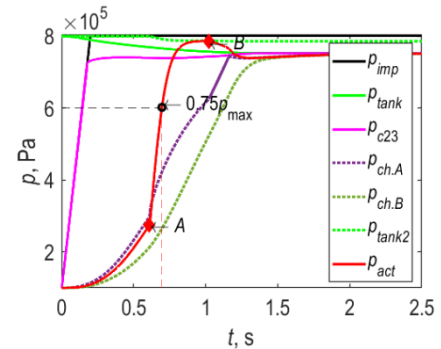


Fig. 4. Pressure curves in selected control volumes for the system with a differential valve and for the pipe length variant (20 m) at a control pressure rise time of 0.2 s and throughput $(\mu A)_{dv} = 3.5 \times 10^{-7}$ m²; indexes: *imp* – control impulse; *tank* and *tank2* – tank; *c23*, *ch.A* and *ch.B* – chamber 23; *act* – actuator; p. A – opening of the valve; p. B – closing of the differential valve

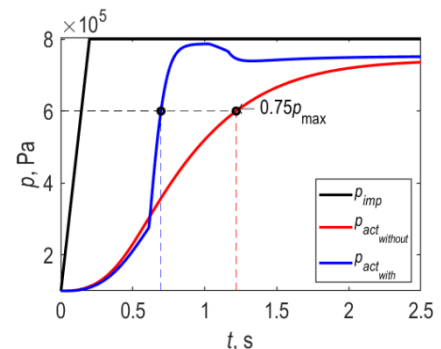


Fig. 5. Pressure curves in selected control volumes for the system without and with a differential valve and for the pipe length variant (20 m) at a control pressure rise time of 0.2 s and throughput $(\mu A)_{dv} = 3.5 \times 10^{-7}$ m²; indexes: *imp* – control impulse; *act* – actuator

The action ceases to be tracked, and because of the proximity of tank 8, the pressure in the actuator p_{act} increases rapidly until it equals the pressure p_{tank2} (Fig. 4). The throughput $(\mu A)_{dv}$ allows the pressures in the chambers $ch.A$ and $ch.B$ to equalise and, by the additional action of the spring force, return to the tracking action (point B). Furthermore, the pressure in the actuator will tend to equalise with the pressure p_{tank} . The mode of operation of the combined chambers $ch.A$ and $ch.B$ (Fig. 2) in the differential valve differs from that in the relay valve [4,6].

Next, simulations were performed for all variants of wire length 4 and throughputs $(\mu A)_{dv}$ included in Tab. 1. The throughputs $(\mu A)_{dv}$ were graded in steps of 0.5×10^{-7} m². As before, the control pressure increment p_{imp} was assumed at 0.2 s to a maximum value.

Calculations showed that for $(\mu A)_{dv}$ throughputs of (4.0, 5.0, 7.5 and 12.5) $\times 10^{-7}$ m², respectively, successive variants of 4 (20,

15, 10 and 5) m pipe length cease to show an accelerating effect in the variant with the differential valve (Tab. 3 and Fig. 6). At

$(\mu A)_{dv} = 3.5 \times 10^{-7} \text{ m}^2$, all length variants exhibit an accelerating effect with respect to the system without the differential valve.

Tab. 3. Comparison of the times for reaching $0.75 p_{max}$ at different lengths of pipe 4 (Fig. 2)

Variant pipe length (m)	Without valve (s)	With differential valve (s) at throughput $(\mu A)_{dv} \times 10^{-7} \text{ m}^2$									
		3.5	4.0	4.5	5.0	5.5	6.0	6.5	7.0	7.5	
5	<u>0.360</u>	0.230	0.232	0.235	0.237	0.239	0.242	0.244	0.246	0.250	
10	<u>0.596</u>	0.342	0.347	0.354	0.363	0.370	0.379	0.394	0.414	<u>0.676</u>	
15	<u>0.880</u>	0.482	0.501	0.526	<u>0.986</u>	0.979	0.989	0.988	0.987	0.978	
20	<u>1.218</u>	0.697	<u>1.339</u>	1.337	1.342	1.338	1.337	1.338	1.348	1.337	
Variant pipe length (m)		With differential valve (s) at throughput $(\mu A)_{dv} \times 10^{-7} \text{ m}^2$									
		8.0	8.5	9.0	9.5	10.0	10.5	11.0	11.5	12.0	12.5
5		0.252	0.255	0.259	0.263	0.267	0.272	0.275	0.282	0.295	<u>0.410</u>
10		0.677	0.675	0.677	0.674	0.676	0.672	0.672	0.678	0.672	0.678
15		0.979	0.988	0.982	0.988	0.981	0.987	0.983	0.977	0.978	0.984
20		1.338	1.339	1.346	1.343	1.334	1.343	1.335	1.338	1.340	1.339

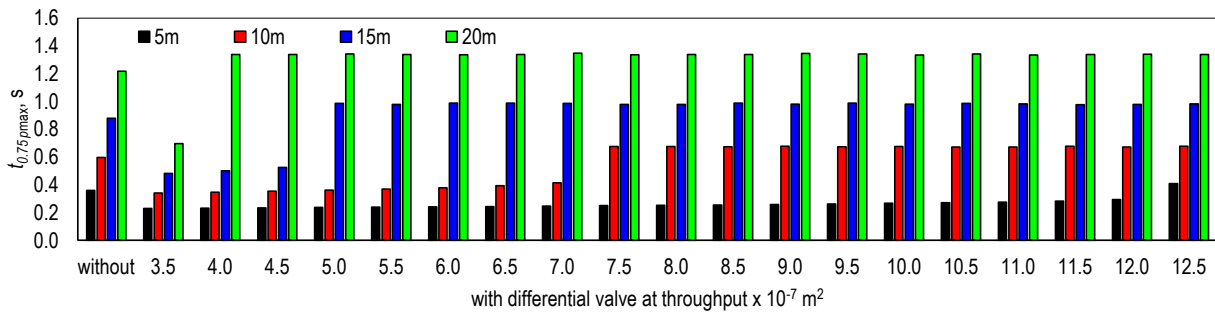


Fig. 6. Values of the times for reaching $0.75 p_{max}$ at different lengths of pipe 4 (Fig. 2)

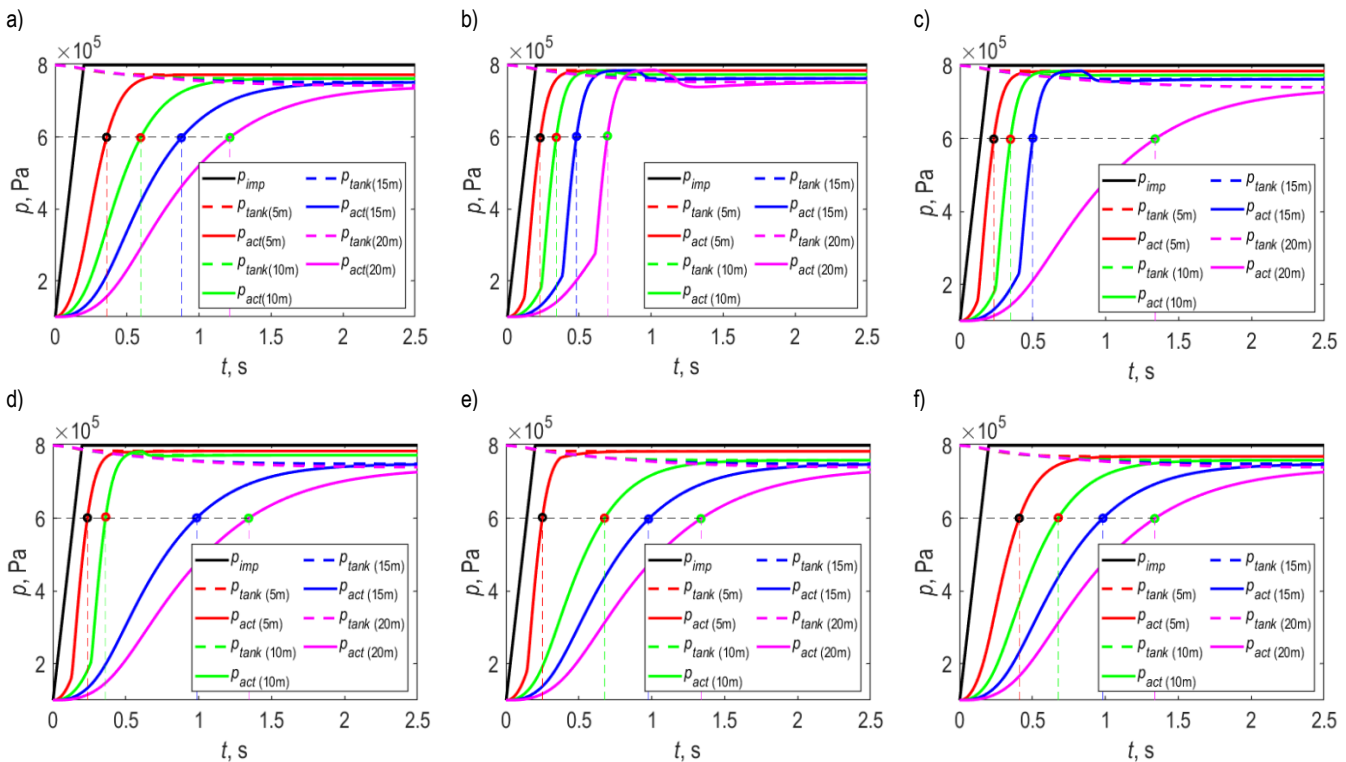


Fig. 7. Pressure curves in selected control volumes at a control pressure rise time of 0.2 s and at different lengths of pipe 4 (according to Tab. 1): (a) system without a differential valve, (b–f) system with a differential valve at throughputs $(\mu A)_{dv} \times 10^{-7} \text{ m}^2$: b - 3.5; c - 4; d - 5; e - 7.5; f - 12.5; indexes: *imp* – control impulse; *tank* – tank, *act* – actuator; (5, ..., 20) m – pipe length variants

In order to graphically represent the disappearance of the accelerating action of the differential valve, Fig. 7 shows the pressure waveforms in selected control volumes of the tested systems without and with the valve. For the differential valve, the throughputs $(\mu A)_{dv}$ were $(3.5, 4.0, 5.0, 7.5 \text{ and } 12.5) \times 10^{-7} \text{ m}^2$, control pipe lengths 4 (5, 10, 15 and 20) m, respectively.

Taking the throughput step $(\mu A)_{dv}$ preceding the decay of the accelerating action of the differential valve as a reference point, differences in the reduction of the actuator response time were found between the variants.

In the variant of pipe length 4 (20 m) and throughput $(\mu A)_{dv} = 3.5 \times 10^{-7} \text{ m}^2$, the differential valve caused a 42.77% reduction in the time to reach a pressure of $0.75 p_{max}$ in the actuator control volume. The variant (15 m) and $(\mu A)_{dv} = 4.5 \times 10^{-7} \text{ m}^2$ reduced this time by 40.23%. By contrast, the variant (10 m) and $(\mu A)_{dv} = 7 \times 10^{-7} \text{ m}^2$ showed a time reduction of 30.54%. The variant with the shortest wire length of 4 (5 m) and $(\mu A)_{dv} = 12 \times 10^{-7} \text{ m}^2$ showed the least reduction in response time of 18.01%.

This demonstrated the validity of the use of differential valves in braking systems with large lengths of control pipe 4 (Fig. 2), as mentioned in the literature [1,8,9].

At the points of deceleration and tracking action, deceleration in the indicated cases was 13.89, 13.42, 12.04 and 9.93%, respectively, with the lowest value recorded for the variant with the longest pipe 4.

In the last stage of the simulation, the effect of the control pressure rise time (p_{imp}) to the maximum value on the actuator response time was evaluated. The differential valve should guarantee its acceleration action at short override times of the vehicle brake valve. Such a situation replicates sudden braking, and then there is a need to brake the trailer as quickly as possible to prevent the trailer from “dropping” behind the towing vehicle [2,30].

For the analysis, systems without and with a differential valve in the variant (20 m) with a capacity of $(\mu A)_{dv} = 3.5 \times 10^{-7} \text{ m}^2$ were adopted. The times of control pressure rise p_{imp} to a maximum value were taken as 0.2, 0.3, 0.4 and 0.5 s.

Comparing the times t_{tfp} necessary to reach $0.75 p_{max}$ in the control volume of the actuator (Tab. 4, Fig. 8), it is shown that the tracking action of the system with the differential valve is achieved at $t_{tfo} = 0.5 \text{ s}$, where the actuator response time increases by 9.23% relative to the system without the differential valve.

Tab. 4. Comparison of the times for reaching $0.75 p_{max}$ at different control pressure rise times

Variant	Time to full pressure t_{tfp} , s			
	0.2	0.3	0.4	0.5
Without a differential valve	1.218	1.255	1.293	1.331
With a differential valve	0.697	0.756	0.841	1.454

Below this value, an accelerating effect becomes apparent. At $t_{tfo} = 0.2 \text{ s}$, the system with an acceleration valve reduces the response time of the actuator by 42.77%. On the other hand, at $t_{tfo} = 0.3 \text{ s}$, the time reduction is slightly smaller at 39.77%. In the next case, at $t_{tfo} = 0.4 \text{ s}$, the reduction is 34.99%.

The differences in the times to reach $0.75 p_{max}$ in the control volume of the actuator (Fig. 9) are due to the time that must elapse before the transfer section of the differential valve is

switched to supply from tank 8 (Fig. 2). This shows the increasingly later switching of the differential valve depending on the value of t_{tfo} .

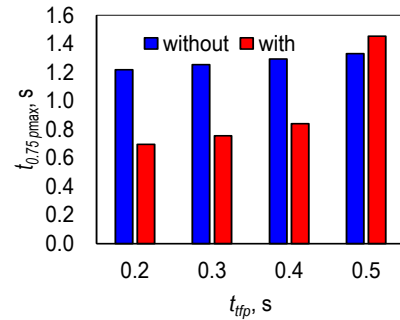


Fig. 8. Values of the times for reaching $0.75 p_{max}$ at different control pressure rise times

In this way, the possibility of a smooth transition of the system with the differential valve from an accelerating action to a tracking action with a small delay in relation to the system without the differential valve is demonstrated.

The choice of conductor parameters and the volume of the concentrated chambers of the analysed system allows to approximate the tracking performance of the system with a differential valve to the system without a valve. An important feature is the throughput $(\mu A)_{dv}$ and its influence on the valve performance when confronted with time t_{tfo} .

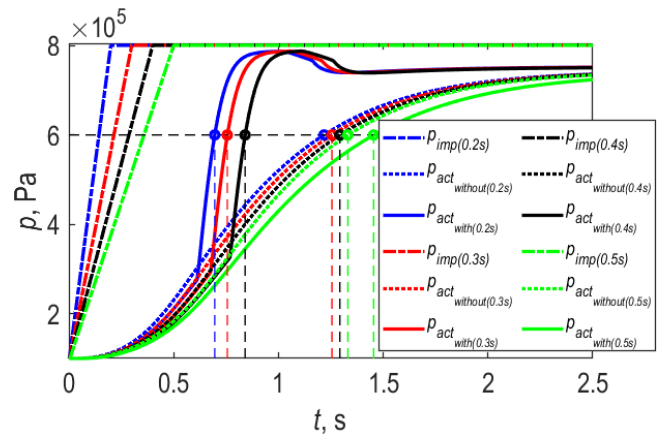


Fig. 9. Pressure curves in selected control volumes for the systems without and with a differential valve for the pipe length variant (20 m) at different control pressure rise times and throughput $(\mu A)_{dv} 3.5 \times 10^{-7} \text{ m}^2$: a - $t_{tfp} = 0.2 \text{ s}$; b - $t_{tfp} = 0.3 \text{ s}$; a - $t_{tfp} = 0.4 \text{ s}$; a - $t_{tfp} = 0.5 \text{ s}$; indexes: *imp* - control impulse; *act* - actuator

It should be emphasised that the mathematical model presented in the article is simplified. It does not include a description of the variable volume of the control or actuator chambers and heat transfer. However, as can be judged from the simulation results obtained, it is useful for preliminary estimation of differences in the nature of operation of systems without and with a differential valve. The parameter that is considered important in the course of design and practical implementation of the differential valve is the throughput between the control chambers *ch.A* and *ch.B* defined as $(\mu A)_{dv}$ (Fig. 2). In

calculations, the value of the throughput was assumed constant in the considered variants and configurations of the system. After the simulations, it was found that designing a system enabling smooth regulation of this throughput via a mechatronic system is worth considering.

In the next steps, further work is planned to complete the mathematical model with variable volume chambers and heat transfer. The simulations performed and the analysis of their results are a prelude to the development of a prototypical differential valve. The design of a system enabling smooth adjustment of the flow rate between the valve chambers via a mechatronic system is also considered. In addition to the commonly used valves with electromagnetic actuation [31,32], piezoelectric actuation [33,34] is a certain hope.

The braking system is one of the components of the whole trailer. Considering broader possibilities of using the mathematical model presented in this article, there is a chance to use it to model the movement of a trailer or a tractor-trailer combination similar to the one presented in a previous study [35]. Additionally, the braking system model can be combined with other component models such as shock absorbers, springs, control arms or wheels, to evaluate vehicle handling. By supplementing the model presented in a previous study [36] with the braking system, one can obtain a model of the entire trailer or tractor-trailer combination.

6. CONCLUSIONS

The simulations presented in the article were intended to demonstrate the purpose of using the differential valve in trailer braking systems. The proposed mathematical model, in spite of its simplifications, turned out to be useful for the preliminary comparative evaluation of the systems adopted without and with a differential valve. Based on the analyses performed, the following conclusions were reached.

1. The application of the differential valve in the braking system in all analysed variants of the control pipe length can result in the reduction of the actuator response time. In the case of a pipe with a length of 20 m and a throughput between the valve chambers of $3.5 \times 10^{-7} \text{ m}^2$, the response time is reduced by 42.77%.
2. The dominant parameter affecting the performance of the differential valve is the throughput between its chambers. The throughput can reduce the response time or, depending on the value, change the valve action from accelerating to tracking. A system with a wire of 20 m length and a $4 \times 10^{-7} \text{ m}^2$ throughput between chambers increases the response time by 9.93% while maintaining the tracking action.
3. The acceleration effect of the differential valve system depends on the course of the forcing pulse. For the rise times of the control pressure to the maximum value below 0.5 s, the acceleration effect was obtained (the maximum at 0.2 s was by 42.77%). At a rise time of 0.5 s, the action changed to tracking with 9.23% retardation with respect to the system without a valve.
4. Based on the calculations and analyses performed, it is suggested that a mechatronic system could be used to enable smooth adjustment of the flow rate between the chambers of the differential valve control system. This type of system could adjust the differential valve to the characteristics of the trailer.

REFERENCES

1. Kamiński Z, Kulikowski K. Determination of the functional and service characteristics of the pneumatic system of an agricultural tractor with mechanical brakes using simulation methods. *Eksplotacja i Niezawodność - Maintenance and Reliability*. 2015;17(3):355–64.
2. Regulation No 13 of the Economic Commission for Europe of the United Nations (UN/ECE) — Uniform provisions concerning the approval of vehicles of categories M, N and O with regard to braking [Internet]. Official Journal of the European Union. 2015 [cited 2022 Apr 3]. Available from: <http://data.europa.eu/eli/reg/2016/194/oj>
3. Krichel S V, Sawodny O. Dynamic modeling of pneumatic transmission lines in Matlab/Simulink. In: International Conference on Fluid Power and Mechatronics - 17-20 Aug 2011, Beijing, China. Beijing, China: IEEE; 2011. p. 24–9.
4. Kulesza Z, Siemieniako F, Mikołajczyk B. Modelowanie zaworu przekaźnikowo-sterującego. *Pneumatyka*. 2008;1:31–5.
5. Kamiński Z. Mathematical modelling of the trailer brake control valve for simulation of the air brake system of farm tractors equipped with hydraulically actuated brakes. *Eksplotacja i Niezawodność - Maintenance and Reliability*. 2014;16(4):637–43.
6. Kulesza Z, Siemieniako F. Modeling the air brake system equipped with the brake and relay valves. *Zeszyty Naukowe*. 2010;24(96): 5–11.
7. Beater P. *Pneumatic Drives. System Design, Modelling and Control*. Springer; 2007.
8. Miatluk M, Avtuszkó F. *Dinamika pniewmaticsckich i gidrawliceskich privodov avtomobilej*. M. Maszynostrojenije; 1980. 231 p.
9. Szpica D. Modeling of the operation of a pneumatic differential valve increasing the efficiency of pneumatic brake actuation of road trains. In: *Transport Means - Proceedings of the International Conference*. 2018. p. 151–6.
10. Mystkowski A. Zastosowanie zaworów różniczkujących w pneumatycznych układach napędowych. *Pneumatyka*. 2004;3:21–3.
11. Patil JN, Palanivelu S, Jindal AK. Mathematical model of dual brake valve for dynamic characterization. In: *SAE Technical Papers*. SAE International; 2013.
12. Jing Z, He R. Electronic structural improvement and experimental verification of a tractor-semitrailer air brake system. *Proceedings of the Institution of Mechanical Engineers, Part D: Journal of Automobile Engineering*. 2020 Jul 1;234(8):2154–61.
13. Yang Z, Cheng X, Zheng X, Chen H. Reynolds-Averaged Navier-Stokes Equations Describing Turbulent Flow and Heat Transfer Behavior for Supercritical Fluid. *Journal of Thermal Science*. 2021;30(1).
14. Matyushenko AA, Garbaruk A V. Adjustment of the k- ω SST turbulence model for prediction of airfoil characteristics near stall. In: *Journal of Physics: Conference Series*. 2016.
15. Yu W, Yang W, Zhao F. Investigation of internal nozzle flow, spray and combustion characteristics fueled with diesel, gasoline and wide distillation fuel (WDF) based on a piezoelectric injector and a direct injection compression ignition engine. *Applied Thermal Engineering*. 2017;114.
16. Michalcová V, Kotrasová K. The numerical diffusion effect on the cfd simulation accuracy of velocity and temperature field for the application of sustainable architecture methodology. *Sustainability (Switzerland)*. 2020;12(23):10173.
17. Cvetkovic D, Cosic I, Subic A. Improved performance of the electromagnetic fuel injector solenoid actuator using a modelling approach. *International Journal of Applied Electromagnetics and Mechanics*. 2008;
18. Szpica D, Mieczkowski G, Borawski A, Leisis V, Diliunas S, Pilkaite T. The computational fluid dynamics (CFD) analysis of the pressure sensor used in pulse-operated low-pressure gas-phase solenoid valve measurements. *Sensors*. 2021;21(24):8287.
19. Subramanian SC, Darbha S, Rajagopal KR. Modeling the pneumatic subsystem of an s-cam air brake system. *Journal of Dynamic Systems, Measurement and Control, Transactions of the ASME*.

- 2004;126(1):36–46.
20. Kumar EA, Gautam V, Subramanian SC. Performance evaluation of an electro-pneumatic braking system for commercial vehicles. In: ICPCES 2012 - 2012 2nd International Conference on Power, Control and Embedded Systems. 2012.
 21. Afshari A, Specchia S, Shabana AA, Caldwell N. A train air brake force model: Car control unit and numerical results. Proceedings of the Institution of Mechanical Engineers, Part F: Journal of Rail and Rapid Transit. 2013;227(1):38–55.
 22. Aboubakr AK, Volpi M, Shabana AA, Cheli F, Melzi S. Implementation of electronically controlled pneumatic brake formulation in longitudinal train dynamics algorithms. Proceedings of the Institution of Mechanical Engineers, Part K: Journal of Multi-body Dynamics. 2016;230(4):505–26.
 23. Kamiński Z. A simplified lumped parameter model for pneumatic tubes. Mathematical and Computer Modelling of Dynamical Systems. 2017;23(5):523–35.
 24. Iwaszko J. Wymiana ciepła podczas opróżniania zbiornika. Zeszyty Naukowe Politechniki Łódzkiej, Ciepłotechniczne Maszyny Przepływowe. 1988;93:12–21.
 25. Grymek S, Kiczowski T. Conversion of the sonic conductance C and the critical pressure ratio b into the airflow coefficient μ . Journal of Mechanical Science and Technology. 2005;19(9):1706–10.
 26. Yang WY, Cao W, Chung T-S, Morris J. Applied Numerical Methods Using MATLAB®. Applied Numerical Methods Using MATLAB®. Wiley & Sons; 2020. 1–502 p.
 27. Shamdani AH, Shameki AH, Basharhagh MZ, Aghanajafi S. Modeling and simulation of a diesel engine common rail injector in Matlab/Simulink. In: 14 th Annual (International) Mechanical Engineering Conference – May 2006 Isfahan University of Technology, Isfahan, Iran. 2006. p. 7.
 28. Demarchi A, Farçoni L, Pinto A, Lang R, Romero R, Silva I. Modelling a solenoid's valve movement. In: Lecture Notes in Computer Science (including subseries Lecture Notes in Artificial Intelligence and Lecture Notes in Bioinformatics). 2018.
 29. Kamiński Z. Experimental and numerical studies of mechanical subsystem for simulation of agricultural trailer air braking systems. International Journal of Heavy Vehicle Systems. 2013;20(4):289–311.
 30. Czaban J, Kamiński Z. Diagnosing of the agricultural tractor braking system within approval tests. Eksploatacja i Niezawodność - Maintenance and Reliability. 2012;14(4):319–26.
 31. Hung NB, Lim O, Yoon S. Effects of Structural Parameters on Operating Characteristics of a Solenoid Injector. In: Energy Procedia. 2017. p. 1771 – 1775.
 32. Plavec E, Ladisic I, Vidovic M. The impact of coil winding angle on the force of DC solenoid electromagnetic actuator. Advances in Electrical and Electronic Engineering. 2019;17(3):244–50.
 33. Mieczkowski G, Szpica D, Borawski A, Diliunas S, Pilkaite T, Leisis V. Application of smart materials in the actuation system of a gas injector. Materials. 2021;14(22):6984.
 34. Mieczkowski G. Static electromechanical characteristics of piezoelectric converters with various thickness and length of piezoelectric layers. Acta Mechanica et Automatica. 2019;13(1):30–6.
 35. Liu Y. Modeling abstractions of vehicle suspension systems supporting the rigid body analysis. International Journal of Vehicle Structures and Systems. 2010;2(3–4):117–26.
 36. Liu Y. Constructing equations of motion for a vehicle rigid body model. SAE International Journal of Passenger Cars - Electronic and Electrical Systems. 2009;1(1):1289–97.

This research was financed through subsidy of the Ministry of Science and Higher Education of Poland for the discipline of mechanical engineering at the Faculty of Mechanical Engineering Białystok University of Technology WZ/WM-IIM/4/2020.

Dariusz Szpica:  <https://orcid.org/0000-0002-7813-8291>

Marcin Kisiel:  <https://orcid.org/0000-0002-4576-0447>

Jaroslav Czaban:  <https://orcid.org/0000-0002-0677-7342>

INFLUENCE OF IMPERFECT INTERFACE OF ANISOTROPIC THERMOMAGNETOELECTROELASTIC BIMATERIAL SOLIDS ON INTERACTION OF THIN DEFORMABLE INCLUSIONS

Heorhiy SULYM^{*}, Andrii VASYLYSHYN^{**}, Iaroslav PASTERNAK^{***}

^{*}Bialystok University of Technology, Wiejska Str 45C, 15-351 Bialystok, Poland

^{**}Ivan Franko National University of Lviv, Universytetska Str. 1, 79000 Lviv, Ukraine

^{***}Lesya Ukrainka Volyn National University, Potapova Str 9, 43025 Lutsk, Ukraine

h.sulym@pb.edu.pl, vasylyshyn.c.h@gmail.com, iaroslav.m.pasternak@gmail.com

received 12 March 2022, revised 30 May 2022, accepted 31 May 2022

Abstract: This work studies the problem of thermomagnetoelastic anisotropic bimaterial with imperfect high-temperature conducting coherent interface, whose components contain thin inclusions. Using the extended Stroh formalism and complex variable calculus, the Somigliana-type integral formulae and the corresponding boundary integral equations for the anisotropic thermomagnetoelastic bimaterial with high-temperature conducting coherent interface are obtained. These integral equations are introduced into the modified boundary element approach. The numerical analysis of new problems is held and results are presented for single and multiple inclusions.

Key words: anisotropic bimaterial, thermomagnetoelastic, imperfect interface, high-temperature conducting, thin inclusion

1. INTRODUCTION

Pyroelectric, pyromagnetic and multifield material structures are widely used in modern engineering design, especially in the developed high-tech manufactures, devices of fine mechanics and of innovative character. These structures allow combining and redistributing the energy of four fields of different physical nature (mechanical, thermal, electrical and magnetic), and therefore have great potential for use in instrument and sensor systems, precision positioning devices, energy converters and more.

The development of such bimaterials can be provided by mechanical combination of pyroelectric (ferroelectric) and magnetostrictive (piezomagnetic) materials. As a result, a thin layer appears at the interface, which affects the temperature and stress fields in a structurally inhomogeneous solid. When modelling the effect of this layer, certain boundary conditions of imperfect thermal and magnetoelctromechanical contact of bimaterial components are used. Mainly in the scientific literature [1], [2], there are two types of imperfect thermal conditions of contact of a thin layer with the environment. These are the high- and low-temperature conducting. There are also two types of imperfect mechanical contact conditions, which are the soft and rigid interfaces. In addition, there can be present some other inhomogeneities in the structural materials (e.g. cracks, thin inclusions etc.), which can also be modelled in conditions of imperfect contact, and they should be taken into account. Thus, the development of effective methods for modelling and studying the distribution of thermal, mechanical, electric and magnetic fields in bimaterial deformable solids with an imperfect material interface and internal thin inhomogeneities is an important scientific problem with wide possibilities of practical use.

The study of bimaterial solids with defects is quite widely cov-

ered in the scientific literature. For example, in [13] the authors studied three models of interfacial cracks (electrically perfectly permeable, semi-permeable and impermeable) in piezoelectric materials using the boundary element method. The article [14] presents an analysis of problems for cracks in homogeneous piezoelectrics and at the interface of two different piezoelectric materials; the corresponding explicit analytical solutions are obtained. In [2] author uses specially designed conditions at the material boundary to model the contact surface between two anisotropic materials. Pan and Amadei in [11] developed an effective boundary-element approach to solving problems for elastic anisotropic bimaterial solids containing cracks and thin inclusions. Wang and Pan [12] constructed Green's functions for an anisotropic thermoelastic bimaterial with a Kapitza-type interface.

An effective method for solving thermomagnetoelastic problems for bimaterials is an approach based on the methods of complex variable calculus and the Stroh formalism. It is widely used in the analysis of anisotropic [6], [7], piezoelectric [7], [15], [16] and magnetoelastic [15] solids with through cracks and inclusions. In [3], [4], boundary integral Somigliana-type equations for the boundary-element analysis of anisotropic thermomagnetoelastic bimaterial with holes, cracks and thin inclusions are obtained.

This paper expands the possibilities of the Stroh formalism-based approach for a thermomagnetoelastic bimaterial solid with a high-temperature conducting interface and perfect magnetoelctromechanical contact of components that may contain thin inclusions sensitive to the influence of fields of different nature. An appropriate mathematical model has been developed. Also, there were obtained integral equations of the Somigliana-type and solved a number of problems for single and interacting inclusions.

2. GOVERNING EQUATIONS OF THERMOMAGNETOELECTROELASTICITY

Consider a piecewise homogeneous anisotropic linear thermomagnetoelastoelectric medium in the reference coordinate system $Ox_1x_2x_3$. According to [6], [7] and [8], the balance equations for stress, electric displacement, magnetic induction and heat flux, as well as constitutive relations can be expressed using the complex variable calculus. The extended Stroh formalism allows to write the general solution of these equations through certain analytical functions $f(z)$ and $g(z)$ as

$$\begin{aligned} \theta &= 2\text{Re}\{g'(z_t)\}, \vartheta = 2k_t\text{Im}\{g'(z_t)\}; \\ \mathbf{u} &= 2\text{Re}\{\mathbf{A}f(z_*) + \mathbf{c}g(z_t)\}, \mathbf{\Phi} = 2\text{Re}\{\mathbf{B}f(z_*) + \mathbf{d}g(z_t)\}; \\ \tilde{u}_i &= u_i, \tilde{u}_4 = \phi, \tilde{u}_5 = \psi; \tilde{\sigma}_{ij} = \sigma_{ij}, \tilde{\sigma}_{4j} = D_j, \tilde{\sigma}_{5j} = B_j \quad (i = 1,2,3) \\ \tilde{\sigma}_{i1} &= -\tilde{\varphi}_{i,2}, \tilde{\sigma}_{i2} = \tilde{\varphi}_{i,1}; z_t = x_1 + p_t x_2, z_\alpha = x_1 + p_\alpha x_2; \quad (1) \\ h_1 &= -\vartheta_{,2}, h_2 = \vartheta_{,1}; k_t = \sqrt{k_{11}k_{22} - k_{12}^2}, \\ \mathbf{f}(z_*) &= [F_1(z_1), F_2(z_2), F_3(z_3)]^T, \end{aligned}$$

where σ_{ij} is a stress tensor; u_i is a displacement vector; h_i is heat flux; D_i is electric displacement; B_i is magnetic induction; q is a density of free charges; f_i is the body force; f_h is the density of distributed heat; ϕ and ψ are electric and magnetic potentials; θ is a change of temperature with respect to the reference one; k_{ij} are thermal conductivity coefficients; ϑ is heat flow function; $\mathbf{f}(z)$ is a vector of Stroh complex potentials; $g(z)$ is a temperature potential; $F_\alpha(z_\alpha)$ are certain analytical functions; and p_t is a complex constant (with a positive imaginary part), which is the root of the characteristic equation of thermal conductivity $k_{22}p_t^2 + 2k_{12}p_t + k_{11} = 0$.

Matrices $\mathbf{A} \equiv [A_{i\alpha}] = [\mathbf{a}_\alpha]$, $\mathbf{B} \equiv [b_{i\alpha}] = [\mathbf{b}_\alpha]$, constants $p_\alpha (\alpha = 1, \dots, 5)$ and vectors \mathbf{c} and \mathbf{d} are determined from the eigenvalue problem of the Stroh formalism [6] on the basis of elastic, piezoelectric, dielectric and piezomagnetic constants of the material.

The Stroh complex potentials, the vector-functions of displacement and stress are related by the following equations [7]:

$$\begin{aligned} \mathbf{f}(z_*) &= \mathbf{B}^T \mathbf{u} + \mathbf{A}^T \mathbf{\Phi} - \mathbf{B}^T \mathbf{u}^t - \mathbf{A}^T \mathbf{\Phi}^t, \\ \mathbf{u}^t &= 2\text{Re}\{\mathbf{c}g(z_t)\}, \mathbf{\Phi}^t = 2\text{Re}\{\mathbf{d}g(z_t)\}. \end{aligned} \quad (2)$$

Function $g'(z_t)$, temperature and heat flux function are related as

$$g'(z_t) = \frac{1}{2} \left(\theta + i \frac{\vartheta}{k_t} \right). \quad (3)$$

3. FORMULATION OF THE PROBLEM

Consider the problem of thermal conductivity and deformation for an anisotropic thermomagnetoelastoelectric bimaterial medium with inclusions. It consists of two thermomagnetoelastoelectric anisotropic half-spaces, which are separated by a surface $x_2 = 0$ and contains cylindrical holes parallel to the x_3 axis on the surface of which arbitrary independent mechanical and thermal boundary conditions are given (Fig.1). In this case, it suffices to consider the temperature and thermomagnetoelastoelectric state in an arbitrary cross-section K which is perpendicular to x_3 .

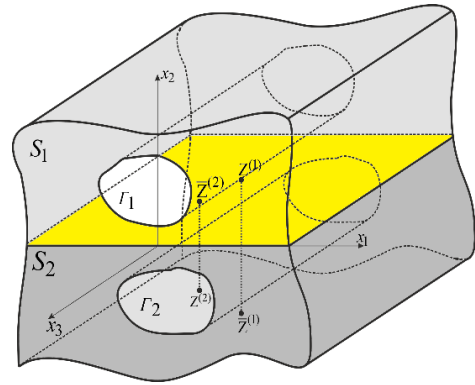


Fig. 1. Geometric scheme of a plane problem for a thermomagnetoelastoelectric anisotropic bimaterial medium

At the interface, the conditions of imperfect thermal contact in the form of a high-temperature conducting interface

$$\begin{aligned} \vartheta^{(1)}(x_1, x_2)|_{x_2=0} &= \vartheta(x_1) + \mu_0 \theta_{,1}(x_1), \mu_0 = 2h^{int} k_{22}^{int}, \\ \vartheta^{(2)}(x_1, x_2)|_{x_2=0} &= \vartheta(x_1), \end{aligned} \quad (4)$$

$$\theta^{(1)}(x_1, x_2)|_{x_2=0} = \theta^{(2)}(x_1, x_2)|_{x_2=0} = \theta(x_1), \forall x_2 = 0; \quad (5)$$

and the conditions of perfect magnetoelastomechanical contact of components are given

$$\mathbf{u}^{(1)}(x_1, x_2)|_{x_2=0} = \mathbf{u}^{(2)}(x_1, x_2)|_{x_2=0} = \mathbf{u}(x_1), \quad (6)$$

$$\mathbf{\Phi}^{(1)}(x_1, x_2)|_{x_2=0} = \mathbf{\Phi}^{(2)}(x_1, x_2)|_{x_2=0} = \mathbf{\Phi}(x_1), \forall x_2 = 0. \quad (7)$$

Here, superscripts 1 and 2 are used to denote the values of the fields acting in half-spaces S_1 and S_2 , respectively. A thin intermediate layer is removed from consideration. Each half-space contains a system of smooth closed contours $\Gamma_1 = \cup_i \Gamma_i^{(1)}$ and $\Gamma_2 = \cup_i \Gamma_i^{(2)}$. On them, it is possible to set various thermal or mechanical boundary conditions.

To derive the integral formulas for the Stroh complex potentials, we use the Cauchy integral formula [5]:

$$\frac{1}{2\pi i} \int_{\partial S} \frac{\phi(\tau) d\tau}{\tau - z} = \begin{cases} \phi(z) & \forall z \in S, \\ 0 & \forall z \notin S. \end{cases} \quad (8)$$

It outlines the relationship between the values of an arbitrary complex function (analytic in $z \in S$) at the boundary ∂S of the domain S outside and inside it. The function $\phi(z)$ is assumed to have no poles in $z \in S$. Here $\tau, z \in \mathbb{C}$ are complex variables that characterise the location of the source points and the field, respectively. Also, in Eq. (8) it is assumed that when the domain S is infinite, then the function $\phi(\tau)$ should vanish at $z \rightarrow \infty$.

4. DERIVATION OF INTEGRAL REPRESENTATIONS FOR BIMATERIAL WITH IMPERFECT THERMAL CONTACT OF COMPONENTS

4.1. Thermal conductivity

The problem of thermal conductivity is linear. Its solution can be represented as a superposition of homogeneous and perturbed solutions. Homogeneous solutions $g_{1\infty}(z_t^{(1)})$ and $g_{2\infty}(z_t^{(2)})$ satisfy Eq. (3). The perturbed solutions are caused by the presence of contours Γ_1 and Γ_2 and certain boundary conditions set on them.

Let us write the Cauchy formulas for the components of the bimaterial as follows:

$$\forall \text{Im} (z_t^{(1)}) > 0,$$

$$g_1'(z_t^{(1)}) = \frac{1}{2\pi i} \int_{\Gamma} \frac{g_1'(\tau_t^{(1)}) d\tau_t^{(1)}}{\tau_t^{(1)} - z_t^{(1)}} + \frac{1}{2\pi i} \int_{-\infty}^{\infty} \frac{g_1'(x_1) dx_1}{x_1 - z_t^{(1)}}, \quad (9.1)$$

$$\forall \text{Im} (z_t^{(2)}) < 0,$$

$$g_2'(z_t^{(2)}) = \frac{1}{2\pi i} \int_{\Gamma} \frac{g_2'(\tau_t^{(2)}) d\tau_t^{(2)}}{\tau_t^{(2)} - z_t^{(2)}} + \frac{1}{2\pi i} \int_{-\infty}^{\infty} \frac{g_2'(x_1) dx_1}{x_1 - z_t^{(2)}}. \quad (9.2)$$

Using the conditions of imperfect thermal contact, Eq. (3) can be written as

$$g_1'(x_1) = \frac{1}{2\pi} \left(\theta(x_1) + \frac{i}{k_t^{(1)}} \vartheta(x_1) + \frac{i\mu_0}{k_t^{(1)}} \theta_{,1}(x_1) \right); \quad (9.3)$$

$$g_2'(x_1) = \frac{1}{2\pi} \left(\theta(x_1) + \frac{i}{k_t^{(2)}} \vartheta(x_1) \right). \quad (9.4)$$

Thus, we substitute now Eqs (9.3) and (9.4) into Eqs (9.1) and (9.2), respectively

$$g_1'(z_t^{(1)}) = \frac{1}{2\pi i} \int_{\Gamma} \frac{g_1'(\tau_t^{(1)}) d\tau_t^{(1)}}{\tau_t^{(1)} - z_t^{(1)}} + \frac{1}{2\pi i} \left(\frac{1}{2} \int_{-\infty}^{\infty} \frac{\theta(x_1) dx_1}{x_1 - z_t^{(1)}} + \frac{i}{2k_t^{(1)}} \int_{-\infty}^{\infty} \frac{\vartheta(x_1) dx_1}{x_1 - z_t^{(1)}} + \frac{i}{2k_t^{(1)}} \int_{-\infty}^{\infty} \frac{\mu_0 \theta_{,1}(x_1) dx_1}{x_1 - z_t^{(1)}} \right);$$

$$g_2'(z_t^{(2)}) = \frac{1}{2\pi i} \int_{\Gamma} \frac{g_2'(\tau_t^{(2)}) d\tau_t^{(2)}}{\tau_t^{(2)} - z_t^{(2)}} + \frac{1}{2\pi i} \left(\frac{1}{2} \int_{-\infty}^{\infty} \frac{\theta(x_1) dx_1}{x_1 - z_t^{(2)}} + \frac{i}{2k_t^{(2)}} \int_{-\infty}^{\infty} \frac{\vartheta(x_1) dx_1}{x_1 - z_t^{(2)}} \right).$$

Excluding integrals along the interface of half-spaces we obtain

$$g_1'(z_t^{(1)}) = \frac{1}{2\pi i} [q_t^{(1)}(z_t^{(1)}) + \bar{q}_t^{(1)}(z_t^{(1)}) - \frac{(1+K)}{\beta_1} \bar{e}_t^{(1)}(\beta_1; z_t^{(1)}) + \frac{(1-K)}{\beta_1} e_t^{(2)}(\beta_1; z_t^{(1)})]. \quad (10)$$

$$g_2'(z_t^{(2)}) = \frac{1}{2\pi i} [q_t^{(2)}(z_t^{(2)}) + \bar{q}_t^{(2)}(z_t^{(2)}) + \frac{(1+K)}{\beta_2} e_t^{(1)}(\beta_2; z_t^{(2)}) - \frac{(1-K)}{\beta_2} \bar{e}_t^{(2)}(\beta_2; z_t^{(2)})]. \quad (11)$$

Here

$$q_t^{(i)}(z_t^{(j)}) = \int_{\Gamma_i} \frac{g_i'(\tau_t^{(i)}) d\tau_t^{(i)}}{\tau_t^{(i)} - z_t^{(j)}}, \quad \bar{q}_t^{(i)}(z_t^{(j)}) = \int_{\Gamma_i} \frac{\overline{g_i'(\tau_t^{(i)})} d\tau_t^{(i)}}{\bar{\tau}_t^{(i)} - \bar{z}_t^{(j)}}.$$

$$K = \frac{k_t^{(1)} - k_t^{(2)}}{k_t^{(1)} + k_t^{(2)}}, \quad \frac{1}{k_t^{(1)} + k_t^{(2)}} = \frac{1+K}{2k_t^{(1)}} = \frac{1-K}{2k_t^{(2)}};$$

$$\beta_1 = -\frac{i\mu_0(1+K)}{2k_t^{(1)}}, \quad \beta_2 = \frac{i\mu_0(1-K)}{2k_t^{(2)}}. \quad (12)$$

$$e_t^{(k)}(\alpha_i; z_t^{(j)}) = e^{-\frac{z_t^{(j)}}{\alpha_i}} \int e^{\frac{z_t^{(j)}}{\alpha_i}} q_t^{(k)}(z_t^{(j)}) dz_t^{(j)};$$

$$\bar{e}_t^{(k)}(\alpha_i; z_t^{(j)}) = e^{-\frac{\bar{z}_t^{(j)}}{\alpha_i}} \int e^{\frac{\bar{z}_t^{(j)}}{\alpha_i}} \bar{q}_t^{(k)}(z_t^{(j)}) dz_t^{(j)}.$$

Thus, there are obtained integral representation for the temperature and heat flux at any point ξ bimaterial

$$\theta(\xi) = \begin{cases} 2\text{Re} \{g_1'(z_t^{(1)}(\xi))\} & (\forall \xi \in S_1), \\ 2\text{Re} \{g_2'(z_t^{(2)}(\xi))\} & (\forall \xi \in S_2) \end{cases} =$$

$$= \int_{\Gamma} [\Theta^{\text{HCl}*}(\mathbf{x}, \xi) h_n(\mathbf{x}) - \text{H}^{\text{HCl}*}(\mathbf{x}, \xi) \theta(\mathbf{x})] ds(\mathbf{x}) + \theta^{\infty}(\xi); \quad (13)$$

$$h(\xi) = \begin{cases} 2k_t^{(1)} \text{Im} \left\{ \left(\delta_{2i} - \delta_{1i} p_t^{(1)} \right) g_1''(z_t^{(1)}(\xi)) \right\} & (\forall \xi \in S_1), \\ 2k_t^{(2)} \text{Im} \left\{ \left(\delta_{2i} - \delta_{1i} p_t^{(2)} \right) g_2''(z_t^{(2)}(\xi)) \right\} & (\forall \xi \in S_2) \end{cases} =$$

$$= \int_{\Gamma} \Theta_i^{\text{HCl}*}(\mathbf{x}, \xi) h_n(\mathbf{x}) d\Gamma(\mathbf{x}) - \int_{\Gamma} H_i^{\text{HCl}*}(\mathbf{x}, \xi) \theta(\mathbf{x}) ds(\mathbf{x}) + h_i^{\infty}(\xi). \quad (14)$$

The functions $\theta^{\infty}(\xi)$ and $h_i^{\infty}(\xi)$ are homogeneous solutions for the bimaterial

$$\theta^{\infty}(\xi) = \begin{cases} 2\text{Re} \{g_{1\infty}'(z_t^{(1)}(\xi))\} & (\forall \xi \in S_1), \\ 2\text{Re} \{g_{2\infty}'(z_t^{(2)}(\xi))\} & (\forall \xi \in S_2); \end{cases}$$

$$h_i^{\infty}(\xi) = \begin{cases} 2k_t^{(1)} \text{Im} \left\{ \left(\delta_{2i} - \delta_{1i} p_t^{(1)} \right) g_{1\infty}''(z_t^{(1)}(\xi)) \right\} & (\forall \xi \in S_1), \\ 2k_t^{(2)} \text{Im} \left\{ \left(\delta_{2i} - \delta_{1i} p_t^{(2)} \right) g_{2\infty}''(z_t^{(2)}(\xi)) \right\} & (\forall \xi \in S_2). \end{cases}$$

4.2. Thermomagnetoelastic elasticity

Using Eq. (8), we write the Cauchy integral formula for vectors $\mathbf{f}^{(1)}(z_*^{(1)})$ and $\mathbf{f}^{(2)}(z_*^{(2)})$ of Stroh complex potentials which are analytical functions in S_1 and S_2 , respectively

$$\mathbf{f}^{(1)}(z_*^{(1)}) = \frac{1}{2\pi i} \left[\int_{\Gamma_i} \left\langle \frac{d\tau_*^{(1)}}{\tau_*^{(1)} - z_*^{(1)}} \right\rangle \mathbf{f}^{(1)}(\tau_*^{(1)}) + \int_{-\infty}^{\infty} \left\langle \frac{dx_1}{x_1 - z_*^{(1)}} \right\rangle \mathbf{f}^{(1)}(x_1) \right],$$

$$\mathbf{f}^{(2)}(z_*^{(2)}) = \frac{1}{2\pi i} \left[\int_{\Gamma_i} \left\langle \frac{d\tau_*^{(2)}}{\tau_*^{(2)} - z_*^{(2)}} \right\rangle \mathbf{f}^{(2)}(\tau_*^{(2)}) + \int_{-\infty}^{\infty} \left\langle \frac{dx_1}{x_1 - z_*^{(2)}} \right\rangle \mathbf{f}^{(2)}(x_1) \right].$$

Introducing notation

$$\mathbf{q}_j(z_{\beta}^{(i)}) = \int_{\Gamma_i} \left\langle \frac{d\tau_*^{(j)}}{\tau_*^{(j)} - z_{\beta}^{(i)}} \right\rangle \mathbf{f}^{(j)}(\tau_*^{(j)}),$$

$$\bar{\mathbf{q}}_j(z_{\beta}^{(i)}) = \int_{\Gamma_i} \left\langle \frac{d\bar{\tau}_*^{(j)}}{\bar{\tau}_*^{(j)} - z_{\beta}^{(i)}} \right\rangle \bar{\mathbf{f}}^{(j)}(\tau_*^{(j)}), \quad (15)$$

we rewrite them in the form of

$$\mathbf{f}^{(1)}(z_*^{(1)}) = \frac{1}{2\pi i} \left[\mathbf{q}_1(z_*^{(1)}) + \int_{-\infty}^{\infty} \left\langle \frac{dx_1}{x_1 - z_*^{(1)}} \right\rangle \mathbf{f}^{(1)}(x_1) \right],$$

$$0 = \bar{\mathbf{q}}_1(z_*^{(1)}) + \int_{-\infty}^{\infty} \left\langle \frac{1}{x_1 - z_*^{(1)}} \right\rangle \bar{\mathbf{f}}^{(1)}(x_1) dx_1, \quad (16)$$

$$0 = \mathbf{q}_1(z_*^{(2)}) + \int_{-\infty}^{\infty} \left\langle \frac{1}{x_1 - z_*^{(2)}} \right\rangle \mathbf{f}^{(1)}(x_1) dx_1;$$

$$\mathbf{f}^{(2)}(z_*^{(2)}) = \frac{1}{2\pi i} \left[\mathbf{q}_2(z_*^{(2)}) + \int_{-\infty}^{\infty} \left\langle \frac{1}{x_1 - z_*^{(2)}} \right\rangle \mathbf{f}^{(2)}(x_1) dx_1 \right],$$

$$0 = \bar{\mathbf{q}}_2(z_*^{(2)}) - \int_{-\infty}^{\infty} \left\langle \frac{1}{x_1 - z_*^{(2)}} \right\rangle \bar{\mathbf{f}}^{(2)}(x_1) dx_1, \quad (17)$$

$$0 = \mathbf{q}_2(z_*^{(1)}) - \int_{-\infty}^{\infty} \left\langle \frac{1}{x_1 - z_*^{(1)}} \right\rangle \mathbf{f}^{(2)}(x_1) dx_1.$$

Excluding from Eqs (16) and (17) integrals along the interface of half-spaces using the Stroh orthogonality conditions we obtain

$$\mathbf{f}^{(1)}(z_*^{(1)}) = \frac{1}{2\pi i} \left[\mathbf{q}_1(z_*^{(1)}) + \sum_{\beta=1}^5 \mathbf{I}_{\beta} \left(\mathbf{G}_1^{(1)} \bar{\mathbf{q}}_1(z_{\beta}^{(1)}) + \mathbf{G}_2^{(1)} \mathbf{q}_2(z_{\beta}^{(1)}) \right) + \langle \bar{Q}_t^{(1)}(z_t^{(1)}) \rangle \delta_1^{(1)} + \langle Q_t^{(2)}(z_t^{(1)}) \rangle \delta_2^{(1)} + \langle \bar{e}_t^{(1)}(\beta_1; z_t^{(1)}) \rangle \mathbf{X}_1^{(1)} + \langle e_t^{(2)}(\beta_1; z_t^{(1)}) \rangle \mathbf{X}_2^{(1)} \right]. \quad (18)$$

Here

$$\begin{aligned} \mathbf{X}_1^{(1)} &= -\delta_1^{(1)} - 2ik_t^{(1)} \left(\mathbf{G}_1^{(1)} \bar{\boldsymbol{\mu}}_1 - \boldsymbol{\mu}_1 \right), \\ \mathbf{X}_2^{(1)} &= -\delta_2^{(1)} + 2ik_t^{(2)} \left(\mathbf{G}_2^{(1)} \boldsymbol{\mu}_2 \right). \\ \delta_1^{(1)} &= -(1+K) \left(\mathbf{G}_2^{(1)} \lambda_2 - \mathbf{G}_1^{(1)} \bar{\lambda}_1 - \lambda_1 \right) + ik_t^{(2)} (1+K) \left(\mathbf{G}_2^{(1)} \mu_2 - \mathbf{G}_1^{(1)} \bar{\mu}_1 - \mu_1 \right), \\ \delta_2^{(1)} &= (1-K) \left(\mathbf{G}_2^{(1)} \lambda_2 - \mathbf{G}_1^{(1)} \bar{\lambda}_1 - \lambda_1 \right) + ik_t^{(2)} (1+K) \left(\mathbf{G}_2^{(1)} \mu_2 - \mathbf{G}_1^{(1)} \bar{\mu}_1 - \mu_1 \right). \\ \mathbf{G}_1^{(1)} &= -[\mathbf{A}_1^T (\bar{\mathbf{A}}_1 \bar{\mathbf{B}}_1^{-1} - \mathbf{A}_2 \mathbf{B}_2^{-1})^{-T} \bar{\mathbf{B}}_1^{-T} + \mathbf{B}_1^T (\bar{\mathbf{B}}_1 \bar{\mathbf{A}}_1^{-1} - \mathbf{B}_2 \mathbf{A}_2^{-1})^{-T} \bar{\mathbf{A}}_1^{-T}], \\ \mathbf{G}_2^{(1)} &= -[\mathbf{A}_1^T (\bar{\mathbf{A}}_1 \bar{\mathbf{B}}_1^{-1} - \mathbf{A}_2 \mathbf{B}_2^{-1})^{-T} \bar{\mathbf{B}}_2^{-T} + \mathbf{B}_1^T (\bar{\mathbf{B}}_1 \bar{\mathbf{A}}_1^{-1} - \mathbf{B}_2 \mathbf{A}_2^{-1})^{-T} \bar{\mathbf{A}}_2^{-T}]. \\ \mathbf{f}^{(2)} \left(z_*^{(2)} \right) &= \frac{1}{2\pi i} \left[\mathbf{q}_2 \left(z_*^{(2)} \right) + \sum_{\beta=1}^5 \mathbf{I}_\beta \left(\mathbf{G}_1^{(2)} \mathbf{q}_1 \left(z_\beta^{(2)} \right) + \mathbf{G}_2^{(2)} \bar{\mathbf{q}}_2 \left(z_\beta^{(2)} \right) \right) + \langle \bar{Q}_t^{(1)} \left(z_t^{(2)} \right) \rangle \delta_1^{(2)} + \langle \bar{Q}_t^{(2)} \left(z_t^{(2)} \right) \rangle \delta_2^{(2)} + \langle e_t^{(1)} \left(\beta_2; z_t^{(2)} \right) \rangle \mathbf{X}_1^{(2)} + \langle \bar{e}_t^{(2)} \left(\beta_2; z_t^{(2)} \right) \rangle \mathbf{X}_2^{(2)} \right]. \end{aligned} \quad (19)$$

and

$$\begin{aligned} \mathbf{X}_1^{(2)} &= -\delta_1^{(2)} - 2ik_t^{(1)} \mathbf{G}_2^{(2)} \boldsymbol{\mu}_1, \\ \mathbf{X}_2^{(2)} &= -\delta_1^{(1)} + 2ik_t^{(2)} \left(\mathbf{G}_2^{(2)} \bar{\boldsymbol{\mu}}_2 - \boldsymbol{\mu}_2 \right). \\ \delta_1^{(2)} &= -(1+K) \left(\mathbf{G}_1^{(2)} \lambda_1 - \mathbf{G}_2^{(2)} \bar{\lambda}_2 + \lambda_2 \right) - ik_t^{(2)} (1+K) \left(\mathbf{G}_1^{(2)} \mu_1 - \mathbf{G}_2^{(2)} \bar{\mu}_2 + \mu_2 \right), \\ \delta_2^{(2)} &= (1-K) \left(\mathbf{G}_1^{(2)} \lambda_1 - \mathbf{G}_2^{(2)} \bar{\lambda}_2 + \lambda_2 \right) - ik_t^{(2)} (1+K) \left(\mathbf{G}_1^{(2)} \mu_1 - \mathbf{G}_2^{(2)} \bar{\mu}_2 + \mu_2 \right). \\ \mathbf{G}_1^{(2)} &= -[\mathbf{A}_2^T (\mathbf{A}_1 \mathbf{B}_1^{-1} - \bar{\mathbf{A}}_2 \bar{\mathbf{B}}_2^{-1})^{-T} \bar{\mathbf{B}}_1^{-T} + \mathbf{B}_2^T (\mathbf{B}_1 \mathbf{A}_1^{-1} - \bar{\mathbf{B}}_2 \bar{\mathbf{A}}_2^{-1})^{-T} \bar{\mathbf{A}}_1^{-T}], \\ \mathbf{G}_2^{(2)} &= -[\mathbf{A}_2^T (\mathbf{A}_1 \mathbf{B}_1^{-1} - \bar{\mathbf{A}}_2 \bar{\mathbf{B}}_2^{-1})^{-T} \bar{\mathbf{B}}_2^{-T} + \mathbf{B}_2^T (\mathbf{B}_1 \mathbf{A}_1^{-1} - \bar{\mathbf{B}}_2 \bar{\mathbf{A}}_2^{-1})^{-T} \bar{\mathbf{A}}_2^{-T}]. \end{aligned}$$

The obtained (18) and (19) allow to write integral relations that relate the displacements at an arbitrary point of the thermomagnetoelastic bimaterial with temperature, heat flux and displacement and traction on the contours Γ_i :

$$\begin{aligned} \mathbf{u}(\boldsymbol{\xi}) &= \begin{cases} 2\text{Re} \left\{ \mathbf{A}_1 \mathbf{f}^{(1)} \left(Z_*^{(1)}(\boldsymbol{\xi}) \right) + \mathbf{c}_1 g_1 \left(Z_t^{(1)}(\boldsymbol{\xi}) \right) \right\} & (\forall \boldsymbol{\xi} \in S_1), \\ 2\text{Re} \left\{ \mathbf{A}_2 \mathbf{f}^{(2)} \left(Z_*^{(2)}(\boldsymbol{\xi}) \right) + \mathbf{c}_2 g_2 \left(Z_t^{(2)}(\boldsymbol{\xi}) \right) \right\} & (\forall \boldsymbol{\xi} \in S_2) \end{cases} = \\ &= \mathbf{u}^\infty(\boldsymbol{\xi}) + \int_{\Gamma} [\mathbf{U}^{\text{bm}}(\mathbf{x}, \boldsymbol{\xi}) \mathbf{t}(\mathbf{x}) - \mathbf{T}^{\text{bm}}(\mathbf{x}, \boldsymbol{\xi}) \mathbf{u}(\mathbf{x}) + \mathbf{r}^{\text{HCl}}(\mathbf{x}, \boldsymbol{\xi}) \theta(\mathbf{x}) + \mathbf{v}^{\text{HCl}}(\mathbf{x}, \boldsymbol{\xi}) h_n(\mathbf{x})] ds(\mathbf{x}), \end{aligned} \quad (20)$$

Also, using Eqs (18) and (19) it is possible to write similar expressions to determine the stress in an arbitrary point of thermomagnetoelastic bimaterial

$$\begin{aligned} \sigma_j(\boldsymbol{\xi}) &= \begin{cases} 2\text{Re} \left\{ \mathbf{B}_1 (\delta_{2j} - \delta_{1j} p_*^{(1)}) \mathbf{f}' \left(Z_*^{(1)}(\boldsymbol{\xi}) \right) + \right. \\ \left. 2\text{Re} \left\{ \mathbf{B}_2 (\delta_{2j} - \delta_{1j} p_*^{(2)}) \mathbf{f}' \left(Z_*^{(2)}(\boldsymbol{\xi}) \right) + \right. \\ \left. + \mathbf{d}_1 (\delta_{2j} - \delta_{1j} p_t^{(1)}) g_1' \left(Z_t^{(1)}(\boldsymbol{\xi}) \right) \right\}, & (\forall \boldsymbol{\xi} \in S_1), \\ \left. + \mathbf{d}_2 (\delta_{2j} - \delta_{1j} p_t^{(2)}) g_2' \left(Z_t^{(2)}(\boldsymbol{\xi}) \right) \right\}, & (\forall \boldsymbol{\xi} \in S_2) \end{cases} = \\ &= \sigma_j^\infty(\boldsymbol{\xi}) + \int_{\Gamma} [\mathbf{D}_j^{\text{bm}}(\mathbf{x}, \boldsymbol{\xi}) \mathbf{t}(\mathbf{x}) ds(\mathbf{x}) - \mathbf{S}_j^{\text{bm}}(\mathbf{x}, \boldsymbol{\xi}) \mathbf{u}(\mathbf{x}) + \mathbf{q}_j^{\text{HCl}}(\mathbf{x}, \boldsymbol{\xi}) \theta(\mathbf{x}) ds(\mathbf{x}) + \mathbf{w}_j^{\text{HCl}}(\mathbf{x}, \boldsymbol{\xi}) h_n(\mathbf{x}) ds(\mathbf{x})] ds(\mathbf{x}). \end{aligned} \quad (21)$$

According to [10], stress and displacement discontinuities in the vicinity of tips of thin inhomogeneities are characterised by generalised stress, electric displacements and magnetic induction intensity factors. They are determined by the discontinuity functions at the tip of inhomogeneity by formulas

$$\tilde{\mathbf{k}}^{(1)} = \lim_{s \rightarrow 0} \sqrt{\frac{\pi}{8s}} \mathbf{L} \cdot \Delta \tilde{\mathbf{u}}(s); \quad \tilde{\mathbf{k}}^{(2)} = -\lim_{s \rightarrow 0} \sqrt{\frac{\pi s}{2}} \Sigma \tilde{\mathbf{k}}(s),$$

where $\tilde{\mathbf{k}}^{(1)} = [K_{21}, K_{11}, K_{31}, K_{41}, K_{51}]$, $\tilde{\mathbf{k}}^{(2)} = [K_{12}^{(2)}, K_{22}^{(2)}, K_{32}, K_{42}, K_{52}]$ – are the vectors of generalised stress and electric displacement intensity factors; $\mathbf{L} = -2\sqrt{-1} \mathbf{B} \mathbf{B}^T$ – the real tensor Burnett–Lotte [9]. The first two components $K_{12}^{(2)}, K_{22}^{(2)}$ of the vector $\tilde{\mathbf{k}}^{(2)}$ differ from generalised SIFs K_{12}, K_{22} , which are introduced for purely elastic problems. To find K_{12}, K_{22} , through $\tilde{\mathbf{k}}^{(2)}$ we need to use the formula $k_i^{(2)} = S_{ji} \tilde{k}_j^{(2)}$ ($i = 1, 2; j = 1, \dots, 5$).

Here $\mathbf{k}^{(2)} = [K_{22}, K_{12}]^T$ – the vector of generalised SIF; $\mathbf{S} = \sqrt{-1} (\mathbf{2} \mathbf{A} \mathbf{B}^T - \mathbf{I})$ – the second real Burnett–Lotte tensor [9].

Generalised heat flux intensity factors are defined as

$$K_{h1} = -\lim_{s \rightarrow 0} \sqrt{\frac{\pi}{8s}} k_t \cdot \Delta \theta(s); \quad K_{h2} = -\lim_{s \rightarrow 0} \sqrt{\frac{\pi s}{2}} \Sigma h_n(s).$$

Fields of displacements, stresses, temperatures and heat flux in the vicinity of the inclusion tip are fully characterised by generalised stress and electric displacement intensity factors and are defined by the following relationships:

$$\tilde{\mathbf{u}}(\boldsymbol{\xi}) = \sqrt{\frac{2}{\pi}} \text{Im} \left\{ \mathbf{A} \langle \sqrt{Z_*} \rangle (\sqrt{-1} \mathbf{B}^{-1} \tilde{\mathbf{k}}^{(1)} - \mathbf{2} \mathbf{A}^T \tilde{\mathbf{k}}^{(2)}) \right\},$$

$$\tilde{\boldsymbol{\varphi}}(\boldsymbol{\xi}) = \sqrt{\frac{2}{\pi}} \text{Im} \left\{ \mathbf{B} \langle \sqrt{Z_*} \rangle (\sqrt{-1} \mathbf{B}^{-1} \tilde{\mathbf{k}}^{(1)} - \mathbf{2} \mathbf{A}^T \tilde{\mathbf{k}}^{(2)}) \right\};$$

$$\theta = \frac{1}{k_t} \sqrt{\frac{2}{\pi}} \text{Im} \left\{ (K_{h1} + \sqrt{-1} K_{h2}) \sqrt{Z_t} \right\},$$

$$\vartheta = \sqrt{\frac{2}{\pi}} \text{Im} \left\{ (\sqrt{-1} K_{h1} - K_{h2}) \sqrt{Z_t} \right\}.$$

5. NUMERICAL EXAMPLES

The obtained integral equations are introduced into the scheme of the modified boundary elements method [17]. To solve them, the curves $\Gamma = \cup_j \Gamma_j$ are approximated using n rectilinear segments (boundary elements) Γ_q . At each element, three nodal points are set: one at the centre, and two others at the distance of $\frac{1}{3}$ of element length at both sides of a central node (discontinuous three-node boundary element; if the polynomial shape functions are used it is called the discontinuous quadratic boundary element [7]). The boundary functions of temperature, heat flux, displacement and stress are approximated at the element using their nodal values. This allows solving specific two-dimensional problems of thermomagnetoelasticity for bimaterial solids with imperfect thermal contact of its components in the presence of inhomogeneities inside them.

Example 1. To verify the proposed numerical method, consider a test problem for finite square solid with elementary load given on its faces, which has analytic solution. To proceed with this, let us cut out a square from the upper half-space of a bimaterial solid with high-temperature conducting interface, and consider

the prismatic body of a square cross section. To model the latter, we used only 40 boundary elements. The lower boundary of the body is at a distance r to the interface (Fig. 2). On the upper boundary of the body it is given a temperature θ^0 .

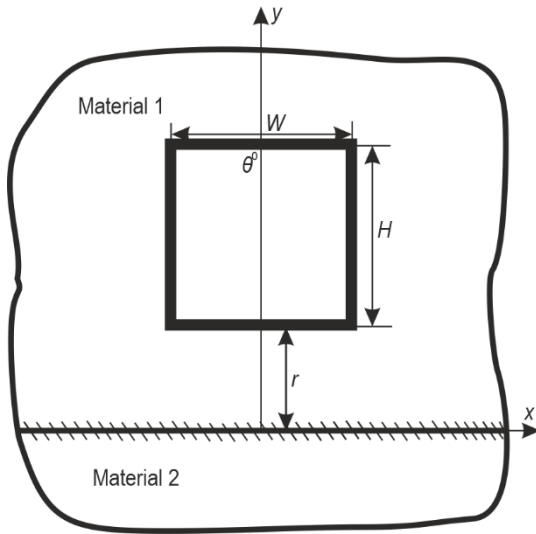


Fig. 2. Cross-sectional scheme of a thermoelastic anisotropic square body

Let us check the influence of the high-temperature conducting interface on the temperature distribution in a given finite solid. To do this, let us fix the coordinate $x = x_0$ ($x_0 \in [-\frac{W}{2}; \frac{W}{2}]$) and find the temperature value at the points $y = y_0 + r$ ($y_0 \in [0; H]$). The obtained plot shows that the temperature change is a linear function of coordinate, which is the exact analytic solution of the problem. Moreover, if one changes x_0 the resulting plot does not change, which also verifies the developed boundary element approach.

Now let us cut out the same prismatic body, with the same conditions, from the lower half-space. As in the previous case, we fix coordinate $x = x_0$ ($x_0 \in [-\frac{W}{2}; \frac{W}{2}]$) and calculate the temperature value at points $y = y_0 - r$ ($y_0 \in [-H; 0]$). The obtained schedule of temperature change is identical to the previous one, which also verifies the obtained kernels of boundary integral equations.

It should also be noted that the change in thermal conductivity of the interface does not change the temperature in these bodies. It is obvious in this case (homogeneous material) that the high thermal conductivity interface does not affect the temperature distribution in the considered finite prismatic bodies, which further verifies the obtained integral formulas and developed computational programs.

Example 2 Finally, consider the problem where the interface crosses the square solid ($W = H$), as shown in Fig. 3. The properties of the materials are the same as in the previous example. On the upper boundary of the solid, for $y = \frac{H}{2}$ the temperature is set as follows: $\theta = 4x^2/W^2$, $x \in [-\frac{W}{2}; \frac{W}{2}]$. On the bottom boundary of the cut out square a temperature $\theta^0 = 0$ is given. At the interface, the conditions of imperfect thermal contact in the form of a high-temperature conducting interface, Eqs (4) and (5), are satisfied.

In addition to the boundary elements method, another approach was used to solve the problem for their mutual verification.

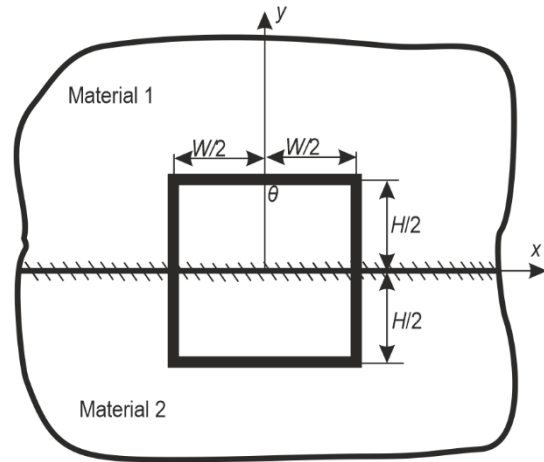


Fig. 3. Sketch of a thermoelastic anisotropic square solid with HCI

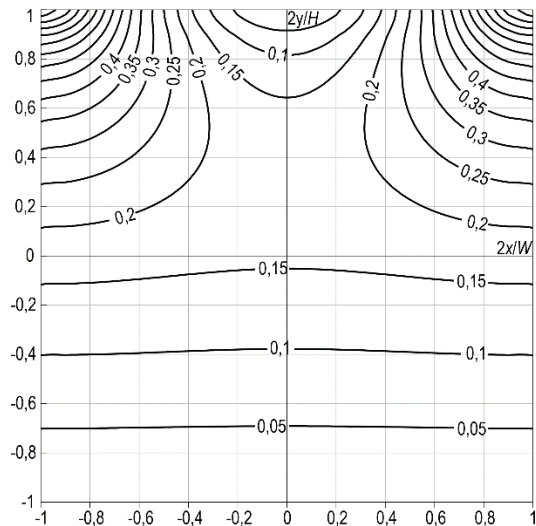


Fig. 4. Temperature change in the cross section of a square body with HCI

This approach is based on the Stroh formalism. The complex potentials (3) for a square solid with high-temperature conducting interface can be taken as the following finite sums of Laurent series, which are analytic in the selected domain

$$\begin{aligned} g_1'(z_t) &= \sum_{k=0}^N C_k^{(1)} z_t^k, y > 0; \\ g_2'(z_t) &= \sum_{k=0}^N C_k^{(2)} z_t^k, y < 0. \end{aligned} \tag{22}$$

Here N is the number of terms. Utilising interface conditions (4) and (5) one can easily find the dependence between $C_k^{(1)}$ and $C_k^{(2)}$. After this these coefficients are determined in the following way. First, one computes the sum of squares of difference between given boundary conditions and temperature or heat flux obtained in Eq. (22) in a set of M points at the boundary of the square solid. Then this functional is minimised as in the least square approach to determine $C_k^{(1)}$ and $C_k^{(2)}$. Thus, the complex potentials (22) are obtained explicitly. Using Eqs (1) and (22) it is then easy to plot temperature change in the cross-section of a

square solid depending on the distance to the interface (for instance, Fig. 4 depicts plot for HCl with $\mu_0/\mu_0^* = 1$). Since, on the boundary $y = \frac{H}{2}$ temperature is $\theta = x^2$, then the graph of temperature change for $y > 0$ is parabolic (Fig. 4). The $y < 0$ plot shows that the temperature change is a linear function of coordinate, since we selected very high-temperature conductivity of the interface, and thus the temperature of the latter should be constant.

The same results were obtained using developed modified boundary elements method, which once again confirms its correctness.

Example 3. Consider the problem of plane strain for a thermomagnetoelastic anisotropic bimaterial consisting of two half-spaces. It contains a rectilinear elastic isotropic thermally insulated electro- and magnetically permeable inclusion of finite length $2a$. For its modelling the coupling principle for continua of different dimension is used [10]. In this example, it is assumed that the coefficients of linear thermal expansion of the inclusion material are zero. Its cross section is perpendicular to the bimaterial boundary (Fig. 5). One inclusion tip is located in the half-space $x_2 > 0$, and the other in the half-space $x_2 < 0$. The singularity at the point of intersection of the inclusion with the material interface is not accounted for. The centre of inclusion coincides with the origin. Inclusion thickness is $h = 0,01a$, and its relative rigidity is $k = \frac{G_i}{C_{11}}$.

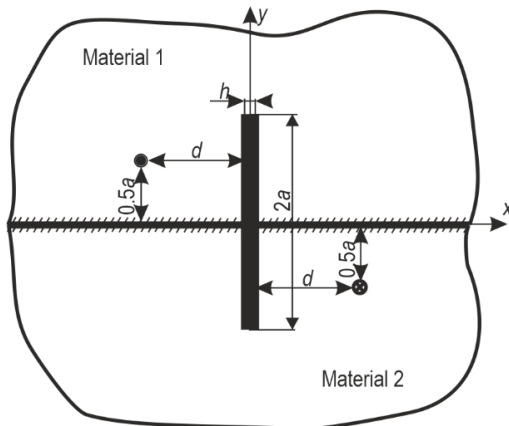


Fig. 5. Scheme of the problem for a thermomagnetoelastic anisotropic bimaterial containing a thin inhomogeneity

The heat source of intensity q is located in the half-space $x_2 > 0$ at a distance of $0,5a$ to the interface; heat drain of the same intensity q is located in the half-space $x_2 < 0$ also, at a distance of $0,5a$ to the interface antisymmetrically.

Two problems are considered:

- I) both bimaterial components are made of barium titanate (BaTiO_3);
- II) the component $x_2 > 0$ is made of barium titanate, and $x_2 < 0$ of cadmium selenide (CdSe).

According to [18], the properties of BaTiO_3 are as follows:

elastic moduli: $C_{11} = C_{33} = 150$, $C_{22} = 146$, $C_{12} = C_{13} = C_{23} = 66$, $C_{44} = C_{66} = 44$, $C_{55} = 42$;
 piezoelectric constants: $e_{21} = e_{23} = -4.35$, $e_{22} = 17,5$, $e_{16} = e_{34} = 11,4$;
 dielectric constants: $\kappa_{11} = 9,86775$, $\kappa_{22} = 11,151$;
 heat conduction coefficients: $k_{11} = k_{22} = 2.5$;

thermal expansion coefficients: $\alpha_{11} = 8.53 \cdot 10^{-6}$, $\alpha_{22} = 1.99 \cdot 10^{-6}$; pyroelectric constants: $\lambda_2 = 13,3 \cdot 10^{-6}$.

The properties of CdSe are as follows [19]:

elastic moduli: $C_{11} = C_{33} = 74.1$, $C_{22} = 83.6$, $C_{12} = C_{23} = 39.3$, $C_{13} = 45.2$, $C_{44} = C_{66} = 13.17$, $C_{55} = 14.45$;
 piezoelectric constants: $e_{21} = e_{23} = -0,160$, $e_{22} = 0,347$, $e_{16} = e_{34} = -0,138$;
 dielectric constants: $\kappa_{11} = 0.0826$, $\kappa_{22} = 0,0903$;
 heat conduction coefficients: $k_{11} = 1$, $k_{22} = 2.5$;
 thermal expansion coefficients: $\beta_{11} = \beta_{33} = 0,621$, $\beta_{22} = 0,551$;
 pyroelectric constants: $\chi_2 = -2,94 \cdot 10^{-6}$.

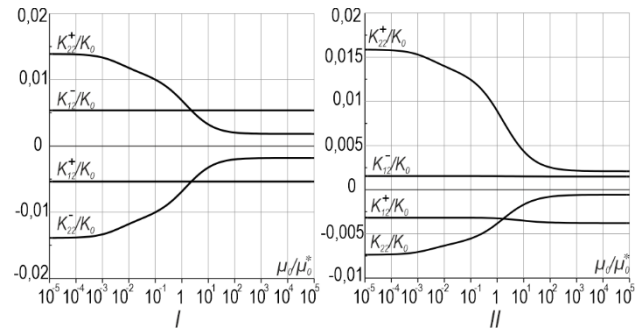


Fig. 6. Dependence of dimensionless generalised SIFs of the inclusion in an infinite body on the parameter of the interface μ_0

The plots in Fig. 6 show the dependence of the dimensionless stress intensity factors on the thermal conductivity parameter of the interface μ_0 . All calculations were performed by the above-mentioned method of boundary elements [6], [8]. 20 boundary elements were used to model the inclusion surface. With a further increase in the number of elements, the results obtained differ by $< 0.5\%$. Generalised SIFs and thermal conductivity parameter are normalised by $K_0 = q\beta_{11} \sqrt{\pi a}/k_{11}$ and $\mu_0^* = ak_{11}$, respectively. Here k_{11} and β_{11} are coefficients of BaTiO_3 .

It is noticed that in the first case in Fig. 6 (I), when the components of the matrix are made of the same materials with geometric symmetry of the problem and asymmetry of temperature load, the values of stress intensity factors at opposite tips of the inclusion are expected to be the same in magnitude and opposite in sign. The maximum are dimensionless SIFs $K_{22}^+/K_0 = K_{22}^-/K_0$, $\approx 0,014$ for the high-temperature conducting interface at $\mu_0/\mu_0^* = 10^{-5}$.

When half-spaces have different properties but the same geometry of the problem and the same heat load (Fig. 6 (II)), the symmetry of the solution is obviously not observed. Since the material of the half-space $x_2 > 0$ is the same as in the previous case, the values of the SIFs at the inclusion tip located in this half-plane will change very little. However, at the inclusion tip, which is located in the lower half-space, the change in coefficients is more noticeable: when $\mu_0/\mu_0^* = 10^{-5}$ K_{22}^-/K_0 changes from 0.014 to 0.0075, and K_{12}^-/K_0 from 0.005 to 0.002.

Example 4. Now consider the bimaterial containing two identical inclusions that are perpendicular to the boundary. Their properties are the same as in the previous example. They are placed at a distance d to the axis x_2 . The heat source and drain of the same magnitude are located at a distance of $0,5a$ to the material interface and at the distance of $2d$ to the axis x_2 (Fig. 7).

As in the previous problem, we study the dependence of stress intensity factors on the thermal conductivity parameter of the interface μ_0 , ($\mu_0^* = ak_{11}$).

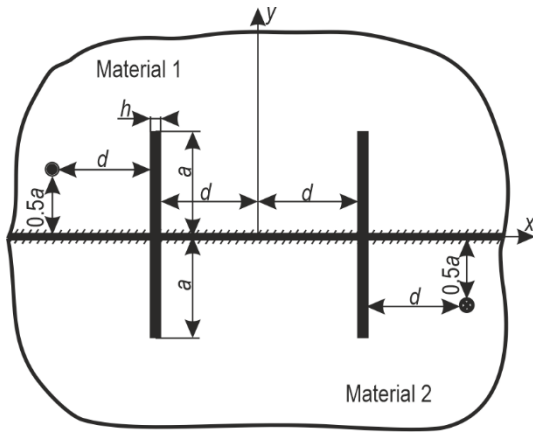


Fig. 7. Scheme of the problem for thermoelastic anisotropic bimaterial with two inclusions

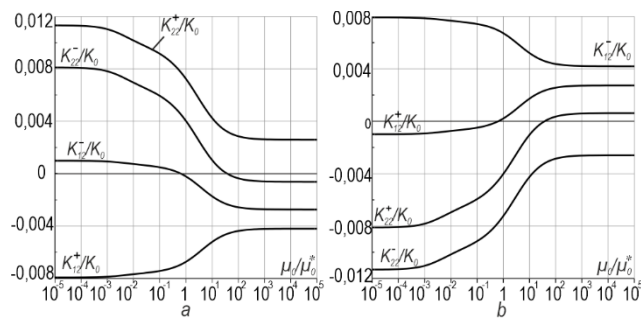


Fig. 8. Dependence of dimensionless generalised SIFs of two inclusions in an infinite body on the parameter of the interface μ_0 , when the components are made of the same materials

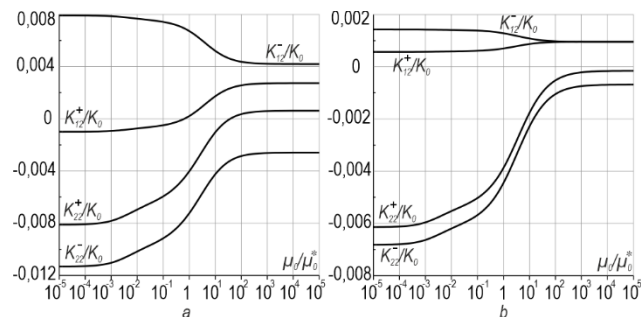


Fig. 9. Dependence of dimensionless generalised SIFs of two inclusions in an infinite body on the parameter of the interface μ_0 , when the components are made of different materials

The plots (Fig. 8) show the values of generalised SIFs for the (a) first and (b) second inclusions, when the components of the matrix are made of the same materials.

Due to the fact that the inclusions are identical in their properties and located symmetrically about the axes x_2 and x_1 , and the materials of the components have the same properties, the plots for both inclusions have a similar behaviour and differ only in sign. As in the previous problem, the maximum values of $K_{22}^+/K_0 = 0,011$ were obtained for $\mu_0/\mu_0^* = 10^{-5}$

Somewhat different results are observed in the case when the component $x_2 < 0$ of the bimaterial is made of a material, whose properties are different from $x_2 > 0$.

Fig. 9(a) shows that in this case the values of SIFs at the vertex of the first inclusion have undergone significant changes in comparison with the matrix of Fig. 8(a). The maximum value

K_{22}^+/K_0 increased from 0.011 to 0.014; and K_{22}^-/K_0 from 0.008 to 0.012. The values K_{12}^-/K_0 have also increased.

By contrast, at the tip of the second inclusion, the values of SIFs decreased. Fig. 9(b) shows that the maximum value K_{22}^-/K_0 decreased from 0.011 to 0.0078; K_{22}^+/K_0 from 0.008 to 0.0061. Also, at the upper and lower ends of the second inclusion approach the value of 0.001 at $\mu_0/\mu_0^* = 10^2$.

6. CONCLUSION

A mathematical model of a thermomagnetoelastic bimaterial solid with a high-temperature conducting coherent interface and a perfect magnetoelastomechanical contact of components has been developed, which in turn may contain thin deformable inclusions. In a closed form, purely boundary integral equations of the formulated problem are derived. That is, equations in which there is no need to take into account the integrals along the interface; thus, the boundary element mesh is required only for the boundary of the composite body and the midline of the thin inclusions.

The method can be extended to account for inclusions at the bimaterial interface; however, the oscillating singularity at its tip should be accounted for, which is beyond the scope of the present publication. Nevertheless, the present paper accounts for imperfect interface, which physically means a thin layer of different properties on the bimaterial interface, which is very important in practical applications.

The use of the obtained integral equations in combination with the boundary element method allows to solve several new problems for bimaterials consisting of the same and different anisotropic thermomagnetoelastic materials, as well as containing thin deformable inclusions. Graphical dependences of generalised SIFs on the thermal conductivity parameter are derived. The obtained results show that the high thermal conductivity interface significantly affects the stress fields at the vertices of thin inclusions.

All this allows to state that the developed method allows to solve with high accuracy the problem of thermomagnetoelasticity for bimaterial solids with a high-temperature conducting interface with thin ribbon-like deformable inclusions or cracks, which has not been possible so far using traditional numerical approaches.

REFERENCES

1. Kaessmair S, Javili A, Steinmann P. Thermomechanics of solids with general imperfect coherent interfaces. *Archive of Applied Mechanics*. 2014;84: 1409-1426. <https://doi.org/10.1007/s00419-014-0870-x>
2. Benvensite Y. A general interface model for a three-dimensional curved thin anisotropic interphase between two anisotropic media. *Journal of the Mechanics and Physics of Solids*. 2006;54: 708-734. <https://doi.org/10.1016/j.jmps.2005.10.009>
3. Pasternak I, Pasternak R, Sulym H. Boundary integral equations and Green's functions for 2D thermoelectroelastic biomaterial. *Engineering Analysis with Boundary Elements*. 2014;48: 87-101. <https://doi.org/10.1016/j.enganabound.2014.06.010>
4. Pasternak I, Pasternak R, Sulym H. 2D boundary element analysis of defective thermoelectroelastic bimaterial with thermally imperfect but mechanically and electrically perfect interface. *Engineering Analysis with Boundary Elements*. 2015;61: 194-206. <https://doi.org/10.1016/j.enganabound.2015.07.012>

5. Muskhelishvili NI. Singular Integral Equations: Boundary Problems of Function Theory and Their Application to Mathematical Physics. First Edition. Mineola: Dover Publications; 2008.
6. Hwu C. Anisotropic elastic plates. London: Springer; 2010.
7. Ting TC. Anisotropic elasticity: theory and applications. New York: Oxford University Press; 1996.
8. Pasternak I. Boundary integral equations and the boundary element method for fracture mechanics analysis in 2D anisotropic thermoelasticity. *Engineering Analysis with Boundary Elements*. 2012;36(12): 1931-41.
<https://doi.org/10.1016/j.enganabound.2012.07.007>
9. Pasternak I. Coupled 2D electric and mechanical fields in piezoelectric solids containing cracks and thin inhomogeneities. *Engineering Analysis with Boundary Elements*. 2011;23: 678-90.
<https://doi.org/10.1016/j.enganabound.2010.12.001>
10. Sulym GT. Bases of the Mathematical Theory of Thermoelastic Equilibrium of Deformable Solids with Thin Inclusions [inUkrainian]. Lviv: Dosl.-Vyd. Tsentr NTSh; 2007.
11. Pan E, Amadei B. Boundary element analysis of fracture mechanics in anisotropic bimetals. *Engineering Analysis with Boundary Elements*. 1999;23: 683-91.
[https://doi.org/10.1016/S0955-7997\(99\)00018-1](https://doi.org/10.1016/S0955-7997(99)00018-1)
12. Wang X, Pan E. Thermal Green's functions in plane anisotropic bimetals with spring-type and Kapitza-type imperfect interface. *Acta Mechanica et Automatica*. 2010;209: 115-128.
<https://doi.org/10.1007/s00707-009-0146-7>
13. Sladek J, Sladek V, Wuensche M, Zhang, Ch. Analysis of an interface crack between two dissimilar piezoelectric solids. *Engineering Fracture Mechanics*. 2012;89: 114-27.
<https://doi.org/10.1016/j.engfracmech.2012.04.032>
14. Wang TC, Han XL. Fracture mechanics of piezoelectric materials. *International journal fracture mechanics*. 1999;98: 15-35.
<https://doi.org/10.1023/A:1018656606554>
15. Qin QH. Green's function and boundary elements of multifield materials. Oxford: Elsevier Science; 2007.
16. Yang J. Special topics in the theory of piezoelectricity. London: Springer; 2009.
17. Pasternak I, Pasternak R, Sulym H. A comprehensive study on the 2D boundary element method for anisotropic thermoelectroelastic solids with cracks and thin inhomogeneities, *Engineering Analysis with Boundary Elements*. 2013;37(2): 419-33.
<https://doi.org/10.1016/j.enganabound.2012.11.002>
18. Dunn ML. Micromechanics of coupled electroelastic composites: Effective thermal expansion and pyroelectric coefficients. *Journal of Applied Physics*. 1993;73: 5131-40.
<https://doi.org/10.1063/1.353787>
19. Berlincourt D, Jaffe H, Shiozawa LR. Electroelastic properties of the sulfides, selenides, and tellurides of zinc and cadmium. *Physical Review*. 1963;129: 1009-17.
<https://doi.org/10.1103/PhysRev.129.1009>

Heorhiy Sulym:  <https://orcid.org/0000-0003-2223-8645>

Andrii Vasylyshyn:  <https://orcid.org/0000-0002-5703-6894>

Iaroslav Pasternak:  <https://orcid.org/0000-0002-1732-0719>

REVERSE ENGINEERING OF PARTS WITH ASYMMETRICAL PROPERTIES USING REPLACEMENT MATERIALS

Mehmet ALADAG^{***}, Monika BERNACKA^{****}, Magdalena JOKA-YILDIZ^{****},
 Wojciech GRODZKI^{*}, Przemysław ZAMOJSKI^{*}, Izabela ZGŁOBICKA^{*}

^{*}Faculty of Mechanical Engineering, Białystok University of Technology, ul. Wiejska 45C, 15-351 Białystok, Poland

^{**}Faculty of Mechanical Engineering, Gaziantep University, Osmangazi, Üniversite Blv., 27410 Sehitkamil/Gaziantep, Turkiye

^{***}Technology Applied Sp. z o.o., ul. Wiejska 42/3, 15-509 Sobolewo, Poland

^{****}Faculty of Civil Engineering and Environmental Sciences, Białystok University of Technology, ul. Wiejska 45E, 15-351 Białystok, Poland

mmehmetaladag@gmail.com, monika6@wp.pl, m.joka@pb.edu.pl,
w.grodzki@pb.edu.pl, p.zamojski@doktoranci.pb.edu.pl, i.zglobicka@pb.edu.pl

received 17 March 2022, revised 31 May 2022, accepted 13 June 2022

Abstract: Reverse engineering (RE) aims at the reproduction of products following a detailed examination of their construction or composition. Nowadays, industrial applications of RE were boosted by combining it with additive manufacturing. Printing of reverse-engineered elements has become an option particularly when spare parts are needed. In this paper, a case study was presented that explains how such an approach can be implemented in the case of products with asymmetric mechanical properties and using replacement materials. In this case study, a reverse engineering application was conducted on a textile machine spare part. To this end, the nearest material was selected to the actual material selection and some mechanical tests were made to validate it. Next, a replacement part was designed by following the asymmetric push-in pull-out characteristic. Finally, the finite element analysis with Additive Manufacturing was combined and validated experimentally.

Keywords: material characterisation, reverse engineering, additive manufacturing, finite element analysis, rapid prototyping

1. INTRODUCTION

Reverse engineering (RE) is nowadays widely used for solving problems related to the fabrication of spare parts for devices already in use for which full technical documentation is no longer available and/or spare parts can hardly be found. The frequency of such situations is expected to be increasing in the coming years because of current trends for extending the service time of devices stimulated by environmental concerns (R3 principle: reduce, re-use, re-cycle) [1]. Moreover, the parts that are remanufactured with high-added value by various manufacturing methodologies have claimed to gain environmental benefits. Accordingly, comparing the life cycle assessment with the parts which are manufactured, remanufactured parts have the advantage regarding environmental attractiveness [2].

The popularity of RE has also increased with easier access to 3D printers, particularly using polymeric materials. However, standard printers are utilising a relatively low number of substrates, far lower than the number of construction and functional engineering materials. Thus, an efficient approach to RE and fabrication of replacement parts might require, in some cases, the use of replacement materials with properties differing from the ones used by a manufacturer of the original element [3].

In this case study of industrial importance, the selected replacement part is made from a rubber material since rubber as such is not as of yet a printing material [4–8]. Thermoplastic polyurethane (TPU) was selected as a replacement [9, 10], which

is an additively manufacturable material and has good material properties in terms of ductility, shock absorption resistance and excellent biomedical application compatibility [11–16]. There are several studies reported in the literature on the mechanical properties of elements made of TPU by additive manufacturing [17–19]. In addition, TPU allows for printing high-porous, low-density structures. Thus, functionally graded parts can be printed and by printing lattice type structures, elements of pre-defined stiffness can be produced [20–24].

The similar studies have been made by the researchers. Ponticelli et al. [25] studied the RE of an Impeller for submersible electric pump. In their study, an impeller was engineered by using RE techniques and fabricated by selective laser melting (SLM) method. In addition, Hernández and Fragoso [26] studied manufacture of a pump impeller by integration of 3D sand printing and casting. An impeller was scanned by 3D scanner. After that, the cavity geometry was manufactured by 3D sand printer by using binder jet printing method to make a casting operation. By following the casting steps, the part cast with a AISI 316 cast stainless steel. To obtain thin final geometry, a post-processing operation was made on the cast part and, thus, the final geometry was obtained.

In this paper, an approach was demonstrated that can be used to RE geometry (reproduction of size and shape) and material properties (reproduction properties using replacement materials) at the same time. The advantages of the approach proposed, which is based on Finite Element Modelling, are

demonstrated using a case study of industrial relevance. The current paper can also be viewed as presenting advantages of additive manufacturing (AM), in the fabrication of replacement parts, RP, in a wide range of industries [27–29].

2. PROBLEM DEFINITION

The proposed approach to RE allowed the use of replacement materials demonstrated for a rubber machine part as shown in Fig. 1. This is a textile machine yarn pass that has been damaged in extended in-service conditions.



Fig. 1. Damaged textile machine yarns pass analyzed

The original yarn pass was made of rubber, for which as of yet no 3D printing technology exists. In this situation, a decision was made to print the part in question using thermoplastic polyurethane, TPU. This is a block copolymer consisting of alternating sequences of hard segments (isocyanates) and soft segments (reacting polyol). Because of those properties, TPU can be shaped by adjusting the number of hard segments. Its hardness may range from 60A (similar to soft silicones) to 80D (equivalent to nylons or rigid PVC) [10]. In addition, it has good thermal stability and is quite easy to print using fused deposition modelling (FDM) or selective laser sintering (SLS) 3D printers. The SLS process has been chosen in the current case, which is considered a friendly manufacturing technique for plastic parts [30]. In addition, in the SLS method, complex parts can be fabricated without building support, printing time and cost. Also, the surface quality of the part manufactured by the SLS method is higher than the other 3D printing methods and does not require additional post-processing operation [31–33].

3. MATERIALS AND METHODS

3.1. Textile Machine Yarn Part Pass Geometry Engineering

The part was initially digitalized by a 3D scanner and, the dot clouds were generated. After that, it was converted to polygon and, exported polygon geometry as STL file format. Using NX 12 the part was re-designed with the tolerances ± 0.1 mm and, obtained a fully parametric solid model. The polygon model and solid model were given in Fig 2.

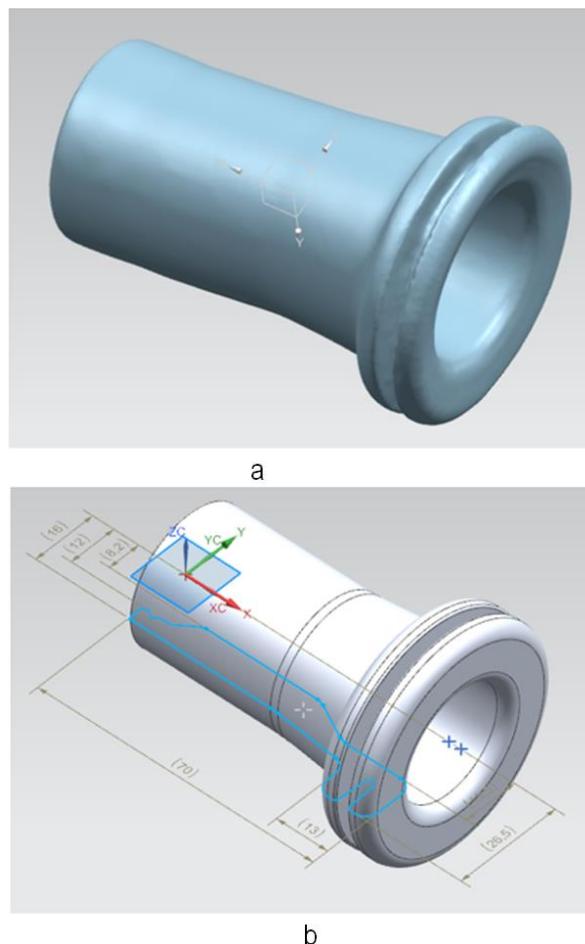


Fig 2. Textile machine yarn pass part; a) 3D scanned file polygon model, b) engineered solid model

3.2. Powder Characterisation

In this study, the TPU powder size distribution is a parameter in the context of selecting printing parameters. Accordingly, the size distribution of the powder was obtained with Analysette 22 MicroTec (Fritsch, Germany). For the same reasons, thermal properties of TPU used were investigated by a differential scanning calorimetry (DSC) and, thermogravimetric analysis (TGA). The thermal analyses were carried out using the TG 209 F1 Libra (Netsch, Germany) devices. Consequently, the powder shape is the last parameter that has significance in terms of the distribution quality on the bed. Thus, the powders were imaged under the Scios2 (ThermoFisher, USA) scanning electron microscopy (SEM). Results of the respective investigations are presented and results are discussed..

3.3. Part Characterisation

Replacement of original with some alternatives obviously requires thorough characteristics of materials considered. Usually, the needed characteristics were made available by materials suppliers. However, in the case of fabrication by 3D printing we should consider that the properties of printed material depend on the printing parameters. Thus, in order to replace the rubber part with TPU printed one, the mechanical properties of printed samples were measured in tensile and compression tests.

3.4. Tensile Test Specimen

Tensile tests specimens were prepared according to ISO 527-2 polymer tensile test standard [34] in the size and shape as given

in Fig. 3. The tensile tests samples were printed in two direction layouts; three of them are in the x-direction and, the others were in the y-directions as explained in Fig. 4.

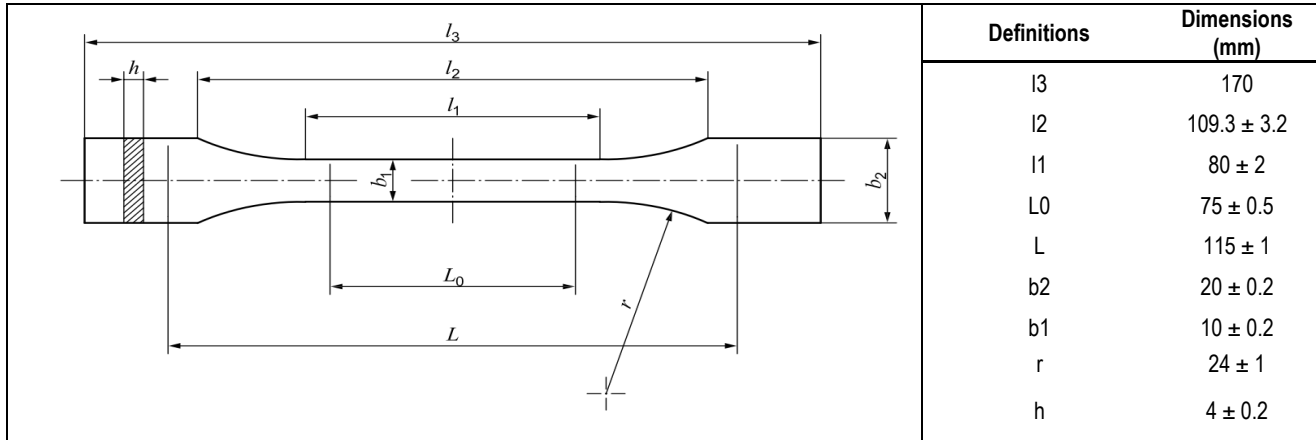


Fig. 3. Tensile test sample drawing and its dimensions



Fig. 4. Layout view on building table and specimens

3.5. Compression Test Specimen

In this study, two compression tests were conducted; one is full dense printed specimen and, the second one is lattice-type high porous specimen. The full dense printed specimen compression tests were conducted according to the ISO 7743 standard [35] using the specimens of width, height and depth of 10 ± 0.05 mm, shown in Fig. 5.

In addition to fully dense specimens, mechanical properties of lattice-type highly porous elements are also measured as shown in Fig. 6. The motivation for testing properties of such

structures was the recognition that TPU is significantly stiffer than the rubber used in the original part. Therefore, the replacement of rubber with TPU required a significant reduction in the stiffness which could be achieved by increasing its porosity [36]. To some degree, two specimens that have porous structures tested in this study can be viewed as a meta-material analogue of the rubber used in the original part.



Fig. 5. Compression test specimens

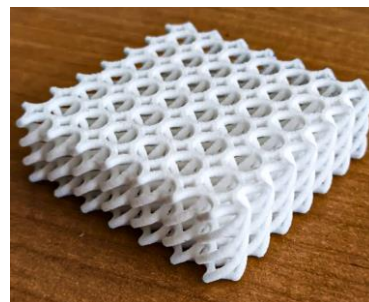


Fig. 6. An example of a highly porous element tested in compression tests

3.6. 3D Printing of the Samples

The specimens for testing mechanical properties were produced by SLS method. A 3D printer EOS P 396 was used, operated by Technology Applied Ltd. [37, 38]. The TPU powder

brand was TPU EOS 1301 white. In addition, the printing parameters were defined in accordance with the powder manufacturer catalogue. The catalogue information about SLS printer settings and TPU powder were given in Tab. 1 and 2.

Tab. 1. Printing parameters

Parameter	Unit	Value
Powder bed temperature	°C	108
Wavelength	µm	10.20–10.80
Process chamber	°C	108
Removal chamber	°C	60
Laser power	Watt	30
Laser scan speed	m/sec	5
Layer thickness	mm	0,1

Tab. 2. TPU Powder properties [39]

Parameter	Unit	Value
Melting temperature	°C	138
Bulk density	g/cm ³	0.49
Flowability	s	17
Particle size d10	µm	22
Particle size d50	µm	72
Particle size d90	µm	138

3.7. FEM-Based Design Replacement Part

The model printed is engineered within the tolerances ± 0.1 mm by using NX 12. The engineered shape of the yarn pass is shown in Fig. 7. In the analytical part of designing, the inner and outer dimensions were kept fixed, and studied the performance of the spare part to-be-printed in the assembly process as well as its in-service stability.

The original part made of rubber was characterized by asymmetrical mechanical properties manifested by the difference encountered in push-in and pull-out actions. It is easy to insert and difficult to remove, assuring that it remains in a fixed position after installing. In the approach reported here, it is assumed that the required properties of the replacement part made of TPU can be obtained by printing an analogue that will contain specifically

located regions of high porosity. Also, the fish-bone concept is proposed to design the architecture of the porous regions. The fish-bone concept schematically was shown in Fig. 8.

An example of a design carried out in the study is shown in Fig. 9. It can be noted that the porous regions are placed in the external flange and that the cell-type architecture of these regions is highly anisotropic.



Fig. 7. The engineered views of textile yarn pass



Fig. 8. Fishbone geometry imparting asymmetric reaction of push-in and pull-out

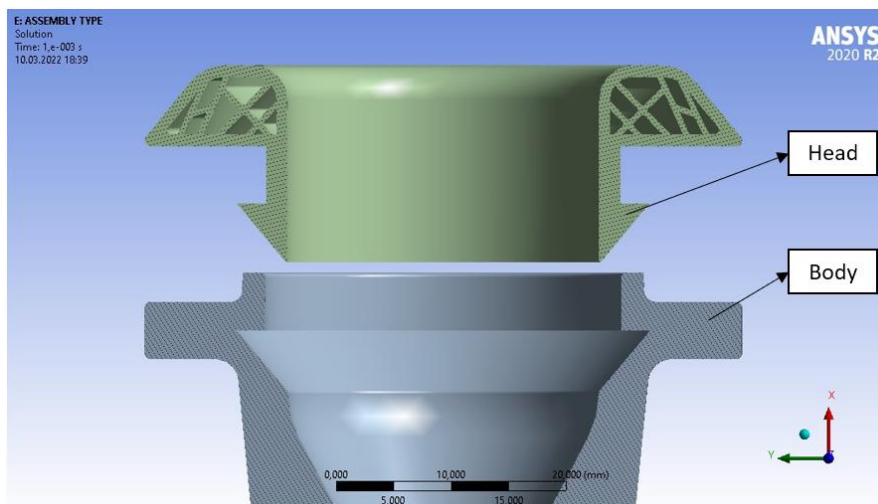


Fig. 9. An example of the design considered in the present study

4. RESULTS AND DISCUSSION

4.1. Characterisation of TPU powder

The TPU powder size distribution and representative SEM images were shown, respectively, in Fig. 10 and 11. It can be noted that the average size is exceeding 0.15 mm and the powder particles are irregular in shape. These two factors contribute to relatively rough surfaces of the prints obtained with this powder. However, high surface roughness in this case has no negative effect on the performance of the spare parts to be printed. Melting and glass transition temperatures estimated by DSC analysis, are 134 and 110°C, respectively (see Fig. 12). These two temperatures define ‘temperature window’ to be exploited in selecting the printing conditions.

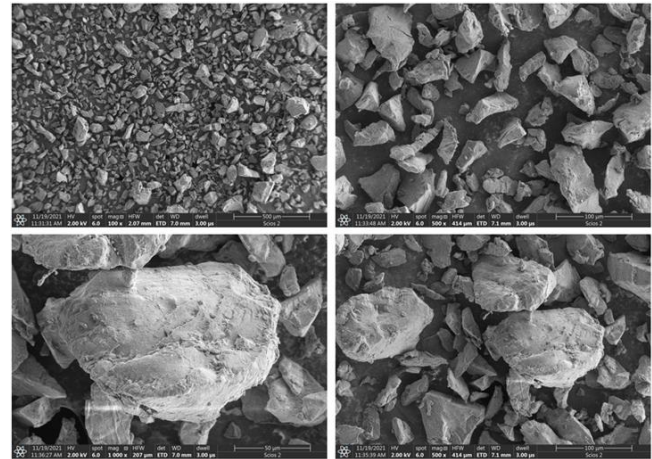


Fig. 11. SEM images of TPU powder shape

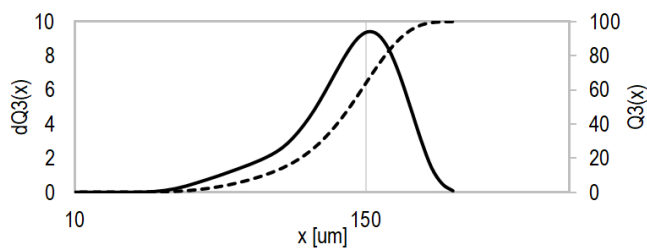


Fig. 10. Particle size distribution of TPU powder

4.2. Full Dense Material Tension Test Results

Compression/tensile tests were conducted using the MTS Bionics machine and a video extensometer. The results of the tensile test of fully dense samples are shown in Fig. 13. The maximum stress value is approximately 6 MPa. The tensile modulus was calculated as 69.5 MPa. The manufacturer’s test values were maximum stress 7 MPa in X and Y-directions and, the tensile modulus was 70 MPa [39]. In addition, the Poisson’s ratio is calculated for each tensile specimen. The Fig. 14 shows that the average value of Poisson’s ratio is 0.48. It is seen that the Poisson’s ratio is also proper for general rubber material class.

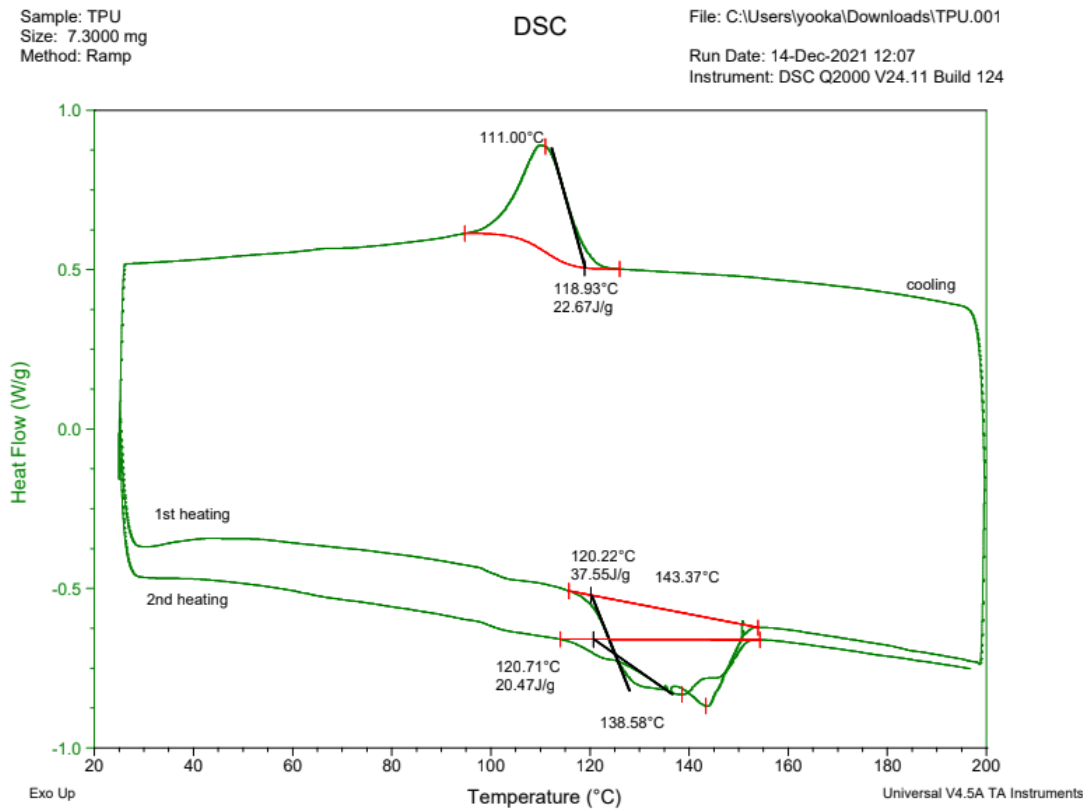


Fig. 12. DSC Scan of TPU powder

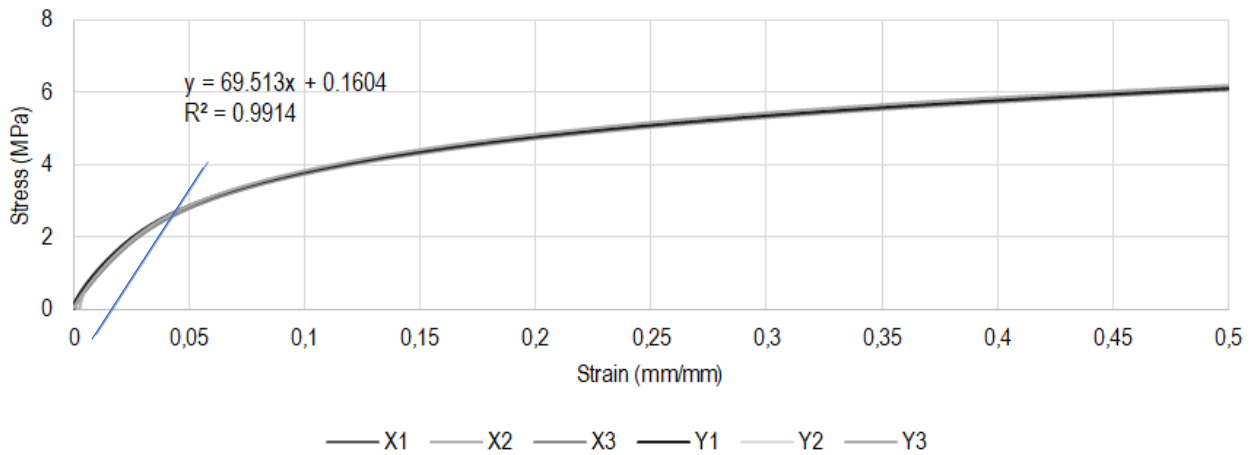


Fig. 13. Strain stress curves for fully dense printed samples of TPU

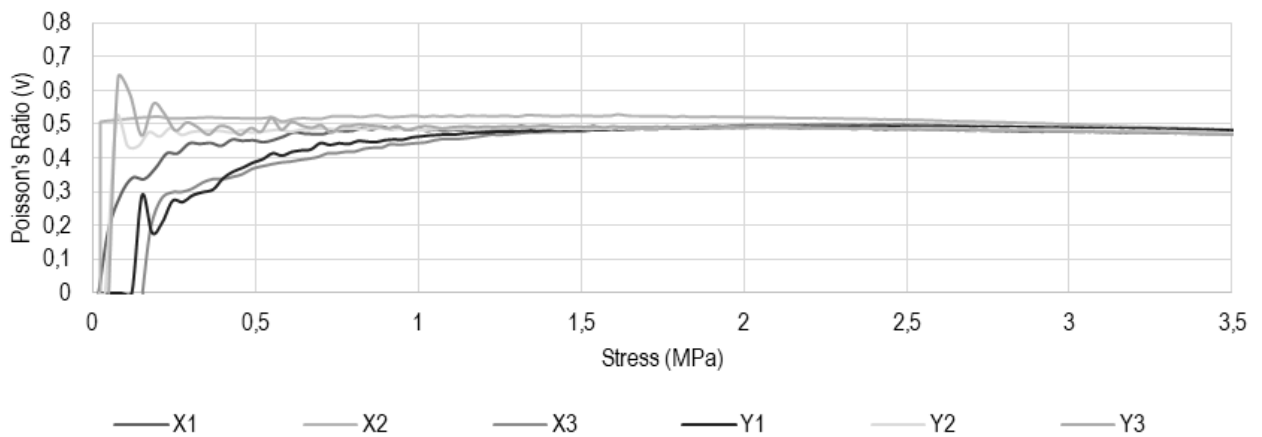


Fig. 14. The Poisson's curves for the specimens tested

4.3. Compression Test Results

The full dense printed sample compression tests were conducted in the MTS Bionics Tensile test machine on six same samples. The plotted stress-strain curves are in a great deal with all the compression test specimen. The load-displacement curve was given in Fig 15. The encountered stress is approximately 28 MPa. The values show that the specimens are stiffer under compressive load comparing to the tensile load. Further, the compressive stress value is approximately 4–5 times larger than the tensile strength.

Compression curves for highly porous structures are shown in

Fig. 16. The stress and strain have been calculated assuming the external dimensions of the specimens. The calculated stress value in the porous specimen is 0.058 MPa. It can be noted that the apparent stress is much lower than the full dense compression specimen.

Experimental Poisson number curves are plotted in Fig. 17. The curves have revealed some differences, which are expected for highly porous lattice-type prints. Nevertheless, one can assume that Poisson ratio of 0.07 can be used as an approximation for the samples obtained in the current study. Note that the latticed structure decreases the stiffness and the Poisson ratio significantly.

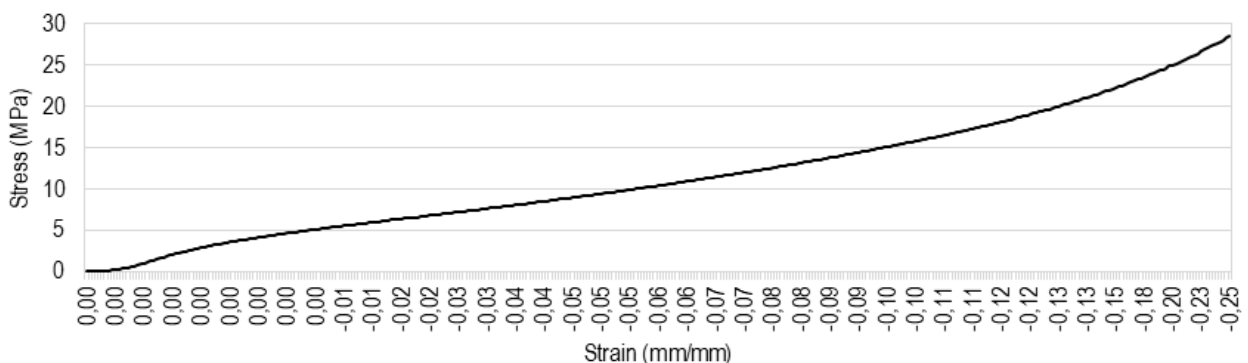


Fig 15. Stress-Strain curve of full dense printed material

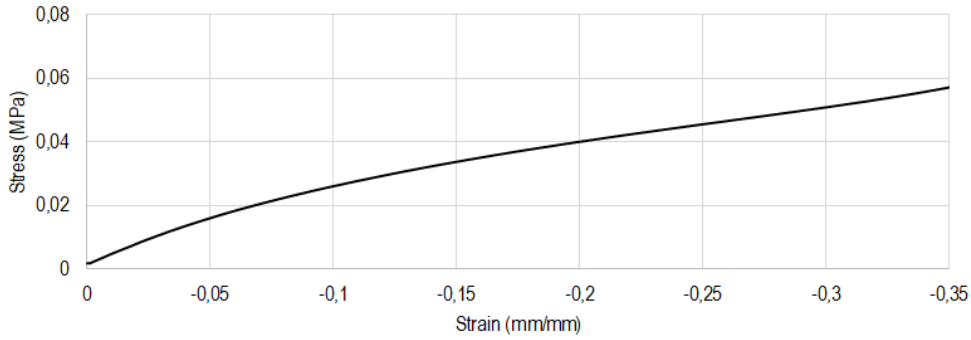


Fig. 16. Stress-strain curves for highly porous structure

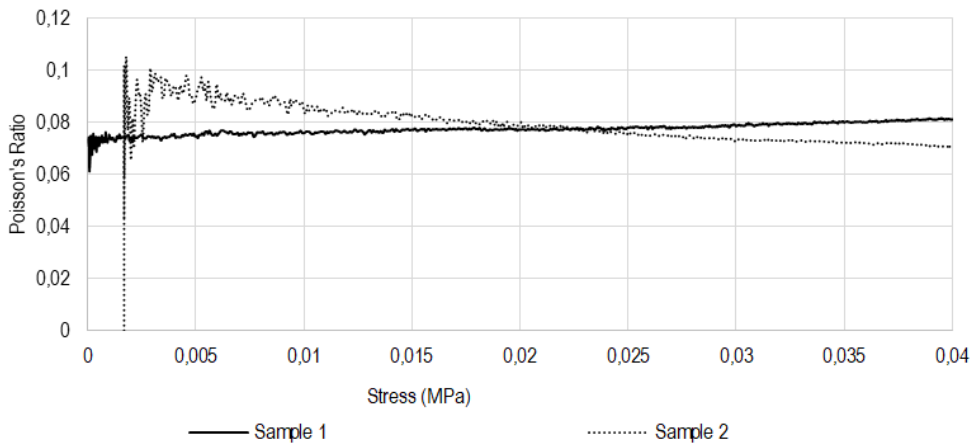


Fig. 17. The Poisson number curves for highly porous structure

4.4. FEA For Designed Replacement Part

The proposed replacement part has been analysed by finite element analysis (FEA) and the results obtained are given in Fig. 18. The equivalent maximum stress is seen not to exceed 5 MPa with the yield strength of the used TPU at 6 MPa. Hence, the maximum elastic strain is approximately 0.058 mm/mm. The value of average contact pressure is approximately 2 MPa. This also will

provide satisfying holding force after assembly. The old replacement part is made as a single part, which makes assembling difficult; it requires more force, and therefore, the part is deformed severely. Thus, the part has a high potential to deform in the beginning. In the recommended design, it has been designed in two parts which make assembly easier. Therefore, thanks to the push-in pull-out characteristic the assembly of the replacement part will be done easily.

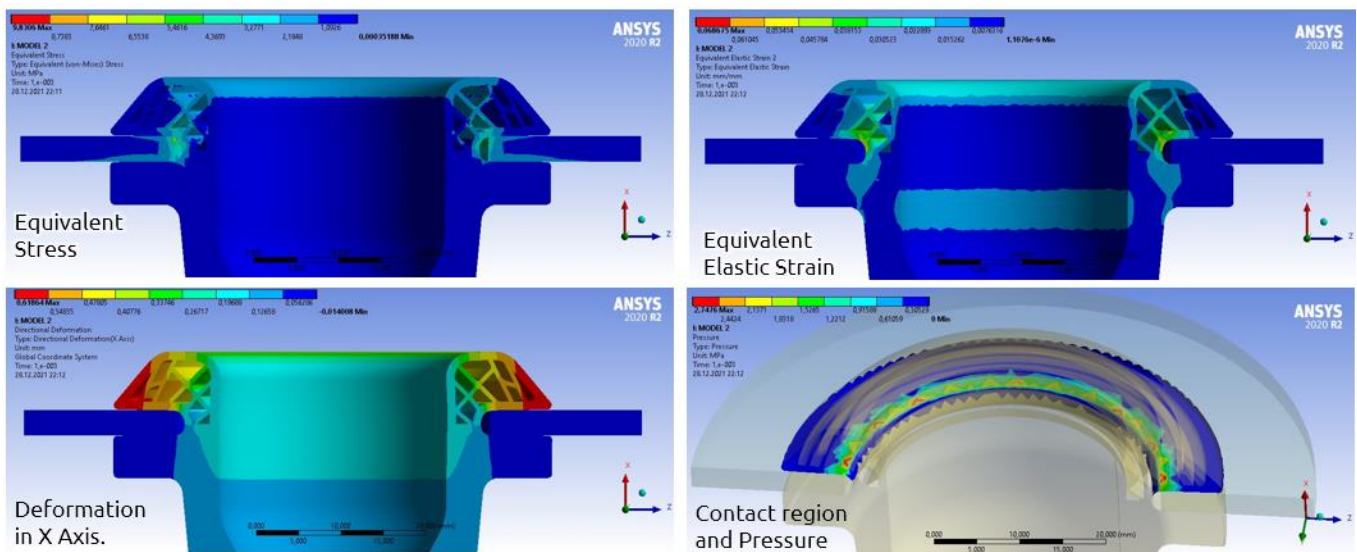


Fig. 18. Results of the stress-strain analysis using FEM for the replacement part schematically shown in Fig. 9

Based on the results of FEM, a design offering the best compliance with the characteristics of the original part has been selected. In further steps, the replacement part was printed and successfully tested. Fig. 19 shows selected replacement parts view after printing.

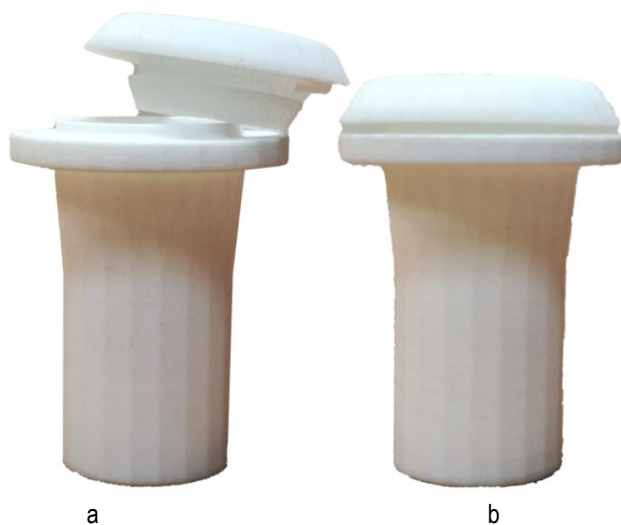


Fig. 19. Printed view of FEM based designed part; a) before assembly, b) after assembly

5. CONCLUSIONS

The results presented in the paper demonstrate an efficient approach to the fabrication of parts using efficient materials substituting the ones used in manufacturing of the originals. The approach adopted here can be summarized with the following points.

- The textile machine part that was strategically important was designed by following the RE application procedure, and has been manufactured by AM successfully.
- In the current case, the key characteristic is the asymmetric push-in pull-out characteristic of the part. By using this characteristic, the replacement part has been designed accordingly and hence, the assembly of the part became more easier.
- Selection of replacement material suitable for 3D printing of the part is accomplished and further exploring mechanical properties of the elements printed into fully dense and porous structures were made. Thus, adding geometrical features i.e. lattice structure in some regions, provided less stiffness on the part.
- Tensile and compression tests of TPU material have been conducted to characterize the mechanical properties and the obtained results have been adopted in FEA software and validated.
- The designed replacement part was subjected to FEA in order to analyse the stresses that will be encountered after the assembly. Thus, in accordance with the FEA performance, the stresses developed were observed and concluded there will be no failure after the assembly.
- The printing time is 2 h and the printing cost is c.a.15 USD.
- Finally, the replacement part has been fabricated by an SLS 3D printer and tested. It has been validated as it works properly onsite.

REFERENCES

1. The 3R Initiative, <https://www.env.go.jp/recycle/3r/en/outline.html> (accessed March 11, 2022).
2. Peng S, Ping J, Li T, et al. Environmental benefits of remanufacturing mechanical products: a harmonized meta-analysis of comparative life cycle assessment studies. *Journal of Environmental Management*; 306. 2022. DOI: 10.1016/J.JENVMAN.2022.114479.
3. Geng Z, Sabbaghi A, Bidanda B. Reconstructing Original Design: Process Planning for Reverse Engineering. DOI: 10.1080/24725854.2022.2040761.
4. Shahrubudin N, Lee TC, Ramlan R. An Overview on 3D Printing Technology: Technological, Materials, and Applications. *Procedia Manufacturing* 2019;35:1286–1296.
5. Harris CG, Jursik NJS, Rochefort WE, et al. Additive Manufacturing With Soft TPU – Adhesion Strength in Multimaterial Flexible Joints. *Front Mech Eng* 2019;5:37.
6. Xiao J, Gao Y. The manufacture of 3D printing of medical grade TPU. *Progress in Additive Manufacturing* 2017;3:117–123.
7. Haryńska A, Gubanska I, Kucinska-Lipka J, et al. Fabrication and Characterization of Flexible Medical-Grade TPU Filament for Fused Deposition Modeling 3DP Technology. *Polymers (Basel)*; 10. Epub ahead of print November 25, 2018. DOI: 10.3390/POLYM10121304.
8. Herzberger J, Sirrine JM, Williams CB, et al. Polymer Design for 3D Printing Elastomers: Recent Advances in Structure, Properties, and Printing. *Progress in Polymer Science* 2019;97:101144.
9. Rodríguez-Parada L, de la Rosa S, Mayuet PF. Influence of 3D-Printed TPU Properties for the Design of Elastic Products. *Polymers (Basel)* 2021;13:2519.
10. American Chemistry Council. Thermoplastic Polyurethanes Bridge the Gap between Rubber and Plastics, <https://www.americanchemistry.com/industry-groups/center-for-the-polyurethanes-industry-cpi/resources/library/thermoplastic-polyurethanes-bridge-the-gap-between-rubber-and-plastics> (2002, accessed January 17, 2022).
11. Xu T, Shen W, Lin X, et al. Mechanical properties of additively manufactured thermoplastic polyurethane (TPU) material affected by various processing parameters. *Polymers (Basel)* 2020;12:1–16.
12. Lee H, Eom RI, Lee Y. Evaluation of the mechanical properties of porous thermoplastic polyurethane obtained by 3D printing for protective gear. *Advances in Materials Science and Engineering*; 2019. Epub ahead of print 2019. DOI: 10.1155/2019/5838361.
13. Lu QW, Macosko CW, Horion J. Compatibilized blends of thermoplastic polyurethane (TPU) and polypropylene. *Macromolecular Symposia* 2003;198:221–232.
14. Mi HY, Salick MR, Jing X, et al. Characterization of thermoplastic polyurethane/polylactic acid (TPU/PLA) tissue engineering scaffolds fabricated by microcellular injection molding. *Materials Science and Engineering: C* 2013;33:4767–4776.
15. Li W, Liu J, Hao C, et al. Interaction of thermoplastic polyurethane with polyamide 1212 and its influence on the thermal and mechanical properties of TPU/PA1212 blends. *Polymer Engineering & Science* 2008;48:249–256.
16. Feng F, Ye L. Morphologies and mechanical properties of polylactide/thermoplastic polyurethane elastomer blends. *Journal of Applied Polymer Science* 2011;119:2778–2783.
17. Rodríguez L, Naya G, Bienvenido R. Study for the selection of 3D printing parameters for the design of TPU products. *IOP Conference Series: Materials Science and Engineering* 2021;1193:012035.
18. Schmid M, Amado A, Wegener K. Polymer powders for selective laser sintering (SLS). *AIP Conference Proceedings*; 1664. Epub ahead of print May 22, 2015. DOI: 10.1063/1.4918516.
19. Lupone F, Padovano E, Casamento F, et al. Process Phenomena and Material Properties in Selective Laser Sintering of Polymers: A Review. *Materials* 2022, 2021;15:183.
20. Shen F, Yuan S, Guo Y, et al. Energy Absorption of Thermoplastic Polyurethane Lattice Structures via 3D Printing: Modeling and Prediction. *International Journal of Applied Mechanics*; 8. Epub ahead of print 2016. DOI: 10.1142/S1758825116400068.

21. Kanbur Y, Tayfun U. Development of multifunctional polyurethane elastomer composites containing fullerene: Mechanical, damping, thermal, and flammability behaviors. *Journal of Elastomers and Plastics* 2019;51:262–279.
22. Beloshenko V, Beygelzimer Y, Chishko V, et al. Mechanical properties of flexible tpu-based 3d printed lattice structures: Role of lattice cut direction and architecture. *Polymers (Basel)* 2021;13:1–11.
23. Ursini C, Collini L. Fdm layering deposition effects on mechanical response of tpu lattice structures. *Materials*; 14. Epub ahead of print 2021. DOI: 10.3390/ma14195645.
24. Beloshenko V, Beygelzimer Y, Chishko V, et al. Mechanical Properties of Thermoplastic Polyurethane-Based Three-Dimensional-Printed Lattice Structures: Role of Build Orientation, Loading Direction, and Filler. *3D Printing and Additive Manufacturing* 2021; 3dp.2021.0031.
25. Ponticelli GS, Tagliaferri F, Venettacci S, et al. Re-Engineering of an Impeller for Submersible Electric Pump to Be Produced by Selective Laser Melting. *Applied Sciences* 2021, Vol 11, Page 7375 2021;11: 7375.
26. Hernández F, Fragoso A. Fabrication of a Stainless-Steel Pump Impeller by Integrated 3D Sand Printing and Casting: Mechanical Characterization and Performance Study in a Chemical Plant. *Applied Sciences* 2022;12:3539.
27. Zglobicka I, Chmielewska A, Topal E, et al. 3D Diatom–Designed and Selective Laser Melting (SLM) Manufactured Metallic Structures. *Scientific Reports*. 2019;9:1–9.
28. Zaoui M, Mohamad BA, Amroune S, et al. Manufacturing of rapid prototypes of mechanical parts using reverse engineering and 3D Printing. *J Serbian Soc Comput Mech* 2021;15:1–10.
29. Subeshan B, Abdulaziz A, Khan Z, et al. Reverse Engineering of Aerospace Components Utilizing Additive Manufacturing Technology. 2022;238–246.
30. Goodridge RD, Tuck CJ, Hague RJM. Laser sintering of polyamides and other polymers. *Progress in Materials Science* 2012;57:229–267.
31. Gueche YA, Sanchez-Ballester NM, Cailleaux S, et al. Selective Laser Sintering (SLS), a New Chapter in the Production of Solid Oral Forms (SOFs) by 3D Printing. *Pharmaceutics*. 2021; 13: 1212.
32. Tagliaferri V, Trovalusci F, Guarino S, et al. Environmental and Economic Analysis of FDM, SLS and MJF Additive Manufacturing Technologies. *Materials*. 2019;12:4161.
33. Kellens K, Renaldi R, Dewulf W, et al. Environmental impact modeling of selective laser sintering processes. *Rapid Prototyping Journal* 2014;20:459–470.
34. ISO527-2: Plastics — Determination of tensile properties — Part 2: Test conditions for moulding and extrusion plastics. *International Standard*.
35. ISO 7743: Rubber, vulcanized or thermoplastic — Determination of compression stress-strain properties. *International Standard*; 2017.
36. Bates SRG, Farrow IR, Trask RS. Compressive behaviour of 3D printed thermoplastic polyurethane honeycombs with graded densities. *Materials and Design* 2019;162:130–142.
37. Additive Manufacturing solutions & industrial 3D printer by EOS, <https://www.eos.info/en> (accessed January 18, 2022).
38. [Technology Applied - Zaufany dostawca części dla przemysłu, <https://ta.parts/> (accessed January 18, 2022).
39. EOS. Thermoplastisches Polyurethan EOS TPU 1301, https://webcache.googleusercontent.com/search?q=cache:90GEoHlUXOwJ:https://www.eos.info/03_system-related-assets/material-related-contents/polymer-materials-and-examples/tpu-1301/material_datasheet_eos_tpu_1301_core_de_web.pdf+&cd=3&hl=tr&ct=clnk&gl=pl&cl (accessed January 11, 2022).

Mehmet Aladag:  <https://orcid.org/0000-0002-2484-7519>

Monika Bernacka:  <https://orcid.org/0000-0003-3481-0768>

Magdalena Joka-Yildiz:  <https://orcid.org/0000-0002-4745-5972>

Wojciech Grodzki:  <https://orcid.org/0000-0002-0068-9683>

Przemysław Zamojski:  <https://orcid.org/0000-0002-3736-8840>

Izabela Zglobicka:  <https://orcid.org/0000-0002-4432-9196>

IMPACT OF CUTTING UNITS' DESIGN ON BIOMASS CUTTING RESISTANCE

Marcin ZASTEMPOWSKI^{*}, Andrzej BOCHAT^{*}, Lubomir HUJO^{**},
Juraj JABLONICKY^{**}, Maciej JANIEC^{*}

^{*}Bydgoszcz University of Science and Technology, Faculty of Mechanical Engineering,
Al. prof. S. Kaliskiego 7, 85-796 Bydgoszcz, Poland

^{**}Slovak University of Agriculture in Nitra, Faculty of Engineering, Trieda Andreja Hlinku 2, 949 76 Nitra, Slovakia

marcin.zastempowski@pbs.edu.pl, bochat@pbs.edu.pl, lubomir.hujo@uniag.sk, juraj.jablonicky@uniag.sk, macjan002@pbs.edu.pl

received 13 May 2022, revised 1 July 2022, accepted 10 July 2022

Abstract: The paper presents mathematical models describing the moments of resistance to cutting on the cutting drum shafts in the biomass cutting process. The mathematical procedures described in the paper have been verified on a test stand developed and constructed by the authors, which reflects real conditions of the process of cutting plant material into pieces of specified lengths. Experimental verification proved that the developed mathematical models are adequate for drums of both cylindrical and conical constructions. The value of the average error did not exceed 13%. Following the mathematical elaboration and verification studies, the authors carried out calculations for machines currently available on the market that are equipped with drum cutting units. The calculations were carried out for the most commonly cut material, i.e. for maize, straw and green plant materials. The obtained results confirm the complexity of the problem arising from a wide range of numerical values of cutting resistance, which is contained in the range of 400–1,800 nm. The compiled database can be practically applied in the selection of machines for specific field works, and the mathematical models developed and verified in the study can be applied at the stage of designing new designs of cutting drums used in forage harvesters.

Key words: biomass cutting, drum cutting unit, plant material, mathematical modelling, cutting of fibrous materials

1. INTRODUCTION

The drum cutting unit is one of the basic work units of a forage harvester. Its purpose is to cut the plant material into pieces of specific lengths called chaff. The most common design, the so-called open drum, consists of a shaft on which discs with holes are mounted. Knives are screwed to the discs by means of tool posts. Depending on the construction of the drum, the knives may be straight or bent along a screw line. In addition, a distinction is made between solid and split knives. The cutting drum is supported on the side plates of the machine and makes a rotating movement that causes the knives to move. The moving knives cut the material layer into pieces at the contact line between the knife and the counter-cutting edge. The material is fed to the cutting line from the space of rotating intake and compression rollers, where the biomass is pre-formed and compressed.

The characteristics of the construction and functioning of the drum cutting unit result, among other things, from the fact, that the cutting process performed by it concerns biomass, i.e. plant materials whose structures are not homogeneous, and the physical and mechanical properties are not fully identified [1-7]. Due to the punctuality of the research conducted so far, it is not possible to unambiguously determine the features and design parameters of the drum cutting unit that have a decisive influence on the cutting efficiency and the load on the working unit.

The results obtained from these experimental studies are valuable for the purposes of designing new constructions of chopper cutting units. However, in order to accelerate and optimise the design stage of the mentioned working units, it is

necessary to have a verified and adequate mathematical model describing the biomass layer cutting process [8-14].

In view of this, the authors of this paper have developed mathematical models of the moment of resistance to cutting on the shaft of a cutting drum of cylindrical and conical structure. Further, they carried out experimental verification of the developed models. The models developed have been formulated taking into consideration important features and design parameters of cutting drums and characteristic properties of the material being cut.

2. MATHEMATICAL MODEL OF CUTTING MOMENT

Figs.1 and 2 show photographs and diagrams of the analysed cutting drums. Based on observation and the analysis of the actual process of cutting a material layer with the use of a cutting drum knife of cylindrical type, the system of forces acting on the material layer and the reaction of the layer on the knife were determined (Fig. 3) [15].

By analysing the system of forces occurring in the process of cutting with a cylindrical drum (Fig. 3), it can be stated that the task of the peripheral force P is to overcome the resultant resistance to cutting P_c , equal in value to the reaction R , which consists of the normal force N and the friction force T , resulting from the interaction of the material with the knife. The normal force N depends on the unit cutting resistance p_c and the active length of the knife, which is expressed as

$$N = p_c \Delta l \quad (1)$$

However, the friction force T depends on the friction angle φ and is represented as

$$T = N \operatorname{tg} \varphi \quad (2)$$

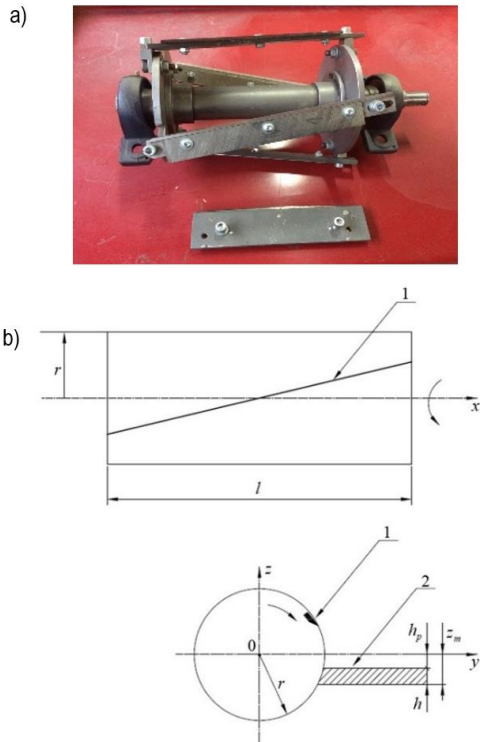


Fig. 1. Drum cutting unit of cylindrical type with straight knives. a) actual view of the drum being at the test stand equipment; and b, graphic diagram. 1 - cutting knife, 2 - the layer of material to be cut

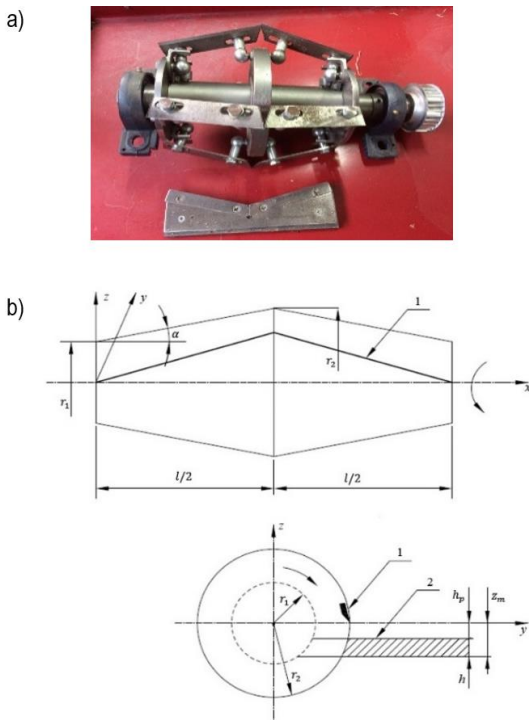


Fig. 2. Diagram of the drum cutting unit of conical type. a) actual view of the drum being at the test stand equipment; and b) graphic diagram. 1 - cutting knife, 2 - the layer of material to be cut

Therefore, the cutting resistance P_c , which is the resultant of the normal force N and the friction force T , is expressed as

$$P_c = \frac{p_c \Delta l}{\cos \varphi} \quad (3)$$

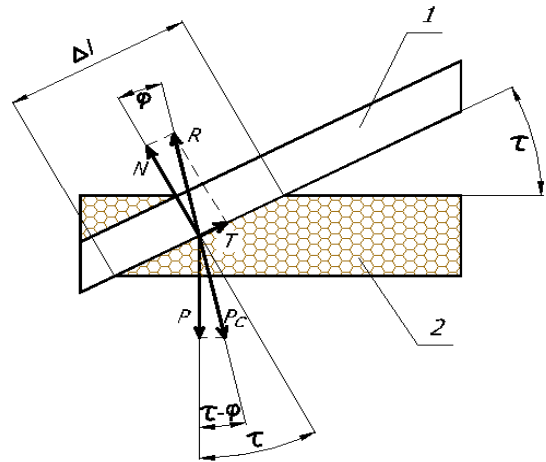


Fig. 3. The arrangement of forces occurring during the cutting of the biomass layer by the knife of a cylindrical type cutting drum. 1 - cutting knife, 2 - the layer of material

The circumferential force P is the vertical component of the cutting resistance P_c and is represented by the dependence

$$P = P_c \cos(\tau - \varphi) = \frac{p_c \Delta l}{\cos \varphi} \cos(\tau - \varphi) \quad (4)$$

From the trigonometric dependence, we obtain

$$\cos(\tau - \varphi) = \cos \tau \cos \varphi (1 + \operatorname{tg} \tau \operatorname{tg} \varphi) \quad (5)$$

After considering that $\operatorname{tg} \tau = \mu$, where μ is the coefficient of friction of the knife against the layer of the plant material to be cut, we obtain the equation for the circumferential force P :

$$P = \frac{p_c \Delta l}{\cos \varphi} \cos \tau \cos \varphi (1 + \mu \operatorname{tg} \tau) = p_c \Delta l \cos \tau (1 + \mu \operatorname{tg} \tau) \quad (6)$$

The cutting moment M_c is the product of the force P acting on the circumference of the drum and the radius of the drum r , on which the knives are mounted. Therefore, we have:

$$M_c = P r \quad (7)$$

Taking into account the dependencies in Eqs (6) and (7), the cutting moment equation M_c takes the form

$$M_c = p_c \Delta l r \cos \tau (1 + \mu \operatorname{tg} \tau) \quad (8)$$

Assuming that the expression $p_c r \cos \tau (1 + \mu \operatorname{tg} \tau)$ takes a constant value of C at the time of cutting, the moment M_c will be represented by the equation

$$M_c = C \Delta l \quad (9)$$

where C is a constant value and Δl is the active length of the knife.

Assuming that the number of knife lines of the cutting drum is z , with only one knife line crossing the layer each time, the equation for the mean moment \bar{M}_c , acting on the shaft of the cutting drum, is obtained as

$$\bar{M}_c = \frac{L_n z}{2\pi} \quad (10)$$

where L_n is the work done by the chopper knife during one pass through a layer of plant material and z is the number of knife lines of the chopping drum.

However, operation L_n is expressed by the equation

$$L_n = \int_{\psi_p}^{\psi_k} M_c(\psi) d\psi \quad (11)$$

where $M_c(\psi)$ is cutting resistance moment dependent on the angle of rotation of the knife, ψ_p is angle of start of cut and ψ_k is angle of end of cut.

The following parameters were adopted as design features of the cutting unit: h – height of cut layer and b – width of cut layer.

The integral calculated over the angle $d\psi$ is replaced by the integral calculated over the arc length $dx = r d\psi$, where r is the drum radius. Then the work done by a single knife line during its passage through the biomass layer will be described by the equation

$$L_n = \frac{1}{r} \int_{\psi_p}^{\psi_k} M_c(\psi) r d\psi = \frac{1}{r} \int_0^{x_k} M_c(x) dx \quad (12)$$

When analysing the cutting of a rectangular layer of material, the process was divided into three phases under the following assumptions:

- each time the material layer is cut by only one line of knives;
- the height of the layer of material to be cut is equal to the path taken by a given point of the knife through this layer.

PHASE I: Penetration of the knife into the layer (the active length of the knife Δl increases)

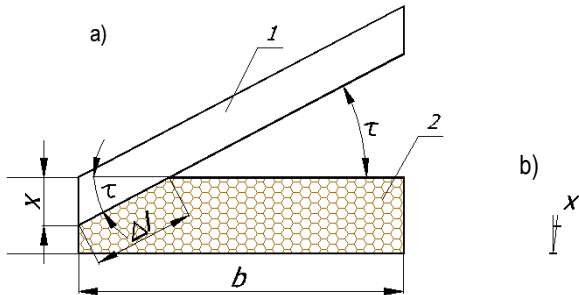


Fig. 4. Penetration of the knife into the layer (phase I). a, cross-section through the layer; b, comparison of the length of the arc drawn by the knife x and the height of the layer h : 1 - cutting knife and 2 - the layer of material

According to Fig. 4b, the difference between the length of the arc drawn by any point of the knife from the top to the bottom edge of the cut layer is approximately equal to the layer height h , which follows from the fact that we assume $h \approx h \frac{\psi}{\sin \psi}$ for small angles, because $\sin \psi \approx \psi$.

By using the trigonometric dependence $\frac{x}{\Delta l} = \sin \tau$, we get

$$\Delta l = \frac{x}{\sin \tau} \quad (13)$$

For $x = h$ the Eq. (13) takes the form: $\Delta l = \frac{h}{\sin \tau}$.

The cutting work L_{nI} in the phase I of the knife movement can be represented by the dependence:

$$L_{nI} = \frac{1}{r} \int_0^h M_c(x) dx \quad (14)$$

where $M_c(x)$ is the cutting moment dependent on knife position.

By substituting the Eq. (13) into the Eq. (9), we obtain

$$M_c = C \frac{x}{\sin \tau} \quad (15)$$

On the other hand, after substituting Eq. (15) into Eq. (14), the work of cutting in the interval $0 \leq x \leq h$ is described by the dependence:

$$L_{nI} = \frac{C}{r} \int_0^h \frac{x}{\sin \tau} dx = \frac{C}{r} \left[\frac{x^2}{2 \sin \tau} \right]_0^h = \frac{C}{r} \frac{h^2}{2 \sin \tau} \quad (16)$$

PHASE II: Cutting through the layer (the active length of the knife Δl remains constant)

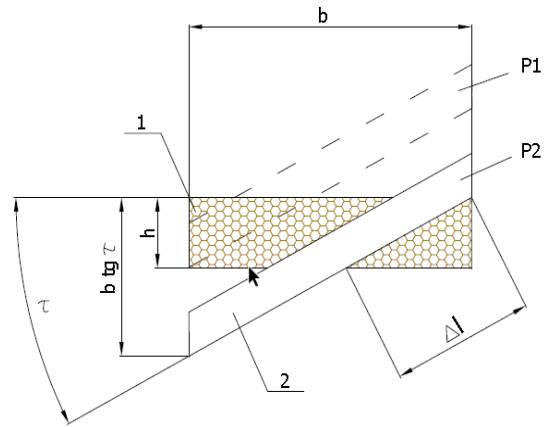


Fig. 5. Cutting through a layer (phase II). 1 - the layer of material, 2 - cutting knife, P1 - initial position of the knife, P2 - final position of the knife

According to Fig. 5, the cutting in the second phase takes place in the interval $h \leq x \leq b \tan \tau$. In the interval $h \leq x \leq b \tan \tau$, the value Δl is invariant and is expressed by the equation $\Delta l = \frac{h}{\sin \tau}$. Therefore, the cutting work is described by the dependence

$$L_{nII} = \frac{C}{r} \int_h^{b \tan \tau} \frac{h}{\sin \tau} dx = \frac{C}{r} \frac{h}{\sin \tau} (b \tan \tau - h) \quad (17)$$

PHASE III: Withdrawal of the knife from the layer (the active length of the knife Δl decreases).

According to Fig. 6, the cutting in phase III takes place in a range $b \tan \tau \leq x \leq h + b \tan \tau$ i.e. over the same length as in phase I.

In the range $b \tan \tau \leq x \leq h + b \tan \tau$, the value of $\Delta l = \frac{x - b \tan \tau}{\sin \tau}$.

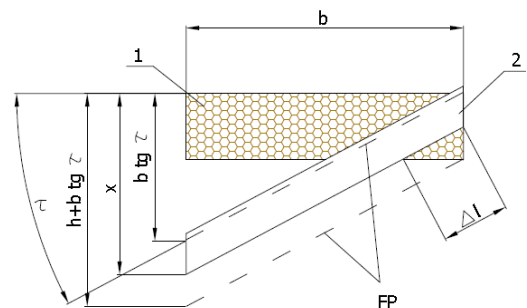


Fig. 6. Coming out of the knife from the layer (phase III). 1 - the layer of material, 2 - knife of the cutting drum, FP - extreme position of the cutting edge

Therefore, the cutting work in phase III is described by the dependence

$$L_{nIII} = \frac{c}{r} \int_b^{h+b} \frac{tg\tau}{\sin\tau} \frac{(x-b)tg\tau}{\sin\tau} dx = L_{nI} = \frac{c}{r} \frac{h^2}{2 \sin\tau} \quad (18)$$

Therefore, the overall work done by the knife during one passage through the layer of cut material will be expressed by the following equation:

$$L_n = L_{nI} + L_{nII} + L_{nIII}$$

$$L_n = \frac{c}{r} \left(\frac{h^2}{2 \sin\tau} + \frac{hb \, tg\tau}{\sin\tau} - \frac{h^2}{\sin\tau} + \frac{h^2}{2 \sin\tau} \right) = \frac{c}{r} \frac{hb}{\cos\tau} \quad (19)$$

After substituting into Eq. (10) the expressions for L_n and C , we obtain, in conclusion, Eq. (20) for the mean moment of resistance to cutting on the drum shaft, which is given as

$$\overline{M}_c = \frac{p_c(1+\mu tg\tau) b h z}{2\pi} \quad (20)$$

Eq. (20) describes the average moment of resistance to cutting for a drum of cylindrical type. However, for a conical drum, according to Fig. 7, the material layer is not cut along the length b and height h but along the length $2a$ and height h . However, it follows from the geometrical analysis that we have

$$2a = \frac{b}{\cos\alpha} \quad (21)$$

where α is the cutting angle of the material layer in the case of a cutting drum of the conical type what is shown in Fig. 8..

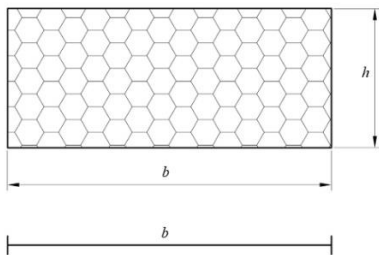


Fig. 7. Cross-section of a cut material layer using a cutting drum of cylindrical type

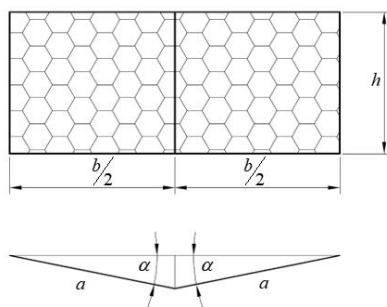


Fig. 8. Cross-section of a material layer being cut by a cutting drum of the conical type

Therefore, for a cutting drum of the conical type, the equation for the mean moment of resistance to cutting on the shaft assumes the following form:

$$\overline{M}_c = \frac{p_c(1+\mu tg\tau) \frac{b}{\cos\alpha} h z}{2\pi} \quad (22)$$

3. METHODOLOGY FOR EXPERIMENTAL STUDIES

In order to verify the mathematical models developed, a test stand was designed and constructed to test the biomass layer cutting process. The test stand allows the process of cutting a layer of material to be carried out with the use of cutting drums of cylindrical and conical construction. A schematic representation of the test stand construction is shown in Fig. 9.

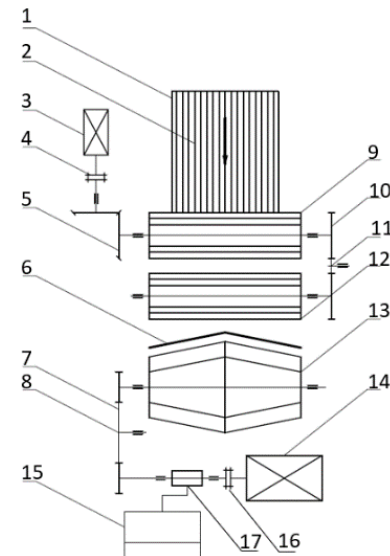
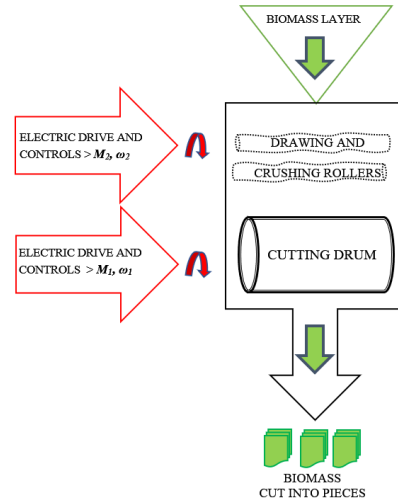


Fig. 9. Scheme of the test stand construction. 1 - trough of chaff cutter, 2 - material to be cut (biomass layer), 3 - electric motor, 4 - coupling, 5 - angular gearbox, 6 - cutting counter edge, 7 - belt transmission, 8 - tensioning roller, 9 - upper drawing-crushing roller, 10 - belt transmission, 11 - tensioning roller, 12 - lower drawing-crushing roller, 13 - cutting drum, 14 - electric motor, 15 - computer (recorder of measuring system), 16 - clutch, 17 - measuring system for moment and rotational speed on the drum shaft

Fig. 10 presents an example of the construction of a cutting drum of the conical type mounted in a chaff cutter. Therefore, the constructional form of the test stand, according to the assumptions of the authors of this paper, allows for experimental research on the process of cutting a layer of material with a cylindrical drum – cross cutting of a layer of material ($\alpha = 0^\circ$) and with a conical drum – cutting a layer of material at an angle ($\alpha = 20^\circ$).



Fig. 10. Mounted design of the cutting drum of the conical type in the chaff cutter

For the measurement of torque and revolutions on the cutting drum shaft during its idling and working runs, a torque meter with a tachometer type MT200Nm was used, which was directly coupled to a two-channel meter MW2006-3. During the tests, a computer system with a data recording program and the author's calculation program RB01 were used. It was assumed that the cutting speed of the knife would be $3.00 \text{ m} \cdot \text{s}^{-1}$. The aforementioned cutting speed ensures proper cutting of the material layer and corresponds to the actual value of the cutting speed in the known designs of chaff cutters. The cutting speed v_c is the resultant speed of the peripheral speed of the cutting blade v_b and the feed speed of the crop v_m intake and compression rollers. The dependence between these speeds is described by the following equation:

$$v_c = \sqrt{v_m^2 + v_b^2 + 2v_m v_b \cos\varphi} \quad (23)$$

where φ is the angle contained between the speed vectors v_m and v_b .

For a cutting drum of the conical type, the cutting speed was determined at the midpoint of the cutting edge of the knives. The degree of compaction of the material was assumed as the ratio of the height of the layer of plant material after compaction h to the height of the material before compaction h_o . In the course of the tests, the degree of material compaction $h \cdot h_o^{-1} = 0.5$ was used. The value of the degree of material compaction adopted in the test programme corresponds to the values recommended in the professional literature [16].

The experimental tests were conducted for the width of the cut layer $b = 0.25 \text{ m}$ and the height $h = 0,012; 0,016; 0,020; 0,024; 0,028; 0,032 \text{ i } 0,036 \text{ m}$.

In order to experimentally determine the cutting resistance on the shaft of the cutting drum, a layer of rye straw was cut, from which test samples were prepared. During the experimental tests, the ears were cut and the individual stalks tied together to form so-called sheaves with an average length of $l = 855 \text{ mm}$. Each sample was then weighed using an electronic balance (ELDOM, model EK3130) with an accuracy of 2 g. The estimated number of stalks per sample was 280. In addition, the diameter of the stalks was measured with an electronic slide calliper with an accuracy of up to 0.01 mm. The diameter of the stalks ranged from 2.5 mm to 6.3 mm. The plant material was stored in a dry room before testing and the humidity on the day of testing was 12%. Moisture content of the material was determined based on randomly selected samples

using the dryer method. The prepared samples, in the form of sheaves, were placed in the feeding chute of the test stand, the bindings were cut and the cutting was carried out. The degree of material compaction $h \cdot h_o^{-1}$ was determined based on measurement of layer height before and after compaction. Implementation of the plant material compaction was carried out by means of sets of pulling and compacting rollers and pressure elements that maintain a constant value of the material compaction level $h \cdot h_o^{-1}$ while moving the material towards the cutting drum (Figs. 9 and 10). The desired values of plant material v_m feeding were obtained by a proper selection of the rotational speed of the lower roller. The rotational speed of the roller was accurately measured on its shaft using an LCD contact tachometer. At the stage of determining the value v_m , the slippage of plant material in relation to the surface of pulling and crushing rollers was taken into consideration. The slip value was assumed as 10%, which was confirmed by experimental tests.

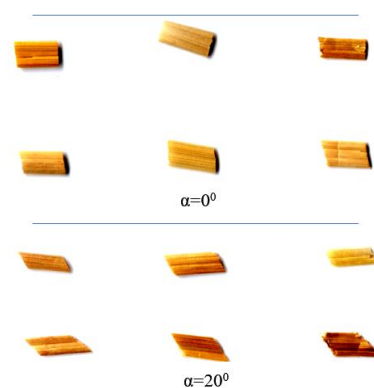


Fig. 11. Exemplary chopped pieces for cutting angles. $\alpha = 20^\circ$ (two upper rows); $\alpha = 20^\circ$ (two lower rows)

4. VERIFICATION OF MATHEMATICAL MODELS

In order to verify the mathematical models developed in Section 2 of this work, the results obtained from calculations of the models were compared with the results of experimental tests. The comparison was carried out individually for the moments of resistance to cutting \overline{M}_c , with the same systems of independent variables.

During the calculations carried out on the models developed, the unit resistance of straw cutting $p_c = 8.5 \cdot 10^3 \text{ Nm}^{-1}$ was assumed. However, the coefficient of friction of the knife against the cut material layer $\mu = 0.7$ was assumed in the calculations.

In mathematical statistics there are no unambiguously described methods of comparing the results of experimental tests with the results obtained from mathematical models derived a priori. Therefore, the criterion of adequacy of the mathematical model to the results of experimental tests was assumed to be the value λ , which is the ratio of the value obtained from the tests \overline{M}_{cE} to the value obtained from the model \overline{M}_{cM} :

$$\lambda = \frac{\overline{M}_{cE}}{\overline{M}_{cM}} \quad (24)$$

Furthermore, the average calculation error $\overline{\lambda}$ was calculated at the stage of comparing the results. A synthetic summary of the compared values of the cutting resistance moment on the shaft for the cylindrical and conical drum types is presented in Tables 1 and 2, respectively.

Based on the comparison results, it can be confirmed that there exists a good conformity of the trend of the changes of the cutting resistance moment determined from the model and the experimental tests for the cutting drum of cylindrical and conical types. The average values of $\bar{\lambda}$ amount to 1.12 and 1.13, respectively, with the experimental test results, which clearly indicates that the developed models of the cutting resistance moment on the drum shaft give lower cutting resistance values by about 12%–13% from the simulation calculations. This may indicate that during the experimental tests a higher unit cutting resistance p_c of the rye straw layer occurred than that reported in the literature [17].

The authors of the study were not able to directly compare the results of their studies with the ones presented in the literature by other researchers. This is because the results of the studies presented in this article mainly concern a new design on the drum cutting assembly, which is covered by legal protection. In the specialised literature, there are no data that would describe the

process of cutting rye straw into chopped straw with the use of a chaff cutter drum of the double truncated cone shape. The first proposal of the cutting drum's design of that shape, which realised diagonal cutting in both directions, has been presented by Bochat [15]. Other studies presented only the data connected with the commonly functioning design constructions of cutting drums realising lateral cutting. The results presented in the present study concerning the classic design of the drum cutting assembly are comparable with the data presented in the literature from within that scope [3,12,13,19,20].

The authors also carried out simulation calculations for the developed mathematical model, which showed good conformity with the trend of changes in cutting resistance moment, for real designs of drum cutting units found in leading manufacturers of chaff cutters. Structural solutions and parameters of cutting units of chaff cutters of the following manufacturers were analysed: John Deere, Fendt, Krone, New Holland, Claas and Rostselmash. The results of the analysis are presented in Table 2.

Tab. 1. Summary of the compared values of the cutting resistance moments on the shaft \bar{M}_{cM} and \bar{M}_{cE} for the cutting drum of cylindrical type ($\alpha = 0^\circ$) and conical type ($\alpha = 20^\circ$)

$z = 4; \mu = 0.7;$ $\tau = 20^\circ; b = 0.25m;$ $h \cdot h_0^{-1} = 0.5$	No.	$\alpha[...^\circ]$	$h[m]$	$\bar{M}_{cM}[Nm]$	$\bar{M}_{cE}[Nm]$	λ	$\bar{\lambda}$
	1	0	0.012	20.33	22.56	1.11	1.12
	2		0.016	27.11	29.34	1.11	
	3		0.020	33.89	38.12	1.12	
	4		0.024	40.67	45.82	1.13	
	5		0.028	47.45	53.78	1.13	
	6		0.032	54.23	61.32	1.13	
	7		0.036	61.01	69.21	1.13	
	8	20	0.012	21.96	24.63	1.12	1.13
	9		0.016	29.28	32.98	1.13	
	10		0.020	36.60	41.20	1.13	
	11		0.024	43.92	49.03	1.12	
	12		0.028	51.24	58.33	1.14	
	13		0.032	58.56	67.68	1.14	
	14		0.036	65.88	75.12	1.14	

Tab. 2. Summary of design parameters of actual cutting units

	John Deere	Fendt	Krone	New Holand	Rostselmash
Drum diameter [mm]	670	720	660	630, 700	630
Drum width [mm]	670, 850	800	630, 800	750, 880	703
Number of cutting knife sections [pcs.]	10, 12, 14, 16	10, 14, 20	10, 14, 18, 20	10, 12, 14, 18, 20	12

For the simulation calculations, the material most frequently cut in this type of machines was adopted, i.e. for straw of cereals, maize and green fodder. Following Dmitrewski, the following unit values of energy consumption were assumed: straw, $p_c = 8.5 \cdot 10^3 Nm^{-1}$; maize, $p_c = 16 \cdot 10^3 Nm^{-1}$; and green fodder, $p_c = 6 \cdot 10^3 Nm^{-1}$.

The results obtained were illustrated in the form of graphs. Fig. 12 shows the cutting moment as a function of the cutting drum width for three types of material: green forage, straw and maize.

On the other hand, Fig. 13 shows the plot of cutting moment as a function of the number of knife lines used to cut the biomass into pieces of a given length and as a function of the drum width.

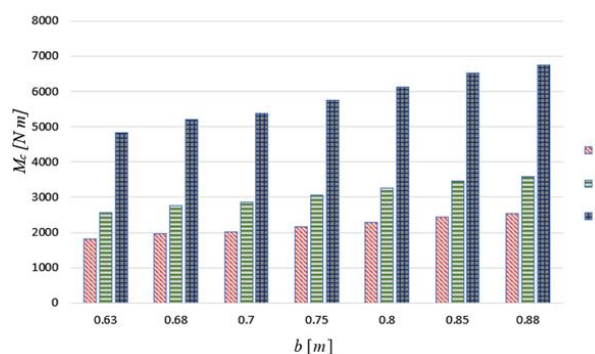


Fig. 12. Cutting moment as a function of drum width for three types of material. 1 - green material, 2 - straw, 3 - maize

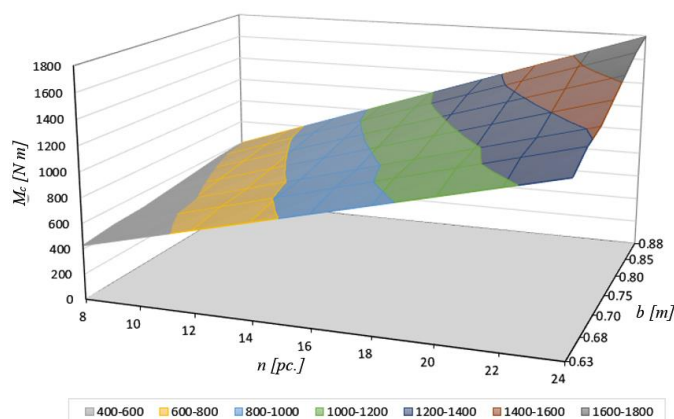


Fig. 13. Cutting moment M_c as function of the drum width b and the number of knife lines on the circumference of the drum for straw type material

5. CONCLUSION

The developed mathematical models, representing the average moment of resistance to cutting a layer of material on the rolls of cutting drums of cylindrical and conical types, can be considered adequate.

Adequate mathematical models of mean cutting resistance moment are of significant importance to speed up the design process of new cutting drum designs of this type.

The developed mathematical models can be applied with the use of computer simulation in the research of the cutting process of the plant material layer and in the optimisation of the design of cutting drums.

The development of mathematical models of the moment of resistance to cutting on the cutting drum shaft is significant due to the seasonality of work in agriculture, which means that, despite sometimes many years of experimental research, it might not be possible to generate a corpus of information sufficient for the rapid design of such working units.

The developed database of cutting resistance moment results for actual design solutions of drum cutting units gives the possibility to assess energy efficiency in terms of selection of the cutting drum design for the type of material to be cut.

REFERENCES

- Guarnieri A, Maglioni C, Molari G. Dynamic analysis of reciprocating single-blade cutter bars. *T Asabe*. 2007;50(3):755-64.
- Igathinathane C, Pordesimo LO, Schilling MW, Columbus EP. Fast and simple measurement of cutting energy requirement of plant stalk and prediction model development. *Industrial Crops and Products*. 2011;33(2):518-23.
- Kruszelnicka W, Kasner R, Baldowska-Witos P, Flizikowski J, Tomporowski A. The Integrated Energy Consumption Index for Energy Biomass Grinding Technology Assessment. *Energies*. 2020;13(6).

- Persson S, Engineers ASOA. *Mechanics of Cutting Plant Material*: American Society of Agricultural Engineers; 1987.
- Bochat A, Zastempowski M. Impact of the beater shredder design on the granulometric composition of the shredded grain material. *Przem Chem*. 2019;98(9):1499-504.
- Zastempowski M, Bochat A. Impact of design and parameters of the drum cutting assembly operation on non-uniformity of biomass length cutting. *Przem Chem*. 2020;99(3):457-61.
- Zastempowski M, Bochat A. Mathematical Modelling of Elastic Deflection of a Tubular Cross-Section. *Pol Marit Res*. 2015;22(2):93-100.
- Zastempowski M, Bochat A. Gyroscopic Effect in Machine Working Assemblies. *Acta Technol Agr*. 2020;23(1):24-9.
- Zastempowski M, Bochat A. Modeling of Cutting Process by the Shear-Finger Cutting Block. *Appl Eng Agric*. 2014;30(3):347-53.
- Zastempowski M. Dynamics of Movement in Scissor-Finger Cutting Assembly. *Engineer Mechan*. 2017:1114-7.
- Zastempowski M, Borowski S, Kaszkowiak J. New Solutions in Harvesting Plants for Power Purposes. *Trends in Agricultural Engineering 2013*. 2013:673-6.
- Zhang M, Sword ML, Buckmaster DR, Cauffman GR. Design and evaluation of a corn silage harvester using shredding and flail cutting. *Transactions of the American Society of Agricultural Engineers*. 2003;46(6):1503-11.
- Abilzhanov D, Abilzhanuly T, Golikov V, Adilshyeyev A, Alshurina A. Development of universal pick-up chopper for harvesting of chopped hay and haylage. *Journal of Engineering and Applied Sciences*. 2017;12(13):3309-14.
- Du DD, Wang J. Research on mechanics properties of crop stalks: A review. *Int J Agr Biol Eng*. 2016;9(6):10-9.
- Bochat A. Theory and construction of cutting units of agricultural machines. In: UTP, editor. UTP University of Science and Technology. Bydgoszcz 2010.
- Zastempowski M. Theory and construction of cutting units of agricultural machines. In: UTP, editor. UTP University of Science and Technology. Bydgoszcz 2017.
- Dmitrewski J. Theory and construction of agricultural machines. State Agricultural and Forest Publishing House, Editor, 1978: Warsaw.
- Zastempowski M, Bochat A. Innovative Constructions of Cutting and Grinding Assemblies of Agricultural Machinery. *Proceeding of 6th International Conference on Trends in Agricultural Engineering 2016*. 2016:726-35.
- Savoie P, Tremblay D, Theriault R, Wauthy JM, Vigneault C. Forage Chopping Energy Vs Length of Cut. *T Asae*. 1989;32(2):437-42.
- Kruszelnicka W, Baldowska-Witos P, Kasner R, Flizikowski J, Tomporowski A, Rudnicki J. Evaluation of emissivity and environmental safety of biomass grinders drive. *Przem Chem*. 2019;98(9):1494-8.

Marcin Zastempowski: <https://orcid.org/0000-0001-6492-6281>

Andrzej Bochat: <https://orcid.org/0000-0003-0769-7077>

Lubomir Hujo: <https://orcid.org/0000-0002-5497-536X>

Juraj Jablonicky: <https://orcid.org/0000-0003-4512-4675>

Maciej Janiec: <https://orcid.org/0000-0001-6772-5450>

EXPERIMENTAL EVALUATION OF ECCENTRIC MECHANISM POWER LOADING OF MOVABLE PRESSURE PLATE IN DIE-CUTTING PRESS

Oleh KNYSH[✉], Ivan REHEI[✉], Nazar KANDIAK[✉], Serhij TERNYTSKYI[✉], Bohdan IVASKIV[✉]

^{*}Department of Computerized Complexes of Printing and Packaging Industries, Faculty of Computer Printing Engineering, Ukrainian Academy of Printing, 19 Pid Goloskom Street, Lviv 79020, Ukraine

knolehb@gmail.com, regey.ivan@gmail.com, kandyak.nazar@gmail.com, serhij86@gmail.com, ivaskivbohdan@gmail.com

received 18 May 2022, revised 28 July 2022, accepted 31 July 2022

Abstract: The paper reports experimental research on torques during cardboard cutting in the die-cutting press with eccentrics in the drive of the movable pressure plate. To conduct the research, an experimental bench with eccentrics in the drive of the die-cutting press is designed and manufactured. The manufactured experimental device for the research on cardboard blanks provides the possibility of getting dependencies of loadings at different parameters of the die-cutting process. The experimental approach envisages the use of the strain gauge measurement method and the wireless module for data collecting, as well as the software for its processing, for getting trustworthy results with minimum faults. The method gives an opportunity to study the torque values during the cardboard-cutting efforts on the drive shaft. The paper shows changes in the torque value on the drive shaft during the kinematic cycle with and without the use of cardboard blank. The angle of the drive shaft rotation during the cutting process was evaluated at selected values of the cardboard thickness. The relationship between the linear cutting efforts and the cardboard thickness, its fibre direction, cutting rule type and rotational speed of the drive shaft is elaborated. This kind of data is approximated by a logarithmic function (logarithmic curve), at R^2 from 0.90 to 0.98. The thickness of the cardboard significantly influences the value of the linear cutting effort at all the studied parameters.

Key words: die-cutting press, cutting, cardboard, linear cutting effort, cutting rule, torque, eccentric

1. INTRODUCTION

As a consequence of the current trend of customer-driven economies, today's world markets are characterised by high fluctuations in market demand and the frequent arrival of new technologies and new products [1]. Cardboard packaging takes a significant segment of the consumer packaging market. According to the information [2], the segment of cardboard packaging holds 36% of the general market, with a value of US\$400 billion. According to the prognosis of the World Packaging Organisation, the packaging market continues to grow and the segment of cardboard packaging will stay significant despite the constant rivalry with the plastic one.

The main features that made paper and cardboard a significant part of the total packaging market are the raw material's properties, principles of manufacture and environmental and waste management [3]. Paper and cardboard packaging has good appearance and performance properties that allow using it in a wide range of packaging.

For cardboard packaging manufacture, the main technology is die-cutting of packaging cut-outs and the further forming of 3D packaging of different kinds. As mentioned [2, 4], the use of a flat die-cutting forme allows the manufacturing of cardboard packaging of different sizes and shapes. Manufacturing cardboard packaging requires the performance of some technological operations. As determined [4], the chain of technological operations is accomplished automatically at cardboard blank stops during its periodical transportation through sections of equipment. Modern die-cutting equipment is built on a section principle. The main part of modern die-cutting equipment is a die-cutting press, for which

strict requirements are put forward. The technological process of cardboard packaging manufacture utilises flatbed die-cutting presses with flat die-cutting forme, which contains cutting and creasing rules (knives) and additional tools in case of need. The feature of the flatbed die-cutting press is the simultaneous contact of tools with the cardboard blank on all surfaces. This can be conducted at the high-quality level if the values of loading are significantly high because they enable to obtain a final product with nominal features. In addition, providing parallel displacement of the movable pressure plate of the die-cutting press during the kinematic cycle is needed. Non-parallel displacement of the movable pressure plate causes unevenness of the loading dispersion and decrease in the quality of the future cardboard package.

Several different mechanisms are used to ensure the displacement of the movable pressure plate of the die-cutting press. The analysis on existing mechanisms of pressure plate drive and their design in the modern die-cutting equipment [5] indicated that these mechanisms are required to overcome a significant technological loading at the end of the movement of the executive link. The main segment of the drive mechanisms of the pressure plate is built based on the wedging effect, which provides sufficient effort value for the pressure plate with comparatively little loading on the driving links. Such a design causes asymmetry of the right and left parts of the pressure plate during the movement cycle. The symmetry of plate movement can be seen only at the final stage of its displacement when the work surface of the pressure plate becomes parallel to the surface of the base plate and begins the die-cutting of cardboard blanks. This asymmetry causes unevenness of loading distribution and shows oscillations in the press values, which reduces the quality of cardboard packaging and

production efficiency. Similar results have been reported by Kuznetsov et al. [6]: the occurrence of unevenness in the pressure plate movement during the press cycle and the method of its avoidance have been proven. However, the proposed method does not enable full elimination of plate movement unevenness during the press cycle. In a later work [7], it has been proposed the use of a combined lever mechanism for the drive of the movable pressure plate of the die-cutting press. It was made with the aim to minimise the drawbacks of existing equipment. The proposed mechanism consists of two pairs of the crank–slider contours: leading and executive. The use of this mechanism decreases the total loading and peak of kinetic power consumption. Nonetheless, besides the significant advantages of the proposed mechanism, it has a quite complicated design, and its dimensions are equal to existing mechanisms of the pressure plate drive of die-cutting presses.

The study [8] shows results of the research of die-cutting presses with dual-elbow-bar mechanisms to improve pressure plate movement characteristics with maximum simplicity and use of designed mechanisms for the pressure plate drive such that it has 10 links that make the mechanism complicated during operation. Moreover, the mechanism causes a decrease in press productivity. It was proposed to use a cam mechanism in the drive of the pressure plate. However, such a mechanism design is characterised by the complexity of the manufactured drive cams that have two contacting profiles because of the requirement of manufacturing high-accuracy drive cams. Besides, such drive cams occupy a significant part of the die-cutting press. A new design of wedging cam mechanisms for the lower pressure plate drive in a die-cutting press has been proposed [9]. Despite some simplification of design, the mechanism remains complicated in set-up and exploitation. Presses that are built using such schemes would have complications in set-up and exploitation.

A new design of the pressure plate drive of the die-cutting press using a screw–nut transmission in the drive mechanism of the pressure plate has been proposed [10] and an evaluation [11] of components of the consumed kinetic power in the pressure plate drive with screw–nut transmission has been conducted. Experimental research on torques during cardboard cutting in the die-cutting press with the screw–nut transmission in the drive mechanism of the movable pressure plate [12] show that the use of die-cutting presses built on such design enables and allows avoiding drawbacks of existing die-cutting presses in the area of pressure plate movement unevenness during the kinematic cycle. However, the practical use of such equipment requires complicated and costly parts. Moreover, the proposed design causes complexity during set up and exploitation of the equipment.

One of the options to make the technological process of cutting contours in cardboard blanks less energy- and resource-consuming is the use of modular pneumatic systems [13]. This allows solving an important issue regarding the accelerated deterioration of cutting knives and supporting contact elements. It is necessary to consider that pneumatic modules are operated based on compressed and rarefied air and practically do not have a negative effect on ecology. However, such a design of the die-cutting presses is difficult to use in industrial production and requires a pneumatic system that causes increase in value of the equipment. Furthermore, availability of such modernisation has not been proven.

Use of laser cutting technology for paper and cardboard cutting [14], potential and possible challenges of laser cutting of paper and cardboard-based materials were discussed [15]. In this

case, the results showed the perspective of laser use in paper and cardboard cutting. However, laser cutting does not provide the necessary productivity of equipment, due to its low speed. The possible increase in laser cutting speed significantly affects the cost of the process. Such a method of manufacturing cardboard packaging cartons is innovative and progressive.

Another type of cardboard packaging is the packaging made of corrugated cardboard. The research [16] on corrugated cardboard in different conditions (in standard conditions and refrigerated conditions) and studied the strength of corrugated cardboard as the structural property. However, the proposed method needs to be revised for better results or a small range difference between yield breaking and strain breaking. A modified analytical formula for estimating the static top-to-bottom compressive strength of corrugated board packaging with different perforations has been presented [17], that allow to adopt the method to include perforation influence on the box's compressive strength estimation.

As a result of the analysis, the conclusion could be made that, during recent years, several significant types of research on the die-cutting process have been conducted, given the analysis of the reference literature on the use of eccentric mechanisms for the drive of the movable pressure plate of the flatbed die-cutting press. The use of such mechanisms provides the opportunity to avoid the drawbacks of die-cutting presses that are built using multilink mechanisms and – as an alternative – cam mechanisms regarding the specific applied problem of the experimental evaluation of the power loads of the eccentric mechanism that is used as the drive mechanism for the movable pressure plate of the flatbed die-cutting press. Therefore, there is reason to believe that the research of the power characteristics that arise during cardboard blank cutting using the die-cutting press with the eccentric mechanism drive of the movable pressure plate is a relevant scientific task.

The paper is focused on loading determination during the application of the flatbed die-cutting press with the eccentric mechanism in the drive of the movable pressure plate.

To achieve the goal of the study, the following tasks need to be completed:

- to design and manufacture the experimental device with the eccentric mechanism as a drive of the movable pressure plate;
- to elaborate the method for measuring loading in the flatbed die-cutting press;
- to propose a method on experimental research: the placement of measuring instruments and carrying out measurements of torque values in the mechanism;
- to determine the torque values on the drive shaft of the experimental bench;
- to carry out the impact of the cardboard blank thickness, the direction of the fibres (cross-direction [CD] and machine direction [MD]), the type of the cutting rule (knife) and the rotational speed of the drive shaft on the value of the linear cutting effort;
- to elaborate the relationship between the cutting effort values on parameters of cardboard blanks.

2. DEVICE, MATERIALS AND METHODS

The experimental approach to the cutting process of the cardboard blanks was conducted on the specially designed and manu-

factured device of the die-cutting press with the eccentric mechanism as a drive of the movable pressure plate. This device consists of the entablement 1 (Fig. 1), on which the supports 2, 2' and 3 of the drive shaft 4 are fixed. On shaft 4, between the supports 2 and 2', the eccentrics 5 and 5' with eccentricity of $e = 10$ mm are placed. Moreover, on shaft 4, the gear wheel of the gear transmission 17 is set cantilever relative to the support 3. Rolling bearings 6, 6' are fixed to the eccentrics. The bearings contact the hasps 9 and 9' of the movable pressure plate 8, which moves in the guides 7 and 7'. On the pressure plate 8, the cardboard blank CB is placed. The base plate 10 with the placed die-cutting forme 11 is fixed to the guides 7 and 7'. The die-cutting forme 11 contains the cutting rule 12. The adjustment of the die-cutting forme 11 with cutting rule 12 relative to the movable pressure plate is provided by adjusting threaded joints 13 and 13'. This allows the change of the pressure level during cardboard blank cutting and to adjust the quality of the cut.

For the experiment, the strain gauge technique was used to follow variations in loading. For measurement of the torque values on the drive shaft of the experimental bench in area A, strain

gauges are placed, which change their resistance depending on the values of loads, according to the recommendations [18].

According to the recommendations [19], strain gauges 16 (Fig. 2) are glued on the drive shaft 4 of the experimental bench at an angle of 45° to the axis of the shaft and 90° relative to each other.

The most common material for packaging manufacture – cardboard of type folding boxboard (FBB) – has been used [2, 3], which has inner plies of mechanical pulp and outer plies of chemical pulp. Cardboard blanks of a local manufacturer with thicknesses of 0.3 mm (250 grams per square metre [gsm]), 0.45 mm (310 gsm), 0.5 mm (380 gsm), 0.6 mm (440 gsm) and 0.7 mm (520 gsm) were chosen for the experimental research on the torque values that arise during cardboard blank cutting. The thickness of cardboard blanks was measured and controlled during the experiments according to the recommendations of the International Organisation for Standardisation (ISO) 3034:2011. For experimental research, paperboard blanks were conditioned at a temperature of 23°C and relative humidity of 50% for 4 h.

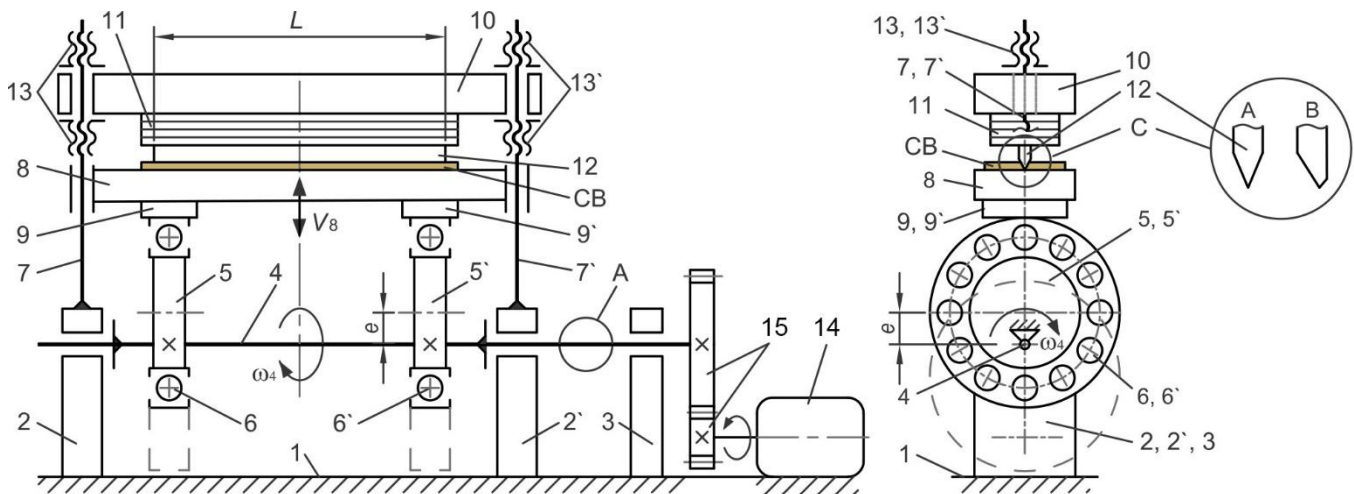


Fig. 1. Scheme of the experimental device for determining torque values on drive shaft during cardboard cutting in die-cutting press with eccentric mechanism drive of the movable pressure plate: 1 – entablement; 2, 2' – supports; 3 – support; 4 – drive shaft; 5, 5' – eccentrics; 6, 6' – rolling bearings; 7, 7' – guides; 8 – movable pressure plate; 9, 9' – hasps; 10 – base plate; 11 – die-cutting forme; 12 – cutting rule (knife); 13, 13' – threaded joints; 14 – stepper motor; 15 – gear transmission; A - area on the drive shaft, strain gauges are placed

As a cutting tool, two types of the cutting rules should be used:

- A, centre face (CF): cutting rules with symmetrical double-side face. Such rules are usually used for cutting the material with thickness up to 0.6 mm.
- B, side face (SF): SF cutting rules have one side face to get the perfectly straight cutting edge (90°) on the side against the face. Such cutting rules are used for cutting the material (cardboard, plastics, etc.) with thickness up to 0.6 mm.

The cardboard blank CB (Figs. 1 and 2) is placed onto the movable pressure plate 8 during its placement in the down position. The stepper motor 14 drives the shaft 4 through the gear 15. The rotation of shaft 4 goes to eccentrics 5 and 5', with roller bearings 6 and 6' providing their rotation with the angular velocity of ω_4 . The movable pressure plate 8 gets the motion from rolling bearings 6 and 6' trough hasps 9 and 9'. It moves vertically in the guides 7 and 7'. At the moment when the cardboard blank CB gets the cutting rule, cutting rule 12 starts the cutting process. In the end upper position of the movable pressure plate, the cutting

process stops, and with further eccentrics' rotation, the idling continues the kinematic cycle.

For measurements of torques on the drive shaft of the eccentric mechanism during the experimental research, we used foil strain gauges N2A-06-T007R-350 (VPG MicroMeasur, Shanghai, China) with an electrical resistance of 350Ω and a base of 150 mm. To prevent the influence of temperature fluctuations and reduce the influence of the bending of the drive shaft, four strain gauges are used for measurements, which are connected according to the complete bridge circuit. Power was supplied to one of the diagonals of the bridge circuit, and the output signal that shows the value of the loading was captured from the strain gauges on the other diagonal of the bridge circuit, which is connected to the specially designed module of gathering, processing and transmission of the data from strain gauges. The module for wireless data transmission consists of three elements: a 24-bit analogue-to-digital converter (ADC) with an integrated amplifier, microcontroller and Bluetooth module [12, 20].

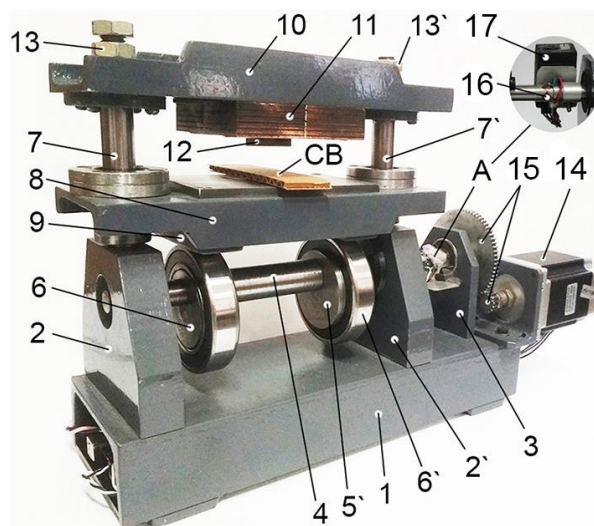


Fig. 2. Photo of the experimental device at following torque value on drive shaft as an effect of cardboard cutting in die-cutting press with eccentric mechanism drive of the movable pressure plate: 1 – entablement; 2, 2' – supports; 3 – support; 4 – drive shaft; 5, 5' – eccentrics; 6, 6' – rolling bearings; 7, 7' – guides; 8 – movable pressure plate; 9, 9' – hasps; 10 – base plate; 11 – die-cutting forme; 12 – cutting rule (knife); 13, 13' – threaded joints; 14 – stepper motor; 15 – gear transmission; 16 – strain gauges; and 17 – module of gathering, processing and transmission of the data

To establish the compliance of ADC data with the real torque values on the drive shaft of the drive mechanism of the pressure plate, calibration of the measuring equipment was done. For this purpose, the drive shaft 4 (Fig. 3) with the bearing 6 is fixed at the position of 90° (dashed line) relative to the upper position of the movable pressure plate 8. To pressure plate 8, the etalon force F_E with elbow h is applied. For getting the calibration diagram (Fig. 4), variations of loading were followed. These changes were used to convert the values of the ADC to real values of the torques.

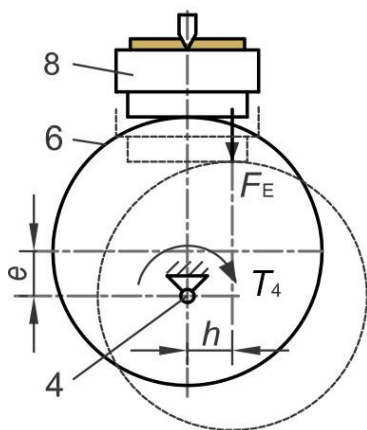


Fig. 3. Scheme of the torque value measurements for the drive shaft calibration

To convert the values of the ADC into the value of torque, the following dependence was used:

$$T_4 = F_E \cdot h = (n - n_0) \cdot k, \tag{1}$$

where n_0 – ADC starting value, n – ADC current value, k – coefficient for ADC value conversion into the torque values on the drive shaft.

Coefficient k for ADC value conversion was determined using the following expression:

$$k = m \cdot g \cdot e / n_t \tag{2}$$

where m – the mass of used weights, e – eccentricity of the eccentric mechanism ($e = 10$ mm), n_t – quantity of ADC values, which refers to the change of the used mass.

The calibration diagram (Fig. 4) shows the reference of the obtained ADC values to the real torque. Here, the y -axis represents the torque T_4 value on the drive shaft, reached by the change of the mass on the movable pressure plate 8 (Fig. 3). Along the x -axis, the current ADC values are presented. As can be seen, the graph is represented by a linear relationship. This shows that the strain gauges were cemented correctly, and the results of the experiment should be valid.

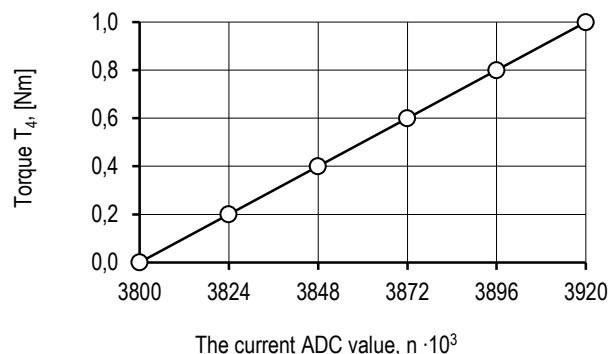


Fig. 4. Calibration diagram of torque values on the drive shaft

3. RESULTS

The results are represented by variations of torque value versus the rotation angle. They are collected from the process conducted using both approaches. In the first approach to the problem, the process was conducted without cardboard blanks (Fig. 5a), while in the second one, this process was used including the cutting stage (Fig. 5b).

The process without cardboard blanks is shown in Fig. 5a, with the following observations:

- Arc-shaped change of the torque as a result of overcoming the pressure plate and eccentrics' masses (the segment AB).
- Insignificant increase of torque value consequent to the contact of the cutting rule edge with the surface of the pressure plate (the segment BC).
- Linear torque value changes because of the end of the contact of the cutting rule with the pressure plate (the segment CD).
- Insignificant decrease of the torque due to the pressure plate and eccentrics' masses (the segment DE).
- Arc-shaped change of the torque on the drive shaft that contributes to its turn and is caused by the pressure plate and eccentrics' mass (the segment EF).

During the research of the cutting process of cardboard blank, the following points were recorded (Fig. 5b):

- Arc-shaped change of the torque as a result of overcoming the pressure plate and eccentrics' masses (the segment A₁B₁). At point B₁ begins the contact of the cutting rule edge

with the cardboard blank (the angle of the drive shaft rotation equals $\varphi = \varphi_0$).

- Impetuous increase of the torque consequent to the cutting of the cardboard blank by the cutting rule (the segment B₁C₁). At the same time, compression deformation arises, which can be explained by the fibrous nature of the cardboard. It is known [21, 22] that the destruction of the cardboard begins at the point of the cardboard deformation at a level of about 0.9 of its thickness, which corresponds to point C₁ (the angle of the drive shaft rotation equal to $\varphi = \varphi_1$).
- Impetuous decrease of torque on drive shaft (the segment C₁D₁). This is caused by further movement of the pressure plate and the appearance of a crack in the cardboard.
- Decrease of the torque during idle movement of the pressure plate (the angle of the drive shaft rotation equals $\varphi = 180^\circ$), which is caused by the pressure plate and eccentrics' masses (the segment D₁E₁).

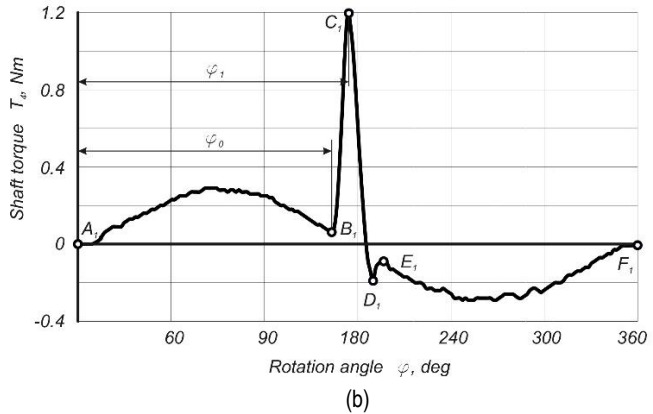
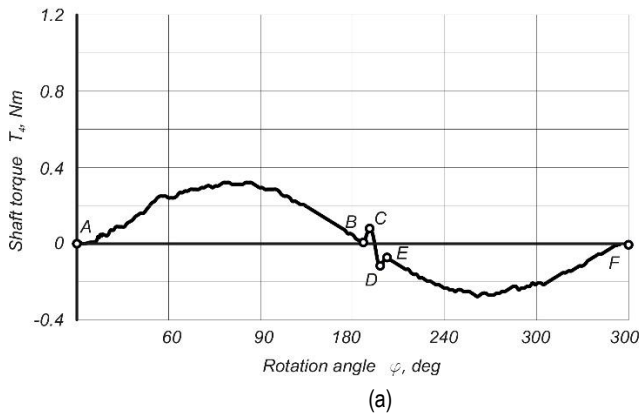


Fig. 5. Torque versus rotational angle at vertical displacement of the pressure plate without (a) and with (b) the cardboard blank process

The arc-shaped change of torque on the drive shaft contributes to its turn and is caused by the pressure plate and eccentrics' mass (the segment E₁F₁). As a result of the experimental research, the dependence of the torque is obtained (Fig. 5b). This dependence can be presented as $T_4 = f(\varphi)$, and as a result of its analysis, the maximum values of the torques on the drive shaft were observed when the cutting rule incut to the cardboard blank to a thickness of 0.9. The relative angle of the drive shaft rotation φ_1 was determined by the following dependence:

$$\varphi_1 = \arccos\left(-\frac{e-0.9\Delta}{e}\right), \quad (3)$$

where e – eccentricity ($e = 10$ mm); Δ – the cardboard blank thickness.

In mathematical statistics, it is proved that the selective arithmetic mean is the best (capable, irremovable and effective) estimate of the mathematical expectation of a random value [23]. The selective arithmetic mean method obeys the normal law of distribution. During the experimental research, we obtained a certain amount of data on torque values. The torque values were processed based on the calibration dependencies in accordance with the experimental research programme. With the aim to obtain valid results, we used the method of point estimation, which consists of acceptance as the unknown true value of the distribution parameter. The processed experimentally obtained data of the average value of seven measurements (minimal and maximum

values were neglected) eventually give the value of the torque values that arise during cardboard blank cutting.

For the researched cardboard thicknesses, the angle φ_1 was set as follows: for $\Delta = 0.3$ mm $\rightarrow \varphi = 166.7^\circ$; $\Delta = 0.4$ mm $\rightarrow \varphi = 164.6^\circ$; $\Delta = 0.5$ mm $\rightarrow \varphi = 162.7^\circ$; $\Delta = 0.6$ mm $\rightarrow \varphi = 161.1^\circ$; $\Delta = 0.7$ mm $\rightarrow \varphi = 159.6^\circ$.

The impact of the cardboard thickness, the fibres' direction (MD, CD), the type of the cutting rule and the rotational speed of the drive shaft on the value of the linear cutting effort was determined. The rotational speed of the drive shaft was changed discreetly: $n = 60$ rpm; 90 rpm; 120 rpm. The graphical results of these dependencies are shown in Figs. 6 and 7.

For the determination of the linear cutting effort, the dependence of a power balance was used:

$$T_4 \cdot \omega_4 = F_c \cdot V_8 \cdot \eta \quad (4)$$

where T_4 – maximum value of the torque on the drive shaft; ω_4 – angular velocity of the drive shaft ($\omega_4 = \pi \cdot n / 30$); F_c – cutting effort; V_8 – linear speed of the pressure plate displacement; η – efficiency coefficient of the experimental bench ($\eta = 0.9$).

Considering that $F_c = q \cdot L$ and $V_8 = \omega_4 \cdot e \cdot \sin\varphi_1$ from the dependence of power balance in Eq. (4), the linear cutting effort was calculated:

$$q = \frac{T_4}{L \cdot e \cdot \sin\varphi_1 \cdot \eta} \quad (3)$$

where q – linear cutting effort; L – the length of the cutting rule ($L = 20$ mm); e – eccentricity ($e = 10$ mm).

As can be seen from Fig. 6, the increase of the thickness Δ of the cardboard blank causes the increase of the linear cutting effort q during the process of cutting cardboard blanks in the MD. During cardboard cutting in the CD, a similar dependence was seen (Fig. 5b). For rotational speed of the drive shaft at 90 rpm, the increase of the cardboard thickness from 0.3 mm to 0.7 mm causes the increase of the linear cutting effort by 1.87 times (from 8.6 N/mm to 16.1 N/mm) during cutting in the CD and by 1.57 (from 12.1 N/mm to 19.0 N/mm) during cutting the blank in the MD. The obtained results can be logically explained. It is obvious that the increase in the cardboard thickness and changes in the fibre

direction (from MD to CD) cause the increased resistance of the cutting rule in the destruction of the cardboard.

The research on the impact of the rotational speed of the drive shaft has shown that the increase of the die-cutting velocity causes a decrease in the linear cutting effort. It can be explained by the increase of inertia of the torque T_4 on the drive shaft. Such an effect helps to overcome the resistance of cardboard cutting. As an example, for the cutting process of the cardboard blank with the thickness of 0.7 mm in the MD, a 2× increase of the rotational speed of the drive shaft – from 60 rpm to 120 rpm – causes the decrease of the linear cutting effort by about 1.2 times (from 19.8 N/mm to 16.5 N/mm).

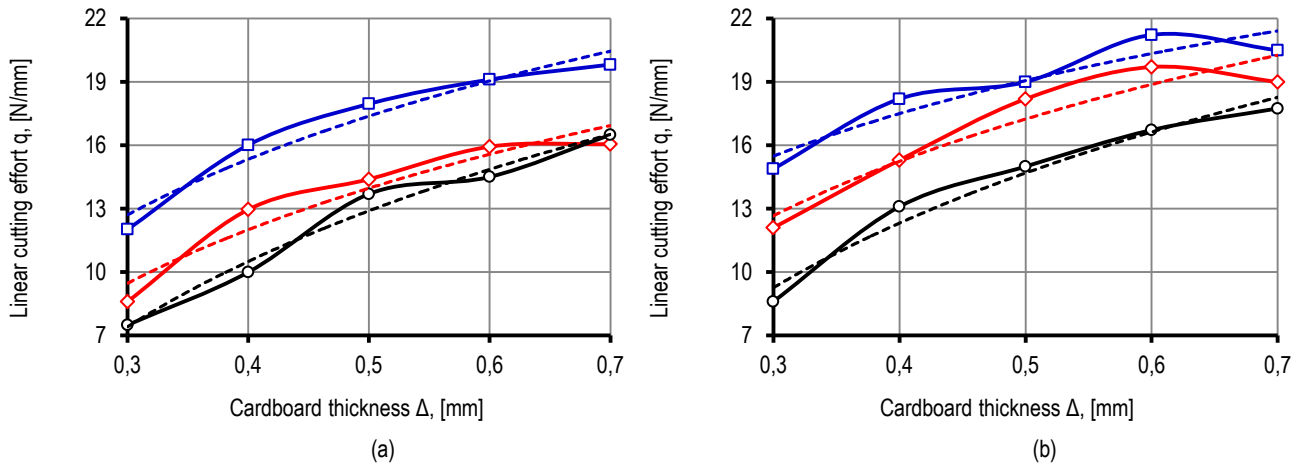


Fig. 6. The linear cutting effort (solid line) and approximated (dashed line) curves in MD (a) and CD (b) as a function of the thickness of the cardboard blank during cutting with the A cutting rule and rotational speed of the drive shaft: □ – 60 rpm., ◇ – 90 rpm., ○ – 120 rpm

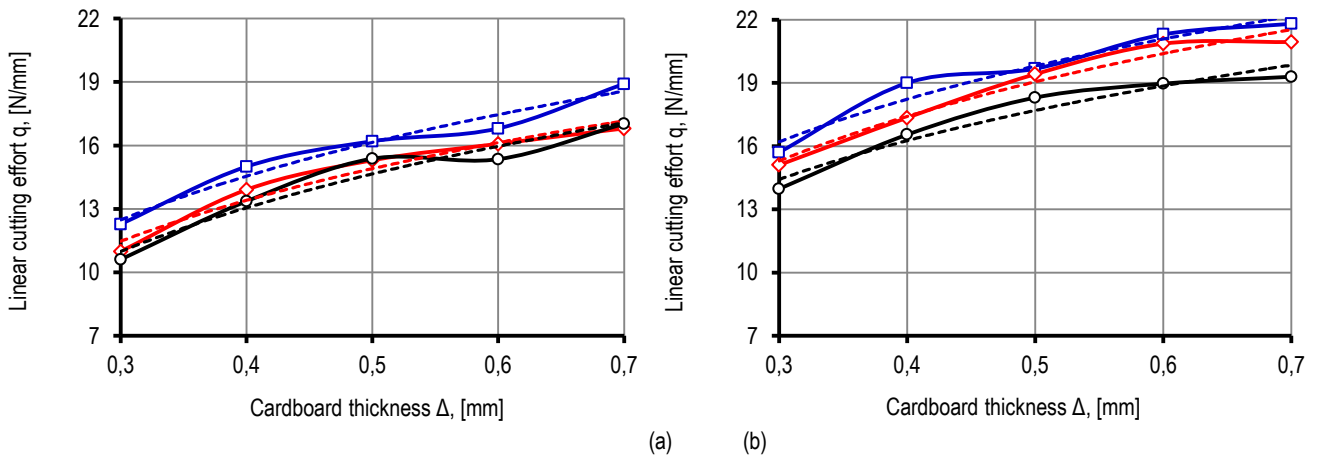


Fig. 7. The linear cutting effort (solid line) and approximated (dashed line) curves in MD (a) and CD (b) as a function of the thickness of the cardboard blank during cutting with the B cutting rule and rotational speed of the drive shaft: □ – 60 rpm., ◇ – 90 rpm., ○ – 120 rpm

Tendencies that were observed for the cutting process with cutting rule type A (the impact of the cardboard thickness, fibre direction and rotational speed on effort value) are similar to those with the rule type B. However, the linear cutting efforts during cardboard cutting with the cutting rule type A are slightly smaller than with the cutting rule type B. This is because of the cutting rule design. The cutting rule type A has two symmetrical faces on both sides and the cutting rule type B has a long one-sided face with the short opposite one at an angle of 90°. This fact can explain the minimal impact of the speed mode (rotational speed of the drive shaft) on the linear cutting efforts for cardboard cutting

with the rule type B. As an example, the 2× increase of the rotational speed from 60 rpm to 120 rpm helps to reduce the linear cutting effort by 1.1 times (from 18.9 N/mm to 17.0 N/mm) for the cutting process of the cardboard blank with a thickness of 0.7 mm in the MD. For comparison, a similar number for rule type A is 1.2 times.

The processed experimentally obtained data and the graphical dependencies of $q = f(\Delta)$ have been approximated by trend lines (logarithmic curves) and are shown in Tab. 1. These eventually give the value of the linear cutting effort values that arise during cardboard blank cutting. It gives an opportunity to determine the

values for any thickness of the cardboard and the direction of its fibres depending on the rotational speed of the drive shaft and the type of cutting rule.

The total dispersion S^2 (dispersion of the output parameter) characterises the scatter of the experimentally observed points relative to the average value. The closer the experimental data is to the diagram of empirical dependence, the closer is the connection, the smaller is the residual dispersion and the greater is the correlation coefficient. According to the results of the experimental research on the cutting process, the dispersion value (coefficient of the reliability of the experimental curve approximation by the trend line) is 0.90–0.98.

Tab. 1. The linear cutting effort dependencies on cardboard thickness and its fibre direction for different cutting rule types and rotational speeds of the drive shaft of the movable pressure plate

Cutting rule type	Rotational speed of the drive shaft n, rpm	Fibre direction	Coefficient of the reliability of the experimental curve approximation	Trend line equation (logarithmic curve)
A	60	MD	0.96	$q = 9.1428 \times \ln(\Delta) + 23.719$
		CD	0.90	$q = 7.0044 \times \ln(\Delta) + 23.921$
	90	MD	0.93	$q = 8.8059 \times \ln(\Delta) + 20.077$
		CD	0.91	$q = 8.9733 \times \ln(\Delta) + 23.467$
	120	MD	0.98	$q = 10.741 \times \ln(\Delta) + 20.349$
		CD	0.97	$q = 10.634 \times \ln(\Delta) + 22.065$
B	60	MD	0.97	$q = 7.1796 \times \ln(\Delta) + 21.126$
		CD	0.95	$q = 7.0399 \times \ln(\Delta) + 24.68$
	90	MD	0.96	$q = 6.7174 \times \ln(\Delta) + 19.563$
		CD	0.97	$q = 7.3551 \times \ln(\Delta) + 24.149$
	120	MD	0.95	$q = 7.1706 \times \ln(\Delta) + 19.624$
		CD	0.95	$q = 6.4038 \times \ln(\Delta) + 22.13$

CD, cross-direction; MD, machine direction.

4. SUMMARY AND CONCLUSION

As a result of the analysis of the references, the use of eccentric mechanisms for the drive of the movable pressure plate of the flatbed die-cutting press has been proposed. The use of such type of mechanisms provides the opportunity to avoid the drawbacks of die-cutting presses that are built using multilink and cam mechanisms. The research of the power characteristics that arise during cardboard blank cutting using the die-cutting press with the eccentric mechanism drive of the movable pressure plate is a relevant scientific task.

The experimental bench with the eccentric mechanism in a drive of the pressure plate has been developed. The experimental bench allows the smooth changing of the rotational speed of the

drive shaft. The process of cutting the cardboard blank using an eccentric die-cutting press has been researched.

The programme of experimental research of the torque values on the drive shaft of the experimental device was developed. For the research, the method of strain gauge measurements was applied. The proposed methods of measurements and data processing using modern hardware and software provide the processing simplification of the measurement results and make it possible to obtain reliable values with minimal faults.

The relationship between torque and rotation angle was captured in two cases of the experiment: with and without cardboard. The values of the rotational angle were determined. It was established that, for cardboard blanks made of FBB with thicknesses in the range of 0.3–0.7 mm, this angle was 160°–167°.

The influence of the cardboard thickness, the direction of its fibres, cutting rule type and rotational speed of the drive shaft on the value of the linear cutting effort was determined. The most impact on the value of the linear cutting effort was exerted by the thickness of the cardboard blank. The increase of the cardboard thickness from 0.3 mm to 0.7 mm causes the increase of the linear cutting effort from 7.5 N/mm to 21.5 N/mm depending on the cardboard fibre direction and the speed mode of the die-cutting press.

The relationship between linear cutting efforts and the cardboard thickness, its fibre direction, cutting rule type and rotational speed of the drive shaft was elaborated. This data was approximated by logarithmic function (logarithmic curve). Thus, the coefficient of the reliability of the experimental curve approximation by the trend line lies in the range of 0.90–0.98.

The obtained results can be very easily used for development of die-cutting equipment with the eccentric drive mechanism of the movable pressure plate.

REFERENCES

- Rudawska A, Čuboňova N, Pomarańska K, Stančeková D, Gola A. Technical and organizational improvements of packaging production process, *Advances in Science and Technology*. 2016;10(30):182–192.
- Emblem A, Emblem H. *Packaging technology Fundamentals, Materials and Processes*. 2012. Oxford: Woodhead Publishing.
- Kirwan MJ. *Handbook of Paper and Paperboard Packaging Technology*. 2013. Oxford: John Wiley & Sons.
- Rehei I. *Consumer Cardboard Packaging: Materials, Materials, Design, Manufacturing Equipment*. 2011. Ukrainian Academy of Printing, Lviv, 1–144. (in Ukrainian).
- Khvedchyn YY, Zelenyi VV. Analysis of The Mechanisms of Press in Die-cutting Automat, *Scientific Papers*. 2014;4(49):21-30 (in Ukrainian).
- Kuznetsov VO, Kolomiets AB, Dmitraschuk VS. Parametric Researches of the Press Plate Drive in Die-cutting Automat, *Upakovka*. 2012;6:31-34 (in Ukrainian).
- Kuznetsov VO, Rehei II, Vлах VV. Modification of a Drive Mechanism of a Press Plate in a Die-cutting, *Press, Printing and Publishing*. 2017;1:56–62 (in Ukrainian).
- Lin W, Zhou C, Huang W. Optimum design for mechanical Structures and material Properties of the dual-elbow-bar mechanism, *Hindawi Advances in Materials Science and Engineering*. 2015.
- Shakhbazov YO, Cheterbukh OY, Shyrokov VV, Palamar OO. The drive mechanism of a pressure plate of a flat die-cutting press, *Printing and Publishing*. 2020;1(79):112-120 (in Ukrainian).
- Behen PI, Radikhovskiy IA, Mlynko OI. Die-cutting Press wit Using a Lead Screw Transmission (Investigation of Pressure Plate Kinematic Parameters), *Upakovka*. 2020;1:44–45 (in Ukrainian).

11. Rehei II, Knysh OB, Behen PI, Radikhovsky IA, Mlynko OI. Drive of The Pressure Plate of the Die-cutting Press on The Basis of Using the Screw Nut Transmission (Method of Evaluation of Consumption Power Components), *Scientific Papers*. 2020;1(60):98–107 (in Ukrainian).
12. Ternytskyi S, Rehei I, Kandiak N, Radikhovskyi I, Mlynko O. Experimental research of paperboard cutting in die cutting press with the screw–nut transmission of drive mechanism of a movable pressure plate, *Acta Mechanica et Automatica*. 2021;15(3):122–131.
13. Ivanko I, Pidvyshenna O. Usage of a two-chamber pneumatic module for cutting contours in cardboard scans, *Technology and Technique of Typography*. 2021;3(73):71–81 (in Ukrainian).
14. Happonen, A, Stepanov A, Piili H, Salminen A. Innovation Study for Laser Cutting of Complex Geometries with Paper Materials, *Physics Procedia*. 2015;78:128–137.
15. Pinčjer I, Miketić N, Tomić I, Adamović S. Exploring the Various Parameters of CO2 Laser in the Cutting of Paper. Paper presented at the 10th International Symposium on Graphic Engineering and Design GRID 2020, Novi Sad, Serbia, November 12–14.
16. Fadji T, Berry T, Coetzee C.J, Opara U. Investigating the mechanical properties of paperboard packaging material for handling fresh produce under different environmental conditions: Experimental analysis and finite element modelling. *The Journal of Applied Packaging Research*. 2017;9:20-34.
17. Garbowski T, Gajewski T, Grabski J. Estimation of the Compressive Strength of Corrugated Cardboard Boxes with Various Perforations, *Energies*. 2021;14(4):1095.
18. Schicher R, Wegener G. *Measuring Torque Correctly*, Hottinger Baldwin MesstechnikGmbH, Germany. 2002.
19. Hilal MM, Mohamed HS, Petroczki K, AwadKhidir E. An Improved Strain Gauge-Based Dynamic Torque Measurement Method. *International Journal of Circuits, Systems and Signal Processing*. 2013;1(7):66-73.
20. Knysh O, Rehei I, Kandiak N, Ternytskyi S. Experimental Evaluation of the Tractive Effort of the Chain Conveyor during Book Block Spine Processing by Cylindrical Milling Cutter at Perfect Binding, *Acta Mechanica et Automatica*. 2019;13(2):101–106.
21. Banakh YO, Chekhman YI, Ternytskyi SV. The research method of technological forces at producing involutes of cardboard packing, *Scientific Papers*. 2011;3(36):229-235 (in Ukrainian).
22. Chekhman YI. Ternytskyi SV. Analysis of the phenomenon that accompany the process of diecutting the involute of cardboard package, *Upakovka*. 2012;3:28–33 (in Ukrainian).
23. Gorvat AA, Molnar OO, Minkovich VV. *Metodiobrobki eksperymentalnykh danikh z vikoristannyam MS Excel*. Vidavnicztvo UzhNU «Goverla». 2019. (in Ukrainian).

Oleh Knysh:  <https://orcid.org/0000-0001-5854-1879>

Ivan Rehei:  <https://orcid.org/0000-0002-3395-2994>

Nazar Kandiak:  <https://orcid.org/0000-0002-4720-3935>

Serhii Ternytskyi:  <https://orcid.org/0000-0002-3814-9762>

Bohdan Ivaskiv:  <https://orcid.org/0000-0001-7637-7160>

NONLINEAR VIBRATION ANALYSIS OF BEAM AND PLATE WITH CLOSED CRACK: A REVIEW

Samrawit A. TEWELDE^{*}, Marek KRAWCZUK^{*}

^{*}Faculty of Mechanical Engineering and Ship Technology, Institute of Mechanics and Machine Design, Gdansk University of Technology, ul. Narutowicza 11/12, 80-233 Gdańsk, Poland

samrawit.alemayehu.tewelde@pg.edu.pl, marek.krawczuk@pg.edu.pl

received 28 May 2022, revised 6 July 2022, accepted 7 July 2022

Abstract: The effect of nonlinearity is high sensitivity in damage detection, especially for closed cracks and delamination. This review illustrates the results of several researchers dealing with nonlinear effects caused by the closure of cracks in the structure, i.e., beam and plate structures. Early detection of damage is an important aspect for the structure and, therefore, continuous progress is being made in developing new and effective methods that use nonlinear effects for early detection of damage and barely visible cracks, i.e., closed cracks and delamination, as well as for the determination of crack size and location. After analysing various methods, the merits, drawbacks and prospects of a number of nonlinear vibration methods for structural damage detection are discussed, and recommendations are made for future researchers.

Key words: closed crack, closed delamination, nonlinearity, crack detection methods

1. INTRODUCTION

Safe structures with high efficiency are a prerequisite for various applications, such as sporting goods, automotive, construction and aerospace industries. Nowadays, structural damage poses a challenging problem in most applications. There are two types of cracks that commonly occur in structural systems: open cracks and closed cracks. Open cracks cause a decrease in physical stiffness, resulting in a largely linear structure with lower load carrying capacity and lower vibration frequencies [1, 2]. Owing to the bilinear stiffness characteristics associated with open and closed circumstances, the formation of breathing cracks not only lead to a reduction in stiffness of the structure, but also causes the linear structure to become nonlinear. The most common cause of structural failure is cracking due to fatigue and corrosion [3, 4].

A closing crack or breathing is a change in the stiffness of the body in the process of cyclic deformation by stretching and compression with opening and closing, respectively. A closing crack is an immediate change in the stiffness structure. This property leads to the nonlinear dynamic behaviour of mechanical systems and nonlinear effects such as the occurrence of subharmonic and superharmonic resonances and the nonlinearity of the vibration response (which includes displacement, velocity, acceleration and deformation) and the main resonance [5-7].

To avoid catastrophic failure in a variety of practical applications, the development of diagnostic techniques that are sufficiently sensitive to incipient fractures in structures and machines is a critical issue [8]. The diagnostics employ vibration-based and wave propagation based approaches; the most important potential advantage of vibration diagnostics based on nonlinear effects is its relatively high sensitivity to closing crack damage. Many vibration-based diagnostic techniques are used and studied by differ-

ent researchers, as well as wave propagation-based approaches. Conventional spectral analysis is an approach based on the existing vibration-based diagnostic system. However, spectrum analysis has the crucial disadvantage that the amplitudes of nonlinear harmonics are extremely susceptible to measurement noise, which may distort the applied damage detection procedure employed [9, 10]. Researchers are still searching for newer methods (for detecting internal cracks in structures based on vibration feature extraction) that have higher sensitivity to the presence of damage, while being simple to use. Vibration characteristics include changes in damping, subharmonic and superharmonic vibrations, nonlinear distortions of vibration at the principal resonance, changes in the transfer function, distortion of phase trajectories and so on [11-13].

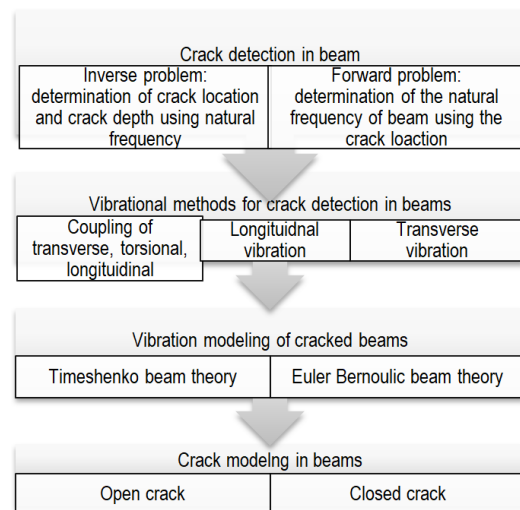


Fig. 1. Crack detection in beam-like structures [14]

The primary objective of this review is to highlight the major accomplishments of numerous researchers who have investigated the nonlinear effects caused by a closing crack in beam and plate structural elements, with the goal of determining the possibility and future prospects of using nonlinear behaviour to detect damage. After a review of current methods, various methods are analysed, the merits, drawbacks and prospects of a number of nonlinear vibration methods for structural damage detection are discussed and a recommendation is made for future researchers.

The rest of the paper is organised as follows. Section 2 discusses various methods for detecting closed cracks in structures using nonlinear vibration methods. Section 3 presents numerical and experimental studies for closed crack detection in beams. Section 4 analyses various methods in plates using a nonlinear effect in the structure. Section 5 concludes the paper.

2. METHODS OF CLOSED CRACK DETECTION IN STRUCTURE

Non-destructive testing of structures and diverse technical components can be performed effectively, economically and quickly using vibration measurements. The features of the linear response of the open crack model can only detect the crack at an advanced level, but the effects of the nonlinearity of the closed crack model can be used to detect the crack at an early stage [15]. Potential structural damage mechanisms in engineering structures are associated with structural nonlinearities, which require extensive measurements and analysis of nonlinear vibration properties to detect and evaluate. The difficulty in finding breathing cracks is that the dynamic properties of a structure with a breathing fracture change significantly more slowly. Researchers have found that a structure with a closing crack behaves more like a nonlinear system, comparable to a bilinear oscillator, and that the nonlinear response characteristics can be used to detect the crack [12]. Early researchers used methods to evaluate changes in natural frequencies and natural modes to detect damage [16]. Changes in natural frequencies and natural modes, according to M. Dilena et al. [17] and Vimal M. et al. [18], are insufficient to detect minor cracks in the structure, i.e. closed cracks.

Cracked structures with one degree of freedom have been simplified as oscillators with single degree of freedoms (DOFs) [19]. In early research on breathing cracks, cracked beams were simplified as single-DOF oscillators whose stiffness in half cycles for tension and compression was represented by asymmetric linear or nonlinear functions. This approach was extended to cracked structures with multiple degrees of freedom, while, periodic changes in crack locations were incorporated into dynamic stiffness matrices to model closing cracks [20]. For continuously cracked beams with infinite DOFs, 'breathing' cracks were modelled analytically [21].

A. Chatterjee [22] applies the nonlinear dynamic model of the cracked structure using higher-order frequency response functions and a bilinear restoring force using a polynomial series. The effect of crack severity on the amplitudes of the harmonic response is investigated and a new method for estimating crack severity by measuring the amplitudes of the first and second harmonics is proposed [1, 23]. Most researchers model closing cracks for beam structures and closing delaminations for plate-like structures to simulate their closing motions during vibration. The crack is modelled as a local flexibility [24] in the structure. The

size of the crack and its location are studied by changing the modal parameters such as natural frequency [25-26] and damping factor [27]. The detection of cracks by the vibro-acoustic method has been performed elsewhere in the literature [28-31]. A well-known approach for vibro-acoustic diagnosis of bilinearity of a mechanical system is the free vibration method [32]. In this method vibro-acoustic signals are used to evaluate the dependencies of the free vibration decrement and the natural frequency as a function of the crack size. Z. Kiral et al. [33] state that the change in decrement is a more sensitive indicator of damage compared to the natural frequency. Some effective and accurate measurement and analysis techniques have been developed and effectively used to detect and identify structural nonlinearities, the effects of which are readily apparent in the observed conventional first-order frequency response functions (FRFs) [34]. The other structural nonlinearities caused by closing cracks do not contribute to the first-order FRFs. Therefore, Riccardo Cappello et al. [35] developed a method to identify the physical parameters of breathing cracks using second-order FRFs, and R.M. Lin and T.Y. Ng [36] report that higher harmonics are efficient indicators of closing cracks. Although higher harmonics may indicate the occurrence of closing cracks [33], the amplification effect of higher harmonics due to differentiation is quantitatively investigated using several scenarios.

The nonlinear behaviour of harmonics generated by breathing cracks is well explained by the nonlinear pseudo-force (NPF) and experimentally validated on a beam with a fatigue crack by non-contact vibration measurement [38]; the same evidence was also provided by M. Cao et al. [39] for the localisation of 'breathing' delamination by using deflection forms at nonlinear harmonics. W. Xu et al. [40] analytically formulated the nonlinear pseudo-force by rearranging the equation of transverse motion of the cracked beam. The concept can be used to localise cracks and elucidate the mechanism needed for the generation of higher harmonics by 'breathing' cracks. Cui et al. [41] used bispectrum analysis to detect 'breathing' cracks by studying the nonlinear dynamic properties of cracked beams. K. Wang et al. [42] developed a two-dimensional analytical model to interpret the modulation mechanism of a breathing crack to guide ultrasonic waves. Semperlotti F. et al. [43] explicitly reveal that the harmonic generation mechanism is a fundamental issue in the study of breathing cracks.

3. NUMERICAL AND EXPERIMENTAL DETECTION OF CLOSED CRACK IN BEAM

3.1. Model of crack beam

The use of nonlinear models for cracked beams is crucial in a closed crack of the structure to detect the crack and fully understand the vibration characteristics generated by the breathing crack. The modelling of the breathing crack is an important step that lays the groundwork for crack analysis and identification.

According to A. Rivola and PR. White et al. [44], the bispectrum can be used to examine the system response and the bilinear oscillator model to mimic the nonlinear behaviour of a beam with a closing crack. As seen in Fig. 2, the breathing crack can have a bilinear stiffness effect. Then, in Figs. 3–5, a single, two, and many cracks in the structure are depicted, respectively, where a is crack depth, b is beam width, h is beam height and L is beam length.

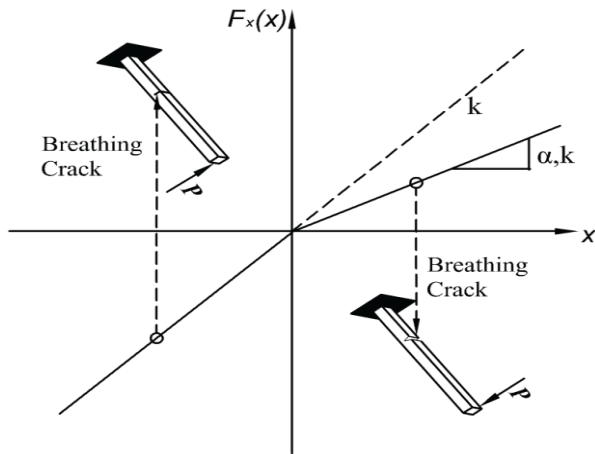


Fig. 2. Cantilever beam with breathing crack [45]

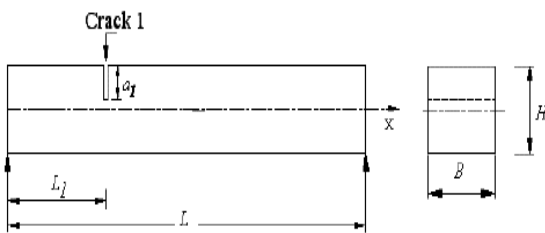


Fig. 3. Schematic diagram of a cracked simply supported beam with single cracks [46]

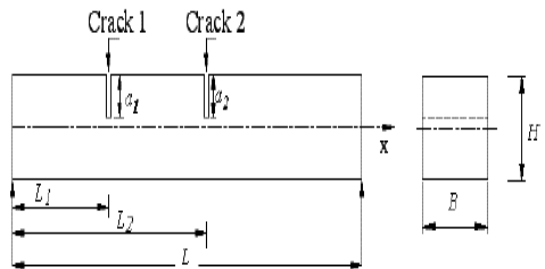


Fig. 4. Schematic diagram of a cracked simply supported beam with two cracks [46]

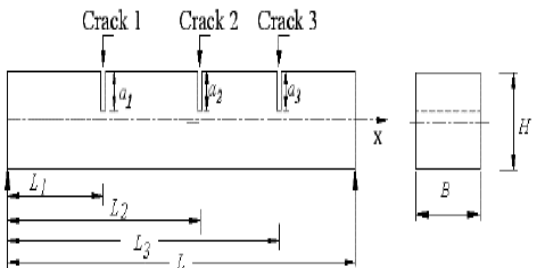


Fig. 5. Schematic diagram of a cracked simply supported beam with three cracks [46]

To model stiffness change in bilinear oscillators, Chu and Shen [47] proposed a replacement closed-form solution for bilinear oscillators under low-frequency excitation utilising two square wave functions. Their study proposes a simple polynomial model

for modelling the beam with a breathing crack. For a cracked cantilever beam with a transverse one-edge non-propagating closing crack, the polynomial model is confirmed. This amplitude-dependent polynomial model can be used to simulate nonlinear systems with bilinear behaviour. According to Caddemi and Calio' [48], the closing crack was approximated using Dirac's deltas, which enabled closed-form evaluation of beam mode forms for a generic crack configuration. It should also be mentioned that the nonlinear effect of the system is stronger if the superharmonic components include more energy in the output spectrum.

3.2. Subharmonic and superharmonic resonance vibration

When a system with a breathing crack is activated by a single harmonic force, the response shows different nonlinear properties, according to F.E. Dotti et al. [49] the excitation causes the crack to open and close, resulting in harmonics that are integer multiples or fractional multiples of the driving frequency. Superharmonic and subharmonic are the terms used to describe these harmonics.

According to Bovsunovskii et al. [50], the vibration of a cantilever beam with a closing crack under the action of a harmonic concentrated force was characterised by superharmonic resonances of order j/i (the symbol j/i denotes the ordinal number of the nonlinear regime, which indicates how many natural periods of vibration j fall at i periods of the external harmonic excitation), with very small amplitudes.

The displacement time history response of the actual system and the corresponding Fourier spectrum of the approximated polynomial system are given in Figs. 6a and 6b, respectively, as depicted in the study of Prawin and Rao [45]. The nonlinear effect of the system is increased if the superharmonic components include more energy in the output spectrum.

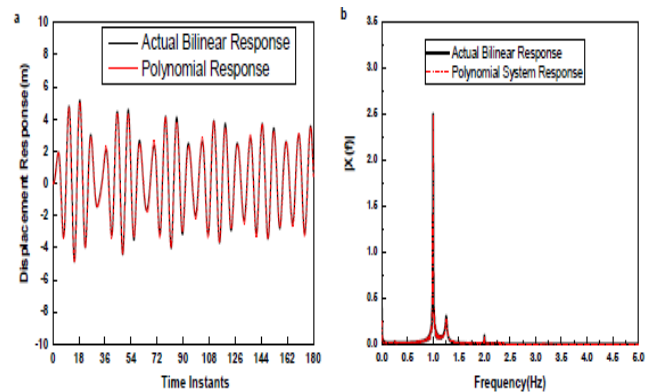


Fig. 6. The actual bilinear response and polynomial response [45]

Nonlinear vibration characteristics, according to Broda et al. [51], are more sensitive to breathing cracks, especially when subharmonic and superharmonic resonances are present. Additionally, Andraeus et al. [52] investigated the cracked beam's forced harmonic response by treating the closing crack interfaces as a contact problem and used finite analysis software. The results of the simulations showed that subharmonic and superharmonic resonances exist in the broken beam. However, the phenomena that caused these several harmonics to appear in the experiment have yet to be fully explained. The fundamental reason for this is that the nonlinear vibration of a beam with a breath-

ing crack is poorly understood, and the intrinsic link between the subharmonic and superharmonic resonance responses and the beam parameters is not well understood, necessitating further research into cracked beams [53]. Pugno et al. [54] created a novel stiffness model that takes partial crack closure into account. The finite element approach was used to generate a nonlinear dynamic equation for a beam with a breathing crack, and the multiple-scales method was used to assess the approximate steady-state response of the cracked beam to a harmonic excitation. According to their findings, the crack parameters, as well as a combination of the crack parameters and excited force parameters, influence the nonlinear vibration of a cracked beam.

Under some circumstances, this system presents third-order superharmonic resonance, second-order superharmonic resonance, 1/2th-order subharmonic resonance, combination resonance and multiple resonances. The most used combinations are the second-order subharmonic when the system is excited at twice its natural frequency; the second-order superharmonic, when the system is excited at half of its natural frequency; and the third-order superharmonic, when the system is excited at one-third of its natural frequency [55, 56].

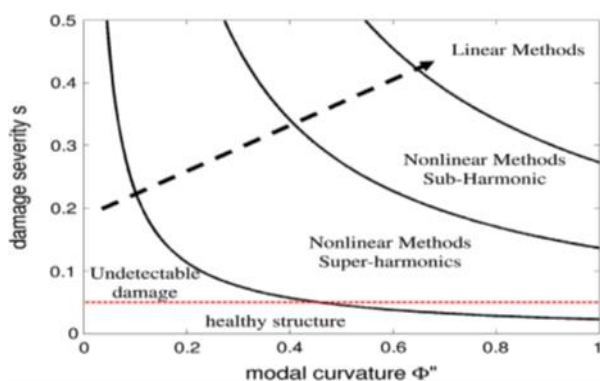


Fig. 7. damage severity with modal curvature [57]

This is especially important when dealing with a more sophisticated structure. In fact, if the chosen forcing frequency only excites modes with curvature-nodes close to the damage position, even huge cracks may go undetected by harmonics approaches. Figure 7 shows how this problem is qualitatively expressed. As the modal-effective damage increases, one moves from a low-damage zone where no identification is possible to a zone where only superharmonic are sensitive to damage; as the damage increases further, one reaches a zone where subharmonic are sensitive and preferable; and finally, a zone is reached where more simple linear methods are effective.

3.3 Forced vibration

3.3.1. Governing equation of forced vibration

The Euler–Bernoulli equation for the beam elements without crack is written as

$$M\ddot{u} + C\dot{u} + Ku = f(t) \tag{1}$$

where $f(t)$ is an external force that can be harmonic, non-harmonic and periodic; M is mass; C is dampness; and K is stiffness.

$$M\ddot{u} + c\dot{u} + ku = f\sin\omega t \tag{2}$$

$$\ddot{u} + 2\xi\omega\dot{u} + \omega n^2u = f\sin\omega t \tag{3}$$

If $\omega = \omega n$ resonance will occur, and that means large amplitude can be expected.

Zhao et al. [58] used Green’s functions approach and the superposition principle to produce closed-form explicit formulations of the steady-state forced vibration of a multi-cracked Euler–Bernoulli beam subjected to a time-harmonic load. The numerical results revealed that crack geometries (depth and location) have a substantial impact on the system’s dynamic behaviour.

X. Zhao et al. [59] built on Zhao et al.’s work [58] to investigate the steady-state forced vibrations of multi-cracked Timoshenko beams, revealing that the effects of shear deformation and rotating inertia on the deflection pattern for a thick beam could not be ignored. Crack beams also infrequently show the mechanical mechanisms of crack geometries, particularly crack positions, in their dynamic behaviours. Also, by examining the dynamic behaviours of a general cracked double-beam system interconnected by a viscoelastic layer sitting on the Winkler–Pasternak elastic foundation, Chen et al. [60] try to fill these gaps. They obtain closed-form solutions for forced vibrations of a cracked beam connected viscoelastic layer, taking into account axial stresses and the Winkler–Pasternak elastic basis.

3.4 Wave propagation

Small or substantial portions of the beams may be damaged. The consequences of nonlinearity of a closed crack in a beam structure can be studied using a variety of methodologies. The Volterra series response representation is used to examine the nonlinear response of a beam with a closed crack, according to Surace et al. [61]. A polynomial series is used to approximate the bilinear restoring force due to closed crack modes, and the first- and second-order frequency response functions are created in terms of bilinear parameter. However, as the selected stimulation frequency is quite distant when the crack is very deep, the response amplitude is not observable [62]. Also, Wang et al. [40, 63] describe the development of a two-dimensional (2D) analytical model to analyse the modulation process of a ‘breathing’ crack to guide ultrasonic pulses (GUWs). The model can analyse the breathing behaviour of the crack as the probing GUWs cross it and reflect the breathing generated by the propagating and decaying waves, allowing for the extraction of nonlinear signal characteristics in contact with acoustic nonlinearity (CAN). Based on an analytical prediction of CAN formation as a function of crack severity, a correlation between CAN in GUW signals and crack parameters is established.

Based on the numerical and experimental detection of high-order harmonic waves or subharmonic waves caused by the interaction of ultrasound with closed cracks, Taizo et al. [64] and Koskinen et al. [65] use piezoelectric contact transducers, which are also studied by Lee and Hong [66]. Since the contact transducer requires a liquid coupling agent, the nonlinearity induced by the transducer into the measurement process could be much greater than the material’s nonlinearity, making it unsuitable for detecting complex structures with curved surfaces.

In complex shapes and hazardous environments, Wu TC et al. [67] employ fully non-contact NUT based on laser ultrasound (LUT) on closed surface cracks. The result reveals a weak second harmonic, which is caused by the material’s or measuring system’s nonlinearity. Higher harmonics are also used to locate closed cracks that are dominated by the initial harmonics, which

appear to be hidden [68, 69]. As a result, these hidden higher harmonics encounter difficulty in detecting the crack. To solve this problem, Cao et al. [69] developed an energy modulation effect phenomenon (EME) based on the concept of quadratic-Teager-Kaiser energy (Q-TKE) to clearly detect hidden higher harmonics in a closed crack. This was accomplished both numerically and experimentally using finite element methods and a Doppler laser vibrometer (DLV). However, noise causes false peaks while using this method. As a result, the stimulation must be carefully chosen, and noise suppression is also necessary.

Based on the vibration concept and the modal decomposition method, X. Sun Xu et al. [70] use the second harmonic Lamb wave modulated by the crack-induced acoustic nonlinearity of the contact. Non-zero energy flux and phase velocity are required due to the dispersion and the multimodal character of Lamb waves. As a result, different researchers [71] have chosen different mode pairs for different damages, although the amplitude of the required second harmonic Lamb mode was always altered by other Lamb waves with double frequency [72]. For Lamb waves in partially closed cracks, W. Zhu et al. [73] use a static component. In the research of Chen B. et al. [74], they use the hypothesised and experimentally studied approach of vibro-acoustic modulation (VAM) based on electromagnetic loading, which concentrates the loading energy around the closed crack. However, in the structure, it is critical to locate the sample's closed crack, after which additional work is required.

Carneiro S. and Inman D. [75] developed a continuous model based on Timoshenko beam theory to consider the nonlinear behaviour of bending and shear vibration in a breathing cracked beam, assuming that stiffness decreases as the distance from the crack position increases. A closed crack's nonlinear vibration inhibits the correct determination of the natural frequency [76]. As a result, crack nonlinear behaviour is included in the models. The closed crack behaviour is shown in the transverse vibration analysis of beam [77], axial beam [78] and longitudinal beam [79] with a single closed crack using the Perturbation method. A beam with numerous cracks may have a more nonlinear structural dynamic response than a beam with a single crack. The singularity of the concentrated cracks along the beam may impact the structure's continuity and geometric aspects. M. Kharazan et al. [80] use Euler-Bernoulli theory to simulate the transverse vibrations of a beam with several breathing cracks.

4. ANALYSING DIFFERENT METHODS IN PLATE USING NONLINEAR EFFECT

4.1. Natural frequency

Due to sinusoidal loading, delamination experiences tensile and compressive cycles. The delamination opens when the delamination surfaces are in tension, modifying the amplitude signal. Since the delamination surfaces come into contact with one another and behave similar to an intact surface during compression, the amplitude does not vary [81]. The area of damage was mapped in nonlinear acoustics by measuring the amplitude of nonlinear harmonic and subharmonic frequencies in the frequency spectrum of all nodes, according to Sun et al. [82]. Near the defect, the ratio between the amplitude of the second harmonic and the amplitude of the linear frequency is more pronounced, giving a qualitative indicator of the damage site. Likewise, the subharmon-

ic amplitude to the excitation frequency amplitude ratio is bigger at the defect zone. Experiments with the nonlinear harmonic imaging approach for defect identification have already been conducted. However, there are some places in both ratios that are not above the delamination but have a bigger ratio value, giving a false sense of the damage in that region. This is because these spots are on the modal pattern, which has very small vibration amplitudes. As a result, doing the experiments at many frequencies could be an option. Also, in the research of Tabatabaeipour et al. [83], it was assumed that nonlinear spring dampers that have been installed between contact states represent a nonlinear interaction of delamination surfaces. The spring stiffness and damping coefficient parameters are not available in the nonlinear spring-damper model; thus, they must be adjusted when the magnitude of the parameters varies sufficiently.

C. Andreades et al. [84] propose an ultrasonic phased array technique based on nonlinear modulation of dual frequency excitation to increase the sensitivity and accuracy of contact detection. The work has shown that the nonlinear array method can detect multiple contact defects in samples and has a higher localisation accuracy than the traditional linear phase array method. However, the work only looks at the bottom surface; phase signals at multiple points on the sample need to be investigated further.

4.2 Velocity/displacement relation

Delamination can also occur in a more complicated instance, where only some zones within the delaminated region are in touch while the rest are not, as shown in Fig. 8.

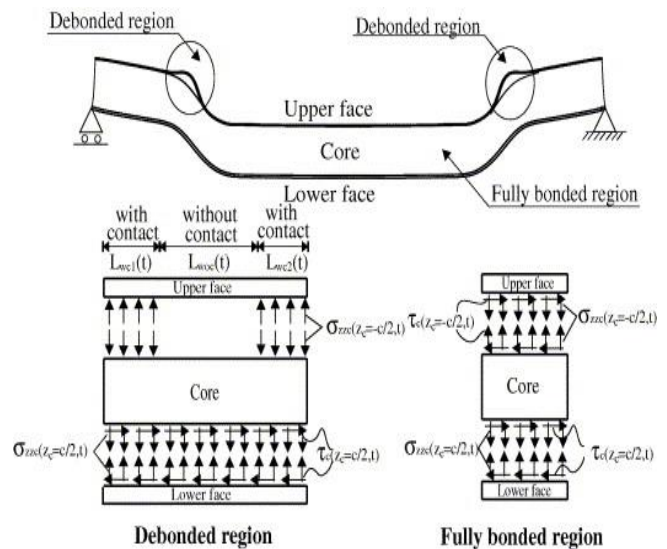


Fig. 8. A delaminated sandwich panel with partial contact conditions [85]

To define the dynamic behaviour of delaminated plates, Schwarts-Givli et al. [85] investigated nonlinear effects associated with time-dependent contact features of delaminated surfaces and large displacements of the face-sheets, at high-order displacement, velocity and acceleration fields in the core. The data clearly demonstrate the nonlinear behaviour's impacts. To characterise the effect of delamination on smart laminated composite plate structures, Shankar et al. [86] performed a numerical analysis using the finite element approach. They employed the time inte-

gration technique in various boundary conditions and locations of active fibre composite (AFC). According to their findings, the amplitude of dynamic responses is higher in the event of delamination and AFC patch locations, with less dynamic displacement when the patches are close to the delamination. The major shift in dynamic displacement response with respect to time history in the simply supported and clamped-clamped boundary is shown in Figs. 9 and 10. The velocity feedback gain is 1 ($G_v = 1$). However, delamination necessitates not only the consideration of boundary conditions and location, but also the analysis of the geometry of the structures.

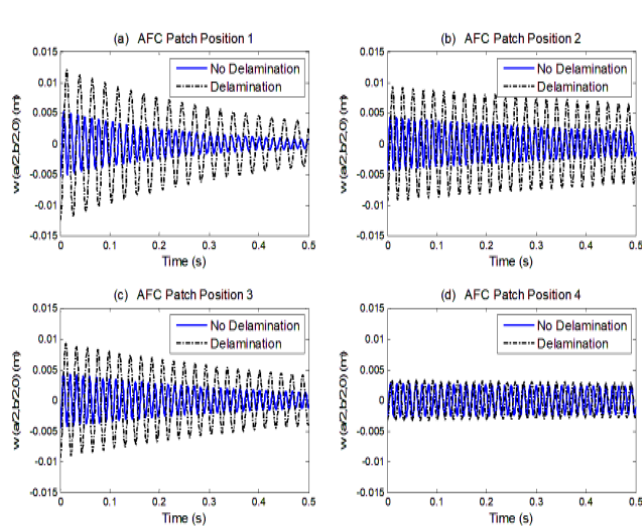


Fig. 9. Time response of delaminated and without delaminated plate at different locations of AFC patches ($G_v = 1$) in simply supported boundary condition [86]

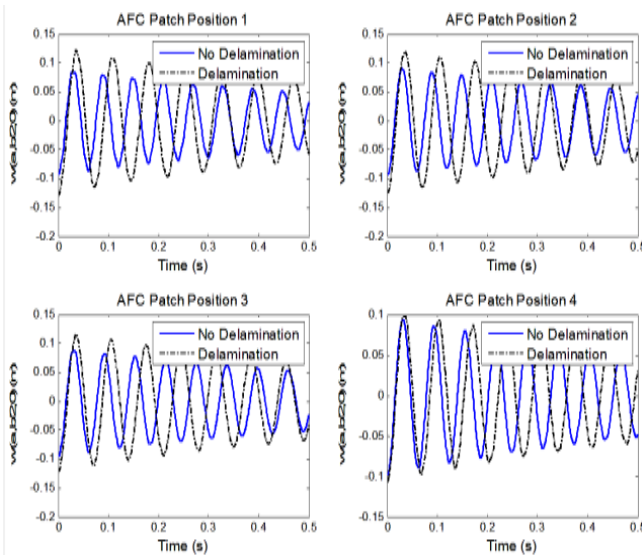


Fig. 10. Time response of delaminated and without delaminated plate at different locations of AFC patches ($G_v = 1$) in clamped-clamped boundary condition [86]

4.3 Forced vibration

Bovsunovskii et al. [50] used forced vibration of a simply supported laminated composite beam with 10 viscoelastic layers to determine delamination characteristics. At frequencies of 1 kHz

and 2 kHz, respectively, 73 and 146 times higher than the beam's initial natural frequency, harmonic excitation was applied. The delamination produced additional multiples of the excitation frequencies as a result of the periodic opening and closing of the delamination, with their value varying depending on the size and location of the delamination, according to the nonlinear analysis. On the other hand MH Kargarnovin et al. [87] discussed the existence of the delamination changes the stiffness of the structure, and the effects of the size, depth, location of the delamination and the load velocity on the dynamic response.

4.4 Wave propagation

The most common damage in plate structures is delamination. The delamination effect in plate structure laminates has been widely modelled for free vibration, transient analysis, frequency analysis and damage detection [88-89]. Nonlinear analysis of regular composite plates and shells for free vibration, bending and buckling has been carried out in many studies based on classical laminate theory [90], first-order shear deformation theory [91], higher-order shear deformation theory [92] and other refined theories [93]. By studying the interaction between the structure and the foundation in the context of the used material, Yushu et al. [94] obtained a good understanding that would enable prediction of the structural response. The composite plate can be predicted using different delamination sites before delamination and modelling is to be performed using layer-by-layer theory and finite element method.

Many researchers have addressed the problem of nonlinearity [95, 96] and are studying the static analysis of laminated shells resting on a nonlinear elastic foundation. They use a method to subsequently determine stresses and strains and initially assume a perfect bond. Shen et al. [97] investigate the nonlinear behaviour of a composite panel resting on an elastic foundation with imperfect bonding using transverse normal stress, transverse shear stress and transverse nonlinear stress transferred from the foundation to the plate. The result was obtained, but they only consider the base of nonlinearity, and the material nonlinearity and geometric nonlinearity are not considered.

N. Houhat et al. [98] focus on the vibro-acoustic modulation (VAM) technique and optimise nonlinear damage detection in multiple scattering. They use automatic optimisation and gain time reduction. It is a good basis for detecting damage to scattering radiators, but information about the local minima of the correlation coefficient is important for locating the nonlinear scattering radiators. X. Zhang et al. [99] proposed a nonlinear Lamb wave imaging technology to detect barely visible impact damage (BVID) in carbon fibre reinforced composites (CFRP). They did this at three different impact energies with corresponding impact surfaces. In their result, the relative nonlinearity coefficients of the second harmonic Lamb wave packets were received at a distance of 103 mm. However, at a distance greater than 103 mm, the relative nonlinearity coefficients become weak. According to their results, the Lamb wave fluctuated after it exceeded a certain value. So it is important to consider the noise.

According to Castellano et al. [100], they used the sideband peak count index (SPC-I) in composite plates to improve the application of the nonlinear ultrasonic technique in the detection of impact-induced damage. They improved the SPC-I technique by introducing a narrow band SPC-I technique. Then, lead zirconate titanate (PZT) of non-permanent adhesive gel was used, and they

reported that it showed reliable results in detecting damage in composite plates both at initiation and propagation. However, these techniques cannot determine the size of the defect and the type of defect that caused the damage. In the case of nonlinearity, it is important to understand the shape, dimensions and location of the cracks. Moreover, nonlinearity is caused not only by the crack, but also by other factors, such as material behaviour [101]. Therefore, such a consideration is essential to detect damage in the structure.

Q. Wei et al. [102] used the nonlinear acoustic resonance method to characterise fatigue damage in composite materials, especially CFRP. Based on their work, the progressive fatigue damage in composites was introduced by pendulum impact tests with different impact energies and investigated by infrared thermography and optical microscopy. They concluded that the damage index (DI) is a complex parameter influenced by the impact energy, impact angle, impact area and other factors; so, these factors should be considered. The boundary conditions and the effects of temperature should also be well thought-out.

S. Sikdar et al. [103] studied a geometric nonlinearity problem based on 3D numerical simulation and experimental analysis of guided wave propagation in smart composite structures based on finite element methods, and compared sources with and without breathing and bonding in the smart composite structures. Based on their results, the online SHM strategy has demonstrated its potential to locate sources with breathing and bonding using elastic wave signals, but operating conditions must be considered.

According to X. Wang et al. [104], the random pore model was introduced to perform nonlinear ultrasonic simulations to account for the randomness of pore size, morphology and distribution properties. They performed nonlinear ultrasonic simulations and experimental investigations for the real porous graphite composites. The results show that the relative nonlinear coefficient increases with increasing pore length and decreases with increasing pore width. However, the question arises as to what the result would be if they considered the effects of pore parameters and excitation parameters on the nonlinear coefficient. Also, a random pore model was used. Is there another way to get the same results?

The secondary or additional mass and spring is a primary structural device used to suppress vibrations [105]. However, such methods produce two resonant peaks with high amplitude. To minimise the vibration structure at both peaks and also at the resonant frequency, researchers have used optimisation techniques. Such optimisation techniques include linear quadratic controllers, genetic algorithms and so on [106, 107]. Both traditional and non-traditional models of vibration dampers are used to minimise the vibration of the structure, but there is a limit to suppressing the vibration of the main structure if the mass of the damper is not increased [108]. Therefore, researchers have used some modifications in absorber design, such as shape-memory alloys, magnetic suspensions and piezoelectric devices [109-110]. These modifications are called semi-active or active vibration absorbers.

According to Mohanty et al. [111], the effectiveness of active traditional and non-traditional vibration dampers in suppressing the vibrations of the main undamped system using PZT has been studied. Their work requires lower tension because the spring exerts a stronger blocking force on the PZT stack actuator, and thus lower tension is required.

Zhang and Zhao [112] studied the nonlinear vibrations of a rectangular cantilever composite plate excited in the plane and

transverse directions. They found that the chaotic responses were sensitive to the change in forced excitation and damping coefficient.

L.S. Yousuf [113] studied the nonlinear dynamic behaviour (non-periodic motion and chaos) of a laminated composite plate due to temperature changes and combined loading using the concept of the largest Lyapunov exponent with the Wolf algorithm and fast Fourier transform (FFT). While their work provides a basis to proceed upon, the question arises as to what the result would be if the algorithm were to differ. According to Dauson et al. [114], they used time reversal (TR) to focus acoustic energy and make acoustic measurements correlated with successive localised damage cycles in a laboratory-scale wellbore. They performed a damage detection study in wellbores by applying time reversal and nonlinear elastic wave spectroscopy, and the wellbore used in their study was a laboratory-scale wellbore. Based on their work, we might infer that this might be another way to locate damage in carbon fibre reinforced plastic (CFRP). J. Wang et al. [115] investigate a nonlinear Lamb wave TR technique for fatigue crack detection and quantification. Using the same technique, which is physical-virtual, TR can be extended to a network of active sensors for fatigue crack localisation and imaging.

According to Zhen et al. [116], a purely output-based approach using the Volterra series model to detect nonlinear structural damage is proposed, quantifying the nonlinear behaviour of structures without prior knowledge of the external excitations. Sometimes the structure responds either linearly or nonlinearly. When it responds linearly, the techniques may not be effective, and thus it is necessary to analyse the structural response. Many factors, such as geometric nonlinearity, nonlinear boundary conditions, connections of prefabricated structures and material nonlinearity, can cause the structural system to exhibit nonlinear behaviour; this needs to be fully considered.

In theory, V. Samaitis et al. [117] have analytically studied the mode conversion of Lamb wave directed from each other at the tip of delamination in a composite plate. According to Wang et al. [118], they have investigated reflection and transmission of wave mode in metal and composite beams containing delamination and inhomogeneity. The spectral element method (SEM) is used to simulate Lamb wave interaction with open and closed cracks. Additionally, cracked spectral element models are individually established for open and closed cracks. Nag et al. [119] used the SEM to model wave scattering at the location of embedded open delamination in composite beams.

5. FUTURE RESEARCH

The current challenges and future suggestions for the application of nonlinear vibration-based method in the detection of closed cracks and other defects in a beam and plate are discussed in this section.

In the beginning, a linear approach was used since the majority of researchers believed that cracks kept opening during vibration. Gudmunson [120] was the first to notice this phenomenon after conducting experiments to determine a correlation between the position and size of a crack and the variation in natural frequencies. N. Pugno et al. [51, 121] used the vibrational response to the harmonic force of a cantilever beam with cracks of different sizes and locations, and their analysis employs the harmonic balance approach. The method involves a significant reduction in

comparison with direct numerical integration.

In order to determine the relative amplitude of the dominant harmonics of a rod-like structure with a closing crack at subharmonic and superharmonic resonances, Matveev et al. [122] presented an approximate analytical method. They demonstrated that the acceleration amplitude of the second harmonic is more sensitive than that of the fundamental harmonic. To accurately describe the stiffness change of the cracked beam, Long H. et al. [53] employed a new stiffness model that takes the influence of partial crack closure into consideration.

Based on the conclusions drawn by various researchers, it may be inferred that modelling of cracks is very important in the detection of the closed crack and in fully understanding its behaviour. The model does not fully consider the behaviour of the closed crack in beam.

Bispectrum analysis was used by Cui et al. [41] to examine the nonlinear dynamic properties of cracked beams in order to identify 'breathing' cracks. Their approach causes the first harmonics, which appear to be hidden, to dominate higher harmonics. M. Cao et al. [69] formulated a new phenomenon of energy modulation effect to enhance hidden higher harmonics, and their approach has shown considerable effectiveness in closed crack detection. However, their techniques caused fake peaks that can be mistaken for the crack-caused peaks. Consequently, subsequent researchers focused on excitation and measurement points, since these need to be properly selected to acquire large amplitudes of vibration responses.

In attempts directed at closed crack detection in both the beam and plate components of a structure, a high priority should be given to nonlinear behaviour in the absence of awareness of external excitations. The structure can sometimes respond linearly or nonlinearly. Analysis of the structural reaction is required because the procedures may not be effective if it responds linearly. The structural system may exhibit nonlinear behaviour due to a variety of causes, including geometric nonlinearity, nonlinear boundary conditions, connections between construction technique, and material nonlinearity; this needs to be fully considered.

6. CONCLUSION

The need for a safe structure has led to the development of diverse damage detection methods. These various damage detection methods have their own advantages and limitations, especially in the early stages and for small cracks. Damage diagnosis based on the use of nonlinear vibration effects is the first preference for use in a variety of structures. Most damage detection methods have been applied to beam structures, and there are few that are practical in laminated plate-like structures. The general advantages of nonlinearity damage detection methods include the high sensitivity in detecting cracks, particularly closed cracks. Under the nonlinearity effects, the closed crack in the structure is detected based on the crack size, and its location is investigated by changes in modal parameters such as natural frequency and damping factor. However, this approach suffers from two major limitations. First, the changes in natural frequencies have been shown to be significant only when the crack size is large, and second, the measured shift in natural frequency cannot be unambiguously attributed to the crack alone, as it may also be influenced by other factors such as wear, relaxation, etc. Modelling a crack is important to identify the closed cracks in a beam-like

structure. It helps to fully understand the vibration characteristics generated by the closed crack. However, modelling is time consuming due to its complexity.

The subharmonic and superharmonic resonance methods have different nonlinear properties. On the other hand, the nonlinear vibration of a beam with a closed crack is poorly understood, the intrinsic relationship between the subharmonic and superharmonic resonance responses and the beam parameters is far from thoroughly understood and cracked beams require further investigation. Wave propagation methods are very sensitive in determining the size and location of cracks in both beams and plate-like structures. However, the various wave propagation methods have their own drawbacks, as there are various factors that affect the structure; and in assessing the effects of nonlinearity, noise and environmental conditions should be considered, even if such a consideration were to also take into account the possibility that different types of nonlinearity—namely nonlinear damping, geometric nonlinearity and nonlinearity of the material—would also affect the response of the methods. In the case of delamination, there are various methods to analyse the nonlinearity effects of the structure, and each method has its own advantages and disadvantages. Various researchers used nonlinear effects based on the subharmonic response of the structure. These methods are effective in detecting damage, but there were also some false indications, leading to an incorrect conclusion about defects.

VAM is a time reduction technique, but it requires additional information. Nonlinear Lamb wave imaging, another method for damage detection, can be used up to a certain distance, but after that distance it is difficult to detect the exact damage. One way to increase the sensitivity and reliability of nonlinear vibration diagnostics would be to develop special mathematical methods that can account for multiple conditions simultaneously, and implementing these methods would mean that even with the presence of closed cracks and delamination in the structure, the damage detection technique employed would prove effective.

REFERENCE

1. Lin RM, Ng TY. Applications of higher-order frequency response functions to the detection and damage assessment of general structure systems with breathing cracks. *Int J Mech Sci* [Internet]. 2018;148:652-66. Available from: <http://dx.doi.org/10.1016/j.jimecsci.2018.08.027>
2. Avci O, Abdeljaber O, Kiranyaz S, Hussein M, Gabbouj M, Inman DJ. A review of vibration-based damage detection in civil structures: From traditional methods to Machine Learning and Deep Learning applications. *Mech Syst Signal Process* [Internet]. 2021;147(107077):107077. Available from: <http://dx.doi.org/10.1016/j.ymsp.2020.107077>
3. Antaki G, Gilada R. Chapter 2 - Design Basis Loads and Qualification, Editor(s): George Antaki, Ramiz Gilada, Nuclear Power Plant Safety and Mechanical Integrity. Butterworth-Heinemann; 2015.
4. Webster M&., Clark L. The structural effects of corrosion - an overview of the mechanisms; 2000.
5. Li YH, Dong YH, Qin Y, Lv HW. Nonlinear forced vibration and stability of an axially moving viscoelastic sandwich beam. *Int J Mech Sci* [Internet]. 2018;138-139:131-45. Available from: <http://dx.doi.org/10.1016/j.jimecsci.2018.01.041>
6. Galvão AS, Silva ARD, Silveira RAM, Gonçalves PB. Nonlinear dynamic behavior and instability of slender frames with semi-rigid connections. *Int J Mech Sci* [Internet]. 2010;52(12):1547-62. Available from: <http://dx.doi.org/10.1016/j.jimecsci.2010.07.002>

7. Wang Y, Yang J, Moradi Z, Safa M, Khadimallah MA. Nonlinear dynamic analysis of thermally deformed beams subjected to uniform loading resting on nonlinear viscoelastic foundation. *Eur J Mech A Solids* [Internet]. 2022;95(104638):104638. Available from: <http://dx.doi.org/10.1016/j.euromechsol.2022.104638>
8. Prawin J, Rama Mohan Rao A. Vibration-based breathing crack identification using non-linear intermodulation components under noisy environment. *Struct Health Monit* [Internet]. 2020;19(1):86–104. Available from: <http://dx.doi.org/10.1177/1475921719836953>
9. Boungou D, Guillet F, Badaoui ME, Lyonnet P, Rosario T. Fatigue damage detection using cyclostationarity. *Mech Syst Signal Process* [Internet]. 2015;58–59:128–42. Available from: <http://dx.doi.org/10.1016/j.ymsp.2014.11.010>
10. Liu P, Sohn H. Damage detection using sideband peak count in spectral correlation domain. *J Sound Vib* [Internet]. 2017;411:20–33. Available from: <http://dx.doi.org/10.1016/j.jsv.2017.08.049>
11. Hu C, Yiyong Y, Kexia P, Hu Y. The Vibration Characteristics Analysis of Damping System of Wall-mounted Airborne Equipment Based on FEM, IOP Conf. IOP Conf Ser: Earth Environ Sci. 2018.
12. Oggü S, Sasmal S. Dynamic nonlinearities for identification of the breathing crack type damage in reinforced concrete bridges. *Struct Health Monit*. 2021;20(1):339–59.
13. Wang X, Liu D, Zhang J, Jiao Y. Damage identification for nonlinear fatigue crack of cantilever beam under harmonic excitation. *J vibroengineering* [Internet]. 2022;435–52. Available from: <http://dx.doi.org/10.21595/jve.2021.22187>
14. Ghadami A, Maghsoudi A, Mirdamad HR. A new adaptable multiple-crack detection algorithm in beam-like structures. *Arch Mech*. 2013;65(6):469–83.
15. Sampath S, Sohn H. Detection and localization of fatigue crack using nonlinear ultrasonic three-wave mixing technique. *Int J Fatigue* [Internet]. 2022;155(106582):106582. Available from: <http://dx.doi.org/10.1016/j.ijfatigue.2021.106582>
16. Zhao B, Xu Z, Kan X, Zhong J, Guo T. Structural damage detection by using single natural frequency and the corresponding mode shape. *Shock Vib* [Internet]. 2016;2016:1–8. Available from: <http://dx.doi.org/10.1155/2016/8194549>
17. Dilena M, Dell’Oste MF, Morassi A. Detecting cracks in pipes filled with fluid from changes in natural frequencies. *Mech Syst Signal Process* [Internet]. 2011;25(8):3186–97. Available from: <http://dx.doi.org/10.1016/j.ymsp.2011.04.013>
18. Mohan V, Parivallal S, Kesavan K, Arunsundaram B, Ahmed AKF, Ravisankar K. Studies on damage detection using frequency change correlation approach for health assessment. *Procedia Eng* [Internet]. 2014;86:503–10. Available from: <http://dx.doi.org/10.1016/j.proeng.2014.11.074>
19. Gelman L, Gorpinich S, Thompson C. Adaptive diagnosis of the bilinear mechanical systems. *Mech Syst Signal Process* [Internet]. 2009;23(5):1548–53. Available from: <http://dx.doi.org/10.1016/j.ymsp.2009.01.007>
20. Giannini O, Casini P, Vestroni F. Nonlinear harmonic identification of breathing cracks in beams. *Comput Struct* [Internet]. 2013;129:166–77. Available from: <http://dx.doi.org/10.1016/j.compstruc.2013.05.002>
21. Caddemi S, Caliò I, Marletta M. The non-linear dynamic response of the Euler–Bernoulli beam with an arbitrary number of switching cracks. *Int J Non Linear Mech* [Internet]. 2010;45(7):714–26. Available from: <http://dx.doi.org/10.1016/j.ijnonlinmec.2010.05.001>
22. Chatterjee A. Structural damage assessment in a cantilever beam with a breathing crack using higher order frequency response functions. *J Sound Vib* [Internet]. 2010;329(16):3325–34. Available from: <http://dx.doi.org/10.1016/j.jsv.2010.02.026>
23. Moore RC, Inan US, Bell TF. Observations of amplitude saturation in ELF/VLF wave generation by modulated HF heating of the auroral electrojet. *Geophys Res Lett* [Internet]. 2006;33(12). Available from: <http://dx.doi.org/10.1029/2006gl025934>
24. Liu J, Zhu WD, Charalambides PG, Shao YM, Xu YF, Fang XM. A dynamic model of a cantilever beam with a closed, embedded horizontal crack including local flexibilities at crack tips. *J Sound Vib* [Internet]. 2016;382:274–90. Available from: <http://dx.doi.org/10.1016/j.jsv.2016.04.036>
25. Nitesh A, Vaibhav S. Analysis of crack detection of a cantilever beam using finite element analysis [IJERT. *Int J Eng Res Technol* (Ahmedabad). 2015;4(04):713–8.
26. Kaushar HB, Sharma DS, Vishal V. Crack detection in cantilever beam by frequency-based method. *Procedia Eng*. 2013;51:770–5.
27. Panteliou SD, Chondros TG, Argyrakis VC, Dimarogonas AD. Damping factor as an indicator of crack severity. *J Sound Vib* [Internet]. 2001;241(2):235–45. Available from: <http://dx.doi.org/10.1006/jsvi.2000.3299>
28. Zhang C, He L, Liu S, Yang Q. A new vibro-acoustic modulation technique for closed crack detection based on electromagnetic loading. *Appl Acoust* [Internet]. 2020;157(107004):107004. Available from: <http://dx.doi.org/10.1016/j.apacoust.2019.107004>
29. Duffour P, Morbidini M, Cawley P. Comparison between a type of vibro-acoustic modulation and damping measurement as NDT techniques. *NDT E Int* [Internet]. 2006;39(2):123–31. Available from: <http://dx.doi.org/10.1016/j.ndteint.2005.07.010>
30. Jiao J, Zheng L, Song G, He C, Wu B. Vibro-acoustic modulation technique for micro-crack detection in pipeline. In: Fan K-C, Song M, Lu R-S, editors. *Seventh International Symposium on Precision Engineering Measurements and Instrumentation* [Internet]. SPIE; 2011. Available from: <http://dx.doi.org/10.1117/12.905550>
31. Trochidis A, Hadjileontiadis L, Zacharias K. Analysis of Vibroacoustic Modulations for Crack Detection: A Time-Frequency Approach Based on Zhao-Atlas-Marks Distribution, Shock and Vibration; 2014.
32. Gelman L, Gorpinich S, Thompson C. Adaptive diagnosis of the bilinear mechanical systems. *Mechanical Systems and Signal*; 2009.
33. Cao MS, Sha GG, Gao YF, Ostachowicz W. Structural damage identification using damping: a compendium of uses and features. *Smart Mater Struct* [Internet]. 2017;26(4):043001. Available from: <http://dx.doi.org/10.1088/1361-665x/aa550a>
34. Wang Z, Lin RM, Lim MK. Structural damage detection using measured FRF data. *Comput Methods Appl Mech Eng* [Internet]. 1997;147(1–2):187–97. Available from: [http://dx.doi.org/10.1016/s0045-7825\(97\)00013-3](http://dx.doi.org/10.1016/s0045-7825(97)00013-3)
35. Cappello R, Cutugno S, Pitarresi G. Detection of crack-closure during fatigue loading by means of Second Harmonic Thermoelastic Stress Analysis. *Procedia struct integr* [Internet]. 2022;39:179–93. Available from: <http://dx.doi.org/10.1016/j.prostr.2022.03.087>
36. Asnaashari E, Sinha JK. Development of residual operational deflection shape for crack detection in structures. *Mech Syst Signal Process* [Internet]. 2014;43(1–2):113–23. Available from: <http://dx.doi.org/10.1016/j.ymsp.2013.10.003>
37. Oks E, Dalimier E, Faenov A, Pikuz T, Fukuda Y, Andreev A, et al. Revealing the second harmonic generation in a femtosecond laser-driven cluster-based plasma by analyzing shapes of Ar XVII spectral lines. *Opt Express* [Internet]. 2015;23(25):31991–2005. Available from: <http://dx.doi.org/10.1364/OE.23.031991>
38. Wei X, Zhongging S, Maosen C, Maciej R, Wiesla O. Nonlinear pseudo-force in a breathing crack to generate harmonics. *J Sound Vibrat*; 2021.
39. Cao M, Su Z, Deng T, Xu W. Nonlinear pseudo-force in breathing delamination to generate harmonics: A mechanism and application study. *Int J Mech Sci*. 2021;192.
40. Xu W, Su Z, Radziński M, Cao M, Ostachowicz W. Nonlinear pseudo-force in a breathing crack to generate harmonics. *J Sound Vib* [Internet]. 2021;492(115734):115734. Available from: <http://dx.doi.org/10.1016/j.jsv.2020.115734>

41. Cui L, Xu H, Ge J, Cao M, Xu Y, Xu W, et al. Use of bispectrum analysis to inspect the non-linear dynamic characteristics of beam-type structures containing a breathing crack. *Sensors (Basel)* [Internet]. 2021;21(4):1177. Available from: <http://dx.doi.org/10.3390/s21041177>
42. Wang K, Liu M, Su Z, Yuan S, Fan Z. Analytical insight into "breathing" crack-induced acoustic nonlinearity with an application to quantitative evaluation of contact cracks. *Ultrasonics* [Internet]. 2018;88:157–67. Available from: <http://dx.doi.org/10.1016/j.ultras.2018.03.008>
43. Semperlotti F, Wang KW, Smith EC. Localization of a breathing crack using super-harmonic signals due to system nonlinearity. *AIAA J* [Internet]. 2009;47(9):2076–86. Available from: <http://dx.doi.org/10.2514/1.38947>
44. Rivola A, White PR. Bispectral analysis of the bilinear oscillator with application to the detection of fatigue cracks. *J Sound Vib* [Internet]. 1998;216(5):889–910. Available from: <http://dx.doi.org/10.1006/jsvi.1998.1738>
45. Prawin J, Rao ARM. Development of polynomial model for cantilever beam with breathing crack. *Procedia Eng* [Internet]. 2016;144:1419–25. Available from: <http://dx.doi.org/10.1016/j.proeng.2016.05.173>
46. Khalkar V, Ramachandran SV. Paradigm for natural frequency of an un-cracked cantilever beam and its application to cracked beam. *Vibrations in Physical Systems*; 2017.
47. Chu YC, Shen MH. Analysis of Forced Bilinear Oscillators and the Application to Cracked Beam Dynamics. *AIAA J*. 1992;30(10):2512–2251.
48. Caddemi S, Calio' I. Exact solution of the multi-cracked Euler–Bernoulli column. *Int J Solids Struct* [Internet]. 2008;45(5):1332–51. Available from: <http://dx.doi.org/10.1016/j.ijsolstr.2007.09.022>
49. Dotti FE, Cortinez VH, Reguera F. Non-linear dynamic response to simple harmonic excitation of a thin-walled beam with a breathing crack. *Appl Math Model* [Internet]. 2016;40(1):451–67. Available from: <http://dx.doi.org/10.1016/j.apm.2015.04.052>
50. Bovsunovskii A, Surace C. Non-linearities in the vibrations of elastic structures with a closing crack: A state of the art review. *Mech Syst Signal Process*. 2015;129–48.
51. Broda D, Pieczonka L, Hiwarkar V, Staszewski WJ, Silberschmidt VV. Generation of higher harmonics in longitudinal vibration of beams with breathing cracks. *J Sound Vib* [Internet]. 2016;381:206–19. Available from: <http://dx.doi.org/10.1016/j.jsv.2016.06.025>
52. Andreaus U, Baragatti P. Cracked beam identification by numerically analysing the nonlinear behaviour of the harmonically forced response. *J Sound Vib* [Internet]. 2011;330(4):721–42. Available from: <http://dx.doi.org/10.1016/j.jsv.2010.08.032>
53. Long H, Liu Y, Liu K. Nonlinear vibration analysis of a beam with a breathing crack. *Appl Sci (Basel)* [Internet]. 2019;9(18):3874. Available from: <http://dx.doi.org/10.3390/app9183874>
54. Pugno N, Surace C, Ruotolo R. Evaluation of the non-linear dynamic response to harmonic excitation of a beam with several breathing cracks. *J Sound Vib* [Internet]. 2000;235(5):749–62. Available from: <http://dx.doi.org/10.1006/jsvi.2000.2980>
55. Ji JC, Zhou J. Coexistence of two families of sub-harmonic resonances in a time-delayed nonlinear system at different forcing frequencies. *Mech Syst Signal Process* [Internet]. 2017;93:151–63. Available from: <http://dx.doi.org/10.1016/j.ymsp.2017.02.007>
56. Zhu J, Cai S, Suo Z. Resonant behavior of a membrane of a dielectric elastomer. *Int J Solids Struct* [Internet]. 2010;47(24):3254–62. Available from: <http://dx.doi.org/10.1016/j.ijsolstr.2010.08.008>
57. Casini P, Vestroni F, Giannini O. Crack detection in beam-like structures by nonlinear harmonic identification. *Frat integrità strutt* [Internet]. 2014;8(29):313–24. Available from: <http://dx.doi.org/10.3221/jgf-esis.29.27>
58. Zhao X, Zhao YR, Gao XZ, Li XY, Li YH. Green's functions for the forced vibrations of cracked Euler–Bernoulli beams. *Mech Syst Signal Process* [Internet]. 2016;68–69:155–75. Available from: <http://dx.doi.org/10.1016/j.ymsp.2015.06.023>
59. Zhao X, Chen B, Li YH, Zhu WD, Nkiegaing FJ, Shao YB. Forced vibration analysis of Timoshenko double-beam system under compressive axial load by means of Green's functions. *J Sound Vib* [Internet]. 2020;464(115001):115001. Available from: <http://dx.doi.org/10.1016/j.jsv.2019.115001>
60. Chen B, Lin B, Zhao X, Zhu W, Yang Y, Li Y. Closed-form solutions for forced vibrations of a cracked double-beam system interconnected by a viscoelastic layer resting on Winkler–Pasternak elastic foundation. *Thin-Walled Struct* [Internet]. 2021;163(107688):107688. Available from: <http://dx.doi.org/10.1016/j.tws.2021.107688>
61. Surace C, Ruotolo R, Storer D. Detecting nonlinear behavior using the volterra series to assess damage in beam-like structures; 2011.
62. Yongfeng Y, Jianjun W, Yanlin W, Chao F, Qingyang Z, Kuan L. Dynamical analysis of hollow-shaft dual-rotor system with circular cracks. *Low Freq Noise Vibr* [Internet]. 2021;40(3):1227–40. Available from: <http://dx.doi.org/10.1177/1461348420948287>
63. Wang K, Li Y, Su Z, Guan R, Lu Y, Yuan S. Nonlinear aspects of "breathing" crack-disturbed plate waves: 3-D analytical modeling with experimental validation. *Int J Mech Sci* [Internet]. 2019;159:140–50. Available from: <http://dx.doi.org/10.1016/j.ijmecsci.2019.05.036>
64. Maruyama T, Saitoh T, Hirose S. Numerical study on sub-harmonic generation due to interior and surface breaking cracks with contact boundary conditions using time-domain boundary element method. *Int J Solids Struct* [Internet]. 2017;126–127:74–89. Available from: <http://dx.doi.org/10.1016/j.ijsolstr.2017.07.029>
65. Koskinen T, Kuutti J, Virkkunen I, Rinta-aho J. Online nonlinear ultrasound imaging of crack closure during thermal fatigue loading. *NDT E Int* [Internet]. 2021;123(102510):102510. Available from: <http://dx.doi.org/10.1016/j.ndteint.2021.102510>
66. Lee SE, Hong JW. Detection of Micro-Cracks in Metals Using Modulation of PZT-Induced Lamb Waves. *Materials (Basel)*. 2020;13.
67. Wu TC, Kobayashi M, Tanabe M, Yang CH. The Use of Flexible Ultrasound Transducers for the Detection of Laser-Induced Guided Waves on Curved Surfaces at Elevated Temperatures. *Sensors (Basel)*. 2017;17.
68. Lu Z, Dong D, Ouyang H, Cao S, Hua C. Localization of breathing cracks in stepped rotors using superharmonic characteristic deflection shapes based on singular value decomposition in frequency domain. *Fatigue Fract Eng Mater Struct*. 2017;40(11):1825–37.
69. Cao M, Lu Q, Su Z, Radziński M, Xu W, Ostachowicz W. A nonlinearity-sensitive approach for detection of "breathing" cracks relying on energy modulation effect. *J Sound Vib* [Internet]. 2022;524(116754):116754. Available from: <http://dx.doi.org/10.1016/j.jsv.2022.116754>
70. Sun X, Ding X, Li F, Zhou S, Liu Y, Hu N, et al. Interaction of Lamb wave modes with weak material nonlinearity: Generation of symmetric zero-frequency mode. *Sensors (Basel)* [Internet]. 2018;18(8). Available from: <http://dx.doi.org/10.3390/s18082451>
71. Song H, Xiang M, Lu G, Wang T. Singular spectrum analysis and fuzzy entropy based damage detection on a thin aluminium plate by using PZTs. *Smart Mater Struct*. 2022;31(3).
72. Li W, Xu Y, Hu N, Deng M. Numerical and experimental investigations on second-order combined harmonic generation of Lamb wave mixing. *AIP Adv* [Internet]. 2020;10(4):045119. Available from: <http://dx.doi.org/10.1063/1.5140588>
73. Zhu W, Xu Z, Xiang Y, Liu C, Deng M, Qiu X, et al. Nonlinear ultrasonic detection of partially closed cracks in metal plates using static component of lamb waves. *NDT E Int* [Internet]. 2021;124(102538):102538. Available from: <http://dx.doi.org/10.1016/j.ndteint.2021.102538>
74. Chen B-Y, Soh S-K, Lee H-P, Tay T-E, Tan VBC. A vibro-acoustic modulation method for the detection of delamination and kissing bond in composites. *J Compos Mater* [Internet]. 2016;50(22):3089–104. Available from: <http://dx.doi.org/10.1177/0021998315615652>

75. Carneiro SHS, Inman DJ. Continuous model for the transverse vibration of cracked Timoshenko beams. *J Vib Acoust* [Internet]. 2002;124(2):310–20. Available from: <http://dx.doi.org/10.1115/1.1452744>
76. Saito A. *Nonlinear Vibration Analysis of Cracked Structures - Application to Turbomachinery Rotors with Cracked Blades*. Turbomachinery Rotors with Cracked Blades; 2009.
77. Rezaee M, Hassannejad R. Free vibration analysis of simply supported beam with breathing crack using perturbation method. *Acta mech solida Sin* [Internet]. 2010;23(5):459–70. Available from: [http://dx.doi.org/10.1016/s0894-9166\(10\)60048-1](http://dx.doi.org/10.1016/s0894-9166(10)60048-1)
78. Liu L, Mei X, Dong D, Liu H. Perturbation methods for dynamic analysis of cracked beams. In: 2011 International Conference on Consumer Electronics, Communications and Networks (CECNet). IEEE; 2011.
79. Stepanova LV, Igonin SA. Perturbation method for solving the nonlinear eigenvalue problem arising from fatigue crack growth problem in a damaged medium. *Appl Math Model* [Internet]. 2014;38(14):3436–55. Available from: <http://dx.doi.org/10.1016/j.apm.2013.11.057>
80. Kharazan M, Irani S, Noorian MA, Salimi MR. Nonlinear vibration analysis of a cantilever beam with multiple breathing edge cracks. *Int J Non Linear Mech* [Internet]. 2021;136(103774):103774. Available from: <http://dx.doi.org/10.1016/j.ijnonlinmec.2021.103774>
81. Singh AC, Tay TE, Lee H. Numerical investigations of non-linear acoustics/ultrasonics for damage detection. 2016.
82. Sun Z, Li F, Li H. A numerical study of non-collinear wave mixing and generated resonant components. *Ultrasonics* [Internet]. 2016;71:245–55. Available from: <http://dx.doi.org/10.1016/j.ultras.2016.06.019>
83. Tabatabaeipour M, Delrue J, Steven VA. Reconstruction Algorithm for Probabilistic Inspection of Damage (RAPID) in Composites. 2014.
84. Andreades C, Malfense Fierro GP, Meo M. A nonlinear ultrasonic modulation approach for the detection and localisation of contact defects. *Mech Syst Signal Process* [Internet]. 2022;162(108088):108088. Available from: <http://dx.doi.org/10.1016/j.ymsp.2021.108088>
85. Schwarts-Givli H, Rabinovitch O, Frostig Y. High-order nonlinear contact effects in the dynamic behavior of delaminated sandwich panels with a flexible core. *Int J Solids Struct* [Internet]. 2007;44(1):77–99. Available from: <http://dx.doi.org/10.1016/j.ijsolstr.2006.04.016>
86. Shankar G, Varuna JP, P.K.Mahato, Effect of delamination on vibration characteristic of smart laminated composite plate. *Journal of Aerospace System Engineering*. 2019;13(4):10–7.
87. Mohammad H, Kargamovin *, Ahmadian MT. Forced vibration of delaminated Timoshenko beams subjected to a moving load. *Sci Eng Compos Mater*. 2012;19(2):145–57.
88. Zhang Z, Shankar K&., Murat & Morozov E. Vibration Modelling of Composite Laminates with Delamination Damage. ICCM International Conferences on Composite Material;. 2015.
89. Chen Y, Huang B, Yan G, Wang J. Characterization of delamination effects on free vibration and impact response of composite plates resting on visco-Pasternak foundations. *Int J Mech Sci*. 2021.
90. Thangaratnam K, Sanjana R. Nonlinear analysis of composite plates and shells subjected to in-plane loading. *Appl Mech Mater* [Internet]. 2018;877:341–6. Available from: <http://dx.doi.org/10.4028/www.scientific.net/amm.877.341>
91. Pradhan SC, Ng TY, Lam KY, Reddy JN. Control of laminated composite plates using magnetostrictive layers. *Smart Mater Struct* [Internet]. 2001;10(4):657–67. Available from: <http://dx.doi.org/10.1088/0964-1726/10/4/309>
92. Mantari JL, Oktem AS, Guedes Soares C. A new higher order shear deformation theory for sandwich and composite laminated plates. *Part B Eng*. 2012;43(3):1489–99.
93. Fares ME, Elmarghany MK. A refined zigzag nonlinear first-order shear deformation theory of composite laminated plates. *Compos Struct* [Internet]. 2008;82(1):71–83. Available from: <http://dx.doi.org/10.1016/j.compstruct.2006.12.007>
94. Yushu L, Zhou H, Huasong Q, Wenshan Y, Yilun L. Machine learning approach for delamination detection with feature missing and noise polluted vibration characteristics. *Compos Struct*. 2022;
95. Civalek Ö. Nonlinear dynamic response of laminated plates resting on nonlinear elastic foundations by the discrete singular convolution-differential quadrature coupled approaches. *Compos B Eng* [Internet]. 2013;50:171–9. Available from: <http://dx.doi.org/10.1016/j.compositesb.2013.01.027>
96. Civalek Ö. Nonlinear dynamic response of laminated plates resting on nonlinear elastic foundations by the discrete singular convolution-differential quadrature coupled approaches. *Compos B Eng* [Internet]. 2013;50:171–9. Available from: <http://dx.doi.org/10.1016/j.compositesb.2013.01.027>
97. Shen H-S, Xiang Y. Nonlinear analysis of nanotube-reinforced composite beams resting on elastic foundations in thermal environments. *Eng Struct* [Internet]. 2013;56:698–708. Available from: <http://dx.doi.org/10.1016/j.engstruct.2013.06.002>
98. Houhat N, Tourmat V, Ménigot S, Boutkedjirt T, Girault J-M. Optimal pump excitation frequency for improvement of damage detection by nonlinear vibro acoustic modulation method in a multiple scattering sample. *Appl Acoust* [Internet]. 2019;155:222–31. Available from: <http://dx.doi.org/10.1016/j.apacoust.2019.06.010>
99. Zhang X, Wu X, He Y, Yang S, Chen S, Zhang S, et al. CFRP barely visible impact damage inspection based on an ultrasound wave distortion indicator. *Compos B Eng* [Internet]. 2019;168:152–8. Available from: <http://dx.doi.org/10.1016/j.compositesb.2018.12.092>
100. Castellano A, Fraddosio A, Piccioni MD, Kundu T. Linear and nonlinear ultrasonic techniques for monitoring stress-induced damages in concrete. *J Nondestruct Eval Diagn Progn Eng Syst* [Internet]. 2021;4(4):1–21. Available from: <http://dx.doi.org/10.1115/1.4050354>
101. Santhakumar S, Hoon S. Detection and localization of fatigue crack using nonlinear ultrasonic three-wave mixing technique. *Int J Fatigue*. 2022;
102. Qin W, Liyong Z, Jianguo Z, Lijun Z, Wenfeng H. Characterization of impact fatigue damage in CFRP composites using nonlinear acoustic resonance method. *Compos Struct*. 2020;
103. Sikdar S, Ostachowicz W, Kudela P, Radziński M. Barely visible impact damage identification in a 3D core sandwich structure. *Computer Assisted Methods In Engineering And Science*. 2018;24(4):259–68.
104. Xianghong W, He C, He H, Wei X. Simulation and experimental research on nonlinear ultrasonic testing of composite material porosity. *Appl Acoust*. 2022;
105. Yang F, Sedaghati R, Esmailzadeh E. Vibration suppression of structures using tuned mass damper technology: A state-of-the-art review. *J Vib Control* [Internet]. 2022;28(7–8):812–36. Available from: <http://dx.doi.org/10.1177/1077546320984305>
106. Buezas F, Rosales MB, Filipich C. Damage detection with genetic algorithms taking into account a crack contact model. *Engineering Fracture Mechanics - ENG FRACTURE MECH*. 2011;78:695–712.
107. Shallan O, Atef &, Tharwat &, Khozam M. Structural Damage Detection using Genetic Algorithm by Static Measurements. *International Journal of Trend Research Development*. 2017;4:2394–9.
108. Qi Y, Rui X, Ji K, Liu C, Zhou C. Study on aeolian vibration suppression schemes for large crossing span of ultra-high-voltage eight-bundle conductors. *Adv Mech Eng* [Internet]. 2019;11(4):168781401984270. Available from: <http://dx.doi.org/10.1177/1687814019842706>
109. Ashtiani M, Hashemabadi SH, Ghaffari A. A review on the magneto-rheological fluid preparation and stabilization. *J Magn Magn Mater* [Internet]. 2015;374:716–30. Available from: <http://dx.doi.org/10.1016/j.jmmm.2014.09.020>

110. Williams K, Chiu G, Bernhard R. Adaptive-passive absorbers using shape-memory alloys. *J Sound Vib* [Internet]. 2002;249(5):835–48. Available from: <http://dx.doi.org/10.1006/jsvi.2000.3496>
111. Mohanty S, Dwivedy S. Linear and nonlinear analysis of traditional and non-traditional piezoelectric vibration absorber with time delay feedback for simultaneous resonance conditions. *Mechanical Systems and Signal Processing*. 2021.
112. Zhang W, Zhao MH. Nonlinear vibrations of a composite laminated cantilever rectangular plate with one-to-one internal resonance. *Nonlinear Dyn* [Internet]. 2012;70(1):295–313. Available from: <http://dx.doi.org/10.1007/s11071-012-0455-6>
113. Yousuf LS. Nonlinear dynamics investigation of bending deflection of stiffened composite laminated plate using Lyapunov exponent conception. In: Volume 7B: Dynamics, Vibration, and Control. American Society of Mechanical Engineers; 2021.
114. Dauson E, Donahue C, DeWolf S, Hua L, Xiao H, Murdoch L, et al. Damage Detection in a laboratory-scale wellbore applying Time Reverse Nonlinear Elastic Wave Spectroscopy. *TR NEWS*; 2021.
115. Wei D, Liu X, Wang B, Tang Z, Bo L. Damage quantification of aluminum plates using SC-DTW method based on Lamb waves. *Meas Sci Technol* [Internet]. 2022;33(4):045001. Available from: <http://dx.doi.org/10.1088/1361-6501/ac4435>
116. Zhen P, Li J, Hao H, Li C. Nonlinear structural damage detection using output-only Volterra series model. *Struct Contr Health Monit*. 2021.
117. Samaitis V, Mažeika L, Rekuviėnė R. Assessment of the length and depth of delamination-type defects using ultrasonic guided waves. *Appl Sci (Basel)* [Internet]. 2020;10(15):5236. Available from: <http://dx.doi.org/10.3390/app10155236>
118. Wang CH, Rose LRF. Wave reflection and transmission in beams containing delamination and inhomogeneity. *J Sound Vib* [Internet]. 2003;264(4):851–72. Available from: [http://dx.doi.org/10.1016/s0022-460x\(02\)01193-8](http://dx.doi.org/10.1016/s0022-460x(02)01193-8)
119. Nag A, Mahapatra D, Gopalakrishnan S, Sankar TS. A spectral finite element with embedded delamination for modeling of wave scattering in composite beams. *Compos Sci Technol*. 2003;63(15):2187–200.
120. Gudmundson P; GUDMUNSON. The dynamic behaviour of slender structures with cross-sectional cracks. *J Mech Phys Solids*. 1983;31(4):329–45.
121. Zhang W, Ma H, Zeng J, Wu S, Wen B. Vibration responses analysis of an elastic-support cantilever beam with crack and offset boundary. *Mech Syst Signal Process* [Internet]. 2017;95:205–18. Available from: <http://dx.doi.org/10.1016/j.ymssp.2017.03.032>
122. Matveev VV, Boginich OE, Yakovlev AP. Approximate analytical method for determining the vibration-diagnostic parameter indicating the presence of a crack in a distributed-parameter elastic system at super- and subharmonic resonances. *Strength Mater* [Internet]. 2010;42(5):528–43. Available from: <http://dx.doi.org/10.1007/s11223-010-9243-z>

Samrawit A. Tewelde:  <https://orcid.org/0000-0001-7504-8680>

Marek Krawczuk:  <https://orcid.org/0000-0002-9640-4696>

NUMERICAL MODEL AND AN ANALYSIS OF INERTIAL ACCUMULATOR OPERATION UNDER SELECTED WORKING CONDITIONS

Mateusz KUKLA^{*} , Maksymilian RACHEL^{*}

^{*}Faculty of Mechanical Engineering, Poznan University of Technology, ul. Piotrowo 3, 61-138 Poznan, Poland

mateusz.kukla@put.poznan.pl, maksymilian.rachel@student.put.poznan.pl

received 22 May 2022, revised 21 August 2022, accepted 22 August 2022

Abstract: The aim of this paper was to create a computational model that will enable the evaluation of the operation of a conventional inertia accumulator. This is an issue that is relevant as storage of energy is becoming increasingly important, in particular when it comes to generating electricity from renewable sources. In the course of the conducted works, an analytical model was developed based on the available literature, and then, it was introduced into the environment for numerical calculations. Four variants resulting from different geometrical parameters of the flywheel were adopted successively. On this basis, a series of simulations were performed, which allowed for obtaining the characteristics of the analysed solutions. As a consequence, a number of characteristics related to the mechanical power and energy of the simulated kinetic energy accumulators were obtained. The test results therefore provide a basis for comparing kinetic energy accumulators with different geometries and drive solutions.

Key words: mechanical energy accumulator, flywheel, inertial accumulator, numerical simulations, non-conventional technical solutions

1. INTRODUCTION

The generation of energy, in particular electric energy, using renewable sources is growing rapidly. This increase is expected to continue as it is associated with an overall increase in energy demand but also with progressive trends in reducing environmental impact [1]. Moreover, a significant decrease in the costs of generating energy from renewable sources has been observed in recent years [2], which additionally increases the demand.

Some of the methods of producing energy from renewable sources are characterised by a discontinuous nature of work. Examples include solar panels and wind farms that need sunlight and wind, respectively, in order to operate, which are not always adequately abundant. Moreover, the demand for electricity is also not constant and is characterised by periods of increased demand in cycles that may result from the time of the day or the season of the year. Since the production of energy from renewable sources is increasing, the inevitable interruptions in their operation of some of them make it necessary to have the capacity to store large amounts of energy in order to be able to meet the possible demand at any time [3]. Therefore, the legitimacy of developing energy storage systems can be indicated. An energy storage system allows electricity to be produced when needed and stored when energy generation exceeds demand. Energy storage is especially advantageous during low demand, low production cost period or interruptions in the continuity of available sources. Thanks to this, the stored energy reserve can be used in the event of high demand, increase in generation costs or the lack of availability of an alternative generation [4–6].

Among the energy storage systems, one can point out kinetic energy accumulators, which are an extension of the flywheel concept. The major advantage of inertial accumulators is the high

power density [7]. It results from the very low achievable mass of the accumulator being maintained in compact construction. Furthermore, it is characterised by good overload resistance and low effect of temperature on correct operation. Its other advantages include low maintenance requirements and the possibility to determine the exact amount of stored energy by measuring rotation speed. In addition, they are resistant to cyclical degradation but also to deep discharges, which is typical for classic electrochemical batteries. Additionally, the efficiency of their cycle can reach values up to 95% [8, 9]. High charging and discharging rates, projected service life exceeding 20 years as well as specific energies that may exceed the value of 100 Wh/kg [10, 11] should also be considered favourable. Moreover, when the stored energy is converted into electricity, the fast response time of the inertial accumulators means that they are capable of balancing the grid frequency. It should be expected that as a result of the increase in the share of energy generated with the use of irregular energy sources, this feature will play an increasingly important role [15].

Its main disadvantage includes the very limited time of energy storage because the motion resistance of the inertial accumulator cannot be completely eliminated. Therefore, inertial accumulators are characterised by relatively average ratio of stored energy per unit of mass [13]. This is one of the main reasons for the limited application for kinetic energy accumulators. Another limitation is the type of stored energy. Electrical energy is much more versatile, and a large number of devices can be powered directly by it by utilising relatively simple systems with a very low number of mechanical components.

Despite their flaws, inertial accumulators can be employed in devices which do not operate in a continuous cycle, for example, which are engaged for a limited time or operate under variable load. The potential for their application involves fast transmission of large amounts of energy which is achievable due to high power

density of the inertial accumulators. Some of the current applications of kinetic energy accumulators include the following examples: stabilising satellites on an orbit [14], short-term energy storage from photovoltaic panels [15], recovery of brake energy in automobiles [16–18], trolleybus drives [19], etc.

The aim of the research was to create a computational model, thanks to which it will be possible to evaluate the work of a conventional inertial accumulator. To achieve this, an analytical model was developed based on the available literature and then introduced into the numerical computing environment. This allowed for a series of simulations and, as a result, the evaluation of the parameters of the modelled solution.

Within the scope of this work, a rotor fulfilling the requirements of a conventional inertial accumulator was analysed. It is a solid of revolution with a plane of symmetry perpendicular to the axis of rotation and height much lower than its radius. The material for the rotor is assumed construction steel grade 18G2A (S355J2); it is further assumed that the material characteristics are homogeneous and isotropic. With the use of analytical calculations following a methodology provided in item [20], the rotor parameters were determined, based on allowable stress for the assumed material. These include the following: external radius $r_z = 0.15$ m, internal radius $r_w = 0.018$ m, height $h = 0.018$ m, moment of inertia $J_B = 0.112$ kg·m², inertial accumulator mass $m_B = 9.844$ kg and maximum kinetic energy $E_{max} = 61,411$ J.

2. MATHEMATICAL MODEL

There are two sources of loss in kinetic energy accumulators. The first one results from friction in the bearing system. The other source is related to liquid viscosity (the gas filling the interior of the accumulator) in which the rotor is moving. To determine the approximate value of these losses, formulas used to determine the loss of power in discs and cylinders were employed [21]. The loss of energy occurring on the one side of the rotor disc N_T can be described with the following equation:

$$N_T = 1.96 \cdot 10^{-5} \rho_g C_T \omega^3 (d_z^5 - d_w^5) \text{ [kW]}, \quad (1)$$

where ρ_g is mass density of the gas (kg/m³), C_T is moment of friction indicator and d_z and d_w are, respectively, the external and internal diameter of the inertial accumulator (m). It was assumed that the inertial accumulator chamber will be filled with air with reduced pressure, maximum $p = 0.3$ bar, which is the upper threshold of the so-called low vacuum. Air density is calculated from the following equation:

$$\rho_g = \frac{p M_g}{R T_0}, \quad (2)$$

where M_g is molar mass of the gas (kg/mol), T_0 is gas temperature (K) and $R = 8.314$ (J/[kg·mol]) is universal gas constant. The molar mass for air is $M_g = 0.029$ kg/mole. Assuming average gas temperature as 40°C = 313.15 K, one can calculate the air density as the following value: $\rho_g = 0.334$ kg/m³. The next factor is the moment of friction coefficient C_T . It is calculated based on Reynolds number for the disc Re_T , the gap between the rotor and its enclosure s as well as the relative roughness of the rotor surface k . Assuming the gap size is $s = 0.006$ m and the fact that the manufactured disc roughness is $Rz = 6.3$ ($Ra = 1.25$), $k = 6.3 \cdot 10^{-6}$ m. Reynolds number Re_T is calculated based on the external radius of the inertial accumulator r_z , angular velocity ω

and kinematic viscosity index ν_k , which is dependent on gas density ρ_g and dynamic viscosity μ (Pa·s). Gas density is calculated as above, whereas for air in temperature at 40°C, dynamic viscosity is equal to $\mu = 1.91 \cdot 10^{-5}$ Pa·s. The kinematic viscosity is derived with the following equation:

$$\nu_k = \frac{\mu}{\rho_g}, \quad (3)$$

and is equal to $\nu_k = 5.72 \cdot 10^{-5}$ m²/s. Therefore, Reynolds number, calculated from the below equation:

$$Re_T = \frac{r_z^2 \omega}{\nu_k}, \quad (4)$$

is equal to $Re_T = 411,923$. Subject literature provides ranges of values for the Re_T with each one being assigned a respective equation to determine the moment of friction coefficient. The limit value between ranges is defined with the following equation:

$$Re_{gr} = 1,100 \left(\frac{r_z}{2k} \right)^{\frac{2}{5}} \cdot \left[3.8 \log \left(\frac{r_z}{2k} \right) - 2.4 \left(\frac{s}{r_z} \right)^{\frac{1}{4}} \right]. \quad (5)$$

After substituting the values and solving, the following is obtained: $Re_{gr} = 676,828$. Accordingly, the calculated Reynolds number is included in the third range (satisfying the inequality $10^5 < Re_T < Re_{gr}$). Therefore, the index of friction may be determined from the equation:

$$C_T = 0.0102 \left(\frac{s}{r_z} \right)^{1/10} \cdot \frac{1}{Re_T^{5/1}}, \quad (6)$$

which allows to determine the value $C_T = 5.57 \cdot 10^{-4}$. Considering the above, after solving Eq. (1), one arrives at $N_T \approx 0.01$ kW.

Employing the limit values of the Reynolds number allows us to calculate the limit values of angular velocities for the third range, according to the following equation:

$$\omega_{gr} = \frac{Re_T}{Re_{gr}}, \quad (7)$$

Consequently, one obtains the minimum and maximum value of angular velocity: $\omega_{min} = 636.85$ rad/s and $\omega_{max} = 4,310.35$ rad/s, respectively.

Power losses on the side surface of the rotor are also dependent on the Reynolds number value Re_C , as in the equation:

$$Re_C = \frac{r_z \omega s}{\nu_k}, \quad (8)$$

and are equal to $Re_C = 16,477$. Analogous to the calculations involving the disc, the form of the loss equation is dependent on the range of the Reynolds number value Re_C . These are described with Taylor-Wendt equations. Since the inequality $1.6 \cdot 10^4 < Re_C$ is true, therefore the power of the losses on the side surface of the rotor shall be described with the equation:

$$N_C = 2.3 \cdot 10^{-5} d_z^4 \omega^3 h \rho_g \sqrt{\frac{\nu_k}{r_z \omega s}}, \quad (9)$$

and for the discussed case shall be equal to $N_C \approx 0.01$ kW. The total surface of the inertial accumulator is the sum of the upper and lower side surface as well as the side surface, which can be represented as follows:

$$N_B = 2N_T + N_C, \quad (10)$$

therefore, allowing to calculate $N_B = 0.03$ kW = 30 W.

Losses in bearings result from the friction between the rolling components and races. They are dependent on numerous factors,

including the lubrication method. The losses are determined approximately, based on the braking moment resulting from gravity. Its value is independent from rotational speed and can be calculated with the following equation:

$$M_{h1} = \frac{1}{2} m_B g f d. \tag{11}$$

Assuming the rolling resistance for steel of $f = 0.016$ and the diameter of the journal (depending on preliminary strength calculations) of $d = 0.035$ m, one arrives on: $M_{h1} = 0.026$ Nm. As per the subject literature [21], it is assumed to be the main source of braking moment in bearings and is therefore sufficient for the purpose of energy analysis.

Due to the high variance of the angular velocity during accumulator operation, it is efficient to express the total braking moment as:

$$M_h = c_1 \omega^2 + c_2, \tag{12}$$

where c_1 is a constant obtained after factoring out from the maximum aerodynamic loss Eq. (10) (the value ω^3) and $c_2 = M_{h1}$ is constant moment of resistance in the bearings, according to Eq. (11). The values are $c_1 = 2.64 \cdot 10^{-8}$ kg·m² and $c_2 = 0.026$ Nm.

3. NUMERICAL CALCULATIONS

3.1. Numerical model

Numerical value determination is based on the power balance in the system expressed as follows:

$$N_{lad}(t) = N_{mag}(t) + N_{str}(t), \tag{13}$$

where $N_{str}(t)$ is the power of losses, which is the product of the moment M_h and the angular velocity of the rotor at a given moment $\omega(t)$, $N_{mag}(t)$ is power stored in the accumulator and $N_{lad}(t)$ is the power supplied to the inertial accumulator shaft. By substituting the equations established previously, the equation can be expressed as follows:

$$N_{lad}(t) = [J_B \dot{\omega}(t) + c_1 \omega^2(t) + c_2] \cdot \omega(t). \tag{14}$$

For the purpose of numerical calculations, a source of charging energy was assumed as a hypothetical electrical permanent magnet synchronous motor (PMSM). The characteristics of this motor are shown in Fig. 1.

This serves as a basis for deriving the three methods of charging the accumulator. Since the developed model is based on the flow of power, it is possible to charge the accumulator in the full variance range of speed and torque. However, this requires to utilise the correct type of variable ratio transmission. The present study does not account for losses of power occurring in such a transmission as the performed analysis focuses on the kinetic energy accumulator. The inertial accumulator charging time was selected to allow it to reach the maximum speed, i.e., where the maximum kinetic energy value is close to $E_{max} = 61,411$ J. For the motor, the following nominal parameter values were assumed: rotational speed $n_0 = 8,000$ rpm, torque $M_0 \approx 1.2$ Nm and power $N_0 \approx 1$ kW.

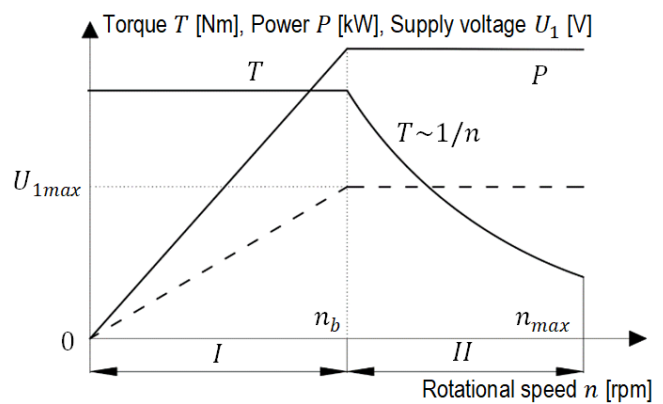


Fig. 1. PMSM drive characteristics. Below the nominal speed n_n , the drive operates with a constant torque of T (range I); after, it is exceeded, it operates at a constant power of P (range II), developed based on [20]

Based on the variance of rotational speed $n(t)$ and torque $M(t)$, the model calculates power supplied to the energy accumulator with the following equation:

$$N_{lad}(t) = \frac{M(t)n(t)}{9.55}. \tag{15}$$

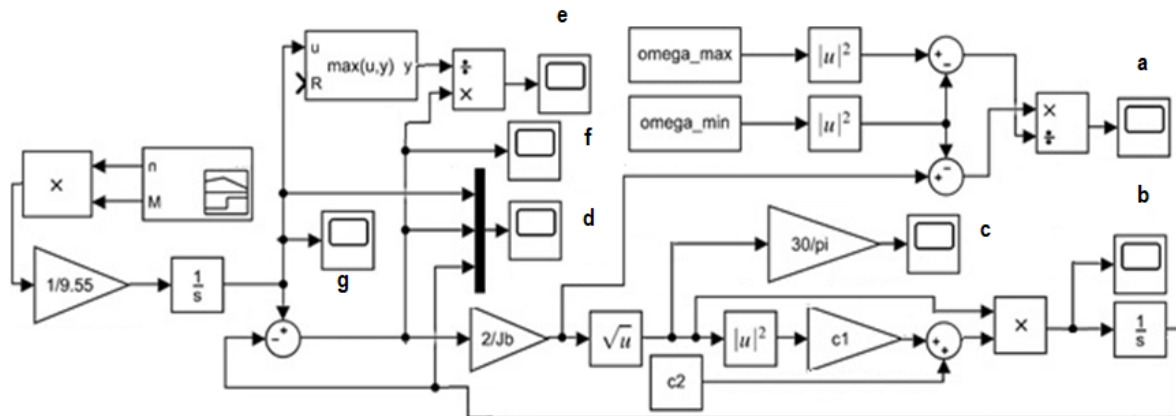


Fig. 2. Numerical calculations model diagram; a – charge degree, b – loss power, c – rotational speed, d – energy variance, e – efficiency, f – stored energy, g – charging energy (supplied by drive)

After integrating the calculated power, we arrive at the energy supplied to the accumulator $E_{lad}(t)$. However, the energy stored in the accumulator $E_{mag}(t)$ is expressed with the following equation:

$$E_{mag}(t) = E_{lad}(t) - E_{str}(t), \quad (16)$$

where is $E_{str}(t)$ is energy loss. Eq. (16) describes the value of $E_{mag}(t)$, which is also calculable from the kinetic energy equation. The equation can be transformed as follows:

$$\omega(t) = \sqrt{\frac{2E_{mag}(t)}{J_B}}. \quad (17)$$

Eq. (17) is employed to calculate the loss power $N_{str}(t)$; after integration, it allows us to calculate the loss energy $E_{str}(t)$. Additionally, accumulator efficiency ratio $\eta(t)$ was determined by referencing to energy stored in a given moment $E_{mag}(t)$ and the maximum value of supplied energy $E_{lad\ max}$. This can be expressed in the form of the following equation:

$$\eta(t) = \frac{E_{mag}(t)}{E_{lad\ max}} \cdot 100\%. \quad (18)$$

The charge of the accumulator can be expressed as an equation comprising the previously established values:

$$k(t) = \frac{\omega^2(t) - \omega_{min}^2}{\omega_{max}^2 - \omega_{min}^2} \quad (19)$$

MATLab Simulink software package was used to develop the previously defined model. It allows us to carry out simulations and make calculations in real time. The model view as developed in the software environment is provided in Fig. 2.

3.2. Numerical model

There are three states of accumulator operation: charge, discharge and self-discharge. When loading, the inertial accumulator accelerates to high speed due to the torque and velocity applied to the shaft. Analogously, during discharge, an external load is applied to the inertial accumulator shaft. During self-discharge, which usually is the longest of the states, the rotor shaft is decoupled and rotates freely. The speed of revolution at this point is close to nominal; the only load is affected by motion resistances and causes a slow reduction of speed [21]. Consequently, a simulation of operation of the modelled device was carried out for each described state of operation, resulting in three cases: C1, C2 and C3.

Tab. 1. Adopted properties and marking of individual rotors

Rotor marking	B1	B2	B3	B4
External radius r_z (m)	0.15	0.15	0.13	0.13
Internal radius r_w (m)	0.018	0.018	0.018	0.018
Height h (m)	0.018	0.015	0.018	0.02
Moment of inertia J_B (kg·m ²)	0.112	0.094	0.063	0.07
Mass m_B (kg)	9.844	8.203	7.358	8.176
Maximum kinetic energy E_{max} (J)	61,411	51,332	34,746	38,607
Constant c_1 (kg·m ²)	2.78 ·10 ⁻⁸	2.5 ·10 ⁻⁸	1.081 ·10 ⁻⁷	1.191 ·10 ⁻⁷
Constant c_2 (Nm)	0.027	0.02	0.016	0.018
Minimum value of angular velocity ω_{min} (rad/s)	636.82	636.82	516.38	516.38

In order to conduct the simulations, four variants of the analysed rotors were adopted. Apart from the rotor described in the previous chapters (marked as B1), calculations were also made for three other variants differing in radius r or height h . As they have different moments of inertia, the maximum kinetic energy for each of them varying charging times has been adopted. The dimensions and properties of selected variants are presented in Tab. 1.

As it can be seen from the presented description, 12 simulation variants were finally obtained, resulting from the combination of three charging methods (C1, C2 and C3) with four different rotors (B1, B2, B3 and B4).

4. RESULTS AND DISCUSSION

The first simulated scenario (Fig. 3) involves motor deceleration from the speed ($n = 9,500$ rpm). Since the motor operating range was at constant power, the initial torque was $T = 1$ Nm. It achieved the nominal value at speed $n = 8,000$ rpm and subsequently entered the stage of operation with constant torque until stopped. The entire operation took place over 108 s. The second scenario (Fig. 4) was performed with the motor operating under nominal conditions, i.e., with speed of $n = 8,000$ rpm and torque value of $T = 1.2$ Nm. This type of charging simulates a situation when the shaft (transmission) of the rotor is coupled with the motor without load. In this case, the acceleration took only 62 s. The third charging scenario (Fig. 5) involved an arrangement in which the accumulator is charged as the motor accelerates to achieve nominal operating conditions. This is by far the longest operation (120 s)

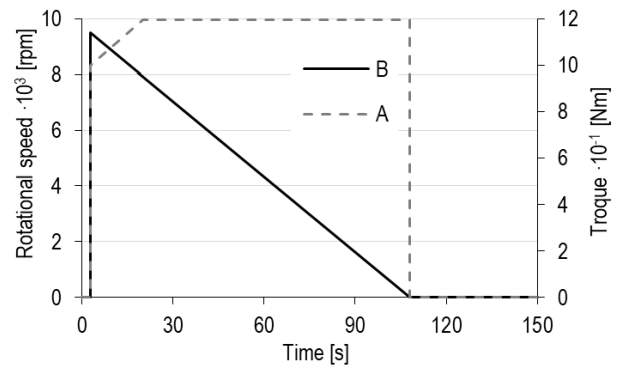


Fig. 3. Charging characteristics for the first scenario C1; A – torque, B – rotational speed

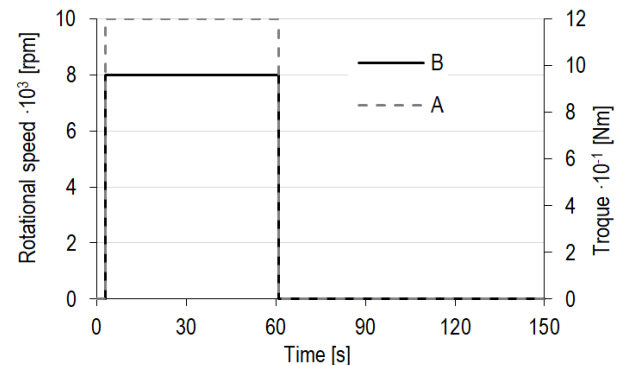


Fig. 4. Charging characteristics for the first scenario C1; A – torque, B – rotational speed

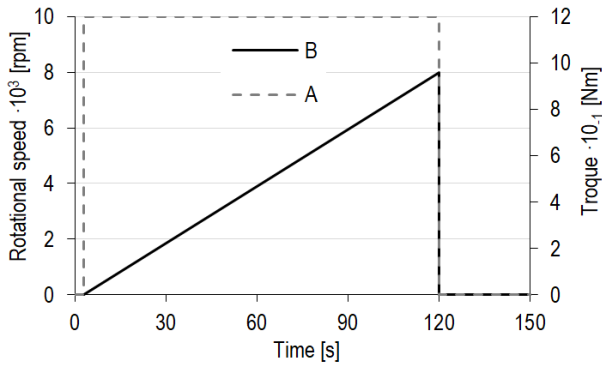


Fig. 5. Charging characteristics for the third scenario C3; A – torque, B – rotational

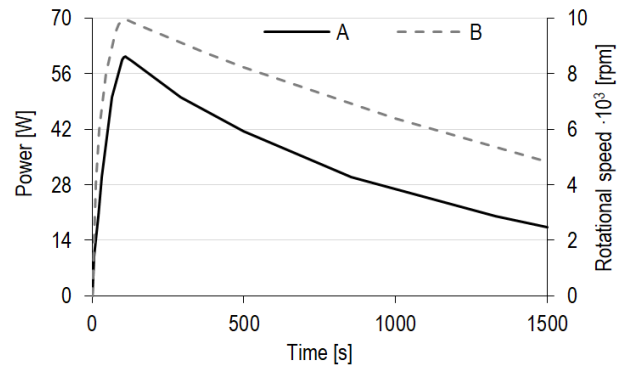


Fig. 7. Graph lines variability as a function of time: A – loss power, B – rotational speed

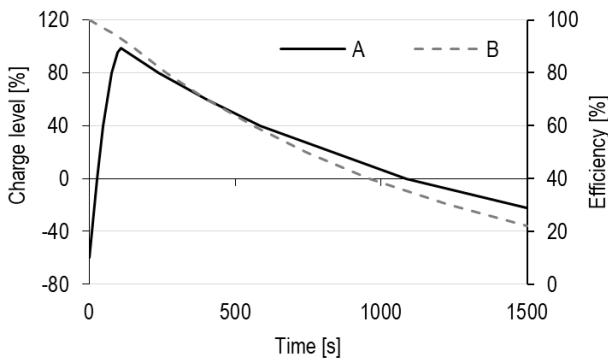


Fig. 6. Percentage variability graphs: A – charge level, B – efficiency

From the proposed group of variants, the rotors B1 and B2 should be considered the best because despite their slightly larger dimensions, they are able to accumulate almost twice as much energy as compared with rotors with smaller radii. Moreover, after about 5 min (300 s), they still have an energy of 4,000 J and a charge level of about 0.5. Ultimately, however, due to the greater energy capacity, it should be pointed out that the most effective solution is the rotor B1. Fig. 6 shows the degree of charge and efficiency of the system. Fig. 7 presents the variance in rotational speed of the rotor and power loss as a function of time.

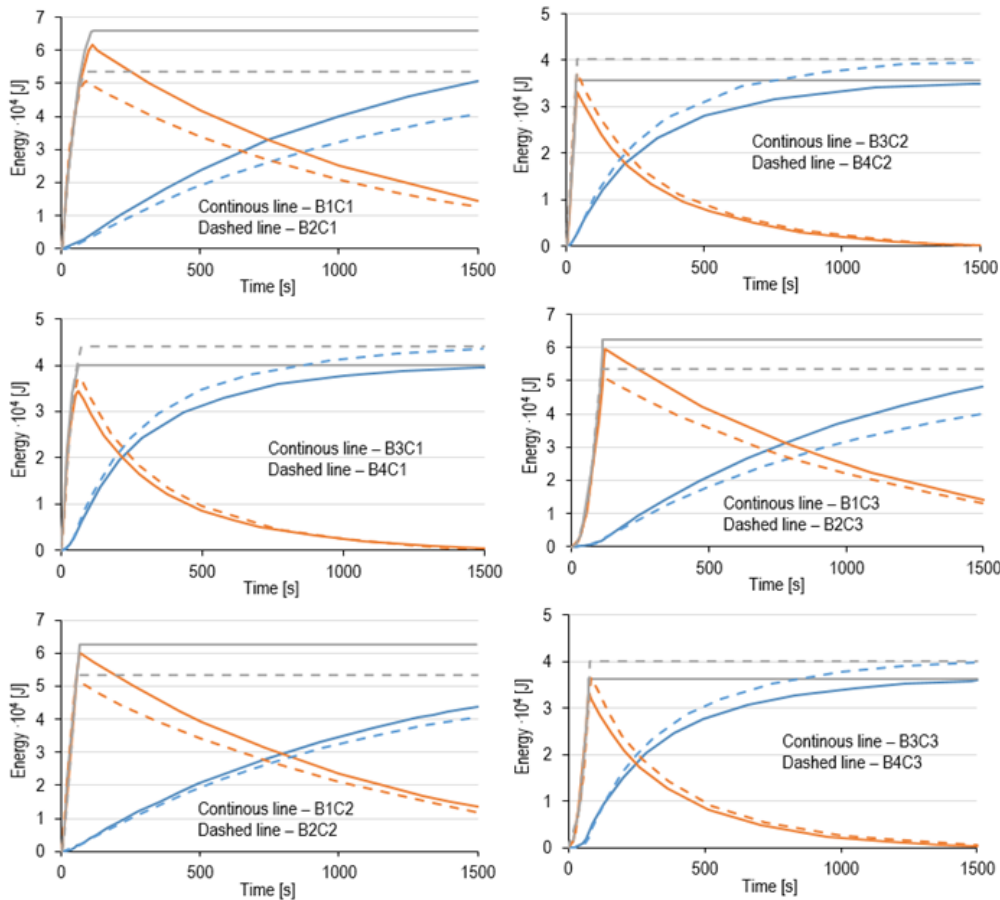


Fig. 8. Variance of energy as a function of time; blue lines represent energy loss, orange lines represent accumulated energy and gray lines represent charging energy; continuous and dashed lines represent different variants according to the legend

The graphs presented in Fig. 8 show the energy values in the system for different variants. It should be noted that the constants used in the model and the relationships on the basis of which they were determined rely on theoretical considerations and thus may not cover all the phenomena affecting the operation of the energy storing device or describe them only to a limited extent. The use of the charge level allows for a slightly more accurate reflection of the actual state of the accumulator capacity, due to the possible change in the value of the start power when operating at a speed lower than the minimum value of angular velocity.

The analysis of the presented graphs shows that the energy loss of the rotors B3 and B4 progresses much faster. This is due not only to the much lower maximum stored energy (more than by a half) but also to the much larger losses due to the smaller rotor diameter, which largely influenced the aerodynamic drag.

The different charging methods have little effect on the behaviour of the accumulator, except that charging with constant power is by far the shortest. The times for decreasing and increasing speeds are similar, and the difference is the result of the engine entering the state of work with constant power. However, it is worth bearing in mind that in the case of charging with a braking engine, the transition from the charging state to the self-discharging state is the smoothest, which in the case of a longer period of use may be important in terms of the durability of cooperating elements such as bearings.

5. SUMMARY

The analysis of presented data allows us to observe the operation of the modelled system. Based on the established graph lines, it is possible to determine that different charging methods do not materially affect the operation of the accumulator; on the other hand, charging time with constant power is by far the shortest. Charging times for acceleration and deceleration are similar, the difference being the result of the motor entering the state of operating under constant power. One should keep in mind that in the case of supplying energy to the system with decelerating motor, the transition from the charging state to self-discharging state is the smoothest. With longer times of operation, this may affect the durability of the mechanical system components, such as, bearings.

To summarise, the mathematical model was developed and implemented within the framework of software environment for numerical calculations. This allowed us to identify a series of graph lines and characteristics for the analysed system. The results of carried out works enable the comparison of different kinetic energy accumulators with different geometries and different methods of operation. Consequently, it is possible to develop the basis and a number of input data to be used in the design of this type of equipment.

REFERENCES

- Chen H, Cong TN, Yang W, Tan C, Li Y, Ding Y. Progress in electrical energy storage system: A critical review. *Prog Nat Sci*. 2009;19:291–312.
- Káberger T. Progress of renewable electricity replacing fossil fuels. *Global Energy Interconnection*. 2018;1:48–52.
- Moriarty P, Honnery D. Can renewable energy power the future? *E Policy*, 2016;93:3–7.
- Medina P, Bizuayehu AW, Catalao JPS, Rodrigues EMG, Contreras J. Electrical Energy Storage Systems: Technologies' State-of-the-Art, Techno-economic Benefits and Applications Analysis. *Proc of the 47th Hawaii Int Conf on Syst Sci*; 2014 Jan 6–9; Waikoloa, HI, USA, 2014;2295–2304.
- Hadjipaschalis I, Poullikkas A, Efthimiou V. Overview of current and future energy storage technologies for electric power applications. *Renew Sust Energ Rev*. 2009;13:1513–1522.
- Del Granado PC, Wallace SW, Pang Z/The value of electricity storage in domestic homes: A smart grid perspective. *E Systems*, 2014;5:211–232.
- Amiryar ME, Pullen KR, A Review of Flywheel Energy Storage System Technologies and Their Applications. *Appl Sci*, 2017;7(3):286, 1–22.
- Skinner M. Characterization of Passibe Sischarge Losses in a Flywheel Energy Storage System [Masters's Thesis], Edmonton, (AB, Canada): University of Alberta; 2017.
- Luo X, Wang J, Dooner M, Clarke J. Overview of current development in electrical energy storage technologies and the application potential in power system operation. *Appl E*. 2015;137:511–536.
- Hadjipaschalis I, Poullikkas A, Efthimiou V. Overview of current and future energy storage technologies for electric power applications. *Renew Sust Energ Rev*, 2009;13,1513–1522.
- Skinner M, Mertiny P. Energy Storage Flywheel Rotors – Mechanical Design, *Ency*, 2022;2(1):301–324.
- Bolund B, Bernhoff H, Leijon M. Flywheel energy and power storage systems, *Renew Sust Energ Rev*, 2007;11(2):235–258.
- Łyskojć D, Duer S, Zajkowski K, Sokołowski S. Możliwości zwiększenia zasięgu pojazdu z napędem elektrycznym przy wykorzystaniu niekonwencjonalnych rozwiązań technicznych (English title.: The ability to increase the range of electric vehicle using unconventional technical solutions), *Autobusy Technika, Eksploatacja, Systemy Transportowe*, 2012;12(5):273–278.
- Jansen RH, Dever TP. G2 Flywheel Module Design, NASA Technical Reports Server [Internet]. 2006, NASA/CR-2006-213862 [cited 22 May 2022]. Available from: <http://large.stanford.edu/courses/2020/ph240/barnett2/docs/nasa-aug06.pdf>
- Ferrofluidowe koło zamachowe (English: Ferrofluid flywheel), KRAKsat, [Internet]. KrakSat [cited 16 Dec 2019]. Available from: <https://www.kraksat.pl/space/ferrofluidowe-kolo-zamachowe/>
- Shah H. Volvo Flywheel KERS offers 25% improved economy [Internet]. 2013, article for paultan.org, [cited 16 Dec 2019]. Available from: <https://paultan.org/2013/05/01/volvo-flywheel-kers-offers-25-improved-economy/>
- Chase C. Volvo Refreshes 2020 XC90 With Energy Recovery Braking System [Internet]. 2019, article for autotrader.ca, [cited 16 Dec 2019]. Available from: <https://www.autotrader.ca/newsfeatures/20190222/volvo-refreshes-2020-xc90-with-energy-recovery-braking-system>
- Merksiz J, Pielecha I. Układy mechaniczne pojazdów hybrydowych (English title: Mechanical systems of hybrid vehicles). Poznań: Publishing house of Poznań University of Technology, Poznań; 2015.
- Złoty P., Od koła garncarskiego do systemu KERS (English title: From the potter's wheel to the KERS system [Internet]. 2013, article for gazeo.pl, [cited 16 Dec 2019]. Available from: <https://gazeo.pl/samochody-hybrydowe-elektryczne/samochody-hybrydowe/Od-kola-garncarskiego-do-systemuKERS,artykul,6798.html>
- Pawelski Z, Maciejczyk A, Wróbel T. Prototype of Electric Bus of AMZ Kutno, *J KONES Powertrain and Trans*, 2014;21(1):197–204.
- Szumanowski A., Akumulacja energii w pojazdach (English title: Accumulation of energy in vehicles), Warsaw: Publishing House of Communication and Connectivity, 1984.

Mateusz Kukla:  <https://orcid.org/0000-0003-3456-3824>

EXPERIMENTAL AND NUMERICAL INVESTIGATIONS AND OPTIMISATION OF GRAIN-ORIENTED SILICON STEEL MECHANICAL CUTTING PROCESS

Radosław PATYK^{*ID}, Łukasz BOHDAL^{*ID}, Szymon GONTARZ^{**ID}

*Faculty of Mechanical Engineering, Koszalin University of Technology, ul. Raclawicka 15-17, 75-620 Koszalin, Poland

**Faculty of Automotive and Construction Machinery Engineering, Warsaw University of Technology, ul. Narbutta 84, 02-524 Warszawa, Poland

radoslaw.patyk@tu.koszalin.pl, lukasz.bohdal@tu.koszalin.pl, szymon.gontarz@pw.edu.pl

received 9 June 2022, revised 24 August 2022, accepted 24 August 2022

Abstract: The process of mechanical cutting of magnetic materials has many advantages in the form of high efficiency with reduced process costs in relation to other cutting technologies; no thermal stresses in the material, which significantly deteriorate the magnetic properties; or the possibility of shaping materials taking into account long cutting lines. In industrial practice, it is very difficult to ensure appropriate conditions for the cutting process and its proper control. Currently, there are no data on the selection of technological parameters of the mechanical shear slitting process of grain-oriented silicon steel in terms of the obtained cutting surface quality and the obtained magnetic properties of the workpiece. The article presents the possibilities of forecasting the characteristic features of the cut edge and selected magnetic properties of grain-oriented silicon steel. For this purpose, proprietary numerical models using FEA (Finite Element Analysis) were used. Then, experimental studies were carried out, and the optimisation task was developed. The developed results enable the correct selection of technological parameters of the process, ensuring the appropriate quality of the cut edge of steel and minimal interference with the magnetic properties.

Key words: magnetic materials, shear slitting, sheared edge, magnetic properties

1. INTRODUCTION

Mechanical cutting is a very popular technological process in shaping electrical steel. This is due to the high efficiency of the process and its lower costs compared with other cutting techniques. Electrical steel, as soft magnetic materials in industrial practice, must be characterised by low magnetic losses and high magnetic induction because it is used in the construction of electrical machines and devices such as magnetic circuits of electric motors, transformers and generator cores. Negative changes in the magnetic properties of these materials after production processes often cause problems with obtaining appropriate technical and operational properties of these devices. The main influence on the deterioration of the magnetic properties of steel is the successive technological operations it is subjected to, as well as its transport and storage (impact, compression, bending). This causes stresses, deformations and microcracks in these materials [1–3].

In the mechanical cutting process, material separation is accompanied by large plastic deformations, which leads to the deterioration of the integrity of the material. Therefore, in the area of the cut edge, zones of stress concentration and deformation, as well as changes in the orientation of the grains of the microstructure, are formed. In many cases, the process is accompanied by the phenomenon of burr formation on the cut edge, which is difficult to analyse and predict because it depends on many factors. Excessive burr formation causes breaking insulating layers among laminated cores. The negative influence of burrs on the shapes of the magnetic hysteresis loop of electrical steel and its characteris-

tic parameters was also demonstrated [4, 5].

Among the works in the processing of electrical steel by means of cutting operations, attention is paid mainly to the influence of cutting technology (e.g., mechanical, water and laser) on selected magnetic properties [6, 7]. Much less consideration concerns the appropriate configuration and optimisation of these technologies and the determination of their impact on both the stress and deformation states, the characteristic features of the cut edge of the material and its magnetic properties. Some works have focussed on searching for connections between the mechanical properties of the materials cut, the geometrical properties of the tools and the quality of the cut edge [8, 9].

Much less work concerns the analysis of cutting forces, cutting technological parameters on the stress and strain concentration in the shearing region, burr formation and change magnetic properties. The available works concern mainly punching and blanking processes, where the decisive factor for the quality of the product is the appropriate selection of the blanking clearance [10].

In the work [3], experimental tests were carried out on the process of cutting silicon electrical steel with thicknesses $t = 0.2$ mm and $t = 0.35$ mm. It was found that a significant parameter influencing the degree of deformation in the cutting zone is the punching speed, which also affects punching forces. The deformation values in the cutting zone were analysed using the digital image correlation (DIC) method. Impact was also found for the blanking speed on the hysteresis losses, where cutting at high speed can reduce this magnetic loss. In the study mentioned in Ref [11], the effect of three different cutting techniques such as punching, waterjet and laser cutting on the magnetic properties of

the grain-oriented electrical steel sheets was investigated. The comparative analysis shows the superiority of the punching and waterjet cutting techniques over laser cutting. For the punching process, a significant influence of the clearance between the punch and the die on the level of material distortion was demonstrated. It was assumed that it is possible to control the clearance of the cut so as to obtain the least interference in the magnetic properties, but it is necessary to know the characteristics of the hysteresis loop in the areas of the cut edge. The authors of the study mentioned in Ref [12] showed that stresses in electrical steel actually increase the total losses and that compressive stress aggravates the total losses much more than tensile stress.

In the study mentioned in Ref [13], the authors evaluated the influence of the grain size of the material on its iron losses after the blanking process. Samples for the single sheet test were blanked at different cutting clearances (15–70 μm) from sheets with identical chemical composition (3.2 wt.% Si) but varying average grain size (28–210 μm) and thickness ($t = 0.25\text{ mm}$ and $t = 0.5\text{ mm}$). The measurements of blanking force and punch travel were carried out. In the study mentioned in Ref [14], the influence of the blanking process on the magnetic properties of non-oriented electrical steel lamination was analysed. The influence of residual stress distribution on selected magnetic property deterioration was investigated. A flat punch and concave punch were used as blanking tools. The magnetic property deterioration of non-oriented electrical steel lamination was mainly related to peak residual stress. With the help of appropriate tool geometries and clearance values, it was possible to reduce magnetic property deterioration.

In the work mentioned in Ref [15], research was carried out on the determination of changes in the magnetic properties of thin non-oriented electrical sheets depending on their microstructure and clearance. In the study mentioned in Ref [16], the influence of the conditions of the punching process on stresses and the structure of the magnetic domain in the cutting zone of non-oriented silicon steel was investigated. The Suresh theoretical model was characterised, by means of which the stress values on the cut edge were calculated. In the article mentioned in Ref [3], plastic deformations were measured in the cutting zone using the DIC technique. The influence of the clearance on the width of the deformation zone was determined.

The analysis of the state of knowledge shows that the deterioration of the magnetic properties is caused, in addition to the formation of excessive burrs, as well as by the wide deformation-affected zone. The authors of the works mentioned in Ref [17, 18] analysed the influence of the width of this zone on the selected magnetic properties of grain-oriented and non-grain-oriented silicon steel. Based on the results, it can be concluded that the deterioration of the magnetic properties of electrical sheets in the areas along the cut line may occur not only in the vicinity of the cut edge, but also in areas located more than 10 mm from the cut edge. For sheets with a high silicon content, deterioration may be up to 15 mm from the cut edge, while for low silicon content, it is about 10 mm [17]. In the works mentioned in Ref [3, 19], it was shown that the degradation of the magnetic properties of the material depends on the width of the cut elements. This confirms the importance of the influence of the width of the deformation zone on the product quality, which has a particularly negative effect on the magnetic properties in the case of cutting small details. Particularly large changes in magnetic properties occur when cutting narrow 20-mm-wide strips from metal sheets.

The concentration of high-tensile stress values in the cutting

zone causes the instability of the material cracking process, which causes the formation of slivers and burrs on the cut surface of workpieces. According to the authors of the works mentioned in Ref [8, 20, 21], the cutting speed may also have an impact on the stress distributions and their maximum values in the cutting zone.

The analysis of the state of knowledge shows that the goal is to properly control the conditions of the cutting process so as to limit the width of the deformed zone and the concentration of maximum stresses in the cutting zone and to obtain a cutting edge free from defects in the form of edge waviness, burrs and slivers. This may result in minimal changes to the magnetic properties of sheets. This is difficult due to many factors affecting both the plastic flow and material separation process. Information on process conditions and guidelines for their design is often generalised to all cases, which does not give good results in the form of appropriate dimensional accuracy of details and their magnetic properties. Each of the mechanical cutting processes has its own specific features and parameters that do not always occur in another process and may have a crucial impact on the course of physical phenomena in the cutting zone when shaping certain types of steel. There is a lack of information related to the influence of the cutting process parameters on the stress and deformation states, their relationship with the quality of the cut surface and the magnetic properties of the material after the process.

The aim of the work is to analyse the influence of the main technological parameters of the mechanical cutting process on the quality of the cut edge and the magnetic properties of grain-oriented silicon steel with a 3% silicon content. Experimental research was carried out on the shear slitting machine, which is a popular industrial tool for separating electrical sheet strips. The advantage of this device is the possibility of extensive interference in the parameters of the cutting process; however, currently, the knowledge on the correct selection of processing parameters in terms of obtaining a high-quality product is limited. Physical, mathematical and simulation models of the shear slitting process were developed using a finite element method to predict the width of the deformed zone concentrated along the cut line after the process. The developed models take into account the spatial state of stresses and strains, the actual geometries of the sheet and tools, and the length of the cutting line and enable the analysis of crucial physical phenomena of the process at any time during the process. The experimental research included the analysis of the quality of the cut edge and selected magnetic properties of the material. As a result of numerical and experimental research, a multi-criteria optimisation task was formulated, assuming the criteria of maximum process efficiency while maintaining the highest quality of the cutting edge free from burrs and slivers and minimal changes in magnetic properties of workpiece.

2. FE MODELLING OF SHEAR SLITTING PROCESS

Cutting materials are subject to very complex levels of stress. Therefore, in order to analyse this process, it is necessary to use computer methods of mechanics and very advanced mathematical tools. Problems with many variables should be dealt with taking into account their nonlinearity [22, 23]. The cutting process should be viewed as a geometrically and physically nonlinear boundary-start problem with boundary conditions that are unknown in the tool–workpiece contact area. In this work, the cutting process is modelled with variational and finite element methods according to the following steps:

1. Mathematical modelling of physical models from which continuous and incremental mathematical models are obtained are as follows: tool-object contact models, constitutive equations, motion dynamics equations and uniqueness conditions. As a result of the application of the variation formula, one also obtains a variational equation of the motion of the object.
2. Construction of discrete physical models.
3. Physical modelling of real objects. The effect of this phase is the development of a physical model of the cutting process, distinguishing between the adopted assumptions and simplifications.
4. Construction of computer models, creation of proprietary applications enabling comprehensive time analysis of deformation states occurring in objects during the analysis, determining the type of problem, its solution and its essential parameters and finally, preparing the data for calculations, calculating and editing the result – the program performs calculations based on these data and saves the result. The obtained results can be presented, analysed and archived.
5. Approximation of continuous mathematical models using finite element methods or mathematical modelling of discrete physical models. The result is a discrete, incremental mathematical model of the physical model.

The numerical model uses the updated Lagrange description, which was used to describe nonlinear phenomena on a typical incremental step in the cutting process [24, 25]. The task of the incremental analysis is to formulate the geometry of the material being cut, as well as the existing state of increase in displacement, velocity, acceleration, deformation, stress, strain, velocity, etc. in subsequent discrete moments of $\tau = 0, \Delta t, 2\Delta t, \dots$, corresponding to a specific slight increment of time. Within the incremental description, there are many important issues related to the nonlinear analysis of the cutting process. They include the selection of an appropriate coordinate system, determination of measurements of strains and stresses and their increments, as well as determination of the rules of their accumulation at each increment step. The strain increments and stresses are described by the increment of the nonlinear symmetric Green–Lagrange strain tensor and the increment of the second Pioli–Kirchhoff symmetric stress tensor. In order to formulate the incremental variational equation of object motion, in the case of cutting, a variational functional is introduced in which there is only one independent field – the field of incremental displacement.

The constitutive material model reported by Johnson and Cook [26] was employed in this study to represent the cutting material behaviour. The model can be represented by Eq. (1):

$$\sigma_Y = [A + B(\bar{\epsilon}^p)^n][1 + C \ln \dot{\epsilon}^*][1 - (T^*)^m], \quad (1)$$

where A, B and n are strain-hardening constants; C is the strain rate hardening constant; σ_Y is the equivalent flow stress; $\bar{\epsilon}^p$ is the equivalent plastic strain; and m is the thermal softening constant that modifies the homologous temperature term, T^* . The homologous temperature is defined as $T^* = \frac{T - T_r}{T_m - T_r}$, where T is the temperature of the material, T_r is a reference temperature (typically room temperature) and T_m is the melt temperature of the material. The term $\dot{\epsilon}^*$, is the normalised strain rate of the material or $\dot{\epsilon}^* = \frac{\dot{\epsilon}^p}{\dot{\epsilon}_0}$, where $\dot{\epsilon}_0 = 1.0 \text{ s}^{-1}$. ET 122-30 with thickness of $t = 0.3 \text{ mm}$ grain oriented silicon steel was used in analysis (Tabs. 1 and 2).

The mechanical properties of the material were tested on a

Zwick Roell Z400 testing machine (Fig. 1) at a temperature $T = 20^\circ\text{C}$. Ten tensile tests along the length and 10 tests across the direction of rolling were made on standardised specimens. It was found that the material did not exhibit mechanical anisotropy, which was confirmed by photos of the metallographic structure. The material hardness was measured on a table Fervi hardness meter with the measurements repeated 10 times. The value of the arithmetic mean of the measurements is presented in Tabs. 1 and 2.

Tab. 1. Johnson–Cook constitutive model constants for ET 122-30 steel [27]

A (MPa)	B (MPa)	C	n	m
104.3	445.6	0.041	0.46	0.54

Tab. 2. Mechanical properties of ET 122-30 steel

Density (kg/dm ³)	Yield point (MPa)	Elongation (%)	Hardness (HV ₅)
7.65	300 ± 5	11 ± 1,5	160 ± 7

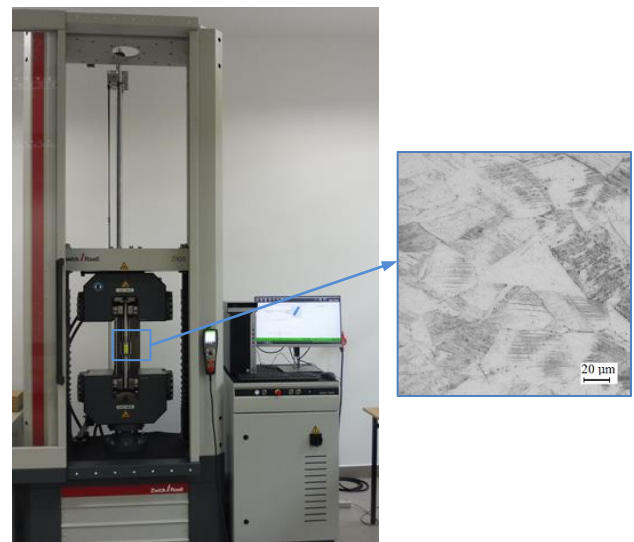


Fig. 1. Zwick/Roell Z400 testing machine for determining material characteristics

An important element in the analysis of the shear slitting process is the correct construction of a geometric model with the same parameters as the real research object. Therefore, it is necessary to take into account the rotation of the knives and the longitudinal movement of the sheet metal during the process. The developed numerical model in the LS-DYNA solver for the 3D state of stresses and strains takes into account the actual boundary conditions of the process (Fig. 2). The model takes into account the value of the rake angle (α), the value of the radius of the knives, the length of the cutting line and the method of supporting the material sheet. In industrial conditions, the first step is to determine the overlap (vertical clearance value c_v) of the knives and then start the rotation of the knives and polyurethane roll with the set cutting speed v_x and horizontal clearance h_c . The tests were carried out for the following geometric parameters of the test stand: $r_1 = r_2 = 15 \text{ mm}$, $r_3 = 20 \text{ mm}$, $l = 80 \text{ mm}$, $w_i = 40 \text{ mm}$ and the process control variables in the range of $v_2 = 3\text{--}24 \text{ m/min}$ and

$h_c = 0.02\text{--}0.1$ mm, and rake angle $\alpha = 5^\circ\text{--}40^\circ$. A constant value of tool overlap $c_v = 0.1$ mm was assumed. Simulation models were used to analyse the influence of technological parameters of the cutting process on the width of the deformed zone (Figs. 3–6).

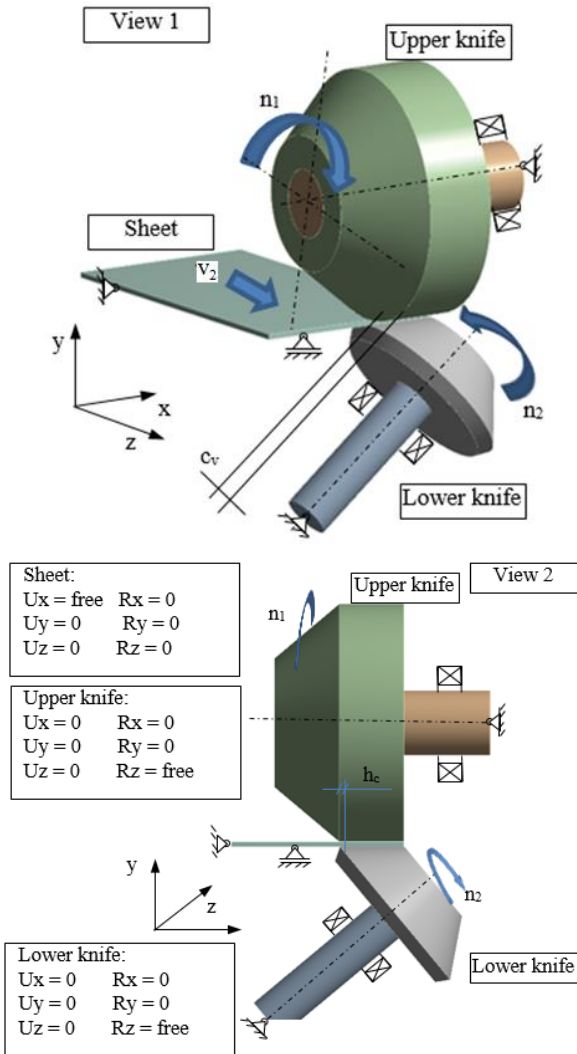


Fig. 2. FE model with boundary conditions

3. FE MODELLING RESULTS

The authors' research so far has shown that the residual stresses after blanking in workpiece extend further into the material than the area reinforced with deformation. According to many studies, the plastic deformation zone after mechanical cutting in the sheared edge is at least $D_{mz} = 0.1$ mm and increases rapidly with increasing wear of the cutting tools [28–30]. Currently, the literature has not specified the extent to which this zone extends inside the material depending on other criteria, for example, the geometry of the cutting tool. It is known, however, that deformations along the cut line may result in the formation of an elastic stress zone in the depths adjacent to the plastically deformed area [31–33]. As a result, both zones strongly influence the magnetic properties. The proposed approach makes it possible to precisely determine both the size of the deformation in the cutting zone and the width of this zone, depending on the adopted machining parameters. During the cutting process, in order to analyse the phys-

ical phenomena in the cutting zone, a high-speed i-SPEED TR camera with a computer was used, which in the subsequent steps of the process recorded a set of consecutive images of the sample surface. The obtained measurement results were used to validate the numerical results by means of comparative analyses of the values of displacement and deformation of the material during and after the end of the process. The DIC technique was used to determine these features. Image-based displacement and deformation measurements are non-invasive, which means that the magnetic properties are not negatively affected. The OLYMPUS LEXT OLS4000 confocal laser microscope was used to measure the burr height after cutting.

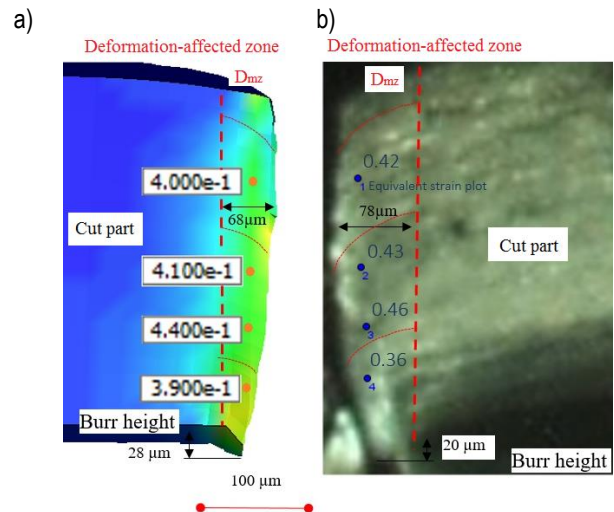


Fig. 3. Analysis of deformation-affected zone and equivalent strain values in shearing region obtained numerically (a) and experimentally (b)

The comparative analysis of the test results showed the maximum differences in the values of equivalent strain values, width of the deformation-affected zone and the burr height amount to about 15%.

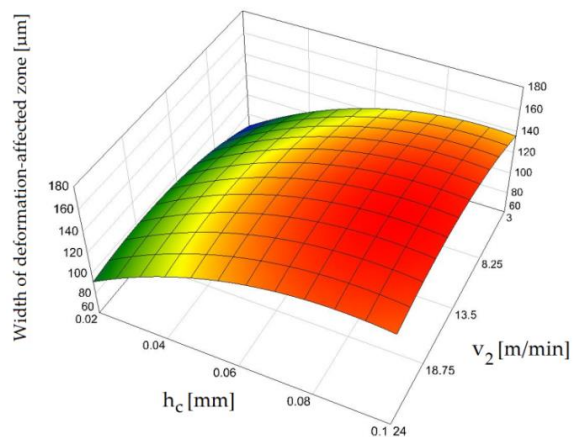


Fig. 4. Influence of the process parameters on the width of the deformation-affected zone for $\alpha = 5$

The obtained results show that the rake angle of the upper knife α , horizontal clearance h_c and the cutting speed v_2 have a key influence on the formation of the deformed zone. With an increase in the clearance value, the width of the deformed zone increases (Figs. 4–6). The maximum width of the deformed zone is approxi-

mately $D_{mz} = 180 \mu\text{m}$ for $h_c = 0.08 - 0.1 \text{ mm}$, when $\alpha = 5^\circ$ and for $h_c = 0.06 - 0.08 \text{ mm}$, when $\alpha = 40^\circ$, where $v = 13.5 \text{ m/min}$. The clearance value is especially important when using $\alpha = 5^\circ - 25^\circ$. In this range of variability, an increase in the horizontal clearance above the value of $h_c = 0.06 \text{ mm}$ is particularly unfavourable. With small clearances $h_c = 0.02 \text{ mm} \div 0.03 \text{ mm}$, the change of the angle α does not significantly change the width of the deformed zone. The minimum width of this zone reaches approximately $D_{mz} = 60 \mu\text{m}$. This value has been obtained for $h_c = 0.02 \text{ mm}$, $\alpha = 5^\circ$ and 40° and $v = 3 \text{ m/min}$. When using an rake angle value $\alpha = 25^\circ$, the zone value increased to about $D_{mz} = 90 \mu\text{m}$ for the same cutting speed and horizontal clearance configuration. When using $\alpha = 40^\circ$ deformation-affected zone, it is less sensitive to changes in the value of clearance and cutting speed than for other variants of α parameter, but such an rake angle value may cause an increased concentration of contact pressures on the edge of the upper knife and cause its accelerated abrasive wear.

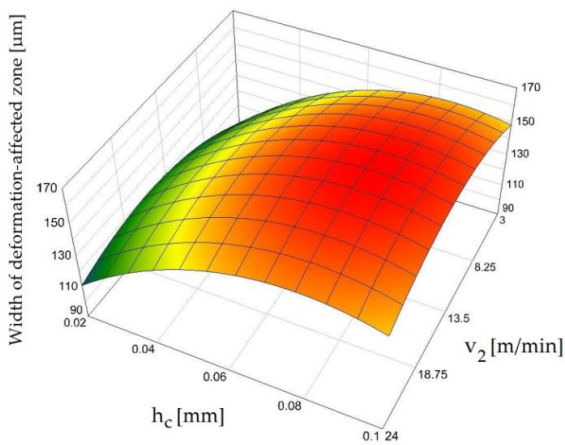


Fig. 5. Influence of the process parameters on the width of the deformation-affected zone for $\alpha = 25^\circ$

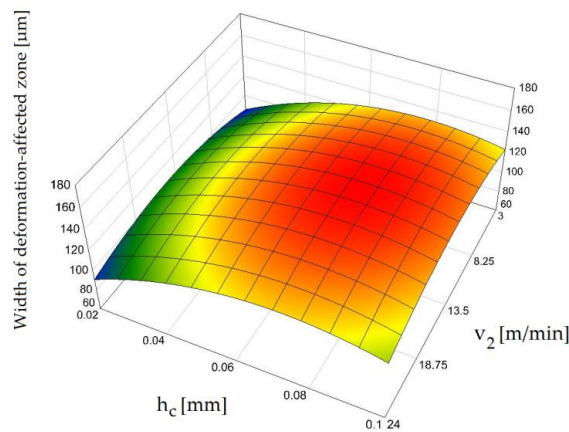


Fig. 6. Influence of the process parameters on the width of the deformation-affected zone for $\alpha = 40^\circ$

4. EXPERIMENTAL RESEARCH

The experimental tests were carried out on a specially designed test stand presented in Fig. 7. The Prinzing Maschinenbau KSE 10/10 circular shears were used for the tests. Specially purchased additional components allow, among others, high cutting speeds, precise settings of the horizontal and vertical

clearances, as well as internal or external flaring on cut discs and rings. As a result of preliminary tests and simulation analysis, factors significantly influencing the cutting process and product quality were distinguished. The input factors include horizontal clearance h_c in the range of variation $h_c = 0.02 - 0.1 \text{ mm}$ and cutting speed v in the range of variation $v_2 = 3 - 32 \text{ m/min}$. These are factors that are mainly controlled on production lines. The constant factors were as follows: rake angle $\alpha = 30^\circ$ and vertical clearance $c_v = 0.1 \text{ mm}$.



Fig. 7. Experimental test stand: 1 – shear slitting machine, 2 – sheet, 3 – i-SPEED TR camera, 4 – light source and 5 – PC

Experimental studies were carried out using a five-level rotatable experimental matrix. The study of magnetic properties was carried out on a test stand consisting of the components shown in Fig. 8. A magnetising winding and a measuring winding were wound on each of the samples, each winding being wound uniformly in order to create a closed magnetic circuit and avoid magnetic flux dispersion in the material. The measurements of the magnetic characteristics were made for various values of the amplitude of the magnetic field intensity H_m . The frequency of the demagnetising waveform was 10 Hz. Measurements of magnetic characteristics were made for variable values of the amplitude of the magnetic field intensity $H_m = 214.35 \text{ (A/m)}$, $H_m = 497.84 \text{ (A/m)}$ and $H_m = 568.79 \text{ (A/m)}$.

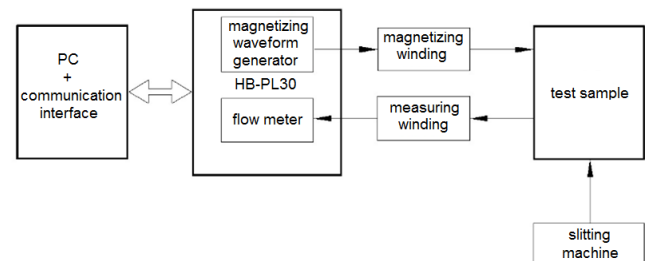


Fig. 8. Diagram of magnetic property measurement

5. RESULTS OF ANALYSIS

Figs. 9–11 show the influence of the analysed conditions of the shear slitting process and configuration of parameters on the burr height on the cut edge. According to the analysis of the

state of knowledge and industrial practice, the burr height above 30% of the sheet thickness generates waste [31, 32, 35–37]. However, due to the negative influence of the burr on the magnetic properties in the cut surface areas, it is recommended to reduce this defect to a minimum.

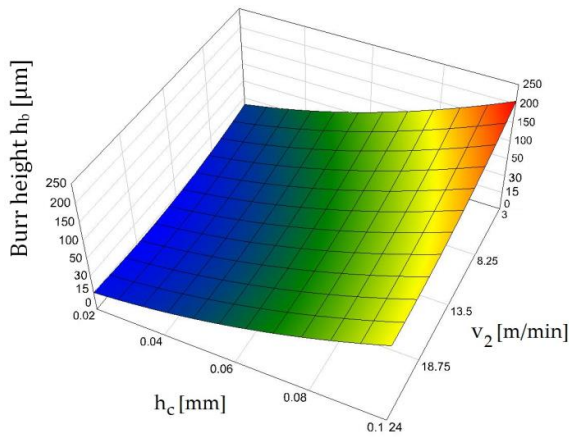


Fig. 9. Influence of the process parameters on burr height for $\alpha = 5^\circ$

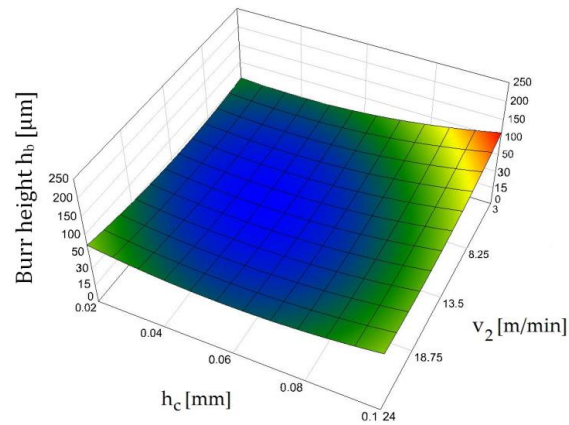


Fig. 10. Influence of the process parameters on burr height for $\alpha = 25^\circ$

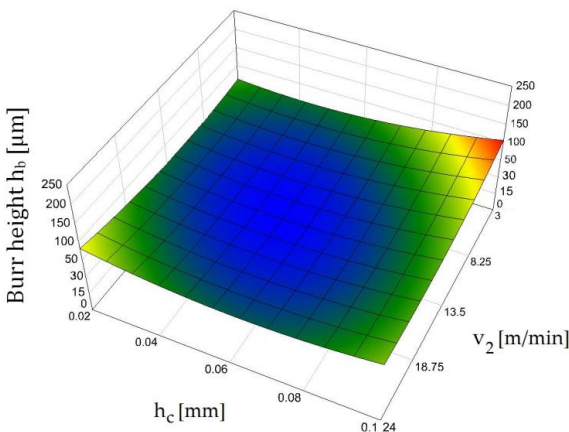


Fig. 11. Influence of process parameters on burr height for $\alpha = 40^\circ$

The aforementioned results show a significant dependence of the burr height on the horizontal clearance. It is preferable to use minimum clearances of $h_c = 0.02\text{--}0.04$ mm for an angle $\alpha = 5^\circ$. In this case, the minimum burr heights can then be achieved. In the case when the rake angle is set $\alpha = 5^\circ$, it is easier

to estimate the height of the burr as a function of the horizontal clearance because there is a linear dependence where the increase in the clearance causes the increase in the burr height. For the maximum clearance $h_c = 0.1$ mm, the burr height is the highest, especially for low cutting speeds, $v_2 = 3\text{--}5$ m/min. By increasing the cutting speed for $h_c = 0.1$ mm clearance value, the burr height can be reduced, but the process conditions will still be unfavourable. When using rake angles of $\alpha = 25^\circ$ and $\alpha = 40^\circ$, the influence of the cutting speed on the burr height decreases, and the horizontal clearance should be selected in the range of $h_c = 0.04\text{--}0.06$ mm. As the authors' previous research has shown, in such a case, an increase in the rollover of the cut edge should be expected, but the burr height will be within the acceptable range [24, 27].

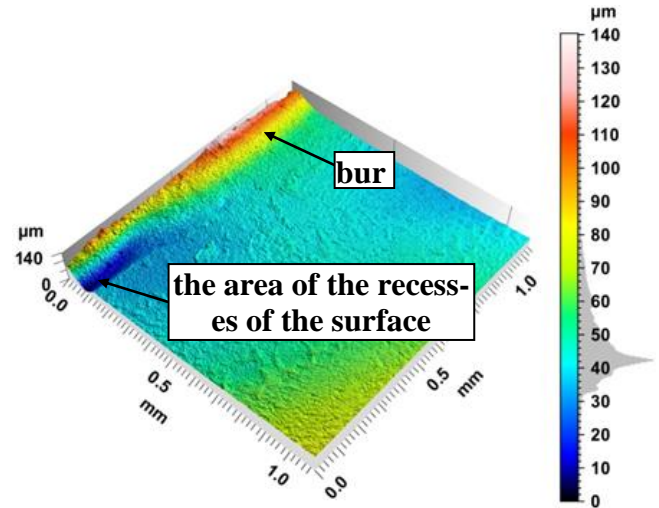


Fig. 12. Geometric structure of the lower surface of the sheet in the area of the cut edge with a visible regular burr for $h_c = 0.08$ mm, $\alpha = 5$ and $v_2 = 8$ m/min

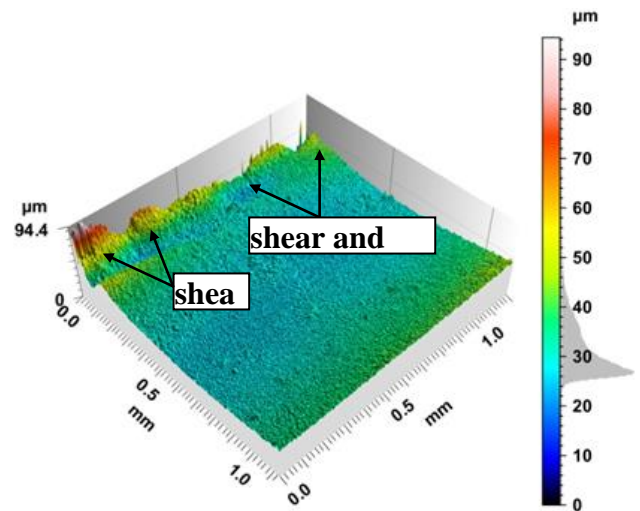


Fig. 13. Geometric structure of the lower surface of the sheet in the area of the cut edge with a visible irregular burr for $h_c = 0.08$ mm, $\alpha = 5^\circ$ and $v_2 = 20$ m/min

In the case of using increased cutting clearances $h_c = 0.08$ mm, the influence of cutting speed on the tensile stress values in the cutting zone was observed, which is reflected in the irregularity of the burr on the cut surface. Similar phenomena occur in the process of cutting metal materials in guillotining [27, 31, 32]. For low cutting speeds $v_2 = 3\text{--}8$ m/min, the burr is higher but more regular along cutting line when $h_c = 0.08$ mm (Fig. 12). It can be

seen that the fracture process becomes less steady as the cutting speed increases and progresses in a non-uniform manner. The transition of the material fracture from the “shear mode” to the “shear and tear mode” is observed (Fig. 13). The burr formation is a result of the transition of the material fracture. As a result, the material may tear locally, the flow phase will be broken and burr-free areas will be formed due to the “shear and tear mode”.

Experimental analysis showed the formation of a characteristic recess just behind the burr line in the case where $h_c = 0.08$ mm and $v_2 = 8$ m/min, which may indicate the area of local microcracks (Fig. 12). It is presumed that the microcracks located in the burr areas damage the magnetic domains and increase the hysteresis losses [28, 30].

Based on numerical research and experimental studies, using the theory of identification of multidimensional objects, regression functions for the following results factors were developed:

1. The width of the deformation-affected zone:
 $D_{mz} = 99.28 + 889.58 \cdot h_c + 1.07 \cdot v_2 + 0.61 \cdot \alpha + -130.83 \cdot c_v - 6.54 \cdot h_c \cdot v_2 - 11.07 \cdot h_c \cdot \alpha + 375 \cdot h_c \cdot c_v - 0.02 \cdot v_2 \cdot \alpha + 3.33 \cdot v_2 \cdot c_v + 2 \cdot \alpha \cdot c_v; R^2 = 0.98$ (1)

2. Burr height:
 $h_b = 82.32 - 195.38 \cdot h_c - 4.32 \cdot v_2 + 8.87 \cdot \alpha + -2735.11 \cdot c_v - 35.11 \cdot h_c \cdot v_2 - 104.64 \cdot h_c \cdot \alpha + 16375 \cdot h_c \cdot c_v + 0.11 \cdot v_2 \cdot \alpha - 20.47 \cdot v_2 \cdot c_v - 36.85 \cdot \alpha \cdot c_v + 16848.95 \cdot h_c^2 + 0.19 \cdot v_2^2 + 0.008 \cdot \alpha^2 + 13783.33 \cdot c_v^2; R^2 = 0.98$ (2)

3. Hysteresis loop area:
 $h_f = c + b_h h_c + b_v v_2 + b_{hv} h_c v_2 - a_h h_c^2 + a_v v_2^2$ (3)
 $R^2 = 0.98.$

The data from the experiments allowed determining the coefficients of Eq. (3) for three average amplitudes of the magnetic field intensity. They are summarised in Tab. 1.

Tab. 1. List of coefficients of Eq. (3) for various field values H_m

$H_m \frac{A}{m}$	c	b_h	b_v	b_{hv}	a_h	a_v
214.32	6,502	281,02 0	282. 6	-449. 9	32,229,25 0	-9.56
497.84	17,30 6	394,35 0	467. 2	763.4	3,451,370	-15.1 7
568.79	22,72 3	358,71 0	295. 5	-558. 9	3,122,970	6.4

Fig. 14 shows three surfaces for three values of the magnetic field intensity. Graph reveals the characteristic maximum hysteresis area for all three surfaces. The value of this parameter is particularly sensitive to changes in vertical clearance.

Fig. 15 shows the hysteresis loops of ET 122-30 steel with a thickness of $t = 0.3$ mm after the cutting process with variable values of the cutting clearance h_c . The example results presented were performed for the value of the rake angle $\alpha = 7^\circ$, cutting speed $v_2 = 15$ m/min, overlap of the knives $c_v = 0.1$ mm and $H_m = 285$ A/m. The hysteresis loop of the soft magnetic material is narrow due to the low values of the coercivity intensity H_k . In the case of hard magnetic materials (permanent magnets), the most important feature is the amount of stored magnetic energy, the aim is to obtain the maximum width of the hysteresis loop and large H_k values. The negative influence of the increased cutting clearance above $h_c = 0.06$ mm on the characteristics of the hysteresis loop is noticed (Fig. 15). Changes in the shapes of the hyste-

resis loop can be observed in the areas of the upper bend of the characteristic and saturation. With cutting clearance $h_c = 0.02$ mm, no significant changes were observed in the characteristics of the saturation area and the maximum saturation induction value B_{max} . This is related to the area of concentration of the maximum plastic deformations occurring only in the vicinity of the cutting edge of the material. In the case of increased cutting clearances, the value of the saturation induction decreases. It is especially visible above the clearance value $h_c = 0.06$ mm. The increase in the h_c parameter also causes an increase in the intensity of coercivity and induction of remanence B_s . This is probably related to the increased deformed zone and the concentration of maximum deformations on a larger area of the cut edge, as well as the occurrence of burr and rollover edges. The least unfavourable changes in the parameters of the hysteresis loop occur for the experiments performed with the cutting clearance $h_c \leq 0.04$ mm. Then, there is the highest maximum induction and the smallest coercivity intensity.

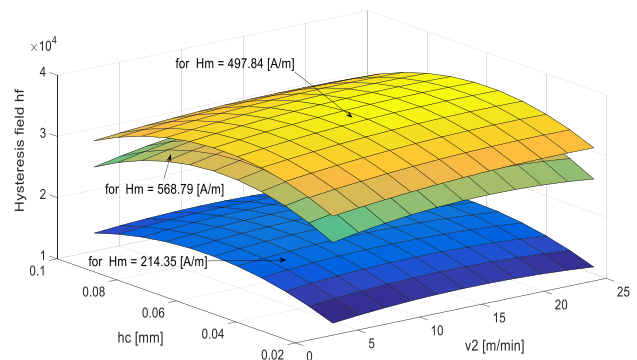


Fig. 14. Graph of the function $h_f = f(h_c, v_2)$ for chosen amplitudes of field intensity H ($H_m = 214.35$ [A/m], $H_m = 497.84$ [A/m] and $H_m = 568.79$ [A/m])

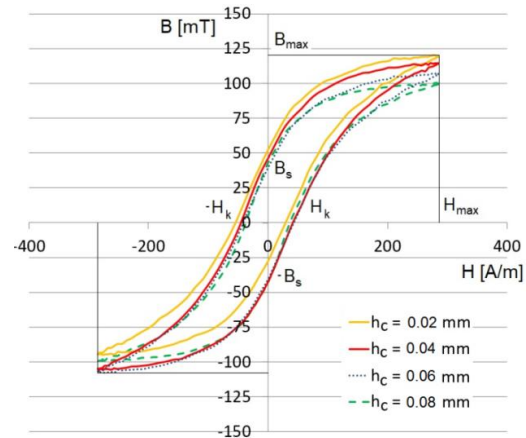


Fig. 15. Influence of selected values of clearance h_c on the magnetic $B(H)$ characteristics of the ET 122-30 steel after shear slitting

6. SHEAR SLITTING PROCESS OPTIMISATION

The available literature includes models that allow controlling the technological quality of the mechanical cutting process, for example, in terms of the obtained quality of the sheared edge of construction steel [15, 31, 32]. However, there are no data and guidelines for the selection of parameters for the mechanical cutting of soft magnetic materials, where apart from the quality of the cut

edge, attention should be paid to the condition of the magnetic properties after the process. A defined problem occurs in the manufacture of electrical machinery such as electric motor cores and transformers.

Based on developed mathematical models of the process (type II regression functions of D_{mz} , h_b and h_r), an optimisation task was developed. From the industrial production point of view, it is necessary to deliver products of planned, repeatable technological quality while maintaining high process efficiency. Therefore, the characteristics responsible for ensuring structural quality (important, e.g., from the point of view of sheet metal assembly) and electromagnetic quality (important, e.g., from the point of view of the efficiency of manufactured machines and electrical devices) should be specified. In order to carry out multi-parameter optimisation of the mechanical cutting process of grain-oriented silicon steel, the gradient method and the MATLAB Optimisation toolbox were used. In the considered case, the efficiency of the mechanical cutting process was defined as $W = v_2$, where v_2 – cutting speed.

The optimisation task has been defined as follows using a type II regression function, which can be an objective function or a constraint function:

$W=f(v_2) \rightarrow \max$ $h_r < 3200 \text{ (mT}\cdot\text{A/m)}$ $D_{mz} < 130 \text{ (}\mu\text{m)}$ $h_b < 60 \text{ (}\mu\text{m)}$ $3 < v_2 < 24 \text{ (m/min)}$ $0.02 < h_c < 0.1 \text{ (mm)}$	}	Cutting process efficiency $W \rightarrow$ maximum Area of magnetic hysteresis loop limitation Limitation on the width of the damage zone Burr height limitation Limitation on cutting speed Limitation on the horizontal clearance
--	---	--

Fig. 16 shows a set of acceptable variants in the area of controllable variables. From a technological point of view, the use of low cutting speeds significantly reduces the efficiency of the process. Therefore, in the case under consideration, it is most advantageous to use the following technological parameters of the process: $v_{2op} = 11.85 \text{ m/min}$ and $h_c = 0.026 \text{ mm}$. The applied approach makes it possible to carry out analyses for other input data. This is important because optimisation analyses should be carried out each time when selecting technological parameters of the electrical sheet cutting process because the elements for the construction of electric transformer cores should be cut with different technological parameters depending on the transformer operating conditions.

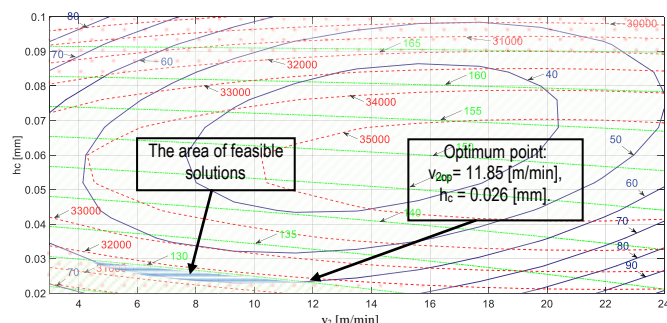


Fig. 16. Result of solving the optimisation task with a set of possible variants in the area of controllable variables

7. CONCLUSIONS

The mechanical cutting process of magnetically soft materials is complicated due to nonlinearities and distortions. The selection

of technological parameters is difficult, which results in the generation of waste on production lines. In the case of industrial production, the process parameters should be selected so as to obtain high production efficiency and high product quality. After the research, the following detailed conclusions can be drawn:

- The obtained test results indicate that the lowest process stability is obtained at high cutting speeds of $v_2 = 20 \text{ m/min}$ or above this value. This especially applies to the variants of clearances $h_c = 0.06\text{--}0.08 \text{ mm}$. The cut edge in this case is characterised by the presence of burrs and an excessive deformation-affected zone.
- The shear slitting process changes the characteristics of the hysteresis loop in the areas of the upper curve and saturation bend. In the case of increased cutting clearances, the value of the saturation induction decreases. It is particularly noticeable with the value of the clearance $h_c = 0.08 \text{ mm}$. The increase in cutting clearance causes an increase in the intensity of coercivity and induction of remanence.
- The increase in the width of the deformation-affected zone and the height of burrs was associated with greater changes in the characteristics of the magnetic hysteresis loop. Therefore, it can be predicted that there are certain ranges of variability of the technological parameters of the process, which will enable obtaining minimal changes in magnetic properties depending on the given thickness of the sheet and the type of material being cut.
- The developed optimisation task makes it easier for the technologist to choose the best solution for the given cutting conditions and optimisation criteria. This is of great importance in practical applications, where the key is to control the performance of the product. For the analysed case, the optimal parameters for shear slitting were determined, which are $v_{2op} = 11.85 \text{ m/min}$ and $h_c = 0.026 \text{ mm}$.

REFERENCES

1. Siebert R, Schneider J, Beyer E. Laser cutting and mechanical cutting of electrical steels and its effect on the magnetic properties, *Mag, IEEE Trans* on. 2014; 50: 1–4. Available from: <https://ieeexplore.ieee.org/document/6798045>
2. Slota J, Kaščák L, Kut S. FEM Modeling of shear cutting of electrical steel sheets under various technological conditions. *Acta Mech Slo2018*; 22 (4): 24–30. Available from: <https://www.actamechanica.sk/pdfs/ams/2018/04/04.pdf>
3. Ghadbeigi H, Al-Rubaye A, Robinson F.C.J, et al., Blanking induced damage in thin 3.2% silicon steel sheets. *Prod Eng.* 2020; 14: 53–64.
4. Weiss H. A, Leuning N, Steentjes S, et al., Influence of shear cutting parameters on the electromagnetic properties of non-oriented electrical steel sheets. *Jl of Magn and Mag Mat* 2017; 421: 250–259. Available from: <https://www.sciencedirect.com/science/article/abs/pii/S030488531631294X>
5. Zhao Z, Song R, Wang Y, Wang Y, Hu Ch, Zhang Y. Slanted blades optimizing grain texture and work hardening of non-oriented electrical steel in stress coverages during shearing and blanking processes. *Steel Res Int* 2021; 92, 2100233, 1-7.
6. Paltanea G, Manescu V, Nemoianu I.V, Gavrilă H, Andrei P.C. Influence of cutting technologies on the magnetic anisotropy of grain oriented electrical steel. In 2017 Electric Vehicles Int Conf, EV 2017, volume 2017-Janua, pages 1–4, 2017.
7. Hofmann M, Naumoski H, Herr U, Herzog H.-G. Magnetic properties of electrical steel sheets in respect of cutting: Micromagnetic analysis and macromagnetic modeling. *IEEE Trans on Mag* 2016; 52, 1–14. Available from: <https://ieeexplore.ieee.org/document/7286823>

8. Moses A.J. Energy efficient electrical steels: magnetic performance prediction and optimization. *Scri Mat* 2012; 67 (6), 560–565. Available from: <https://www.sciencedirect.com/science/article/abs/pii/S1359646212001297>
9. Naumoski H, Riedmüller B, Minkow A, Herr U. Investigation of the influence of different cutting procedures on the global and local magnetic properties of non-oriented electrical steel. *J of Magn and Mag Mat* 2015; 392, 126–133. Available from: <https://www.sciencedirect.com/science/article/abs/pii/S0304885315301554>
10. Lewis N, Anderson P, Hall J, Gao Y. Power loss models in punched non-oriented electrical steel rings. *IEEE Trans on Mag.* 2016; 52(5), 1–4. Available from: <https://ieeexplore.ieee.org/document/77428928>
11. Kuo S.K, Lee W.C, Lin S.Y, Lu C.Y. The influence of cutting edge deformations on magnetic performance degradation of electrical steel. 2014 17th Int Conf on Electr Mach and Systems (ICEMS), 2014; 3041-3046.
12. LoBue M, Sasso C, Basso V, Fiorillo F, Bertotti G. Power losses and magnetization process in Fe–Si non-oriented steels under tensile and compressive stress. *J of Magn and Mag Mat* 2000; 215–216, 124–126. Available from: <https://www.sciencedirect.com/science/article/abs/pii/S0304885300000925>
13. Boehm L, Hartmann C, Gilch I, Stoecker A, Kawalla R, Wei X, Hirt G, Heller M, Korte-Kerzel S, Leuning N, et al. Grain size influence on the magnetic property deterioration of blanked non-oriented electrical steels. *Materials* 2021, 14, 7055. Available from: <https://www.mdpi.com/1996-1944/14/22/7055>
14. Wang X, Wang Z, Cui R, Li Sh. Influence of blanking process on the magnetic properties of non-oriented electrical steel lamination. *J of Shanghai Jiao Tong University.* 2019; 53(9), 1115-1121.
15. Wang N, Golovashchenko S.F. Mechanism of fracture of aluminum blanks subjected to stretching along the sheared edge. *J of Mat Proc Tech* 2016; 233, 142–160. Available from: <https://www.sciencedirect.com/science/article/abs/pii/S0924013616300553>
16. Cao H, Hao L, Yi J, Zhang X, Luo Z, Chen Sh, et al., The influence of punching process on residual stress and magnetic domain structure of non-oriented silicon steel. *J of Magn and Mag Mat* 2016; 406, 42–47. Available from: <https://www.sciencedirect.com/science/article/abs/pii/S0304885315309586>
17. Bayraktar Ş, Turgut Y. Effects of different cutting methods for electrical steel sheets on performance of induction motors. *Proc of the Institution of Mech Eng, Part B: J of Eng Man* 2018; 232 (7), 1287–1294.
18. Dems M, Komezka K, Kubiak W, Szulakowski J. Impact of core sheet cutting method on parameters of induction motors. *Energies.* 2020; 13 (8), 1960. Available from: <https://www.mdpi.com/1996-1073/13/8/1960>
19. Vandenbossche L, Jacobs S, Henrotte F, Hameyer K. Impact of cut edges in magnetization curves and iron losses in e-machines for automotive traction, in *Proc of 25th World Battery, Hybrid and Fuel Cell Electric Vehicle Symp & Exhibition, EVS, (Schenzen, China), November 2010.*
20. Hirsch M, Demmel P, Golle R, Hoffmann H. Light metal in high-speed stamping tools, *Key Eng Mat* 2001; 473, 259–266.
21. Harstick H.M.S, Ritter M, Plath A, Riehemann W. EBSD Investigations on cutting edges of non-oriented electrical steel. *Met, Micr and Analysis.* 2014; 3 (4), 244–251.
22. Kaldunski P, Kukielka L. The numerical analysis of the influence of the blankholder force and the friction coefficient on the value of the drawing force, *PAMM.* 2007; 7 (1), 4010045-4010046. Available from: <https://onlinelibrary.wiley.com/doi/pdf/10.1002/pamm.200701059>
23. Kukielka L. *Podstawy Badań Inżynierskich; Politechnika Koszalińska: Koszalin, Poland; PWN: Warszawa, Poland, 2002. (In Polish)*
24. Bohdal L. Application of a SPH coupled FEM method for simulation of trimming of aluminum autobody sheet. *Acta Mech et Aut.* 2016; 10(1), 56–61.
25. Chodor J, Kukielka L. Using nonlinear contact mechanics in process of tool edge movement on deformable body to analysis of cutting and sliding burnishing processes, *App Mech and Mat* 2014; 474, 339–344.
26. Johnson G.R, Cook W.H. A constitutive model and data for metals subjected to large strains, high strain rates and high temperatures. 7th International Symposium on Ballistics, The Hague, The Netherlands. 1983; 541–548.
27. Bohdal Ł. Teoretyczne i doświadczalne podstawy optymalizacji procesów cięcia mechanicznego stopów metali lekkich i stali elektrotechnicznych. Monografia Wydziału Mechanicznego nr 344, Wydawnictwo Uczelniane Politechniki Koszalińskiej, Koszalin. 2018. ISSN 0239-7129, ISBN 978-83-7365-7481-5 (In polish).
28. Alatawneh A, Saleem A, Rahman T, Lowther D.A, Chromik R. Modeling and analysis of the effects of cutting of core laminations in electric machines, *IET Electric Power Appl* 2020; 14 (12), 2355–2361. Available from: <https://ietresearch.onlinelibrary.wiley.com/doi/full/10.1049/iet-epa.2020.0218>
29. Bratus V, Kosel F, Kovac M, Hidria. Determination of optimal cutting edge geometry on a stamped orthotropic circular electrical steel sheet, *J of Mat Proc Tech* 2005; 210 (2), 396-407. Available from: <https://www.sciencedirect.com/science/article/abs/pii/S092401360903616>
30. Demir A, Ocak O, Ulu Y. Impact of lamination processing methods on performance of permanent magnet synchronous motors. In: *Int conf on electr mach (ICEM), Berlin, 2–5 September 2014, 1218–1223.*
31. Hilditch T.B, Hodgson P.D. Development of the sheared edge in the trimming of steel and light metal sheet, Part 1 - Experimental observations. *J of Mat Proc Tech.* 2005; 169, 184–191. Available from: <https://www.sciencedirect.com/science/article/abs/pii/S0924013605004620>
32. Hilditch T.B, Hodgson P.D. Development of the sheared edge in the trimming of steel and light metal sheet, Part 2 - Mechanisms and modeling. *J of Mat Proc Tech* 2005; 169, 192–198. Available from: <https://www.sciencedirect.com/science/article/abs/pii/S0924013605004632>
33. Klimczyk PK, Anderson P, Moses A. Influence of cutting techniques on magnetostriction under stress of grain oriented electrical steel. *IEEE Trans on Mag* 2012; 48, 1417–1420. Available from: <https://ieeexplore.ieee.org/document/6172341>
34. Kukielka L. Nonlinear modeling for elasto/visco – plastic contact problem in technological processes, *International Scientific IFNA – ANS Journal, Problems of non – linear Analysis in Engineering Systems* (2) (2004) 39-53.
35. Kurosaki Y, Mogi H, Fujii H. Importance of punching and workability in non-oriented electrical steel sheets. *J of Magn and Mag Mat* 2008; 320, 2474–2480. Available from: <https://www.sciencedirect.com/science/article/abs/pii/S0304885308003879>
36. Manescu V, Paltanea G, Gavrilă H. Some important effects of the water jet and laser cutting methods on the magnetic properties of the non-oriented silicon iron sheets. In: *9th intsymp on adv topics in electr eng (ATEE), Bucharest, Romania, 7–9 May 2015, pp.7–9.*
37. Pulnikov A, Baudouin P, Melkebeek J. Induced stresses due to the mechanical cutting of non-oriented electrical steels. *J of Magn and Mag Materials.* 2003; 254–255, 355–357. Available from: <https://www.sciencedirect.com/science/article/abs/pii/S0304885302008533>

 Patyk Radosław:  <https://orcid.org/0000-0003-3148-5488>

 Bohdal Łukasz:  <https://orcid.org/0000-0002-8085-9530>

 Gontarz Szymon:  <https://orcid.org/0000-0002-7507-7243>